NORTHWESTERN UNIVERSITY

Fundamentals and Applications of Surface-Enhanced Coherent Raman Scattering

A DISSERTATION

SUBMITTED TO THE GRADUATE SCHOOL
IN PARTIAL FULFILLMENT OF THE REQUIREMENTS

for the degree

DOCTOR OF PHILOSOPHY

Field of Chemistry

By

Michael O. McAnally

EVANSTON, ILLINOIS

September 2017

© Copyright by Michael O. McAnally 2017

All Rights Reserved

ABSTRACT

Fundamentals and Applications of Surface-Enhanced Coherent Raman Scattering

Michael O. McAnally

Plasmonic chemistry is an emerging field of research that contains great promise for new chemical reactivity, but thus far has been improperly observed. The goals of using plasmonic chemistry typically revolve around the use of nonequilibrium charge carriers that migrate to the surface of a plasmonic substrate to perform redox chemistry on surface adjacent molecular species. The process of plasmonic chemistry encompasses many different time scales from the first few tens of femtoseconds into the nanoseconds for full system relaxation - however, most claims of plasmonic chemistry report steady-state spectroscopic observations. To this end, the work contained in this thesis details the development of a new suite of tools to study plasmonic chemistry on time scales closer to the intrinsic lifetimes of the transient species being studied. This thesis discusses the expansion of surface-enhanced femtosecond stimulated Raman scattering (SE-FSRS), one form of plasmonically-enhanced coherent Raman scattering (PECRS) techniques that are ideally suited for observing the molecule-plasmon interactions involved in chemical change driven or enhanced by plasmonic nanomaterials. Development of new theories for

SE-FSRS, experimental progress in improving SE-FSRS spectrometers, as well as new experiments showing stimulated Raman loss in SE-FSRS will be discussed. An important aspect of this work is the back-and-forth theory-experiment approach that has allowed for continued improvement in the SE-FSRS technique. The classical theory of SE-FSRS explained initial results well, but pushing the experimental techniques further resulted in the need for a new quantum mechanical theory of SE-FSRS. Further developing SE-FSRS experimentally and theoretically will allow for an improved analytical technique that can probe coupled molecule-plasmon interactions, potentially leading to a PECRS spectroscopy that can be used for initiating and tracking plasmonic chemistry.

Professor Richard P. Van Duyne
Research Advisor

Professor George C. Schatz
Research Advisor

Acknowledgements

There are just so many people to thank. First and foremost my incredible wife: Britni Marie McAnally. I'll get back to thanking Britni in a bit, but there is no way I could have completed this endeavour without her assistance.

Focusing on the science, I'd like to thank both of my advisors: Rick and George. Thank you both for giving me the opportunity to work on the research described herein. Both of you have mastered the art of letting your researcher go forth with a long rope and be "happy" regardless of the result: paper or burnt fiber laser amplifier. Thank you for the fun scientific discussions and guidance that pushed me to become better.

Thanks also to my (extended) thesis committee members: Professors Tamar Seideman, Franz Geiger, Neil Kelleher, and Emily Weiss. I wouldn't be the scientist I am today without hearing their outside views and perspectives on how to approach research. Tamar - I've always enjoyed our discussions on how experiment and theory go hand-in-hand in the spectroscopy world. Franz - thanks for your criticisms, it is important to hear views from outside the echo chamber. Emily - thanks for letting me be a failure of a synthetic chemist in your lab during the Summer of 2012. Also, the ever useful guidance of talking to George is something more graduate students should hear. Neil - while my three point shot is still better than your's, I know the one point I got on you in racquetball was a pity point. I'm ok with that. I've greatly enjoyed getting to know both you and your lab professionally (FIRE!) and personally (racquetball).

In thinking about the past five years at Northwestern I'd be remiss if I didn't thank the amazing people I've encountered as mentors, colleagues, and friends. I must thank some of the people who helped train me along in this path - Natalie Gruenke, Bogdan Negru, Lauren Buchanan, Eric Pozzi, Fernanda Cardinal, Jon Dieringer, Jeff McMahon, Nicolas Large, and Ryan Young. This group taught me a lot about optics, lasers, nanoparticles, and electrodynamics. All in the name of understanding how light couples with tiny chunks of metal. In particular, I must thank Bogdan Negru. No matter our disagreements about bacon, cheese, and donkeys, your support early in graduate school was critical for my success. In addition to my mentors, I want to thank all of my colleagues and collaborators over the years. While reading this thesis, always keep in mind this was more than the work of a single individual. Also, I'm keeping an eye on my Team Ultrafast colleagues and students I've helped mentor. I can't wait to see how you all finish off your thesis and postdoctoral research: Emily Sprague-Klein, Tyler Ueltschi, Yinsheng Guo, Yue Wu, Ryan Hackler, and Emma Vander Ende.

In big groups of thanking: Van Duyne group (4:30*ish* is quitting time on Friday), Schatz (and larger sense Theory) groups, ChemBallers (football and basketball - we finally won some games!), Northwestern Chemistry department staff (particularly after the Packers would beat the Bears), TGBC, and P-Chem Plus. Going more in-depth with thanks of people who were incredibly supportive and always down for a quick beer/coffee: Craig Chapman, Andrew Sirjoosingh, Shane Parker, Josh Szekeley, Mike Ross, Owen Skinner, Chad Heapes, and Matt Kelley. Then my UW-Eau Claire friends: Josh Jordan, Jordan Montpetit, and Oakley Moser. Thanks guys for always being up for a chat or a meet up back in America's greatest state.

My family also deserves a big thank you. I still probably haven't convinced you all about why I've been in school til almost the age of 30 to be "one of those doctors," but I promise it was worth it. I think. Thank you for your support and love. Knowing that going back up north with Britni always ended up as an excuse to get family together made those five hour trips worth it.

Coming full circle: thank you Britni for always being there and having a tremendous amount of faith in what I'm doing. Even when I would have terrible days in lab because something broke or didn't work again, I never worried. I knew that I'd come home, see you, and everything would be better. You push me to be better, work harder, and keep an eye on the big picture. Thank you so much for always being confident in my abilities even when I'm not.

Thanks everyone for being a part of this. Can't wait to see what happens next.

List of abbreviations

ACPF	Asymmetric charge partitioning factor
AFM	Atomic force microscopy
ALD	Atomic layer deposition
aSt	Anti-Stokes
AuNR	Gold nanorod
BBO	β-barium borate
BDP	Bonding dipole plasmon
BPE	*trans*-1,2-bis(4-pyridyl)ethylene
BPY	Bipyridine
CAD	Collisionally activated dissociation
CARS	Coherent anti-Stokes Raman scattering
CCD	Charge-coupled device
CHEM	Chemical enhancement mechanism
$\boldsymbol{\chi^{(n)}}$	$\mathrm{n^{th}}$ order nonlinear optical susceptibility
CHX/chx	Cyclohexane
CRS	Coherent Raman scattering
CTP	Charge transfer plasmon
CW	Continuous wave
DFT	Density functional theory

DMACl	Dimethylaluminum chloride
EF	Enhancement factor
EM	Electromagnetic mechanism
ETD	Electron transfer dissociation
FDTD	Finite-difference time-domain
FEM	Finite element method
FIRE	Front-end infrared excitation
FON	Film-over-nanospheres
FRIKES	Femtosecond Raman-induced Kerr-effect scattering
FSRRS	Femtosecond stimulated resonance Raman scattering
FSRS	Femtosecond stimulated Raman scattering
FWHM	Full-width at half-maximum
$\boldsymbol{g_\omega}$	Local field effect evaluated at frequency ω
glu	Glucose
HL	Hot luminescence
Im	Imaginary
IR	Infrared
IRS	Inverse Raman scattering
IVS	Impulsive vibrational scattering
kHz	Kilohertz
LFE	Local field effect
LSPR	Localized surface plasmon resonance
MHz	Megahertz

MWIR	Midwave infrared
NA	Numerical aperture
Nd:YAG	Neodymium-doped yttrium aluminum garnet
NDF	Neutral density filter
NECD	Native electron capture dissociation
nESI	Native electrospray ionization
NIR	Near-infrared
NOPA	Noncollinear optical parametric amplifier
NR	Nonresonant
NRS	Normal Raman scattering
NT	Nanotag
nTDMS	Native top down mass spectrometry
OHD-FRIKES	Optically-heterodyned femtosecond Raman-induced Kerr-effect scattering
OHD-SE-FRIKES	Optically-heterodyned surface-enhanced femtosecond Raman-induced Kerr-effect scattering
OPA	Optical parametric amplifier
$\boldsymbol{P^{(n)}}$	n$^{\text{th}}$ order nonlinear polarization
PE	Plasmonic enhancement
PECRS	Plasmonically-enhanced coherent Raman scattering
PiFM	Photo-induced force microscopy
PLE	Plasmon luminescence/emission
pr	Raman probe field

pu	Raman pump field
q	Fano asymmetry parameter
Q	Vibrational coordinate
Re	Real
RegA	Regenerative amplifier
$\boldsymbol{\rho}$	Linear Raman scattering depolarization ratio
RIKES	Raman-induced Kerr-effect scattering
RRS	Resonance Raman scattering
$\mathbf{Ru(bpy)_3{}^{2+}}$	tris(bipyridine)ruthenium(II)
RWA	Rotating wave approximation
S	Scattering factor
SA	Single aggregate
SECARS	Surface-enhanced coherent anti-Stokes Raman scattering
SEF	Surface-enhanced fluorescence
SE-FSRS	Surface-enhanced femtosecond stimulated Raman scattering
SE-FRIKES	Surface-enhanced femtosecond Raman-induced Kerr-effect scattering
SEM	Scanning electron microscope
SERS	Surface-enhanced Raman scattering
SERRS	Surface-enhanced Ramen Raman scattering or surface-enhanced resonance Raman scattering
SFG	Sum-frequency generation
SHG	Second-harmonic generation

Sig/sig	Signal field
SNR	Signal-to-noise ratio
SPM	Scanning probe microscopy
SRG	Stimulated Raman gain
SRL	Stimulated Raman loss
SRS	Stimulated Raman scattering
St	Stokes
TE-BB-CAR	Tip-enhanced broadband coherent anti-Stokes Raman scattering
TECARS	Tip-enhanced coherent anti-Stokes Raman scattering
TEM	Transmission electron microscopy
TERS	Tip-enhanced Raman scattering
TE-SRS	Tip-enhanced stimulated Raman scattering
Ti:sapph	Titanium sapphire
TMA	Trimethylaluminum
TR	Time-resolved
UV	Ultraviolet
XPM	Cross-phase modulation
YAG	Yttrium aluminum garnet
Yb:doped	Ytterbium-doped

Dedication

This work is dedicated to Britni Marie McAnally.

Table of Contents

ABSTRACT 3

Acknowledgements 5

List of abbreviations 8

Dedication 13

Chapter 1. Introduction to Plasmonic Enhancement and Coherent Raman Scattering 25

- 1.1. Abstract 26
- 1.2. Introduction to Plasmonically-Enhanced Optical Processes 26
- 1.3. Introduction to Coherent Raman Scattering 28
- 1.4. Introduction to Plasmonically-Enhanced Coherent Raman Scattering 38
- 1.5. Conclusion 51

Chapter 2. Continous Wave Theory of SE-FSRS 53

- 2.1. Abstract 54
- 2.2. Introduction 54
- 2.3. Theory 59
- 2.4. Discussion 74
- 2.5. Conclusion 79
- 2.6. Supplementary Information 81

Chapter 3. Towards a Quantum Mechanical Theory of SE-FSRS 93

3.1. Abstract 94
3.2. Introduction 94
3.3. Survey of New Theoretical Methods for SE-FSRS 95
3.4. Conclusion 108

Chapter 4. Optically heterodyned femtosecond Raman-induced Kerr-effect scattering 109
4.1. Abstract 110
4.2. Introduction 110
4.3. Experimental Details 115
4.4. Results and Discussion 116
4.5. Conclusion 121
4.6. Supplementary Information: OHD-SEFRIKES 122

Chapter 5. Improving Surface-Enhanced Femtosecond Stimulated Raman Scattering Spectrometers 127
5.1. Abstract 128
5.2. Improving 100 kHz Surface-Enhanced Femtosecond Stimulated Raman Spectrometers by Removing Cross-Phase Modulation 129
5.3. Surface-Enhanced Femtosecond Stimulated Raman Spectroscopy at 1 MHz Repetition Rates 135
5.4. Studying stimulated Raman gain and loss by wavelength-sampled excitation in surface-enhanced femtosecond stimulated Raman spectroscopy 157
5.5. Towards Single-Aggregate SE-FSRS 173

5.6. Conclusion 187

Chapter 6. Quantitative Determination of the Differential Raman Scattering Cross-Sections of Glucose by Femtosecond Stimulated Raman Scattering 189

6.1. Abstract 190

6.2. Introduction 190

6.3. Experimental Details 194

6.4. Results and Discussion 197

6.5. Conclusions 199

6.6. Supplementary Information 203

Appendix A. Original Research Proposal: Controlling charge transfer plasmons for infrared nanoantennae 215

A.1. Statement of Objectives 215

A.2. Research Effort 216

A.3. Experimental Results, Significance, Application 225

A.4. Conclusion 228

Appendix B. Calculated Surface-Enhanced Raman Spectra of Atomic Layer Deposition Precursors 229

B.1. Abstract 230

B.2. Gas-Phase Trimethylaluminum Raman Scattering Calculations 230

B.3. Silver Cluster-Trimethylaluminum Raman Scattering Calculations 231

B.4. Silver Cluster-DMACl Raman Scattering Calculations 235

Appendix C. Electronic Structure Calculations of Various Spectroscopic Analytes 240

- C.1. Static Raman Scattering of Bipyridine Isotopologues in Neutral and Anionic States 241
- C.2. Static Raman Scattering of Carbon Dioxide Reducing Rhenium Complexes on Gold Clusters 246

Appendix D. Surface-Enhanced Ramen Raman Scattering 252

- D.1. Introduction 253
- D.2. Experimental Methods 253
- D.3. Results and Discussion 254
- D.4. Conclusion 260

Appendix E. Native Electron Capture Dissociation Characterizes Iron-Binding Channels in Horse Spleen Ferritin 261

- E.1. Abstract 262
- E.2. Introduction 262
- E.3. Experimental Methods 264
- E.4. Results and Discussion 265
- E.5. Conclusion 274
- E.6. Supplementary Information 275

References 281

Curriculum Vitae 305

List of Tables

5.1 Summary of experimental conditions for wavelength-sampled SE-FSRS. 160

6.1 DRSCs of glucose measured using SRL and SRG. 198

6.2 Depolarization ratios of glucose and cyclohexane. 206

6.3 Peak position and FWHM of fitted toluene FSRS spectra. 213

A.1 Gantt chart showing project schedule of the research effort described in this proposal. 227

C.1 Tentative mode assignments for simulated Raman of neutral and radical BPY. 242

List of Figures

1.1 Localized surface plasmon resonance (LSPR). 27

1.2 Generalized coherent Raman scattering scheme. 30

1.3 FSRS 4WMEL diagram. 32

1.4 Spectral representation of pulses used in FSRS. 32

1.5 Phase-matching conditions in CARS. 37

1.6 Plasmonically-enhanced coherent Raman scattering. 38

2.1 Field-matter interactions in FSRS. 56

2.2 Structure for molecular polarizability calculations in SE-FSRS simulations. 76

2.3 Simulation of SE-FSRS for BPE coupled to 825 nm LSPR. 77

2.4 Simulation of SE-FSRS for BPE coupled to 900 nm LSPR. 78

2.5 Simulation of SRL in SE-FSRS for BPE. 84

2.6 Spheroidal plasmonic nanoparticle approximation. 85

2.7 Complex frequency dependence of $\tilde{\alpha}_P$ for an LSPR near 825 nm. 86

2.8 Complex frequency dependence of $\tilde{\alpha}_P$ for an LSPR near 900 nm. 87

2.9 SE-FSRS near plasmon resonances from 800 nm to 900 nm. 90

2.10 SE-FSRS near plasmon resonances from 925 nm to 1025 nm. 91

2.11 SE-FSRS near plasmon resonances from 1050 nm to 1125 nm. 92

3.1 The eight resonant Feynman diagrams involved in the FSRS process. 97

3.2 Resonant Feynman diagram for CARS. 106

4.1 Polarization sensitive cyclohexane FSRS. 113

4.2 Experimental setup for FSRS and OHD-FRIKES. 114

4.3 2D experimental plot of cyclohexane OHD-FRIKES. 117

4.4 2D experimental plot of 801 cm^{-1} mode of cyclohexane. 118

4.5 Simulation of 2D OHD-FRIKES for 801 cm^{-1} mode of cyclohexane. 119

4.6 1D cuts of 2D OHD-FRIKES experimental data. 120

4.7 1D cuts of 2D OHD-FRIKES simulated data. 120

4.8 SE-FSRS of BPE NT's used in OHD-SEFRIKES experiment. 124

4.9 Comparison of BPE NT's SEFRIKES to SE-FSRS. 125

4.10 Comparison of BPE NT's OHD-SEFRIKES to SE-FSRS. 126

5.1 Schematic of 100 kHz SE-FSRS laser system. 131

5.2 XPM-suppresion module. 132

5.3 XPM-suppressed CHX FSRS. 133

5.4 XPM-suppressed BPE NT's SE-FSRS 134

5.5 Equal pump power comparison of FSRS and SE-FSRS. 140

5.6 Equal pulse energy comparison of FSRS and SE-FSRS. 143

5.7 FSRS and SE-FSRS signal averaging. 145

5.8 SE-FSRS sample degradation. 147

5.9 Schematic of 1 MHz SE-FSRS laser system. 152

5.10 Schematic of BPE NT's used in SE-FSRS. 153

5.11 Probe field comparison between 100 kHz and 1 MHz. 154

5.12 Anomalous sublinear pump power dependence in SE-FSRS. 155

5.13 SNR of SE-FSRS spectra after 0.3 and 30 minutes. 156

5.14 SRL and SRG FSRS of cyclohexane. 163

5.15 SRL and SRG SE-FSRS of BPE90 pumped at three wavelengths. 165

5.16 SRL and SRG SE-FSRS of BPY60 pumped at three wavelengths. 166

5.17 BPE and BPY NT's samples used in the current study. 171

5.18 1 MHz laser system used in wavelength-sampled SE-FSRS. 172

5.19 Home-made assembly of microscopic FSRS apparatus. 175

5.20 FWMEL diagrams for FSRS/FRIKES and CARS. 176

5.21 Microscope temporal overlap using SFG in a BBO crystal. 177

5.22 CARS and FSRS of cyclohexane using μCRS setup. 178

5.23 Comparison epi- and forward-direction CARS of benzene. 179

5.24 CARS of β-carotene in CHX. 180

5.25 FSRS of β-carotene in CHX. 181

5.26 SECARS of BPE NT's dried on a glass coverslip. 183

5.27 Decay of BPE NT's SECARS signal. 184

6.1 Experimental setup for measuring DRSCs of glucose by FSRS. 194

6.2 Highest and lowest pump energies used in glucose FSRS study. 197

6.3 Comparison of experimental and simulated glucose Raman spectra. 200

6.4 Comparison of experimental and simulated cyclohexane Raman spectra. 201

6.5 Linear regions of stimulated Raman activity in glucose. 204

6.6 Linear regions of stimulated Raman activity in cyclohexane. 205

6.7 FSRS spectral resolution measured by toluene. 212

6.8 Normal Raman scattering (NRS) spectrum of 1 M aqueous glucose. 214

A.1 Creation of tunable plasmon resonances from the NIR to MWIR. 217

A.2 Simulations of AuNR structures by FEM. 218

A.3 Description of proposed work packages. 219

A.4 Pulsed laser concatenation of AuNRs creating CTP modes. 220

A.5 Chemical synthesis of AuNRs. 221

A.6 Transient absorption for measuring plasmonic response of AuNRs. 222

A.7 Creation of transient CTP modes in AuNRs. 224

A.8 Broadband light excitation for AuNR welding. 225

B.1 Optimized gas-phase TMA monomer. 232

B.2 Optimized gas-phase TMA dimer. 233

B.3 Gas-phase Raman of optimized monomer and dimer TMA molecules in the low (A) and high (B) wavenumber regions. 234

B.4 Optimized cluster models for TMA studies. 236

B.5 DFT-calculated Raman spectra in the low wavenumber region of TMA surface species. 238

B.6 DFT-calculated Raman spectra in the low wavenumber region of DMACl surface species. 239

C.1 Calculated Raman scattering of the BPY-d_0 neutral (black) and radical anion (red) species. 243

C.2 Calculated Raman scattering of the BPY-d_8 neutral (black) and radical anion (red) species. 244

C.3 Waterfall plot of BPY SERS spectra. 245

C.4 Comparison of solution-phase NRS, solid NRS, SERS, and DFT-calculated SERS of the Re(bpy)$(CO)_3$Cl system. 248

C.5 Geometry used for DFT-calculated SERS of the Re(bpy)$(CO)_3$Cl system in Fig. C.4. 249

C.6 Normal mode analysis of optimized Re(bpy)$(CO)_3$Cl @ Au_{56} cluster. 249

C.7 Raman scattering of gas-phase Re(bpy)$(CO)_4^+$ structure. 250

C.8 Raman scattering of gas-phase Re(bpy)$(CO)_3CO_2^-$ structure. 250

D.1 Comparison of calculated and experimental BPE SERS from the SERRS substrate. 255

D.2 Control NRS of BPE on Ramen noodle showing only background fluorescence. 256

D.3 Comparison of BPE SERS from a functionalized Ramen noodle and commercial substrate. 257

D.4 SEM image of the SERRS substrate. 258

D.5 FDTD simulation of Ag-coated SERRS substrate. 259

E.1 Analysis of ferritin by native top-down mass spectrometry. 267

E.2 Isolation and CAD fragments provide unambiguous characterization of the NECD-produced c_{44} 5+ fragment ion. 268

E.3 Charge distribution observed in ferritin fragment ions. 271

E.4 The yields of *c*-fragment ions plotted with respect to cleavage site. 273

E.5 Graphical fragment map representation of fragment ions formed from isolation and CAD dissociation of the 14+ ejected ferritin monomer. 276

E.6 Evidence of NECD *c*-fragments from isolation and activation of the intact ferritin complex. 276

E.7 Experimental setup for front-end infrared excitation (FIRE). 277

E.8 Fragment map showing the NECD *c*- and complementary *y*-type cleavage products of cytochrome *c* upon laser activation by FIRE. 277

E.9 Experimental schematic of the FIRE setup highlighting the distance parameters used. 278

E.10 Experimental schematic of the intentionally misaligned FIRE setup. 279

E.11 Fragment map of ferritin activated by FIRE exhibiting *c*-fragments. 280

E.12 Activation of the apo-form of horse spleen ferritin. 280

CHAPTER 1

Introduction to Plasmonic Enhancement and Coherent Raman Scattering

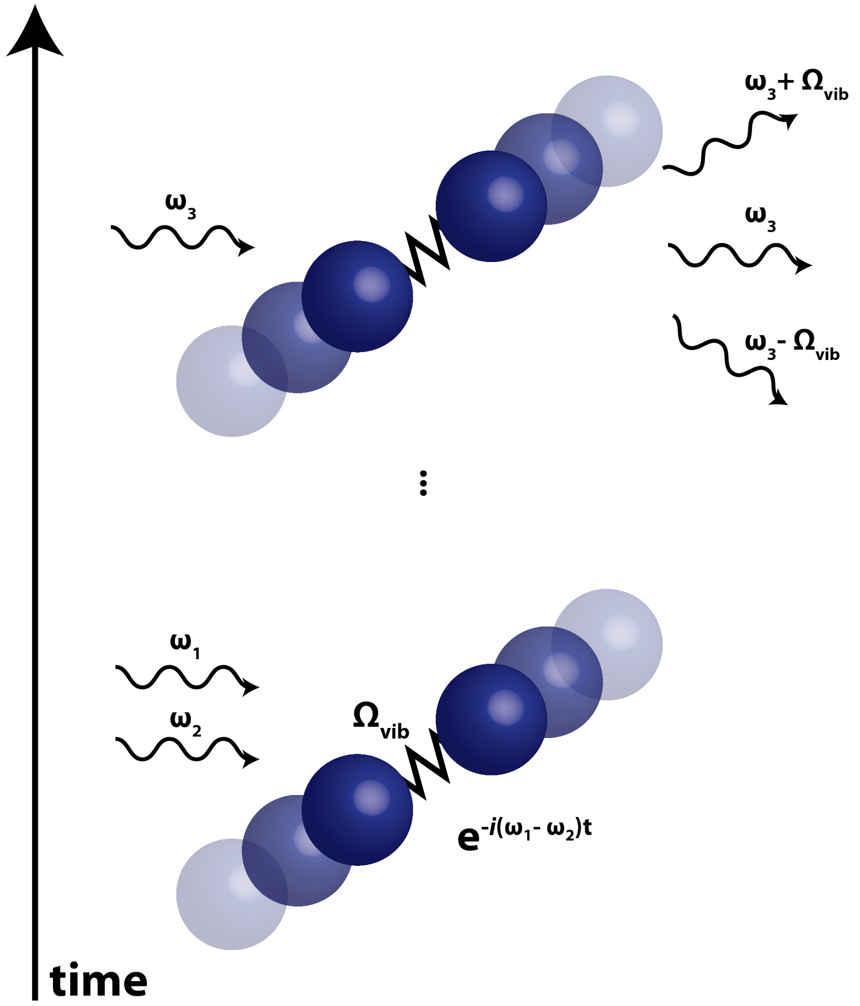

Generalized wave-mixing process in coherent Raman scattering.

1.1. Abstract

This chapter introduces many of the concepts explored throughout this thesis. Namely, the concepts of nonlinear optical spectroscopy and plasmonically-enhanced optical processes. To discuss plasmonic enhancement, a brief survey of surface-enhanced Raman scattering (SERS) and localized surface plasmon resonance (LSPR) spectroscopies will be discussed. SERS and LSPR experiments demonstrate many of the key concepts needed in plasmonically-enhanced coherent Raman scattering (PECRS). Prior to discussing specific coherent Raman scattering experiments, we will cover the basics of nonlinear optics that are required in driving CRS processes. Particular experiments in CRS will be highlighted including: femtosecond stimulated Raman scattering (FSRS), femtosecond Raman-induced Kerr-effect scattering (FRIKES), and coherent anti-Stokes Raman scattering (CARS). After discussing non-surface-enhanced CRS experiments, we'll survey the literature of PECRS experiments that have been performed thus far.

1.2. Introduction to Plasmonically-Enhanced Optical Processes

Plasmons are quasiparticles that consist of an oscillating charge density. An advantageous form of plasmons occur in noble metal nanoparticles. When a plasmon arises in noble metal nanoparticles, these are called *localized surface plasmon resonances* (LSPRs).[1,2] LSPRs are excited when light of the LSPR frequency is incident on the particle surface. The interaction of light with the LSPR creates a distibution of charge carriers near the metal surface (Fig. 1.1). These carriers can then perform 'plasmonic chemistry'.[3] While the focus of this chapter isn't on plasmonic chemistry, we do reference the field for motivation in developing new experimental and theoretical techniques discussed throughout.

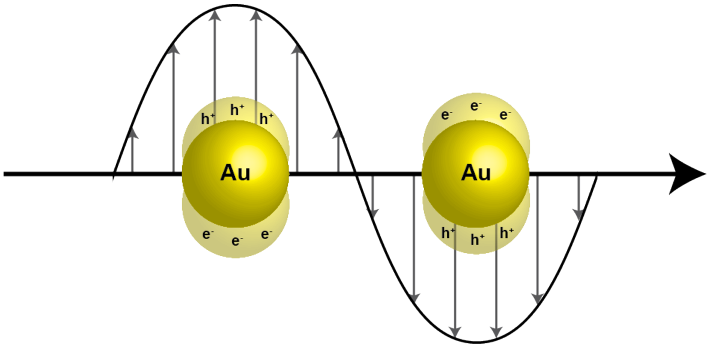

Figure 1.1. Localized surface plasmon resonance (LSPR) in Au nanoparticles. Charges oscillate in the noble nanoparticle structure along the amplitude of the incident field.

The general mechanism of plasmonic chemistry is that charge carriers near the surface can interact with surface-adsorbed molecules performing reductive or oxidative chemistry (electron or hole acceptance by the molecule, respectively). To probe these processes, plasmonically-enhanced optical spectroscopies are highly effective analytical techniques.

In addition to the charge carriers that exciting an LSPR creates, incident and generated light fields observed/created by molecules near an LSPR are augmented. This in turn enhances optical spectroscopies, of which, the most well-established and developed technique is surface-enhanced Raman scattering (SERS). SERS is an analytical technique that has experienced tremendous growth in popularity since it's discovery in 1977.[4–7] Conceptually, SERS is a vibrational spectroscopy that probes the molecular induced polarizability, identical to normal Raman scattering (NRS), near a plasmonic surface.[8] However, SERS has unique capability of observing deeper chemical information than NRS by both the local field effect[9–11] (LFE) and the chemical enhancement effect (CHEM).[12,13] Using a combination of resonance Raman scattering (RRS) along with LFE and CHEM, SERS can observe the vibrational spectrum of a single molecule.[14–16]

A discussion of the enhancement mechanisms in SERS has been reviewed extensively.[8,10,11,17] Briefly, the electromagnetic mechanism (EM) is dominantly from the LFE that uses the particle polarizability to create an enhanced electric field felt by the molecular induced dipole. Meanwhile, CHEM effects arise from direct changes in the molecular polarizability. This has the effect of creating new electronic resonance conditions in the molecule-plasmon system. The Jensen *et al.* have explored the CHEM effect significantly, and have determined a maximum EF of 10^3 compared to the established 10^8 observed by EM.[18–21] Interested readers are directed to the many excellent SERS reviews for further discussion.[5–8,22–25]

1.3. Introduction to Coherent Raman Scattering

When considering optical spectroscopy there is a simple way to consider different processes. One can consider a total system polarization (P_{tot}) and determine what order field interactions govern a specific polarization. In the case of NRS and SERS, the polarization is a linear polarization ($P^{(1)}$), hence the experiment is a linear spectroscopy. However, higher order interactions can occur, we keep track of these by expanding the polarization in a series:

$$P_{tot} = P^{(1)} + P^{(2)} + P^{(3)} + ... \tag{1.1}$$

Each order of polarization contains the dependence on field amplitude and the optical susceptibility ($\chi^{(n)}$) which describes how the system changes relative to the incident fields.

$$P_{tot} = \chi^{(1)} \cdot E + \chi^{(2)} \cdot E^2 + \chi^{(3)} \cdot E^3 + ... \tag{1.2}$$

Different forms of optical spectroscopy follow from understanding the optical susceptibility that governs the optical process. For further information of nonlinear optics and theory of nonlinear polarization many excellent resources are available.[26–28]

Of interest for the work contained in this thesis is the third order polarization and optical susceptibility which describes coherent Raman scattering (CRS) processes. CRS is a diverse family of nonlinear Raman scattering experiements that contain three field-matter interactions to drive the third order polarization and emit a signal field. Using multiple fields, a Raman resonance is stimulated, coherently driving the nonlinear polarization in the medium much stronger than that observed in incoherent Raman processes (Fig. 1.2).[29–32]

The differences between CRS experiments relies primarily on properties of the excitation fields, phase-matching, time ordering, and method of detection: homodyne vs. heterodyne. While all CRS experiments have a *stimulated* Raman resonance, not all will have stimulated detection. Conceptually, the difference between these detection modes is that homodyne detection has no field amplitude at the signal frequency. In heterodyne detection, the signal field is at a frequency that is present at the detector. In heterodyned detection the signal can be self-heterodyned (an excitation field is at the signal field frequency) or can be externally-heterodyned by a local oscillator separate from the excitation fields.[31] Commonly, the heterodyne detection is called 'stimulated' while homodyne is 'spontaneous'. In the following sections we describe more fully different forms of CRS that will be used in the following thesis chapters and the current state of combining plasmonic enhancement with CRS.

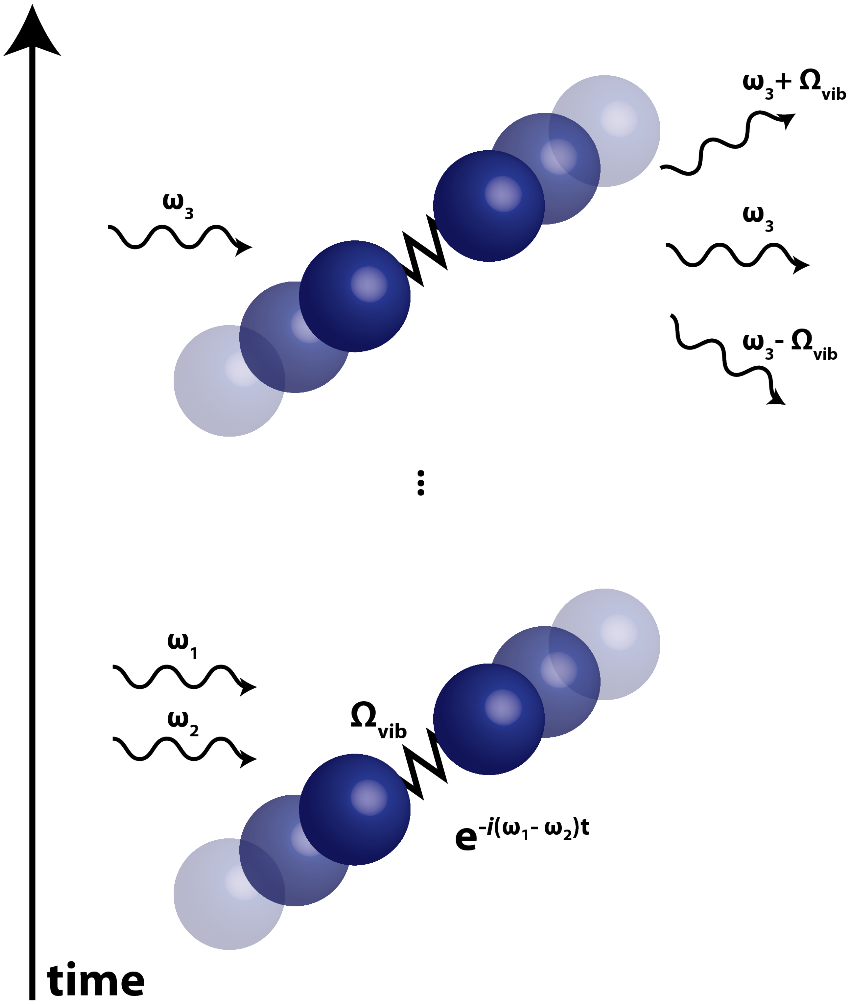

Figure 1.2. Generalized coherent Raman scattering scheme. A vibration (Ω_{vib}) is coherently driven when the difference of two excitation fields (ω_1, ω_2) equals the vibrational energy. This vibration is the stimulated, creating a time-dependent polarization that is probed with a third field interaction (ω_3) at a later time. The third field interaction induces a signal field that is emitted at a Rayleigh (ω_3), Stokes ($\omega_3 - \Omega_{vib}$), or anti-Stokes frequency ($\omega_3 + \Omega_{vib}$).

1.3.1. Femtosecond Stimulated Raman Scattering

Femtosecond stimulated Raman spectroscopy (FSRS) is a CRS technique that can include time resolution.* FSRS is a nonlinear Raman spectroscopy that utilizes stimulated Raman scattering to overcome fluorescence and inherently low Raman scattering cross-sections. This technique allows for one-shot acquisition of a broad, high-resolution Raman spectrum at varying time delays after photoexcitation for both high spectral (typically 5-20 cm^{-1}) and temporal (10-100 fs) resolution. Ground state FSRS spectra are obtained when a narrow bandwidth picosecond Raman pump pulse and a broadband femtosecond probe pulse overlap simultaneously spatiotemporally in a Raman active analyte. As depicted in Fig. 1.3, the probe and Raman pump pulses first interact with a molecule, establishing a vibrational coherence. A second interaction with the pump pulse then leads to the stimulated emission of a Stokes-shifted photon when energy is transferred from the Raman pump to the stimulating probe at the frequency shifts of Raman-active modes in the interrogated molecules. This leads to sharp bands which are Stokes-shifted from the narrowband Raman pump on top of the broad probe spectrum (see Fig. 1.4). A FSRS spectrum is produced by dividing Raman pump ‘off’ spectra from Raman pump ‘on’ to give Raman gain as a function of Raman shift. This implementation provides information on ground state vibrational frequencies, and with a stimulated Raman setup, all Raman information is emitted in a self-heterodyned fashion, enabling easy setup and data acquisition. To study molecular dynamics, FSRS utilizes a femtosecond actinic pump pulse to first photoexcite a molecular system before the probe and Raman pump pulses interact

---

*This section adapted with permission from Ref. 23 FSRS enables the acquisition of vibrational spectra with ultrafast time resolution by incorporating photoexcitation pulses.[33–36] Copyright 2016 Royal Society of Chemistry.

with an analyte. The structural evolution of the transient species is subsequently probed at various time points during a reaction. The evolution of the vibrational spectrum during a chemical transformation provides key structural information on the reaction mechanism.

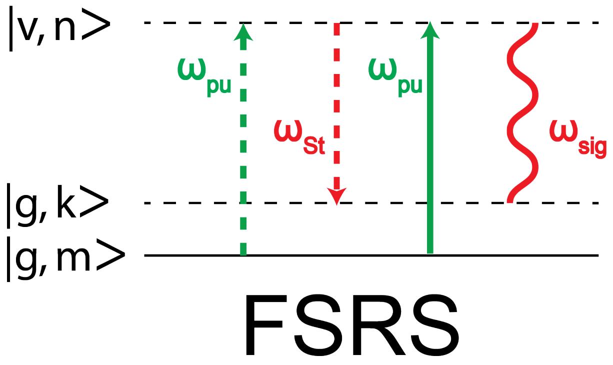

Figure 1.3. Four-wave mixing energy level diagram showing the Raman pump (ω_{pu}) and Stokes (ω_{St}) field interactions in FSRS.

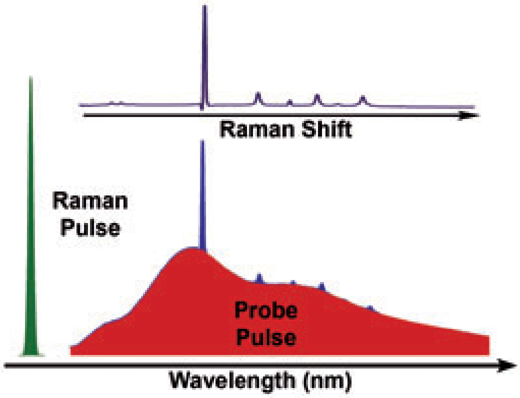

Figure 1.4. Representation of the pulses used in FSRS. The frequency domain demonstrates how a broadband probe red shifted from a narrowband Raman pump pulse interrogates a broad Stokes shifted region of a Raman spectrum. A FSRS spectrum reminiscent of spontaneous Raman is obtained when the probe pulse spectrum is divided out, as seen above the probe spectrum. Figure reproduced from Ref. 35. Copyright 2011 WILEY-VCH Verlag GmbH & Co. KGaA, Weinheim.

This novel approach has been used to reveal excited state vibrational dynamics in a number of biological systems,[37–39] photovoltaic materials,[40–44] and more. For example, FSRS was used to investigate important structural changes that control ultrafast processes like proton transfer in green fluorescent protein[45] and changin metal center oxidation states during ultrafast intersystem crossing in the tris(bipyridine)ruthenium(II) ($Ru(bpy)_3{}^{2+}$) dye.[46]

Despite the coherent Raman scattering advantages, FSRS is typically limited to studying ensemble dynamics of highly concentrated samples with relatively large Raman scattering cross-sections. This necessitates large volumes of sample with some inherent form of heterogeneity. Combining SERS with FSRS could overcome these limitations by amplifying fundamentally weak Raman scattering from a small number of molecules near nanostructured SERS hotspots. Early attempts by Ploetz *et al.* were made to combine FSRS and SERS, looking for enhancement of organic monolayers on gold and silver nanoshells.[47] With 75 nJ/pulse of Raman pump power at a 1 kHz repetition rate and a plasmonic substrate in resonance with the Raman pump, they were unable to observe surface-enhanced FSRS (SE-FSRS) signals. When the high fields from these focused ultrafast pulses are amplified and concentrated by plasmonic materials, the field strengths rapidly approach the dielectric breakdown limit for organic molecules. Thus attempts to obtain SE-FSRS data from typical 1 kHz amplified laser systems have failed at this point. This highlights one of the major difficulties with surface-enhanced ultrafast techniques: it is necessary to consider both peak power and electromagnetic enhancement factors when performing these experiments so as to not damage the plasmonic structures and analyte molecules.

1.3.2. Femtosecond Raman-Induced Kerr-Effect Scattering

As a method of improving the signal-to-noise ratio (SNR) in FSRS, polarization dependent excitation and detection schemes have been applied to FSRS. Taking advantage of the optical Kerr effect, where a transient birefringence is induced in a sample by a strong pump beam, the plane of polarization in a weaker signal beam is rotated - allowing for polarization sensitive detection. This general scheme applied to stimulated Raman scattering is called Raman-induced Kerr-effect scattering (RIKES).[29,48–53] RIKES has been applied mostly to single mode stimulated Raman scattering (SRS), but in recent years more applications have been developed in multiplex RIKES experiments.[54–56]

Similar to the development of FSRS, the Mathies group was essential in the success of a multiplex RIKES experiment: femtosecond Raman-induced Kerr effect scattering (FRIKES). The work of Shim *et al.*,[54] demonstrated FRIKES experiment using a circularly polarized Raman pump and a linearly polarized Stokes field. A 'dark background' FRIKES signal was observed by recording the heterodyned scatter transmitted through a perpendicularly set linear polarizer (relative to the Stokes field). However, this experiment still observed residual Stokes field which necessitated background removal. Subsequent FRIKES experiments[55,56] removed the background transmitted through the polarizer by placing a chopper back in the Raman pump path, essentially making the FRIKES data collection identical to previous FSRS studies.

Using FRIKES, vibrationally-resonant signals have been isolated from interfering background signals and non-interacting Stokes fields.[55–61] Even with the promise of polarization sensitive detection, FRIKES has only had three multiplex pure frequency domain experiment[54,56,62] and a collection of Fourier-transform time domain experiments.[63–66] All other FRIKES research has abandoned the utility of multiplex FRIKES and studied just single mode observations in the frequency domain. In addition, the work of Balakrishnan *et al.* observed unexplained dispersive and negative lineshapes in an optically-heterodyne detected FRIKES (OHD-FRIKES) experiment.[56] As most frequency domain FRIKES experiments are currently being treated as OHD-FRIKES experiments,[55,56] further investigation into the anomalous lineshapes is of strong interest if the polarization sensitive technique is to be applied in future frequency domain studies. This is the central effort discussed further in Chapter 4.

1.3.3. Coherent Anti-Stokes Raman Scattering

A typical CARS experiments utilizes pump (ω_{pu}) and Stokes (ω_{St}) fields which interact in a media, creating a third order nonlinear polarization CARS signal (ω_{AS}).[†] When the frequency difference of the pump and Stokes fields match the frequency of a Raman active mode, the Raman mode is coherently driven by the excitation fields. The resonantly driven Raman mode generates a new field that is spectrally removed from the excitation fields as an anti-Stokes shift from the pump field at $\omega_{AS} = 2\omega_{pu} - \omega_{St}$.[67] Since signal generation is dependent on matching excitation frequencies, phase-matching conditions of the excitation and signal fields are used to maximize CARS signal, as diagrammed in Fig. 1.5a. Phase-matching is a condition that dictates how efficiently a coherent signal is generated from incoming fields. The phase-matching conditions in CARS are typically met by one of three experimental conditions: a collinear geometry with proper frequencies of the excitation fields; spatial arrangement of excitation fields, most typically a BOXCARS

[†] This section adapted with permission from Ref. 23. Copyright 2016 Royal Society of Chemistry.

arrangement (Fig. 1.5b); or high numerical aperture (high-NA) focusing conditions, like that in a microscope (Fig. 1.5c).[67–69]

Using a combination of improved CARS experimental techniques and plasmonic substrate synthesis, surface-enhanced coherent anti-Stokes Raman scattering (SECARS) has developed into one of the most promising fields of plasmonically-enhanced ultrafast Raman spectroscopy.[70] In this section we discuss the initial fundamental experimental studies of SECARS, theory of SECARS to better understand experimental conditions and enhancement factors, and the most recent developments in SECARS: single molecule and time-resolved studies.

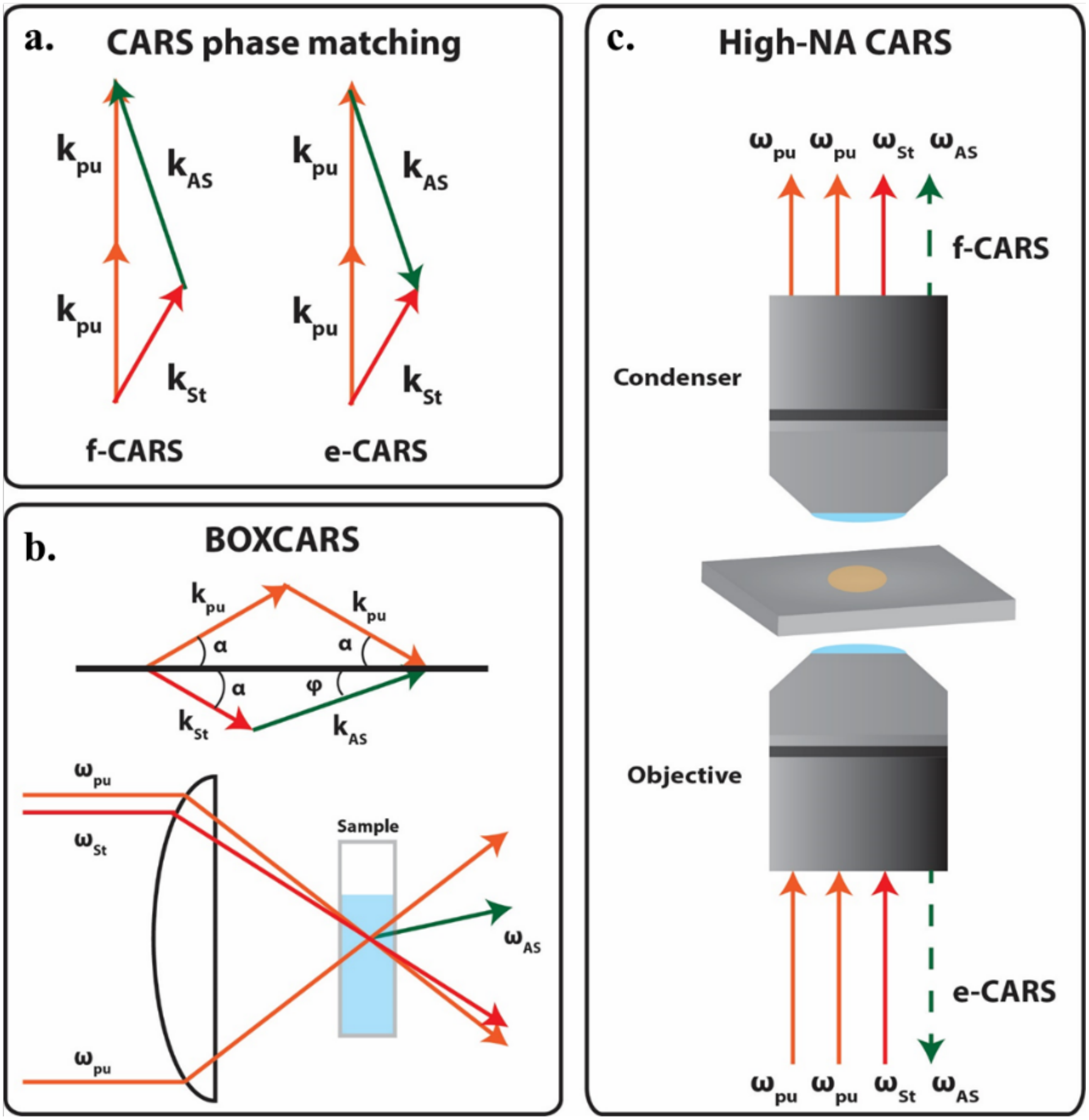

Figure 1.5. a) General phase matching (k) conditions of both forward CARS (f-CARS) and epidirectional CARS (e-CARS) for the pump (pu), Stokes (St), and anti-Stokes fields (AS) for CARS signal generation. b) f-CARS BOXCAR phase-matching experimental geometry showing frequencies (ω). c) High numerical aperture (high-NA) phase-matching experimental geometry using microscope optics. Figure reproduced with permission from Ref. 23. Copyright 2016 Royal Society of Chemistry.

1.4. Introduction to Plasmonically-Enhanced Coherent Raman Scattering

Plasmonically-enhanced coherent Raman scattering (PECRS) brings together two highly successful analytical techniques: SERS and CRS. In the subsequent sections, we will discuss a variety of PECRS techniques that have been developed for nearly fifty years.[71] Dominantly SECARS was the focus for PECRS experiments until SE-FSRS was discovered in 2011[72] and most recently, surface-enhanced impulsive vibrational spectroscopy (SE-IVS).[73] Currently, PECRS experiments have progressed to incorporate scanning probe microscopy (SPM). Similar to the growth of tip-enhanced Raman scattering (TERS) in comparison to SERS, tip-enhanced forms of PECRS are extending the reach of PECRS into smaller spatial dimensions. The following sections will give a comprehensive review of the PECRS literature, but further reading of more recent review papers is recommended for the interested reader.[17,23,32]

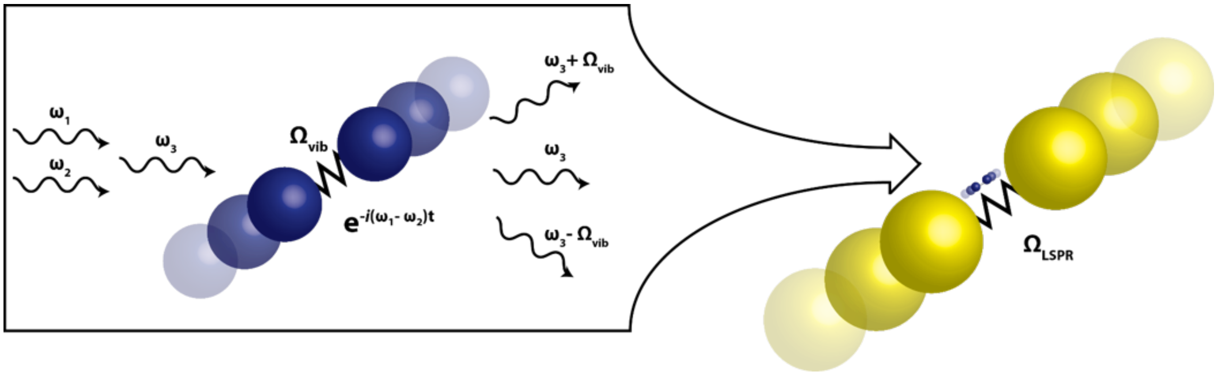

Figure 1.6. The combination of plasmonic-enhancement from an LSPR and coherent Raman scattering allows for plasmonically-enhanced coherent Raman scattering (PECRS).

1.4.1. Surface-Enhanced Coherent Anti-Stokes Raman Scattering

The first report of SECARS came from the Shen group in 1979.[71‡] Like other early studies of CARS,[74] Shen focused on a system of benzene adsorbed on silver surfaces. They obtained a CARS spectrum of the 992 cm^{-1} mode of neat benzene as a control experiment while measuring the SECARS spectrum of benzene on a silver surface in parallel. By exciting the surface plasmons in the silver film, they observed a plasmonically-enhanced CARS signal. Even in this early report, the power of SECARS was suggested to probe sub-monolayer assemblies of molecules on surfaces.[71] As we will see in the following section, this early prediction was verified and extended beyond sub-monolayer coverage to the single molecule limit.[75–77] After this initial study, Liang *et al.* continued work of SECARS by studying mixtures of benzene, N,N'-dimethylformamide, toluene, and chlorobenzene in Ag colloidal solutions.[78] Liang *et al.* used a Q-switched nanosecond Nd:YAG laser to pump two dye lasers for the pump and Stokes pulses. Using the tunability of the dye lasers, they tracked the EF of the 992 cm^{-1} mode of benzene as a function of pulse wavelength and saw strong pump wavelength dependence. As the pump was tuned from 458 nm to 521 nm, an optimum enhancement was observed near 500 nm; likely close to the aggregate Ag colloidal LSPR.[79] This highlights the importance of substrate characterization in modern ultrafast SERS techniques, so as to tune pulses for ideal enhancement. While the authors observed SECARS from a variety of analytes, the EF's reported were only on the order of 10^2 over CARS.

To simplify the phase-matching requirements in SECARS, the Kawata group applied the high-NA CARS microscopy technique[80,81] to perform SECARS microspectroscopy.[82]

[‡] This section adapted with permission from Ref. 23. Copyright 2016 Royal Society of Chemistry.

The experimental setup involved two synchronously pumped Ti:sapph oscillators that were collinearly focused into an objective, and the SECARS signal was recorded from adenine reporter molecules on single Au particle aggregates. The researchers suggested SECARS microspectroscopy could be used to image localized hot spots as only few nanoparticle aggregates with presumably highly enhancing hot spots[83] gave the overwhelmingly largest CARS signal. However, similar to previous SECARS attempts, the EF observed was only 2-6$\times 10^3$ over CARS, far lower than the typical 10^8 enhancements seen in SMSERS.[15]

The Popp group was the first to apply the methods of SECARS to biological applications.[84] Schlcker *et al.* employed SECARS to demonstrate a new method of immunohistochemistry coupled with microscopy to improve optical contrast in biological specimens. Using alloyed plasmonic Au/Ag nanoshells, the authors grew self-assembled monolayers of Raman reporter molecules (DTNB) on the nanoparticle surface and then incubated the substrates in a solution of p63 antibodies (IgG). The completed nanoprobes were then incubated in slices of prostate tissue. They used SECARS microscopy to observe high contrast images of the p63 antibody tagged nanoprobes in the prostate tissue conjugated with p63-(+) basal epithelium and p63-(-) secretory epithelium by tuning the CARS pulse sequence spectrally to be in resonance with a DTNB vibrational mode. This paper clearly suggests the future use of SECARS for its sensitive vibrational imaging and the possible rapid detection of target molecules in complex biological specimens.

In 2009 the Turner group plasmonically enhanced SHG and CARS signals using self-assembled gold nanoparticle substrates.[85] Addison *et al.* deposited layers of 14-nm gold spheres on a glass substrate using dithiol linker molecules to connect nanoparticles in the presence of an oxazine 720 analyte. SECARS signal of oxazine 720 was recorded at

1600 and 3000 cm^{-1} to monitor the plasmonic enhancement of the CARS signal with a maximum enhancement of 10 over CARS.[85] Steuwe *et al.*, also explored new plasmonic substrate designs by recording SECARS of benzenethiol on in-house produced substrates and a commercial plasmonic substrate, Klarite.[86] SECARS showed excellent imaging capabilities, reproducing the SEM-determined structure of Klarite by SECARS imaging of a single vibrational mode in benzenethiol. The enhancements for the in-house fabricated substrates reported were on the range of 10^9-10^{10} over NRS of benzenethiol. Therefore these were the first highly enhancing SECARS substrates as previous studies consistently showed EF's of 10^1-10^3.[78,82,85] With the enhancements observed in this study, the authors suggest that this approach may allow for better photostability in single molecule spectroscopy.

The fundamental studies of SECARS done since the first work in the Shen group[71] have focused on observing various organic analytes in colloidal solutions,[78] demonstrating biological imaging,[84] new experimental CARS microscopy techniques,[82] and improving substrate selection in SECARS.[84–86] The understanding these initial works provided of optimal experimental design choices for both laser and substrate parameters in SECARS was critical to the later successes of the SECARS field that we will discuss in the following sections.

Based on the results of the Shen group,[71] the Kerker group developed an early theoretical framework for the plasmonic enhancement in SECARS.[87] Chew *et al.* considered a system of benzene on Ag nanospheres in solution similar to the system probed by Shen.[71] While the theoretical system Chew *et al.* described didnt include the 'hot spots' that are thought to be the dominant source of highly enhancing Raman signal,[83] they predicted enhancement factors up to 10^{21} over CARS. This early recognition that the multiple coupled fields in CARS all can be enhanced by the plasmon oscillation of the nanoparticle gave predictions based on all fields being resonant with the plasmonic substrate. However, with more realistic experimental considerations including phase-matching and solid angle signal collection, still with all optical fields being plasmonically resonant, the generally accepted enhancement factors of SECARS have been lowered.[76,88–90]

A significant improvement on SECARS theory came from the Aspuru-Guzik group who studied issues associated with modeling SECARS spectra as well as why the originally predicted high EF's[87] have yet to be observed experimentally.[88] One of the difficulties in modeling SECARS spectra is expressing the resonant and nonresonant CARS susceptibilities in simple forms. Significant progress was made on the relevant susceptibilities for SECARS by reducing $\chi^{(3)}$ to a product of dynamic $\chi^{(1)}$ susceptibilities.[91] Using the product of linear susceptibilities, they modeled a few molecular systems including pyridine on Ag cluster complexes. From their calculations they showed enhancement factors between zero and 700 depending on surface adsorption effects in the HOMO-LUMO gap of the pyridine-Ag complex. In addition the authors discuss some of the issues that may contribute to the lack of large EF's; primarily the idea of phase-matching near metal surfaces, background signals from other $\chi^{(3)}$ processes, and vibrational dephasing. While spontaneous Raman scattering experiments have weak dependence on vibrational dephasing, the SECARS spectra will be affected due to the resonant CARS wavepacket needing to pass through a vibrational coherence and interact with an optical field again to contribute signal. Hence, the understanding of the observed plasmonic enhancement in coherent Raman techniques goes beyond the simple optical field plasmonic enhancement in SERS.[88] To understand the plasmonic enhancement of SECARS, or any other surface-enhanced coherent Raman scattering experiment, one must take full consideration of both the coherent scattering process and the plasmonic field enhancements.

Continuing to consider the phase-matching effects near metal surfaces that were proposed by the Aspuru-Guzik group,[88] the Scully group provided a theoretical and experimental study that attempted to address the lack of high EF's in ensemble colloidal SECARS measurements.[89] The researchers postulated that the weaker-than-predicted EF's in SECARS arise from the phase mismatch between the optical fields present in the coherent scattering process of SECARS and the phase of the plasmonically-enhancing field. Using SECARS experimental data of pyridine on Au nanoparticle aggregates, they provided simulations that reproduced the observed varying spectral lineshapes (positive, negative, and dispersive Lorentzian) that varied with respect to the phase of the exciting fields with the plasmon resonance. To further understand the spectral lineshapes indicative of molecular resonance effects,[26] the Scully group focused on a pyridazinegold nanoparticle system.[90] In their study, the lineshapes could be explained by arguing that the spectra observed are dependent on two separate pyridazine-gold complexes that vary in the number of gold atoms over which the pyridazine frontier orbitals are delocalized. The combined work of the Scully group has established the need for considering different interference effects of the excitation and signal fields and the molecule-nanoparticle system at an atomistic level for explaining SECARS spectra.

Theory of SECARS has evolved since the early work of the Kerker group.[87] The SECARS theoretical community has understood that the observed plasmonic enhancement factors in coherent Raman techniques arent as simple as plasmonically enhancing the optical excitation fields. To fully understand surface-enhanced coherent Raman techniques, a combination of phase-matching,[88–90] vibrational dephasing,[88] signal interference,[89,90] and plasmonic enhancement[87–90] are required. This work not only informs recent experimental progress in SECARS but also highlights a number of important points to be considered when studying the enhancement mechanisms of other ultrafast SERS techniques.

Two of the more exciting developments in the SECARS field are the recent proof of single molecule sensitivity and observation of time-dependent phenomenon. Building on the earlier works discussed, these achievements open the door to use SECARS to study ultrafast molecular plasmonics.

Using high-NA SECARS microspectroscopy, the Berlin group had the first single molecule SECARS claim.[77] The system was deoxyguanosine monophosphate (dGMP) in a silver colloidal solution. The authors used two synchronized picosecond Ti:sapph oscillators collinearly focused into a microscope objective and collected epi-direction SECARS signal. Using this technique, a single vibrational mode of dGMP was observed at concentration levels consistent with single molecule[14,15] studies. However, no isotopologue, bianalyte, or large statistical measurements were performed to provide definitive proof for their single molecule claim.

A bianalyte[14] single molecule SECARS study was done by the Halas group in 2014.[76] Zhang *et al.* used SECARS microspectroscopy to obtain spectra of *para*-mercaptoaniline (p-MA) and adenine on lithographically prepared Au quadrumers. The plasmonic substrate was optimized for minimizing losses of the pump wavelength and maximizing the scattering of anti-Stokes emission. The quadrumer substrates were designed with a subradiant mode near the pump and broad superradiant modes in the Stokes and anti-Stokes field regions. Experimentally, a femtosecond 76 MHz Ti:sapph oscillator was used to generate the 800 nm pump and drive continuum generation in a photonic crystal fiber for the Stokes pulse. These pulses were then focused into a microscope and scanned across an array of the lithographically prepared quadrumers to collect the spectrally resolved SECARS signal. With enhancement factors of 10^{11} over spontaneous Raman scattering, the authors measured spectra of each of the two analytes as well as mixed events with signatures from both. They verified single molecule detection by building a histogram representative of single molecule events by the bianalyte approach.[76] With single molecule sensitivity, SECARS can now be applied to an even wider range of potential applications.

The second important development in the field of SECARS is the study of ultrafast dynamics. Introduction of time resolution to SECARS came in 2012 from the Scully group.[92] The first report of TR-SECARS analyzed pyridine-water complexes on gold colloids. In particular, the work was significant as it showed the use of pulse-shaping and timing delays to suppress the nonresonant background signal from the plasmonic particles. By temporally delaying a sinc-shaped probe pulse,[93] the authors observed the ring breathing mode of a pyridine-water complex and vibrational dephasing times greater than ten picoseconds for pyridine near nanoparticles. This first work on TR-SECARS reported an enhancement factor of 10^7 for TR-SECARS compared to bulk CARS.

Bringing together single molecule spectroscopy with time resolution, the Apkarian group performed the first single molecule time-resolved SECARS study.[75] Using silica-coated Au nanoparticle aggregates with *trans*-1,2-bis(4-pyridyl)-ethylene (BPE) as a reporter molecule, Yampolsky *et al.* performed TR-SECARS and observed quantum beating of vibrational modes indicative of a single molecule. This beating behavior was verified by simulated probability distribution functions of the noise in early time responses. At a repetition rate of 80 MHz, the pump and probe pulses at 714 nm and the Stokes pulse at 809 nm drove the oscillation of the strong 1640 cm^{-1} vibrational mode in BPE. The time resolution of this experiment allowed for monitoring the vibrational beating of between the 1647 and 1612 cm^{-1} modes over long periods of time relative to plasmon dephasing processes. In the bulk SECARS experiment, the beating dies in approximately one picosecond, however in the single aggregate experiment, the beating persists for the entire ten picosecond experimental window. This suggests that the vibrational dephasing on the single aggregate level is not strongly perturbed by the near-field LSPR. This illustrates the potential of single molecule photoexcited studies near plasmonic surfaces.

SECARS has grown considerably from the initial report of enhanced benzene CARS spectra on a silver film.[71] The field has now proven single molecule sensitivity,[75,76] ultrafast time resolution,[75,92] and biological relevancy.[84] In addition, theoretical studies were developed[76,88–90] to explain the observed EF's and lineshapes. SECARS is one of the more widely used ultrafast SERS techniques. Thus as one of the most well-developed tools to study coupled molecule-plasmon systems, SECARS will continue to grow as a method of single molecule, time-resolved spectroscopy to track chemistry on ultrafast time scales near plasmonic surfaces.

1.4.1.1. Tip-Enhanced Coherent Anti-Stokes Raman Scattering. One of the earliest and most-developed application of ultrafast TERS has been tip-enhanced coherent anti-Stokes Raman spectroscopy (TECARS).[§] The Kawata group applied their SECARS microscopy studies to TECARS in 2004. First, they reported TE-CAR images of adenine molecules in DNA clusters.[94,95] They were able to couple 5 ps pulses with the plasmonic tip with average powers of approximately 30-100 μW at a 800 kHz repetition rate. The authors reported spatial resolution beyond the diffraction limit of light due to the localization of the electric field enhancement underneath the metallic nanoprobe. Using silver-coated AFM cantilever, they imaged nanoclusters of DNA fragments on molecular resonance with the diazole adenine ring-breathing vibrational mode with an estimated enhancement factor of ~100 over CARS. The Kawata group acquired TE-CAR images and correlated AFM images of single-wall carbon nanotubes using gold-coated cantilevers.[96] Recently, Kawata and coworkers, optimized the technique using a broadband Stokes pulse to quickly measure multiplex Raman spectra without scanning wavelengths.[97] The authors demonstrated tip-enhanced broadband coherent anti-Stokes Raman (TE-BB-CAR) spectra and images of semiconducting carbon nanotubes. They obtained multiplexed TE-BB-CAR images from 900 to 2200 cm^{-1} with a spatial resolution of 60 nm by combining a supercontinuum from a photonic crystal fiber and a gold-coated glass fiber tip on a tuning-fork based shear-force microscope setup. Though their enhancement factors were small (less than one order of magnitude), the authors were able to demonstrate that the TE-BB-CARS signal provided enough positive contrast for high-resolution imaging by combining ultrafast pulses with plasmonic probes. They also observed a longer decay (~3

[§] This section adapted with permission from Ref. 23. Copyright 2016 Royal Society of Chemistry.

ps) of the G-band signal from the S-CNTs in the near field compared to the far field (∼1.5 ps), possibly due to an Auger process induced at unusually high intensities beneath the tip. This is the first reported study of ultrafast dynamics using time-resolved TECARS. Combining the ability to study dynamics with the ability to image material with ultrafast pulses and high sensitivity, TECARS has opened the door to plasmon-mediated dynamics in a variety of materials.

1.4.2. Surface-Enhanced Femtosecond Stimulated Raman Scattering

The Van Duyne group was able to successfully combine SERS and FSRS in 2011 using a 100 kHz repetition rate laser system with pulse energies high enough for signal generation, but low peak powers to avoid substrate damage.[72¶] Frontiera *et al.* demonstrated SE-FSRS on aggregated gold colloids with adsorbed reporter molecules and an encapsulating silica shell, which were later used in TR-SECARS experiments[75] as well. This proof-of-principle paper presented ground-state SE-FSRS spectra with characteristic Fano-like lineshapes. The authors conservatively estimated time- and ensemble- averaged enhancement factors for SE-FSRS to be 10^4-10^6, however this estimated EF was limited by sample degradation. The dependence of SE-FSRS gain on Raman pump power was shown to be linear only in extremely low power regimes, after which the signal saturates. Additionally, the signal decreased on the minute timescale, and the localized surface plasmon resonance saw a loss in the NIR longitudinal resonance after prolonged irradiation with the high-powered Raman pump pulse. These results indicated damage occurred in these original SE-FSRS experiments, most likely to the plasmonic aggregates since no

---

[¶] This section adapted with permission from Ref. 23. Copyright 2016 Royal Society of Chemistry.

changes were observed in the Raman spectrum to indicate photodamage to the molecular analyte.

The following year the Van Duyne group followed up with a more in-depth investigation into the observed Fano-like resonances arising from these colloidal nanoparticle-molecular systems.[98] By varying the size of the nanoparticle substrates, Frontiera *et al.* changed the energy of the plasmon resonances of the substrate with respect to the wavelengths of the Raman pump and stimulating probe pulses. This change in plasmon resonance energy resulted in a change in the phase of the dispersion of the observed peaks, which were fit to a Fano function. This suggests that the Fano-like lineshapes arise from an interaction of the narrow molecular vibrational coherence and the broad plasmon resonance of the colloidal nanoparticles. The authors then studied the effect of this coupling on the vibrational coherence lifetime of the analyte molecules. One concern in using an ultrafast Raman technique such as FSRS in conjunction with SERS is that the vibrational coherences required to generate signal may be quenched when molecules are placed in close proximity to plasmonic surfaces. SERS measurements of highly fluorescent dye molecules have proven that molecular excited electronic states are rapidly quenched by the presence of nearby plasmons, primarily through a resonant energy transfer mechanism. Although vibrational coherences are much lower in energy than the visible and near infrared plasmons, before this SE-FSRS work, it was largely unknown what the behavior and lifetime of the vibrational coherences would be. These long-lived coherences were also observed in time-resolved SECARS measurements by the Scully group,[92] as previously discussed. Using SE-FSRS, the Van Duyne group showed that this lifetime is not significantly shortened, despite the proximity of the metal nanoparticle surface and the observed plasmon-molecule coupling. These results pave the way for SE-FSRS to be used to study ultrafast dynamics in plasmonically-enhanced molecular systems. If SE-FSRS could be coupled with a microscope, similar to the SECARS experiments by the Apakarian and Halas groups,[75,76] and brought close to the single molecule detection level it could be a powerful tool for the study of reaction dynamics near metal surfaces. Efforts to attain this level of investigation will be discussed in Chapter 5.

More recently, new efforts in SE-FSRS has demonstrated the utility of higher repetition rate pulsed lasers.[99,100] As suggested by Crampton *et al.*,[101] decreasing the pulse energy while increasing the total amount of optical events was beneficial in increasing signal-to-noise ratios (SNR) in SE-FSRS. These efforts will also be discussed more in-depth in Chapter 5.

1.4.2.1. Tip-Enhanced Stimulated Raman Scattering.

Tip-enhanced stimulated Raman scattering (TE-SRS) is a new branch of plasmonically-enhanced coherent Raman scattering that brings together SRS, SERS, and spatial probe microscopy (SPM). Taking a lead from the work of Kawata *et al.*[94–97] the Wickramasinghe group developed TE-SRS using two cw lasers, Pockel's cell for field amplitude modulation, and photodiode lock-in amplifier detection.[102] This new technique was the first to combine SRS with TERS, claiming a 'billion-fold' enhancement of the Raman scatter compared to spontaneous NRS of an azobenzenethiol self-assembly monolayer (SAM), and three orders of magnitude higher than spontaneous TERS. We note that this effort was a purely photodriven-photodetected TE-SRS experiment. More recent work from both the Wickramasinghe and Potma groups has focused on a new direction: photoinduced force microscopy (PiFM).[103–107]

PiFM is a generalized technique that can detect concievably any order optical process. A change in polarization driven by the incident laser fields creates a mechanical force that can be detected by atomic-force microscopy (AFM) techniques. This exciting technique has been used for stimulated Raman scattering,[106,108] ultrafast pump-probe measurements,[104] and even infrared absorption-based nanoscopy.[109] This new technique is promising as it contains all of the plasmonic enhancement of the optical fields in the signal generation, but doesn't rely on the plasmonic enhancement of an output signal field being detected in the far-field. Instead, the signal detection (at any order optical process) is performed by sensitive lock-in detection of an AFM cantilever oscillation frequency. This difference in detection mode can at times make the theory simpler for understanding the overall process, without the destructive optical fields that are persistent in SE-FSRS and SECARS.[90,107,110,111]

1.5. Conclusion

PECRS is the culmination of two distinct analytical/physical fields of chemistry. CRS has developed many different techniques including FSRS, FRIKES, and CARS. All of these techniques rely on the stimulated Raman resonance perturbing the overall polarization of the system.[31] Using the multiple fields to drive the Raman resonance of the molecule enhances the total Raman scattering efficiency. Plasmonically-enhanced optical spectroscopy, of which SERS is the most well-developed and established, has pushed molecular detection to the spatial and molecular concentration limits.[14,15] CRS has the ability to increase temporal resolution to the impulsive limit.

Combining SERS and CRS into PECRS has allowed for significant advances described in this chapter. SECARS has succesfully incorporated temporal resolution into single molecule studies.[75] SE-FSRS is a technique that has promise for observing molecular dynamics near plasmonic surfaces, but has thus far been stymied by strongly interfering optical processes.[98] New methods of PiFM promise to incorporate the best of plasmonic enhancement of optical fields with the sensitivity and generality of detecting mechanical force.[105]

This thesis will cover the development of new theories for SE-FSRS (Chapters 2 and 3), development of optically-heterodyned surface-enhanced femtosecond Raman-induced Kerr-effect scattering (OHD-SEFRIKES, Chapter 4), improvements on SE-FSRS spectrometers by using 1 MHz laser systems (Chapter 5), and solving for the lack of glucose SERS signal by determining the differential Raman scattering cross-section of glucose (Chapter 6).

CHAPTER 2

Continous Wave Theory of SE-FSRS

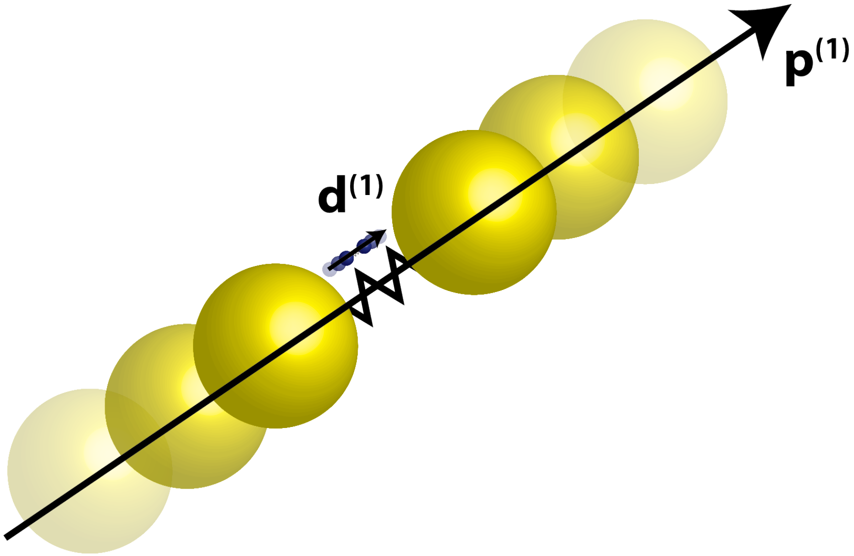

This chapter (excluding Section 2.6.1) has been adapted with permission from Ref. 110. Copyright 2016 American Institute of Physics.

2.1. Abstract

We present a coupled wave semiclassical theory to describe plasmonic enhancement effects in surface-enhanced femtosecond stimulated Raman scattering (SE-FSRS). A key result is that the plasmon enhanced fields which drive the vibrational equation of motion for each normal mode results in dispersive lineshapes in the SE-FSRS spectrum. This result, which reproduces experimental lineshapes, demonstrates that plasmon-enhanced stimulated Raman methods provide unique sensitivity to a plasmonic response. Our derived SE-FSRS theory shows a plasmonic enhancement of $|g_{pu}|^2 Im\left\{\chi_R(\omega) g_{st}^2\right\} / Im\left\{\chi_R(\omega)\right\}$, where $|g_{pu}|^2$ is the absolute square of the plasmonic enhancement from the Raman pump, $\chi_R(\omega)$ is the Raman susceptibility, and g_{st} is the plasmonic enhancement of the Stokes field in SE-FSRS. We conclude with a discussion on potential future experimental and theoretical directions for the field of plasmonically-enhanced coherent Raman scattering.

2.2. Introduction

2.2.1. Stimulated Raman scattering

Vibrational spectroscopy is a versatile technique for understanding chemistry at the physical limits of space, time, and molecular concentration. By understanding the vibrational spectrum as a function of space and time, the evolution of a single chemical species can be elucidated. Raman scattering is a common vibrational spectroscopy technique used to discern molecular vibrational information. A powerful form of Raman spectroscopy is stimulated Raman scattering (SRS). In contrast to normal Raman scattering (NRS) where the optical resonance is a spontaneous measurement of the system polarization, SRS coherently drives an optical resonance resulting in a stimulated measurement of the system polarization.

SRS was discovered by Eckhardt, Woodbury, and Ng at Hughes Research in the early 1960's. Early work on the theory of SRS was performed by Shen and Bloembergen.[112,113] SRS has matured as a field and has been of significant recent interest as a vibrational imaging technique.[114,115] The original theory of SRS by Shen and Bloembergen gave great physical insight into the SRS process by using semiclassical coupled wave equations to describe the system polarization. Coupled wave theory of SRS, while non-quantum mechanical, reproduces many experimental observables.[113] Due to the success of the coupled wave theory of SRS, it was used as the first approximation in the next advancement in stimulated Raman scattering: femtosecond stimulated Raman scattering (FSRS).

2.2.2. Femtosecond stimulated Raman scattering

FSRS was developed by Mathies *et al.* as a method to use the advantages of stimulated Raman (*i.e.*: heterodyne detection, greater Stokes and/or anti-Stokes scattering) with the spectral and temporal advantages of femtosecond spectroscopy (*i.e.*: multiplex vibrational spectroscopy and high temporal resolution).[34,116,117] FSRS is a vibrationally-resonant four-wave mixing spectroscopy that is characterized by the third order nonlinear optical susceptibility, $\chi^{(3)}$. Fig. 2.1 shows the four-wave mixing energy level diagram for FSRS.

Briefly, a ground state FSRS experiment can be described by four field-matter couplings, the first three induce the third order nonlinear polarization: ω_{pu}, ω_{st}, ω_{pu}; which leads to the heterodyned FSRS signal. First, a picosecond bandwidth pulse, the Raman

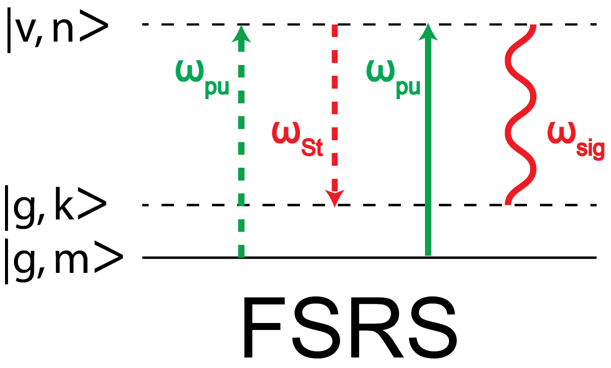

Figure 2.1. Four-wave mixing energy level diagram showing the Raman pump (ω_{pu}) and Stokes (ω_{St}) field interactions in FSRS.

pump, induces a polarization of the media. Coincident in time with the Raman pump is a femtosecond bandwidth, spectrally broad pulse: the Stokes field. The Stokes field creates a coherence between vibrational states of the ground and virtual electronic states in the polarization of the media by the Raman pump. As the coherence evolves in time, a second Raman pump field interaction initiates decoherence of vibrational states between the ground and virtual electronic states. The decoherence then leads to stimulated emission of photons in the Stokes field. This process results in a heterodyned signal where the Stokes field serves as a local oscillator.

As the experiment is an intensity modulation in the Stokes field, FSRS spectra are obtained by performing a division of Stokes field intensity while the Raman pump is coincident with the Stokes field intensity without the Raman pump:

$$\text{Raman Gain} = \frac{I_{\text{Stokes, pump on}}}{I_{\text{Stokes, pump off}}} \tag{2.1}$$

This results in a Raman spectrum that is analogous to a spontaneous Raman scattering spectrum but is measured in terms of amplitude gain in the Stokes field instead of the traditional counts × mW^{-1} × sec^{-1} of a spontaneous Raman scattering experiment.

2.2.3. Plasmonically-enhanced coherent Raman scattering

To improve the sensitivity of vibrational Raman spectroscopy, only one linear optical method has shown enhancements of up to 10^{12}: surface-enhanced Raman spectroscopy (SERS).[4,8,118,119] The concept of electromagnetic field enhancement (EM) that lies at the heart of SERS has grown in importance since the initial observation[118] of what was later recognized as the new physical phenomenon of SERS.[4,119] It has been applied to the coherent Raman scattering techniques of CARS and FSRS, resulting in surface-enhanced coherent anti-Stokes Raman scattering (SECARS)[71,87] and surface-enhanced femtosecond stimulated Raman scattering (SE-FSRS).[23,72,98] Surface-enhancement in Raman scattering techniques primarily comes from the plasmonically-enhanced optical fields used in the vibrational spectroscopy.[9]

Previous SE-FSRS experiments displayed dispersive lineshapes in the Raman gain features of coupled molecule-plasmonic nanoparticle systems.[72,98] The dispersive lineshapes were previously attributed to Fano-like interferences of the discrete molecular vibrational states on the continuum-like plasmon resonance.[120,121] When the energy of the aggregate plasmon oscillation was varied with respect to the Raman pump and Stokes fields, the dispersive lineshapes changed phase.[98] The behavior of resonance dependent dispersive lineshapes in SE-FSRS is qualitatively similar to lineshapes encountered in surface-enhanced infrared absorption (SEIRA) spectroscopy. A key difference however, is that in SEIRA the sharp absorption profile of the molecular oscillator is perturbed by coupling to the infrared resonant broad absorption of the plasmon, while in SE-FSRS the molecule-plasmon coupling is observed by a stimulated scattering event.[122]

Research into the lineshapes observed in surface-enhanced coherent Raman scattering have focused primarily on SECARS.[88,89] In SECARS, dispersive lineshapes in the vibrational spectrum are observed due to interference of the vibrationally-resonant signal with electronically-resonant four-wave mixing signals, similar to the lineshapes seen in CARS. One paper has investigated the plasmonic-enhancement in SE-SRS; however, the theory only considered single vibrational modes and resulted in Lorentzian lineshapes.[123]

More recently, there has been a paper describing SE-FSRS that used a perturbative polarization expansion.[111] This paper modeled a stimulated Raman response that is convoluted with a stimulated resonant surface plasmon optical field (PLE). When the Raman gain signal is observed in the far-field, the cross terms between the heterodyned SE-FSRS signal and the PLE signal lead to dispersive lineshapes with phase-dependence depending on the plasmon resonance energy. Using this time-dependent picture of the SE-FSRS process, and a two state model to evaluate the PLE contribution, numerical lineshapes derived by Fourier transformation of the time-dependent field showed general agreement with previously published experiments for a single vibrational mode.[98] While the previous study used a time-domain picture for SE-FSRS theory and resulted in plasmon energy resonance dependent dispersive lineshapes, they did not retrieve an analytic lineshape equation in the frequency domain which is an important goal for comparing to previous frequency domain experiments.[72,98]

While more exotic theories of plasmonic enhancement in SERS by optomechanical cavity coupling have been explored recently,[124,125] the electromagnetic mechanism has consistently reproduced and predicted experimental observables in SERS.[6,24] Thus, the focus of this chapter is to develop a theory of SE-FSRS that uses the coupled wave theory treatments of Lee,[126] Shen,[112] and Bloembergen[113] with the electromagnetic mechanism of SERS to reproduce experimental observables in SE-FSRS. The SE-FSRS theory is presented in Section 2.3 of this chapter, then in Section 2.4 we present an application of this theory to recent SE-FSRS measurements, showing the origin of the asymmetric lineshapes and how they are changed by modifying the plasmon wavelength. We note that our theory provides an explicit formula for analytical lineshape which involves a different dependence on the electromagnetic enhancement factors than was found in Ref. 111.

2.3. Theory

In a semiclassical picture, FSRS can be described similarly to previous, non-ultrafast versions of stimulated Raman like that derived by Bloembergen and Shen.[112,113] An important limitation to the coupled-wave theory of stimulated Raman scattering includes the lack of proper treatment for the polarization when excited on molecular resonance. To treat the case of electronically-resonant FSRS (FSRRS), quantum mechanical derivations including density matrix and quantum wavepacket simulations are necessary.[126–129] While a quantum mechanical formulation is currently being pursued, all SE-FSRS experiments performed thus far have been far from molecular resonance.[72,98]

Physically, the SE-FSRS process involves a sum of Raman pump and Stokes probe fields inducing a nonlinear response in the molecule-nanoparticle ensemble with total polarization given by $\vec{P}(\vec{r}, t)$. The ensemble with an induced polarization from the optical fields then modifies the incident optical fields as they propagate through the ensemble. The back-and-forth nature of the incident field effecting the polarization and the induced polarization effecting the propagating field is a classical, physical picture of the coupled wave description of SE-FSRS.

The derivation of SE-FSRS theory will proceed in two steps according to the coupled wave equations approach used in previous FSRS theory by Lee *et al.*,[126,130] with special note to issues that are unique to plasmonic enhancement of the optical fields. First, a derivation of the equation of motion for the vibrational coordinate Q by plasmonically-enhanced optical fields will be presented. The resulting expression for Q describes the driven vibration in the infrared region of the electromagnetic spectrum. Once Q is derived the second portion of the SE-FSRS derivation analyzes how the driven oscillator described by Q perturbs the Stokes field. We analyze this perturbation of the Stokes field by Q by solving Maxwell's equation. Once Maxwell's equation is solved, a final expression for the SE-FSRS Raman gain is given and compared to experimental data.

2.3.1. Solving the driven oscillator equations for SE-FSRS

Let's assume that the total system is an assembly of molecular vibrational oscillators and plasmonic oscillators with total polarizability, $\tilde{\alpha}_{tot}$.

Let the molecules have a vibrational mode with angular frequency ω_0, that is described by the vibrational coordinate Q. Using Lagrangian mechanics the coupling of light to the vibrational density is given by the total Lagrangian density:

$$L = L_{rad} + L_{vib} + L_{int} \tag{2.2}$$

L_{rad} is the radiative component of the total Lagrangian density with a transverse electric field $\vec{E}$ and magnetic field $\vec{B}$:

$$L_{rad} = \frac{1}{2}\left(|\vec{E}|^2 - |\vec{B}|^2\right) \tag{2.3}$$

The vibrational Lagrangian is given by:

$$L_{vib} = N\left\{\frac{1}{2}\dot{Q}^2 - \frac{1}{2}\omega_0^2 Q^2\right\}, \tag{2.4}$$

where the number of molecular oscillators per unit volume is given by N and the dot notation on $\dot{Q}$ represents the time derivative of Q.

Before defining the Lagrangian for the interaction of light with the collection of molecular oscillators we define the polarization with spatial distribution $\vec{r}$ from the total response using the Placzek model[131] for classical polarization:

$$\vec{P}(\vec{r}, t) = \tilde{\alpha}_m \cdot \vec{E}(\vec{r}, t) \tag{2.5}$$

Expanding the polarizability $\tilde{\alpha}_m$ in a Taylor series about $Q = 0$ we have:

$$\begin{aligned} \tilde{\alpha}_m &\approx \alpha_{m,0} + \left(\frac{d\tilde{\alpha}_m}{dQ}\right)_0 Q + ... \\ &\equiv \alpha_{m,0} + \alpha_m^{'} Q + ... \end{aligned} \tag{2.6}$$

The Lagrangian for the interaction of light with the collection of molecular oscillators is:

$$\begin{aligned} L_{int} &= -N\left(-\vec{P}\cdot\vec{E}(\vec{r},t)\right) \\ &= N\tilde{\alpha}_m|\vec{E}(\vec{r},t)|^2 \end{aligned} \tag{2.7}$$

We add in a linear dissipation per oscillator force term, F (Rayleigh dissipation):

$$F = \frac{\partial D}{\partial \dot{Q}} \tag{2.8a}$$

$$F = -2\gamma\dot{Q}N \tag{2.8b}$$

$$D = -\gamma\dot{Q}^2 N \tag{2.8c}$$

The equation of motion for the driven, damped vibration ω_0 on the vibrational coordinate Q is then given by the Euler-Lagrange equation:

$$\frac{d}{dt}\left(\frac{\partial L}{\partial \dot{Q}}\right) - \frac{\partial L}{\partial Q} = \frac{\partial D}{\partial \dot{Q}} \tag{2.9a}$$

$$\begin{aligned} &\frac{d}{dt}\left(\frac{\partial}{\partial \dot{Q}}\left(\frac{1}{2}|\vec{E}|^2 - |\vec{B}|^2\right.\right. \\ &\left.\left. +N\left(\frac{1}{2}\dot{Q}^2 - \frac{1}{2}\omega_0^2 Q^2\right) + N\tilde{\alpha}_m|\vec{E}(\vec{r},t)|^2\right)\right) \\ &-\frac{\partial}{\partial Q}\left(\frac{1}{2}|\vec{E}|^2 - |\vec{B}|^2\right. \\ &\left. +N\left(\frac{1}{2}\dot{Q}^2 - \frac{1}{2}\omega_0^2 Q^2\right) + N\tilde{\alpha}_m|\vec{E}(\vec{r},t)|^2\right) = -2\gamma\dot{Q}N \end{aligned} \tag{2.9b}$$

$$\frac{d^2Q}{dt^2} + 2\gamma\frac{dQ}{dt} + \omega_0^2 Q = \alpha_m^{'}|\vec{E}(\vec{r},t)|^2 \tag{2.9c}$$

$$\frac{d^2Q}{dt^2} + 2\gamma\frac{dQ}{dt} + \omega_0^2 Q = \alpha_m^{'}|\vec{E}(\vec{r},t)|^2 \tag{2.10}$$

In $|\vec{E}(\vec{r},t)|^2$ there are two different field products that could drive a vibration ω_0: $E_{pu}E_{st}^*$ and $E_{pu}^*E_{st}$. If we assume that the fields have the time dependence $E_{pu} \sim e^{-i\omega_{pu}t}$ and $E_{st} \sim e^{-i\omega_{st}t}$, then if we are interested in Stokes Raman scattering, the product of $E_{pu}E_{st}^*$ leads to $Q \sim e^{-i\omega_0 t}$ with the damping term in the homogeneous solution to the driven oscillator being divergent. Thus we will consider the driving term $E_{pu}^*E_{st}$, such that $Q \sim e^{i\omega_0 t}$ is coherently driven, but damped:

$$\frac{d^2Q}{dt^2} + 2\gamma\frac{dQ}{dt} + \omega_0^2 Q = \alpha_m^{'} E_{pu}^*(z,t)E_{st}(z,t) \tag{2.11}$$

To describe how the electric field is modified by the collection of oscillators we use Maxwell's equation:

$$\nabla^2\vec{E}(\vec{r},t) - \frac{1}{c^2}\frac{\partial^2\vec{E}(\vec{r},t)}{\partial t^2} = \frac{4\pi N}{c^2}\frac{\partial^2\vec{P}(\vec{r},t)}{\partial t^2} \tag{2.12}$$

To reduce the number of spatial variables present in $\vec{r}$ we assume a linearly polarized field propagating along the z-axis. In addition, we assume that the driven dipoles are orientated along the polarization direction of the propagating fields. This assumption is identical to that made in previous SRS and FSRS theory papers, and can be modified by introducing orientational matrices.[9]

Using the Placzek polarization the equation describing the change of the electric field by the collection of oscillators becomes:

$$\frac{\partial^2 E(z,t)}{\partial z^2} - \frac{1}{c^2}\frac{\partial^2 E(z,t)}{\partial t^2} = \frac{4\pi N}{c^2}\frac{\partial^2(\tilde{\alpha}E(z,t))}{\partial t^2} \tag{2.13a}$$

$$\frac{\partial^2 E(z,t)}{\partial z^2} - \frac{1}{c^2}\frac{\partial^2 E(z,t)}{\partial t^2} = \frac{4\pi N\alpha_{m,0}}{c^2}\frac{\partial^2 E(z,t)}{\partial t^2} + \frac{4\pi N\alpha_m^{'}}{c^2}\frac{\partial^2 (QE(z,t))}{\partial t^2} \tag{2.13b}$$

As $4\pi N\alpha_{m,0} << 1$ we neglect the first term on the right of the equality in Eq. 2.13b, and keep the second term that drives the oscillating field (i.e., produces stimulated Raman gain). This leads to the following expression for Maxwell's equation for the field perturbed by the medium:

$$\frac{\partial^2 E(z,t)}{\partial z^2} - \frac{1}{c^2}\frac{\partial^2 E(z,t)}{\partial t^2} \approx \frac{4\pi N\alpha_m^{'}}{c^2}\frac{\partial^2 (QE(z,t))}{\partial t^2} \tag{2.14}$$

Eq. 2.14 is the general form for the Maxwell's equation that will be solved in the following section. At this point we turn our focus to the fields that drive the coupled wave equations.

We now add in the contribution of the metal nanoparticle to the field, here assuming that the external field induces a dipole in the particle, and then it is the field of this dipole that needs to be added. Here the particle is assumed to be located along the polarization direction.

Using notation from Mullin *et al.*[132] and realizing the total field (either pump or Stokes) is the sum of the incident ($E^0_{st/pu}$) and scattered fields induced in the particle, we first derive the Stokes field:

$$E_{st}(z,t) = E^0_{st}(z,t) + \Lambda\mu_P \qquad = E^0_{st}(z,t) + \Lambda(\tilde{\alpha}_{P,st}(E^0_{st}(z,t) + \Lambda\mu_m)) \tag{2.15a}$$

Where Λ is a parameter determined by the field of the induced dipole that has an inverse cube dependence on distance between dipoles, μ_P is the particle dipole, $\tilde{\alpha}_{P,st}$ is the particle polarizability evaluated at the Stokes frequency, and μ_m is the molecular dipole.

Now dropping the μ_m term as it leads to the image field effect[9] which has been shown to be important only in regions where quantum plasmonic effects dominate,[133] we let $g_{st} = 1 + \Lambda\tilde{\alpha}_{P,st}$ to obtain:

$$E_{st}(z,t) = E^0_{st}(z,t)g_{st} \tag{2.15b}$$

Analogously for $E_{pu}(z,t)$:

$$E_{pu}(z,t) = E^0_{pu}(z,t)g_{pu} \tag{2.15c}$$

Note that g_{pu} and g_{st} are the complex valued electromagnetic enhancement factors associated with the Raman pump and Stokes fields in SERS, with the overall SERS enhancement factor being $|g_{pu}|^2|g_{st}|^2$.[9,10,132] In the present derivation, we assume that these parameters are time-independent, and thus do not change the time profile of these pulses. We also assume that the frequency dependence is weak compared to the linewidth of the pump pulse, and the vibrational line associated with the Stokes probe. While this assumption is approximate for the Stokes pulse, it should be reasonable for order of magnitude estimates.

Finally to approximate experimental conditions we give a Gaussian envelope to the pulses by defining $E^0_{pu}(z,t)$ and $E^0_{st}(z,t)$ (as well as their Fourier transformed frequency domain definitions) as:

$$E^0_{pu}(z,t) = E^0_{pu} e^{-(t-z/c)^2/2\tau^2_{pu}} e^{-i\omega_{pu}(t-z/c)} \tag{2.16a}$$

$$E^0_{st}(z,t) = E^0_{st} e^{-(t-z/c)^2/2\tau^2_{st}} e^{-i\omega_{st}(t-z/c)} \tag{2.16b}$$

$$E^0_{pu}(z,\omega) = E^0_{pu}\sqrt{2\pi}\tau_{pu} e^{-(\omega-\omega_{pu})^2\tau^2_{pu}/2} e^{i\omega z/c} \tag{2.16c}$$

$$E^0_{st}(z,\omega) = E^0_{st}\sqrt{2\pi}\tau_{st} e^{-(\omega-\omega_{st})^2\tau^2_{st}/2} e^{i\omega z/c} \tag{2.16d}$$

Returning to Eq. 2.11 using Eqs. 2.16a and 2.16b for the Raman pump and Stokes fields respectively:

$$\begin{aligned} &\frac{d^2Q(z,t)}{dt^2} + 2\gamma\frac{dQ(z,t)}{dt} + \omega_0^2 Q(z,t) = \\ &\alpha'_m g^*_{pu} E^{0*}_{pu} e^{-(t-z/c)^2/2\tau^2_{pu}} e^{+i\omega_{pu}(t-z/c)} g_{st} E^0_{st} e^{-(t-z/c)^2/2\tau^2_{st}} e^{-i\omega_{st}(t-z/c)} \end{aligned} \tag{2.17a}$$

Letting $t' = t - z/c$ and $(1/\tau^2_{pu} + 1/\tau^2_{st}) \approx 1/\tau^2_{st}$:

$$= \alpha'_m g^*_{pu} E^{0*}_{pu} g_{st} E^0_{st} e^{-t'^2/2\tau^2_{st}} e^{-i(-\omega_{pu}+\omega_{st})t'} \tag{2.17b}$$

To obtain $Q(z,\omega)$ from $Q(z,t)$ in Eqs. 2.17a and 2.17b we solve using Fourier transforms[126,130] to get the following result:

$$Q(z,\omega) = \frac{\alpha'_m g^*_{pu} E^{0*}_{pu} g_{st} E^0_{st} (2\pi)^{1/2} \tau_{st} e^{-(\omega+\omega_{pu}-\omega_{st})^2\tau^2_{st}/2} e^{i\omega z/c}}{\omega_0^2 - \omega^2 - 2i\gamma\omega} \tag{2.18}$$

Thus, $Q(z,\omega)$ is an equation of the coherently driven vibration that occurs in a Raman shifted frequency domain from the pump pulse. Here we note that in the limit of no plasmonic enhancement: $\tilde{\alpha}_P = 0$, $\mathrm{Re}\{g\} \to 1$, and $\mathrm{Im}\{g\} \to 0$; an identical equation of motion to that derived by Lee *et al.* is obtained.[126] This driven vibrational coordinate, $Q(z,\omega)$, will be used to solve Maxwell's equation in the next section.

2.3.2. Solving Maxwell's equation to derive experimental observables in SE-FSRS

To solve for the effect of the driven vibration $Q(z,\omega)$ on the Stokes field, we use the result in Eq. 2.18 to solve Maxwell's equation from Eq. 2.14:

$$\frac{\partial^2 E_{st}(z,t)}{\partial z^2} - \frac{1}{c^2}\frac{\partial^2 E_{st}(z,t)}{\partial t^2} \approx \frac{4\pi N \alpha_m'}{c^2}\frac{\partial^2 (Q(z,t)E_{pu}(z,t))}{\partial t^2} \tag{2.19a}$$

$$= \frac{4\pi N \alpha_m'}{c^2}\frac{\partial^2 (g_{st} Q(z,t)E_{pu}(z,t))}{\partial t^2} \tag{2.19b}$$

In going from Eq. 2.19a to 2.19b, we have added in a factor of g_{st} to include for the effect of the plasmonic particle on the emitted field that drives the Stokes probe. This is analogous to including for dipole re-radiation effects in the SERS enhancement factor calculation,[134] but here it is the driven oscillator Q that generates the dipole field at the Stokes frequency (through the QE_{pu} term). Another issue in Eq. 2.19b is that we have assumed that the dipole fields that are coherently emitted by all the molecules in the sample have been coherently summed to generate a polarization that drives a plane wave solution. This replacement (also used by Lee *et al.*[126]) is essential, as the driven vibration needs to generate a field that can interfere constructively with the incident Stokes plane wave field, and it arises from the fact that coherent sum of dipole fields generates a plane wave in the far field.

A key issue about Eq. 2.19b is that the time dependence of Q ($e^{i\omega_0 t}$) combines with E_{pu} ($e^{-i\omega_{pu}t}$) to drive a field with the Stokes shifted time dependence, as required with the rotating wave approximation (RWA). While this may seem like an obvious point, it means that the driving term in Eq. 2.19b contains the product of g_{st} from Eq. 2.19b and g_{st} from Eq. 2.18, or g_{st}^2 rather than an absolute square. This will play a crucial role in generating dispersive lineshapes later on, and here we see that it is a natural result of the RWA in which the Stokes field acts twice with the same phase. One physical interpretation of this approximation is that we assume the driving fields on the right hand side of Eq. 2.19a are creating a radiating dipole. This dipole re-interacts with the plasmon gaining an additional *local field effect* (LFE) enhancement as g_{st}, before the collection of dipoles are treated as a plane wave as described by Eqs. 2.16b and 2.16d. In contrast to this, the pump field enhancement appears as an absolute square as it applies first as a complex conjugate E_{pu}^* in Eq. 2.11 and then not as a complex conjugate within E_{pu} in Eq. 2.19b.

Ignoring the homogenous solution to Maxwell's equation due to averaging over all possible initial phases of the oscillators,[126] we solve using Fourier transforms:

$$\frac{\partial^2 E_{st}(z,\omega)}{\partial z^2} + \frac{\omega^2}{c^2}E_{st}(z,\omega) = -\frac{4\pi\omega^2}{c^2}N\alpha_m^{'}FT\left\{g_{st}Q(z,t)E_{pu}(z,t)\right\} \qquad (2.20)$$

And focusing on the convolution integral:

$$FT\left\{g_{st}Q(z,t)E_{pu}(z,t)\right\} = (2\pi)^{-1}g_{st}Q(z,\omega) * E_{pu}(z,\omega) \tag{2.21a}$$

$$FT\left\{g_{st}Q(z,t)E_{pu}(z,t)\right\} = (2\pi)^{-1}\int_{-\infty}^{\infty} g_{st}Q(z,\tilde{\omega}) * E_{pu}(z,\omega-\tilde{\omega})d\tilde{\omega} \tag{2.21b}$$

To solve the convolution integral we make identical approximations as used by Lee *et al.*:[126] substitution of $\tilde{\omega} = -\omega_0$ in the $Q(z,\tilde{\omega})$ terms, evaluation of the integrand denominator at $\tilde{\omega} = \omega - \omega_{pu}$, evaluation of the resulting Gaussian integral, finally substitution of $\omega = \omega_{pu} - \omega_0$ to regain the original unperturbed Stokes field from Eq. 2.16d. These approximations and evaluations lead to the following solution for the convolution integral in Eq. 2.21b:

$$FT\left\{g_{st}Q(z,t)E_{pu}(z,t)\right\} = \frac{\alpha_m^{'}|g_{pu}|^2|E_{pu}^0|^2 g_{st}^2 E_{st}^0(z,\omega)}{(\omega_0)(\omega_0+\omega-\omega_{pu}+2i\gamma)} \tag{2.21c}$$

Returning to Eq. 2.20 and evaluating Maxwell's equation more fully:

$$\frac{\partial^2 E_{st}(z,\omega)}{\partial z^2} + \frac{\omega^2}{c^2}E_{st}(z,\omega) = -\frac{4\pi\omega^2 N}{c^2}\frac{\alpha_m^{'2}|g_{pu}|^2|E_{pu}^0|^2 g_{st}^2 E_{st}^0(z,\omega)}{(\omega_0)(\omega_0+\omega-\omega_{pu}+2i\gamma)} \tag{2.22}$$

$$\frac{\partial^2 E_{st}(z,\omega)}{\partial z^2} + \frac{\omega^2}{c^2}E_{st}(z,\omega) = -\frac{4\pi\omega^2}{c^2}\chi_R(\omega)|g_{pu}|^2|E_{pu}^0|^2 g_{st}^2 E_{st}^0(z,\omega) \tag{2.23}$$

where the Raman susceptibility, $\chi_R(\omega)$, is given by:

$$\chi_R(\omega) \equiv N\alpha_m'^2(\omega_0)^{-1}(\omega_0 + \omega - \omega_{pu} + 2i\gamma)^{-1} \tag{2.24}$$

To solve Eq. 2.23, we make the ansatz that can be verified by substitution:

$$E_{st}(z,\omega) = \left(1 + 2\pi i\chi_R(\omega)|g_{pu}|^2|E^0_{pu}|^2 g^2_{st}\left(\frac{\omega z}{c}\right)\right) E^0_{st}(z,\omega) \tag{2.25}$$

From this, the Raman gain in SE-FSRS can be expressed as:

$$G_R(\omega) = \frac{|E_{st}(z,\omega)|^2}{|E^0_{st}(z,\omega)|^2} = \left|1 + 2\pi i\chi_R(\omega)|g_{pu}|^2|E^0_{pu}|^2 g^2_{st}\left(\frac{\omega z}{c}\right)\right|^2 \tag{2.26}$$

For small gain this can be approximated as:

$$\begin{aligned} G_R(\omega) &= \left|1 + 2\pi i\chi_R(\omega)|g_{pu}|^2|E^0_{pu}|^2 g^2_{st}\left(\frac{\omega z}{c}\right)\right|^2 \\ &\approx e^{-4\pi|g_{pu}|^2|E^0_{pu}|^2\left(\frac{\omega z}{c}\right)\left(Re\{\chi_R(\omega)\}Im\left\{g^2_{st}\right\}+Im\{\chi_R(\omega)\}Re\left\{g^2_{st}\right\}\right)} \end{aligned} \tag{2.27}$$

Finally, the experimental observable for stimulated Raman gain (SRG) SE-FSRS is an optical density,

$$\begin{aligned} D_{SRG}(\omega) &\equiv ln\left(G_R(\omega)\right) = -4\pi|g_{pu}|^2|E^0_{pu}|^2\left(\frac{\omega z}{c}\right) \\ &\times \left(Im\left\{\chi_R(\omega)\right\} Re\left\{g^2_{st}\right\} + Re\left\{\chi_R(\omega)\right\} Im\left\{g^2_{st}\right\}\right) \end{aligned} \tag{2.28a}$$

or, analogously:

$$D_{SRG}(\omega) = -4\pi|g_{pu}|^2|E^0_{pu}|^2\left(\frac{\omega z}{c}\right) \times Im\left\{\chi_R(\omega)g^2_{st}\right\} \tag{2.28b}$$

From this expression we can see that if only the pump field were enhanced, it would contribute a factor $|g_{pu}|^2$ to the enhancement of SE-FSRS over FSRS. Analyzing Eqs. 2.28a and 2.28b further we can observe a few more points:

(1) An additional complex plasmonic enhancement comes from the competition of the real and imaginary portions of the LFE from the Stokes field interacting with the plasmon. Rigorously, the total plasmonic enhancement is given as $|g_{pu}|^2 Im\left\{\chi_R(\omega) g_{st}^2\right\} / Im\left\{\chi_R(\omega)\right\}$.

(2) In the case of no plasmonic enhancement, the real and imaginary portions of g go to 1 and zero, respectively. This limiting case of SE-FSRS matches identically with the results of Lee *et al.*[126,130]

(3) SE-FSRS examines an optical process with competing real and imaginary components of the Raman susceptibility that FSRS does not.

(4) Probing both the real and imaginary portions of $\chi_R(\omega)$ will lead to interference and dispersive lineshapes as seen in SECARS (but with a different mechanism)[88,89] and previous SE-FSRS experiments.[72,98]

To more fully understand the Raman gain optical density, we re-evaluate Eq. 20 to separate the full Raman gain optical density expression into Fano lineshapes.

From Eq. 2.28b:

$$D_R(\omega) = -4\pi |g_{pu}|^2 |E_{pu}^0|^2 \left(\frac{\omega z}{c}\right) \times Im\left\{\chi_R(\omega) g_{st}^2\right\} \tag{2.29}$$

and from Eq. 2.24:

$$\chi_R(\omega) \equiv N\alpha_m'^2(\omega_0)^{-1}(\omega_0 + \omega - \omega_{pu} + 2i\gamma)^{-1} \tag{2.30}$$

Recognizing $\omega_{pu} - \omega_0 = \omega_{st}$:

$$\chi_R(\omega) \equiv N\alpha_m'^2(\omega_0)^{-1}(\omega - \omega_{st} + 2i\gamma)^{-1} \tag{2.31}$$

letting $A = -4\pi|g_{pu}|^2|E_{pu}^0|^2 N\alpha_m'^2(\omega_0)^{-1}$, $D_R(\omega)$ becomes:

$$D_R(\omega) = AIm\left\{\frac{g_{st}^2}{\omega - \omega_{st} + 2i\gamma}\right\}\left(\frac{\omega z}{c}\right) \tag{2.32}$$

$$= A\frac{Im\left\{g_{st}^2(\omega - \omega_{st} - 2i\gamma)\right\}}{(\omega - \omega_{st})^2 + (2\gamma)^2}\left(\frac{\omega z}{c}\right) \tag{2.33}$$

Separating g_{st}^2 into real and imaginary parts leads to:

$$= A\frac{Im\{(Re\{g_{st}^2\} + iIm\{g_{st}^2\})(\omega - \omega_{st} - 2i\gamma)\}}{(\omega - \omega_{st})^2 + (2\gamma)^2}\left(\frac{\omega z}{c}\right) \tag{2.34}$$

$$= A\left(\frac{\omega z}{c}\right)\left[\frac{-2\gamma Re\{g_{st}^2\} + Im\{g_{st}^2\}(\omega - \omega_{st})}{(\omega - \omega_{st})^2 + (2\gamma)^2}\right] \tag{2.35}$$

To look for a form of this equation that can be compared to a Fano profile we complete the square in terms of an expansion of the term in square brackets in powers of $(\omega - \omega_{st})$:

$$\begin{aligned}&(x + i(2\gamma Re\{g_{st}^2\})^{1/2})^2 - x^2\\ &= -2\gamma Re\{g_{st}^2\} + Im\{g_{st}^2\}(\omega - \omega_{st})\end{aligned} \tag{2.36}$$

$$x = -iIm\{g_{st}^2\}(\omega - \omega_{st})2^{-3/2}\gamma^{-1/2}Re\{g_{st}^2\}^{-1/2} \tag{2.37}$$

$$x^2 = -Im\{g_{st}^2\}^2(\omega - \omega_{st})^2 2^{-3}\gamma^{-1}Re\{g_{st}^2\}^{-1} \tag{2.38}$$

Then we can rewrite $D_R(\omega)$ as:

$$\begin{aligned} D_R(\omega) = {} & A\left(\frac{\omega z}{c}\right) \\ & \times \left[\frac{(-iIm\{g_{st}^2\}(\omega - \omega_{st})2^{-3/2}\gamma^{-1/2}Re\{g_{st}^2\}^{-1/2} + i(2\gamma Re\{g_{st}^2\})^{1/2})^2}{(\omega - \omega_{st})^2 + (2\gamma)^2}\right. \\ & \left. + \frac{Im\{g_{st}^2\}^2(\omega - \omega_{st})^2 2^{-3}\gamma^{-1}Re\{g_{st}^2\}^{-1}}{(\omega - \omega_{st})^2 + (2\gamma)^2}\right] \end{aligned} \tag{2.39}$$

$$\begin{aligned} & = A\left(\frac{\omega z}{c}\right) \\ & \times \left[\frac{(-iIm\{g_{st}^2\}\left(\frac{\omega - \omega_{st}}{2\gamma}\right)2^{-3/2}\gamma^{-1/2}Re\{g_{st}^2\}^{-1/2} + i2^{-1/2}\gamma^{-1/2}Re\{g_{st}^2\}^{1/2})^2}{1 + (\frac{\omega - \omega_{st}}{2\gamma})^2}\right. \\ & \left. + \frac{Im\{g_{st}^2\}^2 2^{-3}\gamma^{-1}Re\{g_{st}^2\}^{-1}(\frac{\omega - \omega_{st}}{2\gamma})^2}{1 + (\frac{\omega - \omega_{st}}{2\gamma})^2}\right] \end{aligned} \tag{2.40}$$

$$\begin{aligned} & = A\left(\frac{\omega z}{c}\right)\left(Im\{g_{st}^2\}^2 2^{-3}\gamma^{-1}Re\{g_{st}^2\}^{-1}\right) \\ & \times \left[\frac{(i^{-1}((\frac{\omega - \omega_{st}}{2\gamma}) - 2Re\{g_{st}^2\}Im\{g_{st}^2\}^{-1}))^2}{1 + (\frac{\omega - \omega_{st}}{2\gamma})^2} + \frac{(\frac{\omega - \omega_{st}}{2\gamma})^2}{1 + (\frac{\omega - \omega_{st}}{2\gamma})^2}\right] \end{aligned} \tag{2.41}$$

Letting $q = -2Re\{g_{st}^2\}Im\{g_{st}^2\}^{-1}$ as the Fano profile parameter similar to Frontiera *et al.*:[98]

$$= -A\left(\frac{\omega z}{c}\right)\gamma^{-1}2^{-3}Im\{g_{st}^{2}\}^{2}Re\{g_{st}^{2}\}^{-1}\left[\frac{((\frac{\omega-\omega_{st}}{2\gamma})+q)^{2}}{1+(\frac{\omega-\omega_{st}}{2\gamma})^{2}}-\frac{(\frac{\omega-\omega_{st}}{2\gamma})^{2}}{1+(\frac{\omega-\omega_{st}}{2\gamma})^{2}}\right] \tag{2.42}$$

Thus we get that the lineshapes in SE-FSRS are the sum of two Fano profiles where the Fano asymmetry parameter of one of the lineshapes is exactly zero while the other has a Fano parameter that depends on the ratio of $Re\{g_{st}^{2}\}$ to $Im\{g_{st}^{2}\}$.

2.4. Discussion

We now investigate the lineshapes of the optical density in SE-FSRS with our theoretical model developed herein by simulating a model system corresponding to published experiments.

Previous SE-FSRS experiments analyzed systems of 1,2-*trans*(bis-4-pyridyl)ethylene (BPE) adsorbed on gold nanoparticles. The gold nanoparticles were either 60 or 90 nm diameter spherical particles where the 60 nm diameter cores had broad aggregate localized surface plasmon resonances (LSPR) from 750 - 1000 nm. The 90 nm diameter core particles had broad aggregate LSPRs from 825 - 1200 nm. Using a picosecond Raman pump centered at 795 nm and a ∼100 fs spectrally broad (820-930 nm) Stokes field the far-field stimulated Raman spectrum of BPE in the near-field of two different plasmon resonances was observed in separate experiments. Further experimental details are listed in Section 2.6.4 and in Frontiera *et al.*[98]

Using a free-electron Drude model for the particle polarizability (see Section 2.6.2), in addition to static molecular polarizabilities from density functional theory (see Section 2.6.3), we can simulate the optical response of the molecule-nanoparticle system to different field interactions.

Shown in Fig. 2.2 is the structure of the nanoparticle-molecule system used for molecular polarizabilities in the simulations to be discussed: a single BPE molecule symmetrically bridging two Au_8 structures to mimic a real molecule-nanoparticle system.

Using the Au_8-BPE-Au_8 structure for the molecular polarizability parameters, we simulate the full optical response observed in SE-FSRS, the optical density ($D_R(\omega)$) in Eq. 2.28a.

First we simulate a single BPE molecule near an 825 nm LSPR, shown in Fig. 2.3.

The simulated signal in Fig. 2.3 shows frequency dependent asymmetry that qualitatively matches the SE-FSRS gain observed in the experiment of BPE on 60 nm Au nanoparticles aggregates. The SE-FSRS gain observed in BPE on 90 nm Au nanoparticle aggregates is given in Fig. 2.4.

Here we again see qualitative agreement between experiment and theory, showing a reversal in the sign of the dispersive SE-FSRS gain lineshape.

In previous SE-FSRS experiments the dispersive lineshapes were attributed to Fano-like resonances resulting from interference of discrete molecular vibrational states on the broad continuum of the plasmon resonance.[98] The lineshapes observed in simulating the SE-FSRS Raman gain from Eq. 2.28a (Figs. 2.3 and 2.4) are related to this; however, here we see that it is the plasmon enhancement associated with the Stokes probe coherently acting twice that dominates that lineshape asymmetry.

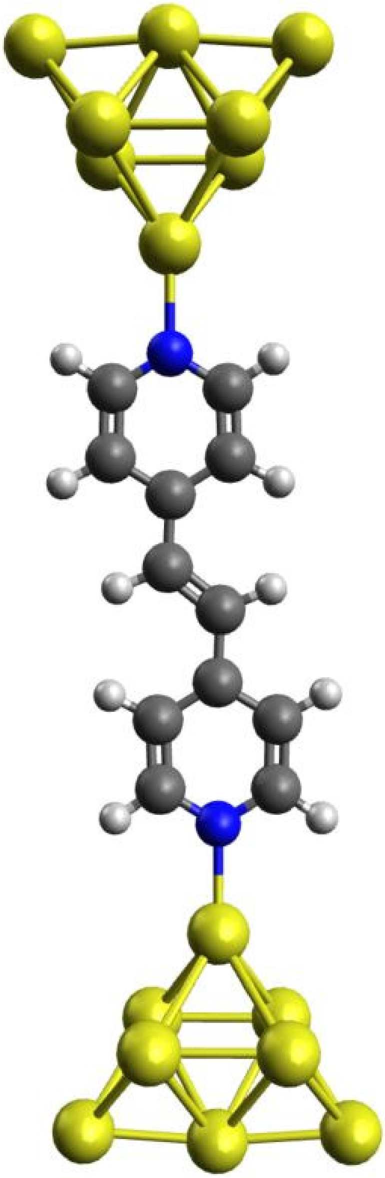

Figure 2.2. Structure for molecular polarizability calculations. Figure reproduced with permission from Ref. 110. Copyright 2016 American Institute of Physics.

Generally, Fano resonances occur when there are two weakly coupled oscillators where one oscillator is resonantly driven. The resonantly driven oscillator then exhibits a force on the coupled oscillator which results in either constructive or destructive interference

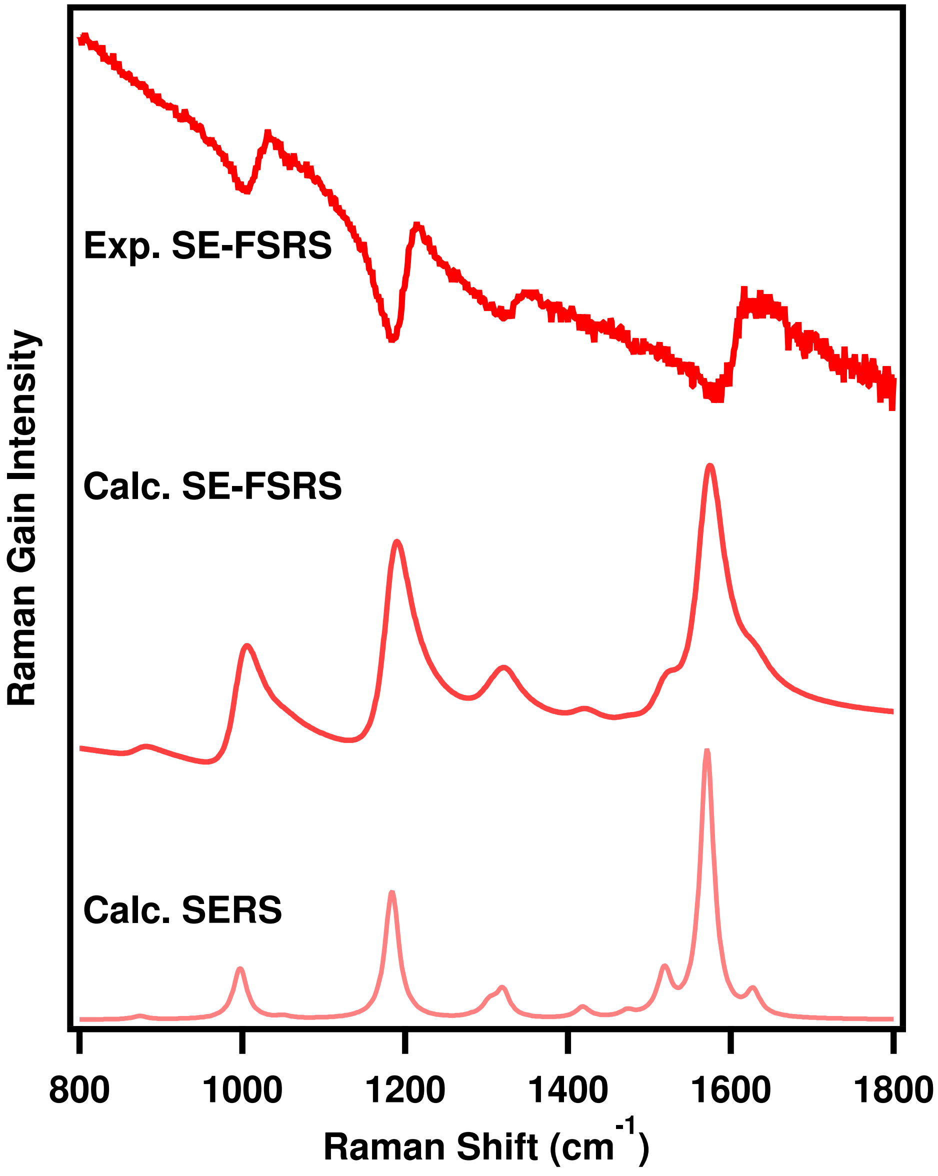

Figure 2.3. Simulation of SE-FSRS gain for a BPE molecule coupled to an 825 nm LSPR. Figure reproduced with permission from Ref. 110. Copyright 2016 American Institute of Physics.

effects in the driven oscillator resonance. This argument is also applicable in the present case, where the driven vibrational oscillator subsequently drives the Stoke's field, resulting

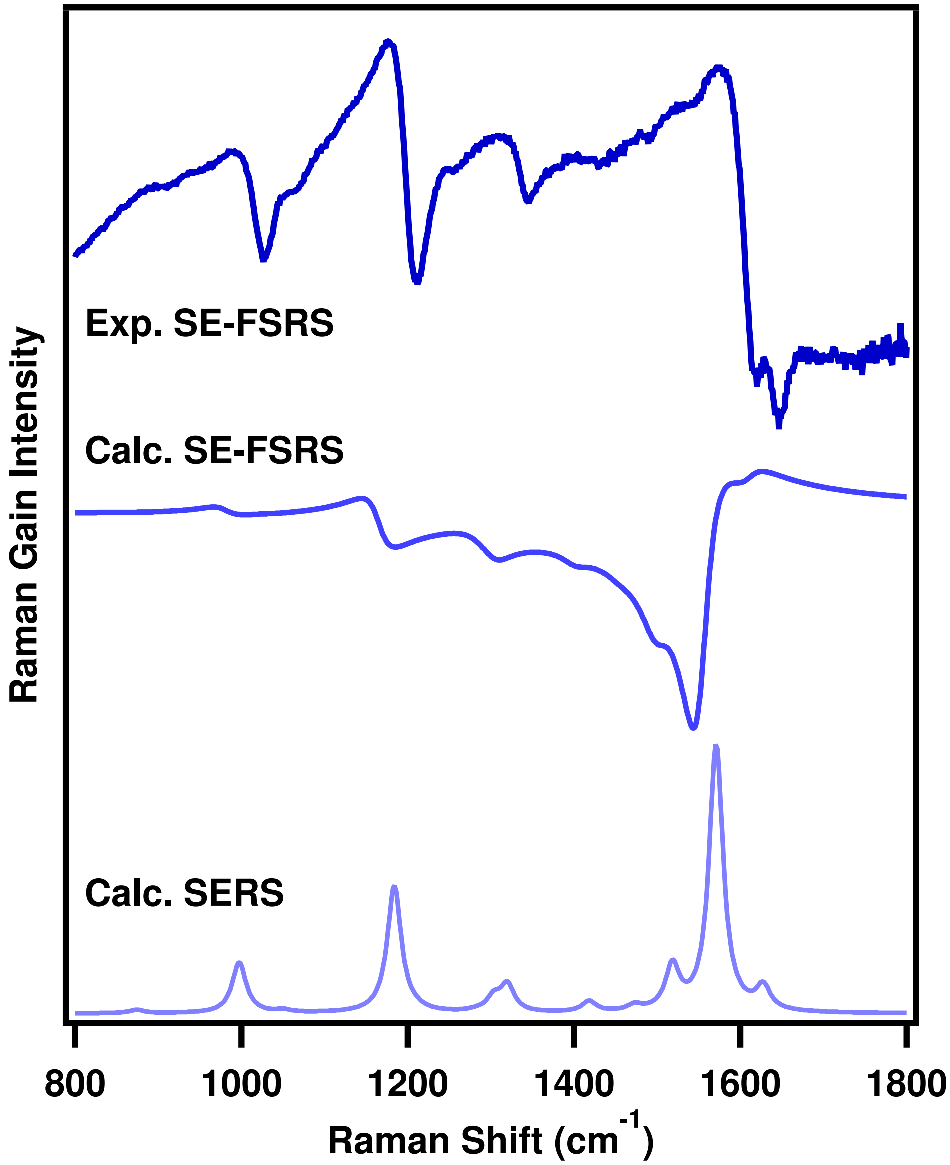

Figure 2.4. Simulation of SE-FSRS gain for a BPE molecule coupled to an 900 nm LSPR. Figure reproduced with permission from Ref. 110. Copyright 2016 American Institute of Physics.

in a gain that includes interference of the real and imaginary components of the Raman susceptibility with the square of the Stokes field LFE (Eq. 2.28a).

To further study the effects of plasmon resonance frequency on SE-FSRS lineshapes, Section 2.6.5 shows the lineshapes associated with Eq. 2.28a in which the LSPR frequencies are allowed to vary. In Fig. 2.10 we observe an abrupt transition from positive to negative SE-FSRS gain signals near 875 nm. At even longer LSPR wavelengths (around 950 nm), another transition occurs where the lineshapes have a mixture of positive and negative character. Also noteworthy is that the intensities of the spectra can vary by orders of magnitude depending on choice of LSPR. These effects are probably exaggerated by the partially unphysical nature of the analytic particle polarizability as described in Section 2.6.2, so it will be important to relax these approximations in further work.

2.5. Conclusion

Using a semiclassical coupled wave theory for SE-FSRS, we have developed an expression for the lineshape which qualitatively reproduces experimental data, including the dispersive lineshapes. In addition, the theory makes important predictions concerning the plasmonic enhancement factor, which is given by $|g_{pu}|^2 Im\left\{\chi_R(\omega) g_{st}^2\right\} / Im\left\{\chi_R(\omega)\right\}$, where $|g_{pu}|^2$ is the absolute square of the plasmonic enhancement from the Raman pump, $\chi_R(\omega)$ is the Raman susceptibility, and g_{st} is the plasmonic enhancement of the Stokes field in SE-FSRS. While the dispersive nature of the lineshapes was originally hypothesized to be purely Fano-like interferences,[98] our analysis suggests that they are a combination of two Fano-like contributions. Similar to previously observed dispersive lineshapes that originate from multiple physical interference processes,[88,89] the lineshapes in this work are attributed to interference of the real and imaginary components of the Raman susceptibility with the LFE of the Stokes field interacting with a plasmonic particle.

The expression obtained from our evaluation is significantly different from that recently published by Ziegler and coworkers.[111] Their expression involves the interference between the Raman susceptibility and a stimulated resonant surface plasmon optical field, for which the enhancement factor is given as being proportional to $|g|^4$, or in our notation is $|g_{pu}|^2|g_{st}|^2$. Thus unlike our expression, where it is the phase of the square of the Stokes field enhancement factor g_{st}^2 that is essential in determining the lineshape asymmetry, in the Ziegler derivation it is the interference of two independent scattering mechanisms that results in asymmetry. Ziegler presents a detailed analysis of the relative sizes of these scattering mechanisms, and argues that they might be close enough to provide meaningful interference. In our derivation the asymmetry is built-in to a single mechanism, and the size of the contributing terms in the asymmetry is easily estimated. While it is possible that the interference involved in the Ziegler derivation could also arise in our work by adding in the PLE contribution, this would be subject to the same ambiguous evaluation as in the Ziegler analysis.

Future directions for SE-FSRS theory will involve treating the case of electronically resonant pulses in the SE-FSRS experiment by using a density matrix formulation. By pursuing a density matrix formulation for SE-FSRS, the resulting theory will include the effects of hot luminescence and other Feynman diagrams to the third order optical response that has been observed in non-plasmonically-enhanced resonant FSRS (FSRRS). Deriving a density matrix theory for SE-FSRS, theory will predict the optical response of as yet unrealized experiments.

2.6. Supplementary Information

2.6.1. Solving for the Stimulated Raman Loss (SRL) in SE-FSRS

As an interesting aside, in the main derivation if we were to have made a different substitution in solving the convolution integral for Maxwell's equation (Eq. 2.21b) the SRL effect in SE-FSRS could be obtained.* We continue the SRL derivation here, starting at Eq. 2.21b:

$$\begin{aligned} &FT\left\{g_{st}Q(z,t)E_{pu}(z,t)\right\} \\ &= \alpha_m^{'}|g_{pu}|^2|E_{pu}^0|^2\tau_{pu}g_{st}^2E_{st}^0\tau_{st}e^{i\omega z/c} \\ &\times \int_{-\infty}^{\infty}\frac{e^{-(\tilde{\omega}+\omega_{pu}-\omega_{st})^2\tau_{st}^2/2}e^{-(\omega-\tilde{\omega}-\omega_{pu})^2\tau_{pu}^2/2}}{\omega_0^2-\tilde{\omega}^2-2i\gamma\tilde{\omega}}d\tilde{\omega} \end{aligned} \tag{2.43}$$

Now substituting $\tilde{\omega}=\omega_0$ in the $Q(z,\tilde{\omega})$ terms:

$$\begin{aligned} &FT\left\{g_{st}Q(z,t)E_{pu}(z,t)\right\} \\ &\approx \alpha_m^{'}|g_{pu}|^2|E_{pu}^0|^2\tau_{pu}g_{st}^2E_{st}^0\tau_{st}e^{i\omega z/c} \\ &\times e^{-(\omega_0+\omega_{pu}-\omega_{st})^2\tau_{st}^2/2}(-\omega_0)^{-1}\int_{-\infty}^{\infty}\frac{e^{-(\omega-\tilde{\omega}-\omega_{pu})^2\tau_{pu}^2/2}}{-\omega_0+\tilde{\omega}+2i\gamma}d\tilde{\omega} \end{aligned} \tag{2.44}$$

---

*This section was not published in Ref. 110.

Recognizing that the Gaussian function peaks at $\tilde{\omega} = \omega - \omega_{pu}$, we evaluate the denominator at that frequency position, then perform the integral to arrive at:

$$\begin{aligned} & FT\left\{g_{st}Q(z,t)E_{pu}(z,t)\right\} \\ & = -\sqrt{2\pi}\alpha_m^{'}|g_{pu}|^2|E_{pu}^0|^2 g_{st}^2 E_{st}^0 \tau_{st} \frac{e^{-(\omega_0+\omega_{pu}-\omega_{st})^2\tau_{st}^2/2} e^{i\omega z/c}}{(\omega_0)(-\omega_0+\omega-\omega_{pu}+2i\gamma)} \end{aligned} \tag{2.45}$$

As we are interested in the anti-Stokes field associated with polarization induced by the driven oscillation, we substitute $\omega = \omega_{pu} + \omega_0$ to the original, unperturbed anti-Stokes field from Eq. 2.16d

$$FT\left\{g_{st}Q(z,t)E_{pu}(z,t)\right\} = -\frac{\alpha_m^{'}|g_{pu}|^2|E_{pu}^0|^2 g_{st}^2 E_{st}^0(z,\omega)}{(\omega_0)(-\omega_0+\omega-\omega_{pu}+2i\gamma)} \tag{2.46}$$

Returning to Eq. 2.20 and evaluating Maxwell's equation more fully for the anti-Stokes field:

$$\frac{\partial^2 E_{st}(z,\omega)}{\partial z^2} + \frac{\omega^2}{c^2}E_{st}(z,\omega) = \frac{4\pi\omega^2 N}{c^2}\frac{\alpha_m^{'2}|g_{pu}|^2|E_{pu}^0|^2 g_{st}^2 E_{st}^0(z,\omega)}{(\omega_0)(-\omega_0+\omega-\omega_{pu}+2i\gamma)} \tag{2.47}$$

$$\frac{\partial^2 E_{st}(z,\omega)}{\partial z^2} + \frac{\omega^2}{c^2}E_{st}(z,\omega) = \frac{4\pi\omega^2}{c^2}\chi_R(\omega)|g_{pu}|^2|E_{pu}^0|^2 g_{st}^2 E_{st}^0(z,\omega) \tag{2.48}$$

where the Raman susceptibility, $\chi_R(\omega)$, is given by:

$$\chi_R(\omega) \equiv N\alpha_m^{'2}(\omega_0)^{-1}(-\omega_0+\omega-\omega_{pu}+2i\gamma)^{-1} \tag{2.49}$$

To solve Eq. 2.48, we make the ansatz that can be verified by substitution:

$$\begin{aligned} &E_{st}(z,\omega) = \\ &\left(1 - 2\pi i\chi_R(\omega)|g_{pu}|^2|E^0_{pu}|^2 g^2_{st}\left(\frac{\omega z}{c}\right)\right) E^0_{st}(z,\omega) \end{aligned} \tag{2.50}$$

From this, the stimulated Raman loss in SE-FSRS can be expressed as:

$$L_R(\omega) = \frac{|E_{st}(z,\omega)|^2}{|E^0_{st}(z,\omega)|^2} = \left|1 - 2\pi i\chi_R(\omega)|g_{pu}|^2|E^0_{pu}|^2 g^2_{st}\left(\frac{\omega z}{c}\right)\right|^2 \tag{2.51}$$

For small loss this can be approximated as:

$$\begin{aligned} &L_R(\omega) = \left|1 - 2\pi i\chi_R(\omega)|g_{pu}|^2|E^0_{pu}|^2 g^2_{st}\left(\frac{\omega z}{c}\right)\right|^2 \\ &\approx e^{4\pi|g_{pu}|^2|E^0_{pu}|^2\left(\frac{\omega z}{c}\right)\left(Re\{\chi_R(\omega)\}Im\left\{g^2_{st}\right\}+Im\{\chi_R(\omega)\}Re\left\{g^2_{st}\right\}\right)} \end{aligned} \tag{2.52}$$

Finally, the experimental observable in the SRL by SE-FSRS will be an optical density,

$$\begin{aligned} &D_{SRL}(\omega) \equiv ln\left(L_R(\omega)\right) = 4\pi|g_{pu}|^2|E^0_{pu}|^2\left(\frac{\omega z}{c}\right) \\ &\times \left(Im\left\{\chi_R(\omega)\right\} Re\left\{g^2_{st}\right\} + Re\left\{\chi_R(\omega)\right\} Im\left\{g^2_{st}\right\}\right) \end{aligned} \tag{2.53a}$$

or, analogously:

$$D_{SRL}(\omega) = 4\pi|g_{pu}|^2|E^0_{pu}|^2\left(\frac{\omega z}{c}\right) \times Im\left\{\chi_R(\omega) g^2_{st}\right\} \tag{2.53b}$$

Simulating Eq. 2.53a for a BPE molecule near an 825 nm LSPR and a 900 nm LSPR results in the lineshapes observed in Fig. 2.5.

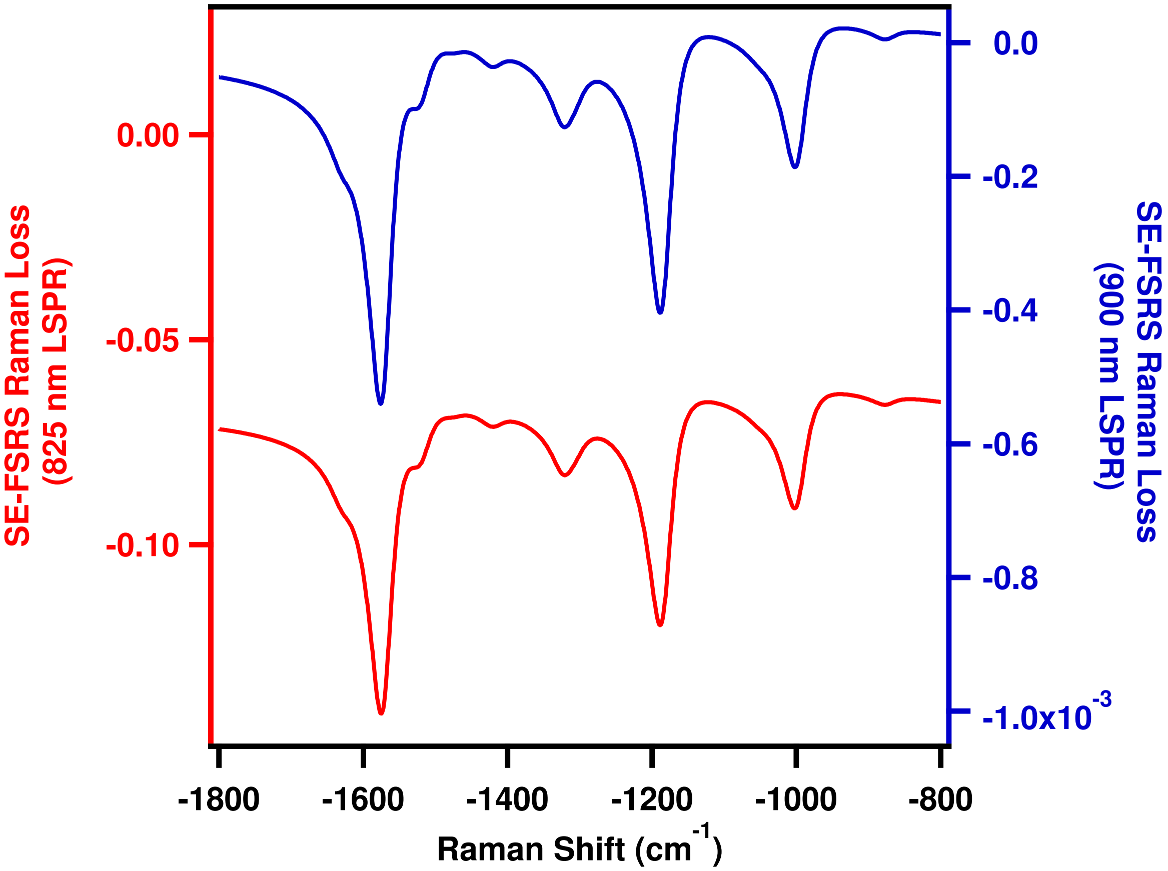

Figure 2.5. Comparing the simulated SRL in SE-FSRS for a BPE molecule near either an 825 nm or 900 nm LSPR.

2.6.2. Varying χ to determine $\tilde{\alpha}_P(\omega)$ in the free-electron Drude model

We have two cases of plasmon resonances that we wish to compare the SE-FSRS response in Eq. 2.28a. The first case is with a plasmon resonance at 825 nm and the second case is at 900 nm. The general method we will use is to solve the shape-dependent spheroidal extinction equation from Schatz *et al.*,[9] by varying a parameter χ, that corresponds to the aspect ratio of a spheroidal particle, then substitute in values for the desired plasmon resonance and the Drude model parameters for the plasma frequency (ω_p) and plasma

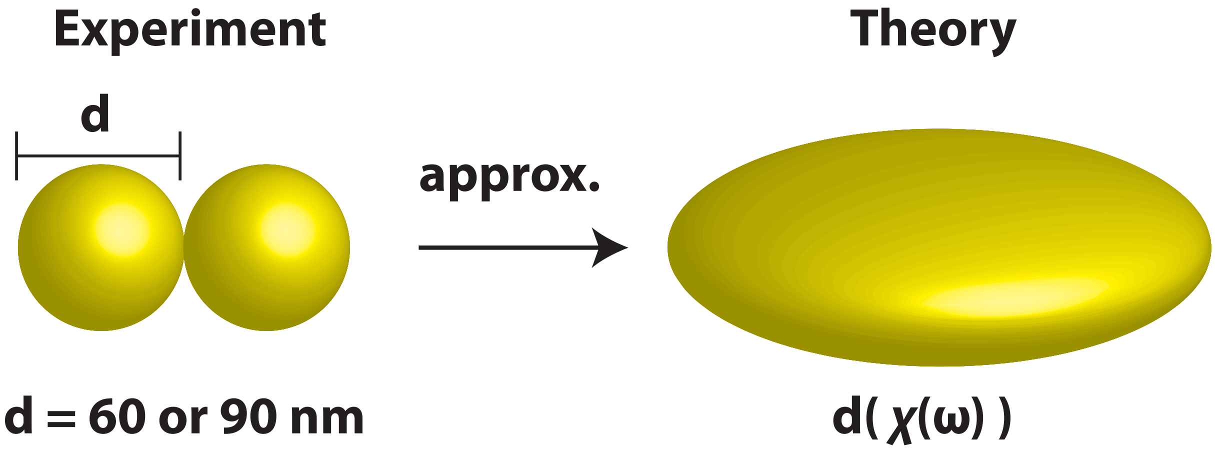

Figure 2.6. Approximating a dimer plasmon resonance as a spheroidal plasmon resonance. Figure reproduced with permission from Ref. 110. Copyright 2016 American Institute of Physics.

decay (γ). In effect this will approximate the dimer type structures in the experiment as a spheroidal particle with an effective plasmon resonance determined by tuning a shape parameter (χ) as shown in Fig. 2.6.

Starting with the extinction spectrum in frequency:

$$E(\omega) = \frac{24\pi^2 N a^3 \epsilon_{out}^{(3/2)}}{\omega ln(10)} \left[\frac{\epsilon_i(\omega)}{(\epsilon_r(\omega) + \chi\epsilon_{out})^2 + \epsilon_i(\omega)^2} \right] \tag{2.54}$$

We observe that tuning the χ parameter allows for changing the aspect ratio of a plasmonic spheroid and thus the resulting plasmon resonance energy. Substituting in values for χ of the desired plasmon resonances and the Drude model parameters for the

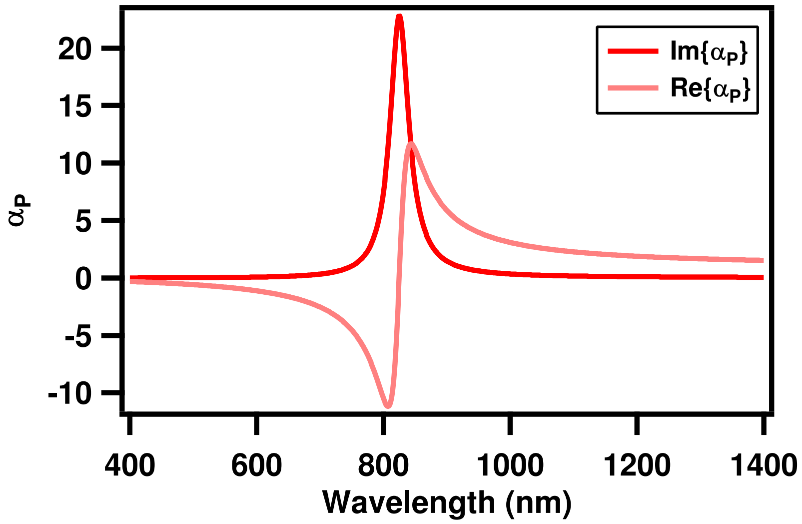

Figure 2.7. Complex frequency dependence of $\tilde{\alpha}_P$ for an LSPR near 825 nm. Figure reproduced with permission from Ref. 110. Copyright 2016 American Institute of Physics.

plasma frequency (ω_p = 8.55 eV) and plasma decay (γ= 0.0184 eV) we get frequency dependent polarizabilities for the two choices of particle dimers.

For a plasmon resonance analogous to the experimental 60 nm dimer aggregate plasmon at ω = 825 nm:

$$\tilde{\alpha}_P(\omega) = \frac{\epsilon_i - 1}{\epsilon_i + 34.45} \tag{2.55a}$$

For a plasmon resonance analogous to the experimental 90 nm dimer aggregate plasmon at ω = 900 nm:

$$\tilde{\alpha}_P(\omega) = \frac{\epsilon_i - 1}{\epsilon_i + 41.19} \tag{2.55b}$$

where ϵ_i is given by the Drude model:

$$\epsilon_i = 1 - \frac{\omega_p^2}{\omega(\omega + i\gamma)} \tag{2.55c}$$

Note that this results in a complex, frequency dependent polarizability.

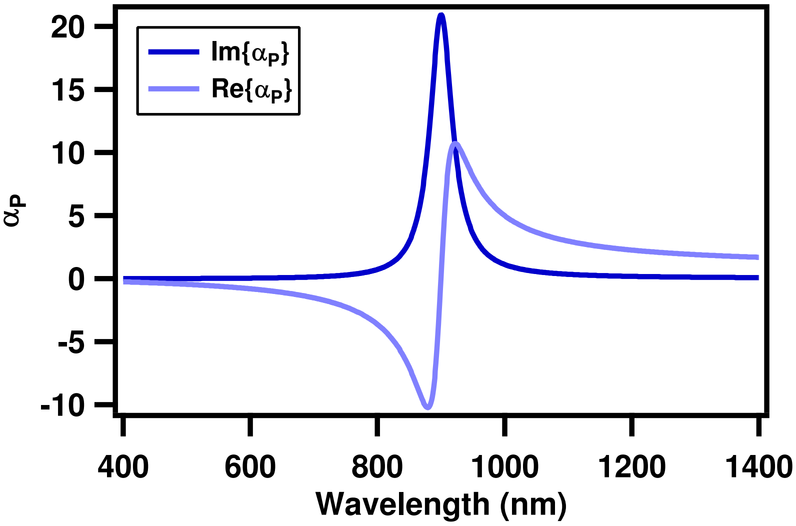

Figure 2.8. Complex frequency dependence of $\tilde{\alpha}_P$ for an LSPR near 900 nm. Figure reproduced with permission from Ref. 110. Copyright 2016 American Institute of Physics.

2.6.3. Density functional theory calculations of nanoparticle-molecule-nanoparticle system polarizabilities

Static polarizabilities of the nanoparticle-molecule-nanoparticle system shown in Fig. 2.2 were calculated using the Amsterdam Density Functional (ADF) computational chemistry package.[135] Frequency and polarizability calculations for the symmetric Au_8-BPE-Au_8 complex were completed using the Becke-Perdew (BP86) generalized gradient approximation (GGA) exchange correlation functional and a triple-ζ polarized (TZP) Slater orbital basis set with zeroth order regular approximation for relativistic effects.

Static Raman polarizabilities (ω=0) were calculated in the RESPONSE package by two-point numerical differentiation using the RAMANRANGE keyword. SERS scattering intensities were determined by the following equation:[136]

$$\frac{\partial\sigma}{\partial\Omega} = \frac{\pi^2}{\epsilon_0^2}(\omega - \omega_j)^4 \frac{h}{8\pi c\omega_j}(S)\frac{1}{45\left(1 - e^{-\frac{hc\omega_j}{k_B t}}\right)} \tag{2.56}$$

where the scattering factor (S) is defined as $45\bar{\alpha}_j'^2 + 7\gamma_j'^2$, and $\bar{\alpha}_j'$, $\gamma_j'^2$ are the isotropic and anisotropic polarizability tensors with respect to the jth vibrational mode.

For SE-FSRS simulations the α_m' used was defined as $\alpha_m' \equiv \sqrt{S}$, where S is the scattering factor defined previously. The SERS line for each mode was broadened to a Lorentzian lineshape with full-width at half-maximum (FWHM) of 20 cm^{-1} for comparison to experimental data.

2.6.4. Experimental methods of SE-FSRS

The experimental methods for collecting data in SE-FSRS have been described previously.[72,98] Briefly, the 1 W, 800 nm output of a 100 kHz regenerative amplifier (Coherent RegA) is split into two paths for the FSRS experiment. Approximately 500 mW of the amplified output is used to generate a picosecond bandwidth Raman pump field by passing through two identical angle tuned bandpass filters (CVI optics) at 795 nm. A portion of the remainder of the amplified output is used for white light continuum generation in a sapphire plate which is then temporally compressed by a prism pair. The continuum is then filtered using a set of short- and longpass filters to create a Stokes field in the spectral region of interest. The pulses are overlapped spatiotemporally in a collinear geometry in a 2 mm cell equipped with a micro stir bar to keep the sample viable in the focal overlap volume. The pump pulse is mechanically chopped so that sequential pump-on and pump-off spectra are obtained in a home-built LabView program. The heterodyned SE-FSRS signal is detected with the Stokes field using a spectrograph (Princeton Instruments SP2538) and CCD (PIXIS:100F). Average powers were 25 μW and 10 μW for the Raman pump and Stokes fields respectively. Each experimental SE-FSRS spectrum shown has a total acquisition time of 6 minutes.

The key difference between the experimental spectra shown in this chapter compared to previous SE-FSRS papers[72,98] of identical substrates is the correction of a chopper phase issue. Previous papers published SE-FSRS spectra as pump-off divided by pump-on while this chapter discusses spectra with the issue corrected, showing proper pump-on divided by pump-off spectra.

2.6.5. Variable plasmon resonance effects on SE-FSRS Raman gain

To examine the effects of plasmon resonance wavelength on SE-FSRS Raman gain of a BPE molecule we simulated Eq. 2.28a with plasmon resonance wavelengths varying between 800 nm and 1125 nm. Varying χ in Eq. 2.54, the plasmon resonance is tuned, and different particle polarizability functions are used in Eq. 2.28a.

By tuning the plasmon resonance with respect to the Raman pump and Stokes fields, the SE-FSRS lineshapes show high sensitivity to the plasmon resonance. In Figs. 2.9, 2.10, and 2.11 we see an abrupt transition from positive to negative gain signals with different mixtures of positive and negative character to the dispersive lineshapes. In addition, the SE-FSRS Raman gain can vary by up to orders of magnitude depending on the plasmon resonance wavelength.

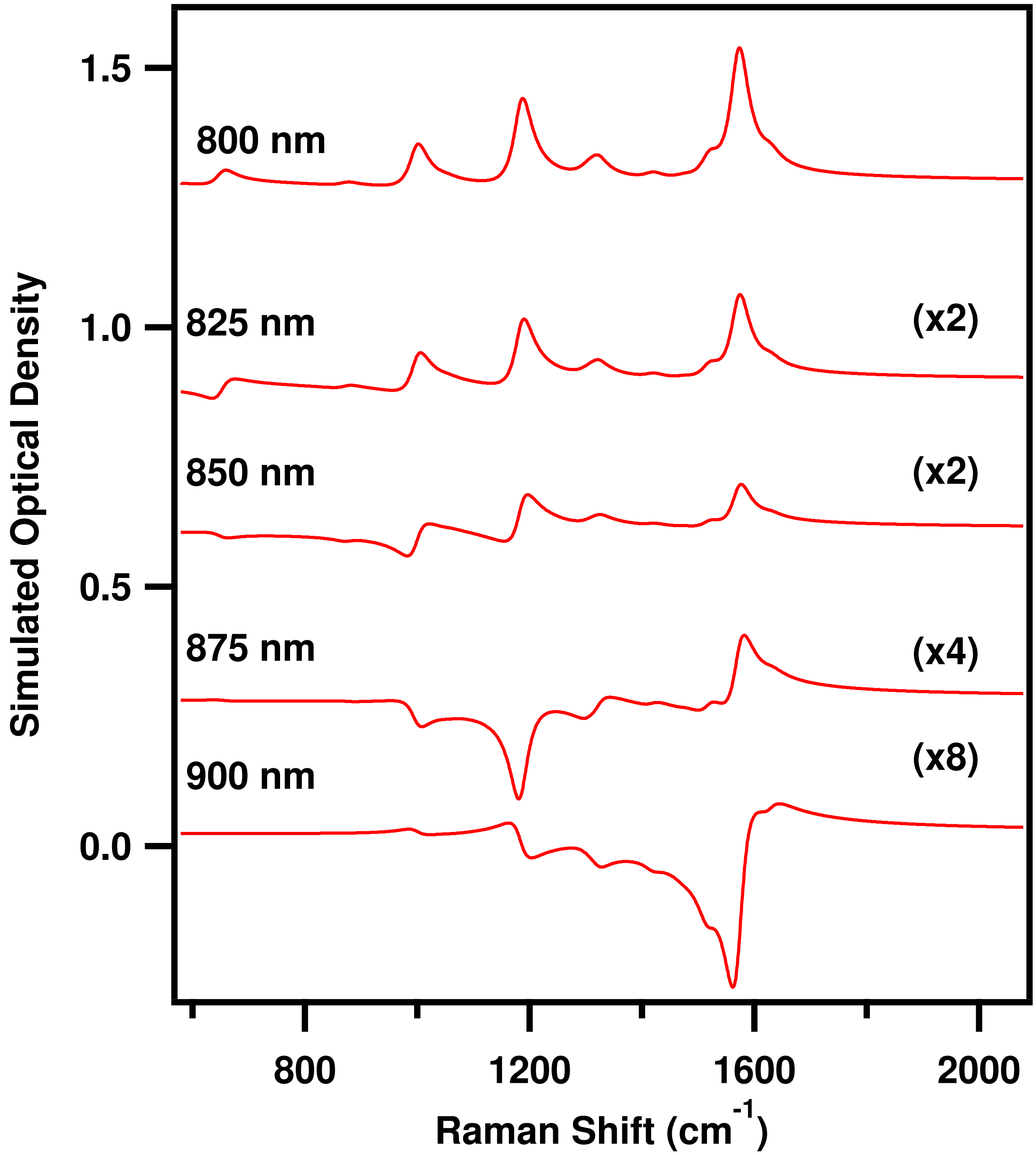

Figure 2.9. Dependence of plasmon resonance from 800 nm to 900 nm on SE-FSRS Raman gain. Spectra are vertically offset for clarity. Figure reproduced with permission from Ref. 110. Copyright 2016 American Institute of Physics.

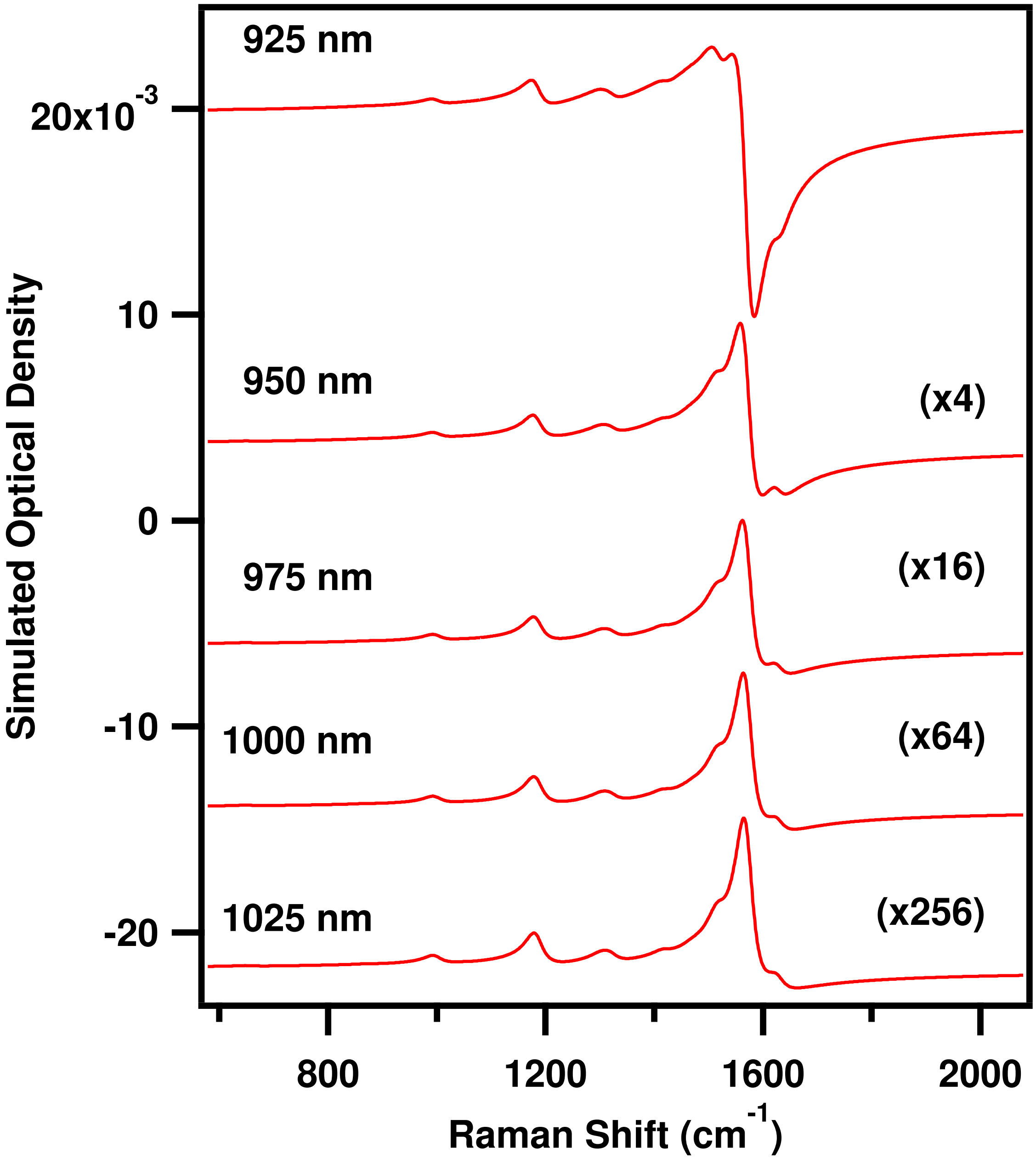

Figure 2.10. Dependence of plasmon resonance from 925 nm to 1025 nm on SE-FSRS Raman gain. Spectra are vertically offset for clarity. Figure reproduced with permission from Ref. 110. Copyright 2016 American Institute of Physics.

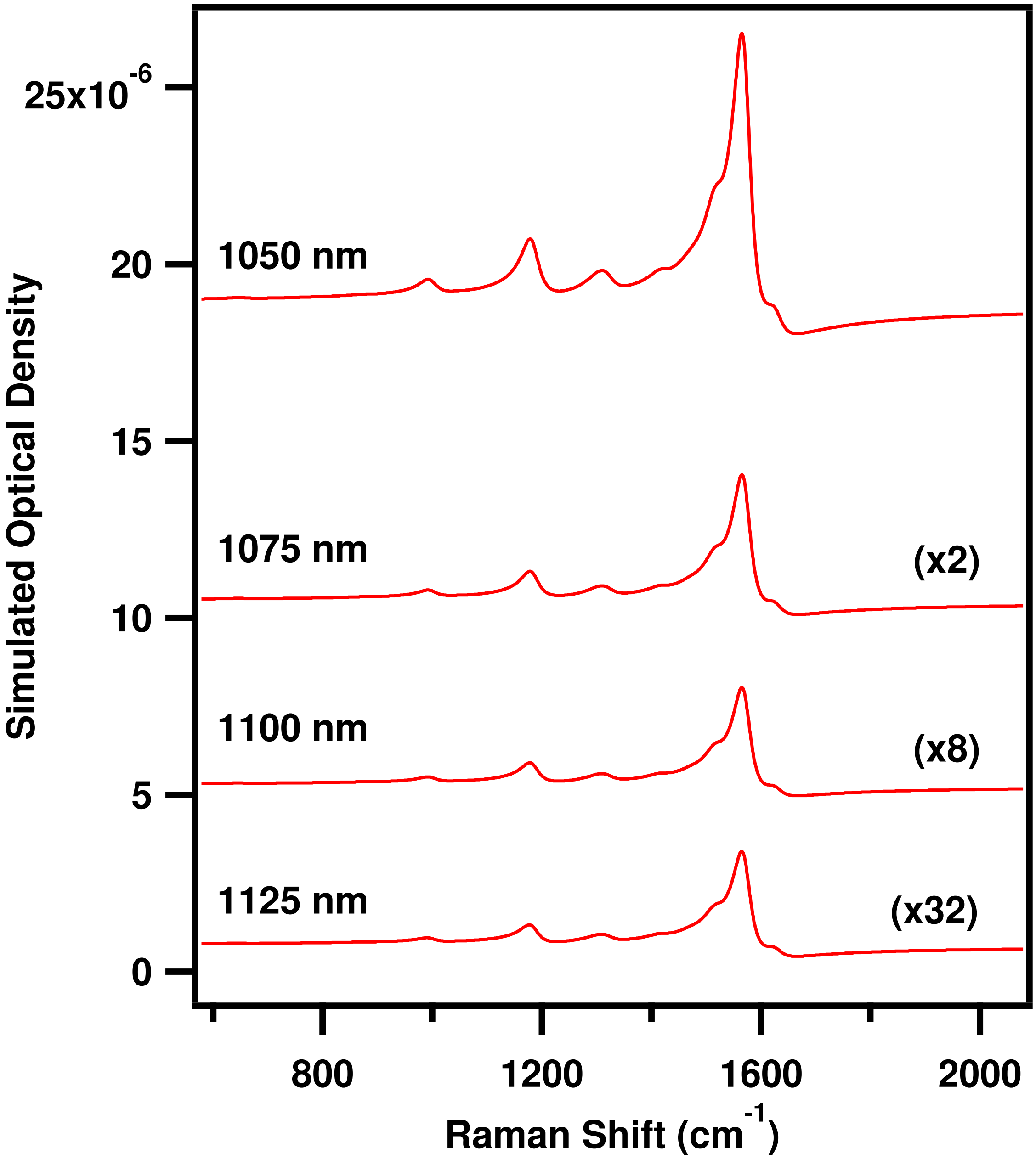

Figure 2.11. Dependence of plasmon resonance from 1050 nm to 1125 nm on SE-FSRS Raman gain. Spectra are vertically offset for clarity. Figure reproduced with permission from Ref. 110. Copyright 2016 American Institute of Physics.

CHAPTER 3

Towards a Quantum Mechanical Theory of SE-FSRS

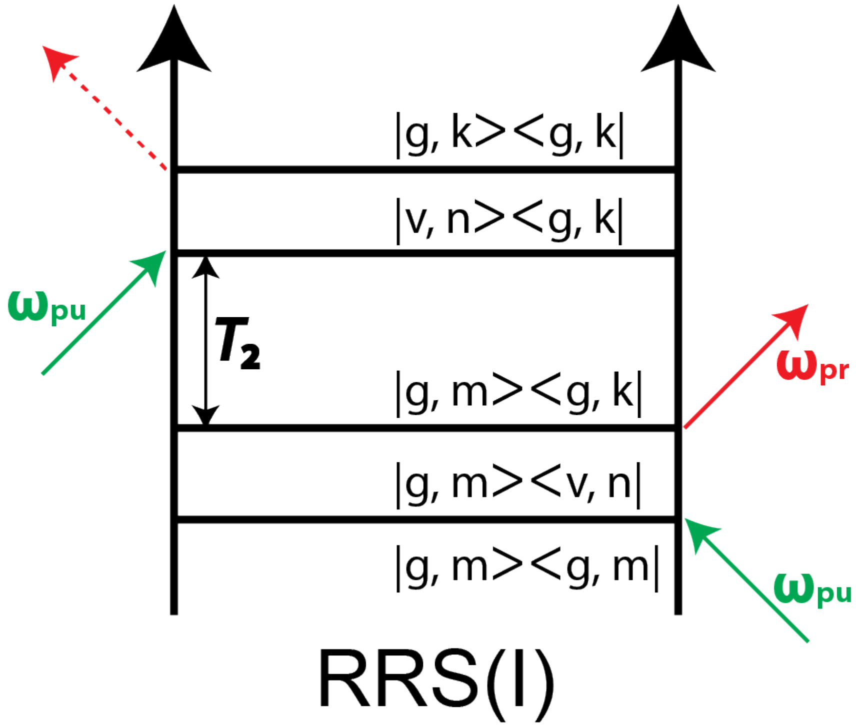

Feynman diagram showing the field-matter interactions involved in ground state FSRS.

3.1. Abstract

This chapter presents work towards a quantum mechanical theory of surface-enhanced femtosecond stimulated Raman scattering (SE-FSRS). In this work, we develop a density matrix formulation for describing the plasmonically-enhanced third order polarization that defines the SE-FSRS signal. Taking a density matrix approach allows for more field-matter interactions to be included in the total signal generation. This is in stark contrast to the previous chapter where only one vibrationally resonant set of field-matter interactions was included. The discussion in this chapter will discuss plasmonic enhancement to a variety of coherent Raman scattering techniques: surface-enhanced femtosecond stimulated Raman scattering (SE-FSRS), surface-enhanced coherent anti-Stokes Raman scattering (SECARS) and surface-enhanced resonant Raman scattering (SERRS). Finally, we conclude with a discussion on future experimental work that can help determine new directions for the currently incomplete theory.

3.2. Introduction

Initial work on surface-enhanced femtosecond stimulated Raman scattering (SE-FSRS) showed dispersive lineshapes are observed when the FSRS process occurs near plasmonic nanoparticles.[72,98] After the initial experimental reports of SE-FSRS, two theories were proposed to explain the Fano lineshapes observed: one semiclassical analytical coupled-wave equations approach,[110] the other a numerical time-domain density matrix theory approach.[111] This chapter attempts to build on the previous theoretical work by applying a density matrix treatment of plasmonic enhancement to surface-enhanced femtosecond stimulated Raman scattering SE-FSRS.

Considering a quantum mechanical treatment for SE-FSRS naturally brings up comparison to SERS. As both techniques probe the same Raman scattering cross-section, we can consider the SERS response similarly to SE-FSRS by substituting vacuum field fluctuations for the Stokes field. These considerations lead to confusion however when considering how to plasmonically-enhance the driven third-order polarization that leads to a signal field.

3.3. Survey of New Theoretical Methods for SE-FSRS

This chapter is organized into the following subsections:

- Applying the initial density matrix formulation of FSRS by S.-Y. Lee to SE-FSRS[126]
- Applying S.-Y. Lee theory[128,129] to SE-FSRS stimulated Raman loss (SRL)
- Applying S.-Y. Lee theory[128,129] to electronically-resonant SE-FSRS (SE-FSRRS)
- Consideration of π phase shifts in PECRS: differences between SE-FSRS and SECARS[89,126,137]
- Possible issues when considering SERS and SERRS
- Applying variation of Ziegler theory to SERRS[111,138]

A key concept in all of these theories is the use of a driven third order polarization ($P^{(3)}(z,t)$) that acts as a source emitter for a signal field.[26,139] In the case of SE-FSRS, this field is solved for by Maxwell's equation as we know the signal field is the same frequency as an input field (Stokes, anti-Stokes, or more generally probe fields).

3.3.1. Applying the initial density matrix formulation of FSRS by S.-Y. Lee *et al.* to SE-FSRS

This section is a step-by-step re-derivation of the density matrix formulation by S.-Y. Lee in Ref. 126 with special consideration given to plasmonic enhancement of the optical fields in identical manner to that performed in McAnally *et al.*.[110]

Starting from Eq. 40 of Ref. 126.

To solve for the SE-FSRS signal in a quantum mechanical theory, we replace the classical Placzek polarization with a third order driven polarization in Maxwell's equation:

$$\frac{\partial^2 E(z,t)}{\partial z^2} - \frac{1}{c^2}\frac{\partial^2 E(z,t)}{\partial t^2} = \frac{4\pi N}{c^2}\frac{\partial^2 \left\langle P^{(3)}(z,t)\right\rangle}{\partial t^2} \tag{3.1}$$

where we are still interested in plane wave solutions to the signal field, but now we use a driven third order polarization as the source emitter. Specifically the expectation value $\langle P^{(3)}(z,t)\rangle$.

We now make the assertion that the source emitter is plasmonically-enhanced:[110]

$$\frac{\partial^2 \left\langle P^{(3)}(z,t)\right\rangle}{\partial t^2} \rightarrow \frac{g_{St}\partial^2 \left\langle P^{(3)}(z,t)\right\rangle}{\partial t^2}. \tag{3.2}$$

This assumption is identical to that made in the semi-classical derivation in Ref. 110

Considering just a two-level electronic system with vibrational states $|g,m\rangle$ and $|g,k\rangle$ with eigenergies $\hbar\omega_m$ and $\hbar\omega_k$ in the lower electronic state $|g\rangle$ and vibrational states $\{|n\rangle\}$ of eigenergies $\{\hbar\omega_n\}$ in the upper electronic state, then the Raman transition is from $|g,m\rangle \rightarrow |g,k\rangle$ as shown in the RRS(I) pathway of Fig. 3.1.

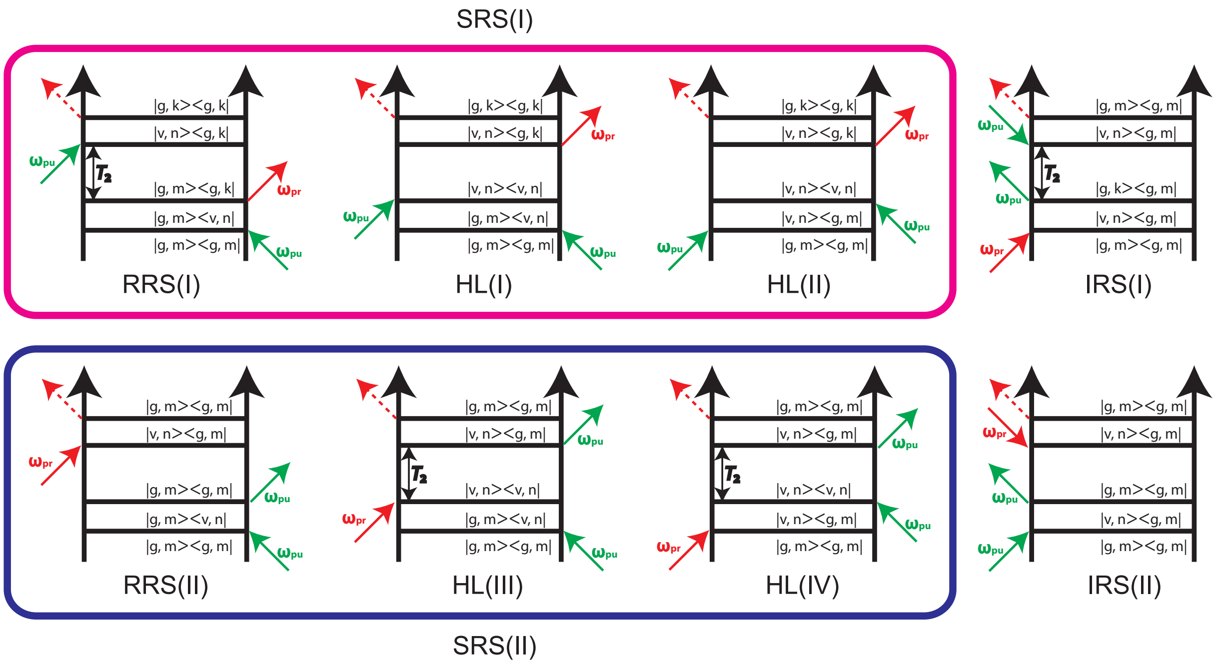

Figure 3.1. The eight resonant Feynman diagrams involved in the FSRS process. In non-electronically resonant FSRS the RRS(I) pathway defines stimulated Raman gain while the IRS(I) pathway defines stimulated Raman loss. Note that the plasmonic enhancement in the quasistatic limit is identical for all pathways.

To describe the system evolution during this Raman scattering process, we consider the time-evolution of the density matrix using the Liouville equation:[26,139]

$$\frac{\partial\hat{\rho}}{\partial t}+\frac{i}{\hbar}[\hat{H}_0,\hat{\rho}]+\hat{\Gamma}\hat{\rho}=\frac{-i}{\hbar}[\hat{H}',\hat{\rho}] \tag{3.3}$$

where $\hat{H}_0$ is the Hamiltonian for the isolated molecular system, $\hat{\Gamma}$ is a superoperator of phenomological damping constants acting on the density matrix, $\hat{H}'=-\vec{\mu}\cdot\vec{E}$ is the electric dipole Hamiltonian describing the dipole-field interaction, and $\vec{\mu}$ is the electric dipole moment. The field here will consist of the plasmonically-enhanced pump field, $g_{pu}E_{pu}(z,t)$, and the plasmonically-enhanced Stokes field, $g_{St}E_{St}(z,t)$.

The perturbative solution to the Liouville equation (Eq. 3.3) in powers of $\hat{H}'$ can be written as:

$$\hat{\rho} = \hat{\rho}^{(0)} + \hat{\rho}^{(1)} + \hat{\rho}^{(2)} + \hat{\rho}^{(3)} + ... + \hat{\rho}^{(n)} \tag{3.4}$$

where $\hat{\rho}^{(n)}$ has n terms in $\hat{H}'$.

We assume initially that only the lowest vibrational state of the ground electronic state is populated:

$$\rho_{ij}^{(0)} = \langle i|\hat{\rho}^{(0)}|j\rangle = \delta_{im}\delta_{jm} = \rho_{mm}^{(0)} = \rho_{eq}. \tag{3.5}$$

The third order polarization relevant to solving Maxwell's equation (Eq. 3.1) is given by:

$$P_{kk}^{(3)}(z,t) = \sum_{n} \mu_{kn}\rho_{nk}^{(3)}(z,t) \tag{3.6}$$

Thus, we need to solve for the third-order density matrix, $\rho_{nk}^{(3)}(z,t)$, by the Liouville equation (Eq. 3.3). Again, the Feynman diagram that describes the Raman scattering event from $|g,m\rangle \rightarrow |g,k\rangle$ and the time-evolution of the third order expression of $\rho_{nk}^{(3)}(z,t)$ is given by the RRS(I) pathway in Fig. 3.1.

Using this diagram we can write a Mukamelian expression for the third-order density matrix directly:

$$\rho^{(3)} = \left(\frac{-i}{\hbar}\right)^3 \int_{-\infty}^{t} dt_1 \int_{-\infty}^{t_1} dt_2 \int_{-\infty}^{t_2} dt_3 e^{-(i\omega_{nk}+\Gamma_{nk})(t-t_1)} H'_{nm}(g_{pu}E_{pu}, t_1) \\ \times \rho^{(0)}_{mm} \sum_{n'} H'_{mn'}(g^*_{pu}E^*_{pu}, t_3) e^{-(i\omega_{mn'}+\Gamma_{mn'})(t_2-t_3)} \\ \times H'_{n'k}(g_{St}E_{St}, t_2) e^{-(i\omega_{mk}+\Gamma_{mk})(t_1-t_2)} \tag{3.7}$$

Now this expression can be difficult to solve analytically. However, if we attempt the same assumptions as that done in Ref. 126, we can try to get to an analytic solution.

Since the Raman pump field (E_{pu}) is temporally long compared to any of the system dynamics and the Stokes field (E_{St}) we can assume a continuous wave exciation such that the pump interactions at t_3 and t_1:

$$H'_{mn'}(g^*_{pu}E^*_{pu}, t_3) = -\langle m|\mu|n'\rangle g^*_{pu}E^{0*}_{pu}e^{i\omega_{pu}(t_3-z/c)} = -\mu_{mn'}g^*_{pu}E^{0*}_{pu}e^{i\omega_{pu}(t_3-z/c)} \tag{3.8a}$$

and

$$H'_{nm}(g_{pu}E_{pu}, t_1) = -\mu_{nm}g_{pu}E^{0}_{pu}e^{-i\omega_{pu}(t_1-z/c)} \tag{3.8b}$$

A further simplification can be made if we assume that the Stokes field is an ultrafast Dirac pulse. Then the upper limit of the integral over t_2 goes to ∞. Then a step-by-step integration of the third-order density matrix, $\rho^{(3)}$, with $\rho^{(0)}_{mm} = 1$ yields:

$$\begin{aligned}\rho^{(3)}_{nk}(z,t) = \left(\frac{-i}{\hbar}\right)^3 g^*_{pu} E^{0*}_{pu} e^{-i\omega_{pu} z/c} \int_{-\infty}^{t} dt_1 \int_{-\infty}^{\infty} dt_2 e^{-(i\omega_{nk}+\Gamma_{nk})(t-t_1)} H'_{nm}(E_{pu}, t_1) \\ \times \sum_{n'} \frac{\mu_{mn'} e^{i\omega_{pu} t_2}}{i(\omega_{pu} - \omega_{n'm} - i\Gamma_{mn'})} H'_{n'k}(E_{St}, t_2) e^{-(i\omega_{mk}+\Gamma_{mk})(t_1-t_2)}\end{aligned} \tag{3.9a}$$

$$\begin{aligned}&\rho^{(3)}_{nk}(z,t) = \\ &\left(\frac{-i}{\hbar}\right)^3 |g_{pu}|^2 g_{St} |E^0_{pu}|^2 E^0_{St} e^{(i\omega_{pu} - i\omega_{km} + \Gamma_{mk}) z/c} e^{[-i(\omega_{pu}-\omega_{km}) - \Gamma_{mk}]t} \\ &\times \sqrt{2\pi}\tau_{St} e^{-(\omega_{pu}-\omega_{St}-\omega_{km}-i\Gamma_{mk})^2 \tau^2_{St}/2} \\ &\times \sum_{n'} \frac{\mu_{nm}\mu_{mn'}\mu_{n'k}}{(\omega_{pu}-\omega_{nm}-i\Gamma_{nk}-i\Gamma_{mk})(\omega_{pu}-\omega_{n'm}-i\Gamma_{mn'})}\end{aligned} \tag{3.9b}$$

Which gives the following plasmonically-enhanced third order polarization:

$$\begin{aligned}P^{(3)}_{kk}(z,t) = \left(\frac{i}{\hbar}\right) |g_{pu}|^2 g_{St} |E^0_{pu}|^2 E^0_{St} e^{(i\omega_{pu} - i\omega_0 + \gamma) z/c} e^{[-i(\omega_{pu}-\omega_0) - \gamma]t} \sqrt{2\pi}\tau_{St} \\ \times e^{-(\omega_{pu}-\omega_{St}-\omega_0-i\gamma)^2 \tau^2_{St}/2} \left| \sum_n \frac{\mu_{mn}\mu_{nk}}{\hbar(\omega_{pu}-\omega_{nm}-i\Gamma)} \right|^2\end{aligned} \tag{3.10}$$

The next steps taken by S.-Y. Lee is to make assumptions about the various Γ constants: ($\Gamma_{nk} = \Gamma_{mn'} \equiv \Gamma \gg \Gamma_{mk} \equiv \gamma$) and $\omega_{km} \equiv \omega_0$. However, the last assumption leads to a disagreement with the coupled-wave theory.

Specifically, the resonance becomes incorrect (Eq. 51 of Ref. 126):

$$P_{kk}^{(3)}(z,\omega) \propto \frac{|g_{pu}|^2 g_{St} f(\omega)}{\omega - \omega_{pu} - \omega_0 + i\gamma} \tag{3.11}$$

Compared to the coupled-wave equation resonance condition (Eq. 32 of Ref. 126):

$$P^{cw}(z,\omega) \sim |g_{pu}|^2 g_{St} \chi_R(\omega) \propto \frac{|g_{pu}|^2 g_{St}}{\omega - \omega_{pu} + \omega_0 + i\gamma} \tag{3.12}$$

But, if we were to make the opposite substitution ($\omega_{km} \equiv -\omega_0$) the fields in Eq. 3.10 would not oscillate at the correct resonant frequency for a Stokes shifted field. Thus, this is the end trying to match up analytic solutions between the coupled-wave and density matrix formulations for SE-FSRS.

For completeness we will write down the expressions for SE-FSRS SRG based on Sun *et al.* with PE.[128] Considering just the RRS(I) pathway of Fig. 3.1 we can write a similar expression to that of Eq. 3.12 in Ref. 127 where the time delay (t_D) between actinic, Raman pump, and Stokes field interactions is zero and the timing of actinic pulse interaction with the system (t_a) is zero. Then the driven third order polarization for stimulated Raman gain in SE-FSRS with plasmonic enhancement is given as:

$$\begin{aligned} P_{RRS(I)}^{(3)}(t) =& |g_{pu}|^2 g_{St} e^{i\mathbf{k}_{St}\cdot\mathbf{R}} \left(\frac{i}{\hbar}\right)^3 \int_0^t dt_1 \int_0^{t_1} dt_2 \int_0^{t_2} dt_3 E_{pu}(t_1) E_{St}(t_2) E_{pu}^*(t_3) \\ &\times \langle\psi_1(0)|\, e^{(ih_1-\gamma_1/2)t_3/\hbar} \mu_{21}^* e^{(ih_2-\gamma_2/2)(t_2-t_3)/\hbar} \mu_{21} e^{(ih_1-\gamma_1/2)(t-t_2)/\hbar} \\ &\times \mu_{21}^* e^{(-ih_2-\gamma_2/2)(t-t_1)/\hbar} \mu_{21} e^{(-ih_1-\gamma_1/2)t_1/\hbar}\, |\psi_1(0)\rangle + c.c. \end{aligned} \tag{3.13}$$

In this expression we have the normal LFE factors (g_{pu}, g_{St}), the phase-matched direction for observation of the signal field from this oscillating polarization ($e^{i\mathbf{k}_{St}\cdot\mathbf{R}}$), interactions of each field with either the bra or ket of the ground state vibrational wavepacket ($\langle\psi_1(0)|\psi_1(0)\rangle$) through action of the electric dipole operator (μ_{ij}) in a Hamiltonian of one dimension harmonic potentials (h_i) with relaxation given by γ_i.

Then to get a final SE-FSRS SRG spectrum in the frequency domain we take the Fourier transform of the above:

$$P^{(3)}_{RRS(I)}(\omega) = (2\pi)^{-1}\int_{-\infty}^{\infty} e^{i\omega t} P^{(3)}_{RRS(I)}(t)dt \tag{3.14}$$

then evaluate the Raman gain cross-section ($\sigma_{SRG}(\omega)$):

$$\sigma_{SRG}(\omega) = -\frac{4\pi}{3\epsilon_0 cn}\omega \times \mathfrak{Im}\left\{g_{St}P^{(3)}_{RRS(I)}(\omega)/E_{St}(\omega)\right\} \tag{3.15}$$

where ϵ_0 is the vacuum permittivity, c is the speed of light, and n is the refractive index.

From this we see that the PE of SE-FSRS in SRG scales as $|g_{pu}|^2 g_{St}^2$, where we made the choice of plasmonically-enhancing the oscillating polarization by a factor of g_{St}, and not g_{St}^*.

3.3.2. Applying theory of Zhao *et al.* to SE-FSRS stimulated Raman loss (SRL)

Now if we consider the other Feynman diagrams in Fig. 3.1, we can see that IRS(I) will lead to sharp vibrational loss features in the anti-Stokes frequency domain. We again can write down a Mukamelian description of this process with plasmonic-enhancement. Using the same formalism as Eq. 3.13 above:

$$\begin{aligned} P^{(3)}_{IRS(I)}(t) =& |g_{pu}|^2 g_{aSt} e^{i\mathbf{k}_{aSt}\cdot\mathbf{R}} \left(\frac{i}{\hbar}\right)^3 \int_0^t dt_1 \int_0^{t_1} dt_2 \int_0^{t_2} dt_3 E_{pu}(t_1) E^*_{pu}(t_2) E_{aSt}(t_3) \\ & \times \langle\psi_1(0)| \, e^{(ih_1-\gamma_1/2)t/\hbar} \mu^*_{21} e^{(-ih_2-\gamma_2/2)(t-t_1)/\hbar} \mu_{21} e^{(-ih_1-\gamma_1/2)(t_1-t_2)/\hbar} \\ & \times \mu^*_{21} e^{(-ih_2-\gamma_2/2)(t_2-t_3)/\hbar} \mu_{21} e^{(-ih_1-\gamma_1/2)t_3/\hbar} \, |\psi_1(0)\rangle + c.c. \end{aligned} \tag{3.16}$$

Then to get a final SE-FSRS SRL spectrum in the frequency domain we take the Fourier transform of the above:

$$P^{(3)}_{IRS(I)}(\omega) = (2\pi)^{-1} \int_{-\infty}^{\infty} e^{i\omega t} P^{(3)}_{IRS(I)}(t) dt \tag{3.17}$$

then evaluate the Raman loss cross-section ($\sigma_{SRL}(\omega)$):

$$\sigma_{SRL}(\omega) = -\frac{4\pi}{3\epsilon_0 c n}\omega \times \mathfrak{Im}\left\{ g_{aSt} P^{(3)}_{IRS(I)}(\omega)/E_{St}(\omega) \right\} \tag{3.18}$$

Again, we see that the PE of SE-FSRS in SRL scales as $|g_{pu}|^2 g^2_{aSt}$, where we made the choice of plasmonically-enhancing the oscillating polarization by a factor of g_{aSt}, and not g^*_{aSt}.

3.3.3. Applying theory of Zhao *et al.* to SE-FSRRS

Now if the Raman pump or probe fields are resonant with a molecular electronic transition, we need to consider all eight diagrams from Fig. 3.1. Then the total observed SE-FSRRS signal is given by expressions derived in Zhao *et al.*[129] and references therein. At this point, Zhao *et al.* have started to condense the expressions by discussing nth-order wave packets that keep track of intermediate electric dipole interactions so that just the final dipole interaction can be written down in the third order polarization. In the condensed version the plasmonically-enhanced FSRRS signal including SRL, SRG, and HL contributions can be written in a succinct form:

$$\begin{aligned} P^{(3)}_{diff}(t) &= P^{(3)}_{\text{pump on}}(\mathbf{k}_{pr};t) - P^{(3)}_{\text{pump off}}(\mathbf{k}_{pr};t) \\ &= g_{pr}P^{(3)}_{SRS(I)}(t) + g_{pr}P^{(3)}_{SRS(II)}(t) + g_{pr}P^{(3)}_{IRS(I)}(t) + g_{pr}P^{(3)}_{IRS(II)}(t) \end{aligned} \tag{3.19}$$

where we are now displaying probe field enhancement (g_{pr}) instead of specific Stokes (g_{St}) or anti-Stokes (g_{aSt}) enhancement, and the CTPL convention of Mukamel *et al.* to collapse all of the SRS(I) and SRS(II) pathways in Fig. 3.1 into one formula each by neglecting dephasing between the ket and bra states.

The individual third order polarizations, assuming the system starts in the ground electronic state, are then given as:

$$P^{(3)}_{SRS(I)}(t) = \langle\psi^{(2)}_0(\mathbf{Q},-\mathbf{k}_{pr},\mathbf{k}_{pu};t)|\mu^*_{21}|\psi^{(1)}_1(\mathbf{Q},\mathbf{k}_{pu};t)\rangle \tag{3.20a}$$

$$P^{(3)}_{SRS(II)}(t) = \langle\psi^{(2)}_0(\mathbf{Q},-\mathbf{k}_{pu},\mathbf{k}_{pu};t)|\mu^*_{21}|\psi^{(1)}_1(\mathbf{Q},\mathbf{k}_{pr};t)\rangle \tag{3.20b}$$

$$P^{(3)}_{IRS(I)}(t) = \langle\psi^{(0)}_0(\mathbf{Q};t)|\mu^*_{21}|\psi^{(3)}_1(\mathbf{Q},\mathbf{k}_{pu},-\mathbf{k}_{pu},\mathbf{k}_{pr};t)\rangle \tag{3.20c}$$

$$P^{(3)}_{IRS(II)}(t) = \langle\psi^{(0)}_0(\mathbf{Q};t)|\mu^*_{21}|\psi^{(3)}_1(\mathbf{Q},\mathbf{k}_{pr},-\mathbf{k}_{pu},\mathbf{k}_{pu};t)\rangle \tag{3.20d}$$

In this formulation, $|\psi^{(i)}_j(\mathbf{Q},\mathbf{k}_l;t)\rangle$ is an ith order vibrational wave packet on the jth electronic surface describing the $\mathbf{Q}$th mode that has picked up momentum of $\mathbf{k}_l$. The order of the wave packet keeps track of how many electric dipole interactions have acted on the wave packet before the final trace operation.

Then to obtain the final SE-FSRRS signal we would again Fourier transform into the frequency domain, then take the imaginary portion of this polarization with plasmonic enhancement:

$$P^{(3)}_{diff}(\omega) = (2\pi)^{-1} \int_{-\infty}^{\infty} e^{i\omega t} P^{(3)}_{diff}(t) dt \tag{3.21}$$

and then the total stimulated Raman scattering activity would be given by the cross-section ($\sigma_{SRA}(\omega)$):

$$\sigma_{SRA}(\omega) = -\frac{4\pi}{3\epsilon_0 cn}\omega \times \mathfrak{Im}\left\{g_{pr} P^{(3)}_{diff}(\omega)/E_{pr}(\omega)\right\} \tag{3.22}$$

Similar to what we've seen above, the PE of SE-FSRRS scales as $|g_{pu}|^2 g_{pr}^2$, where we made the choice of plasmonically-enhancing the oscillating polarization by a factor of g_{pr}, and not g_{pr}^*.

3.3.4. Consideration of phase shifts in PECRS: differences between SE-FSRS and SECARS

There have already been a few papers describing SECARS from a theoretical perspective,[89] and Chapman *et al.* has already done a nice job of describing tr-SECARS,[137] but we've come into some similar questions. First, we know that FSRS signal has a π phase shift of the signal field relative to the oscillating polarization as evident from

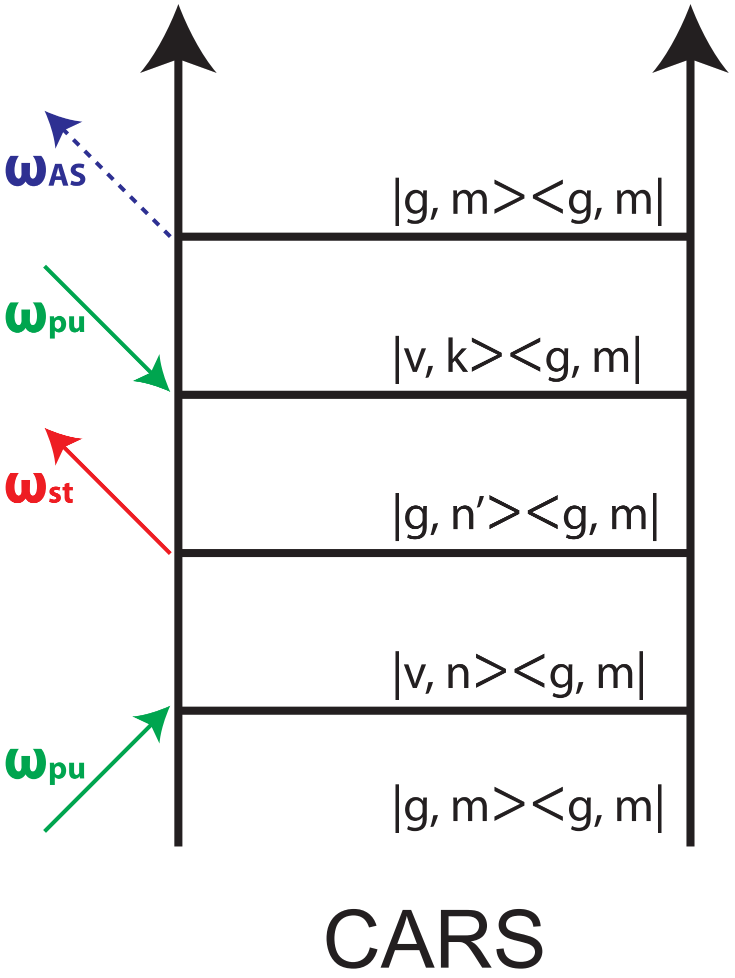

Figure 3.2. Resonant Feynman diagram for CARS.

the final FSRS intensity being proportional to the imaginary portion of the third order polarization.

However, CARS signal does not have the π phase shift, instead it is proportional to the sum of the absolute square of the nonresonant background ($|\chi^{(3)}_{NR}|^2$), the vibrationally resonant signal ($|\chi^{(3)}_{R}(\omega)|^2$), and a cross-term $\left(2\chi^{(3)}_{NR}\mathfrak{Re}\left\{\chi^{(3)}_{R}(\omega)\right\}\right)$. So this begs the question, how can the PE be treated in a consistent manner, particularly the last dipole interaction taken before the trace operation of the density matrix?

3.3.5. Possible issues when considering SERS and SERRS

When considering SERS or SERRS, we can use the RRS(I) or IRS(I) pathways for non-resonant interactions provided we adjust the equilibrium density matrix by a Boltzmann distribution in IRS(I). If we remove the explicit Stokes field interactions and swap for vacuum field interactions that have zero momementum (but LFE at the Stokes frequency) we can have a third order polarization expression for SERS. However, this again brings up how to plasmonically-enhance the final dipole operator interaction. Knowing that the overall SERS enhancement should be $|g_{pu}(\omega)|^2|g_{St}(\omega)|^2$, we could assign the final plasmonic enhancement for the dipole operation as a g^*_{St} interaction for the total emitted signal field. However, this would be inconsistent with how plasmonic enhancment was treated previously in the coupled-wave theory of SE-FSRS.[110]

3.3.6. Applying variation of theory from Mandal *et al.* to SERRS

Now examine SERRS using the Feynman diagrams. The HL pathways would lead to fluorescence that can also be surface-enhanced (SEF). This would lead to the three total signal fields being emitted.

(1) LFE enhanced SERS
(2) LFE enhanced SEF
(3) Possible heterodyning of 1 with 2 to give an additional signal in the far-field

Suppose that we consider a method similar to Mandal *et al.*.[111] Then we would have SERRS, SEF, and a cross-term of the heterodyned contributions. This would be a possible explanation for unpublished data from Zrimsek *et al.*.[138] If we swap the SEF for a plasmon emission field we could possibly explain the recent data from Brandt *et al.* which cited combination of SERS with metal luminescence to the observed spectral lineshapes.[140]

3.4. Conclusion

The theory of SE-FSRS has been previously explored by McAnally *et al.* and Mandal *et al.* with some success in describing the Fano lineshapes that arise experimentally.[110,111] The discussion in this chapter has explored new theoretical directions worth pursuing to explain ‘more of the story’. In addition to the Fano lineshapes, there is the broad background signals that are observed in the ensemble SE-FSRS experiments. While single-aggregate SE-FSRS (SA-SE-FSRS) is an on-going experimental project, there are still aspects to the ensemble measurement to understand.

As SA-SE-FSRS is experimentally realized, some questions will be answered, but new ones will arise. In particular, there are outstanding questions dealing with the heterodyne nature of the SE-FSRS signal that isn’t present in SECARS. Reducing the dimensionality of the experiment by probing individual aggregates will help, but conceptually an understanding of how a self-heterodyned signal field is plasmonically-enhanced is crucial to a deeper knowledge of SE-FSRS. In the same vein, understanding the plasmonic-enhancement of a self-heterodyned signal may lead to clues as to why single-aggregate SECARS experiments have not shown dispersive lineshapes[75,76,101] in comparison to bulk SECARS and solvent experiments.[89,92]

CHAPTER 4

Optically heterodyned femtosecond Raman-induced Kerr-effect scattering

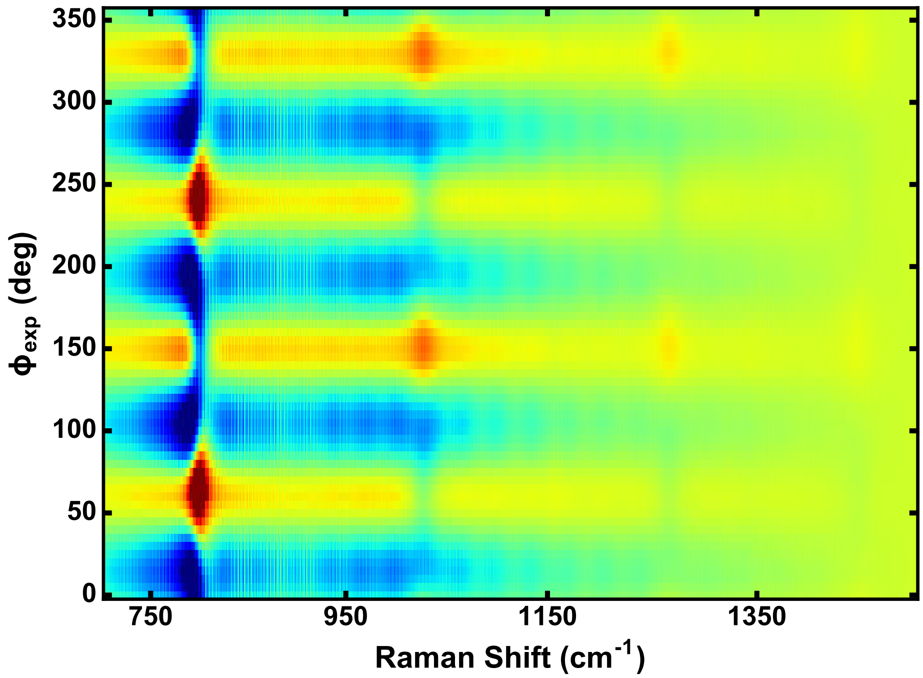

This chapter (excluding Section 4.6) has been reproduced with permission from Ref. 62. Copyright 2016 Optical Society of America.

4.1. Abstract

Optically heterodyne detected femtosecond Raman-induced Kerr-effect spectroscopy (OHD-FRIKES) was observed in neat cyclohexane. In the present study, an examination of the effect of the Raman pump ellipticity on the multiplex OHD-FRIKES spectra is discussed. The Raman pump ellipticity scanned OHD-FRIKES results reproduce anomalous observables from previous OHD-FRIKES experiments, and suggest new methods of tracking transient vibrational mode polarization in complex systems.

4.2. Introduction

Coherent Raman scattering (CRS) is a well established field of vibrational spectroscopy. In particular, femtosecond stimulated Raman scattering (FSRS) has been established as a versatile form of CRS that can deliver simultaneous high temporal and spectral resolutions on the order of tens of femtosecond and wavenumbers. However, transient FSRS signals can have low signal-to-noise ratio (SNR), making positive identification of dynamic vibrational features difficult. Hence developing methods of improving experimental techniques in FSRS by increasing the interaction length of the mixing process and improving the sensitivity by lowering the noise floor are important.

Similar to rotating polarization coherent anti-Stokes Raman scattering (RP-CARS),[81,141–143] polarization dependent excitation and detection schemes have been applied to FSRS. Using an optical Kerr effect, where the plane of polarization in light is rotated by a transient birefringence in a sample induced by an intense pump beam, the Raman-induced Kerr effect scattering (RIKES) has been thoroughly studied in single mode stimulated Raman scattering (SRS).[29,48–53] RIKES occurs where the rotation of light occurs at a stimulated Raman resonance, allowing for a polarization sensitive excitation and detection scheme to be applied to FSRS.

Based on the success of femtosecond stimulated Raman scattering (FSRS), the Mathies group developed a multiplex RIKES experiment: femtosecond Raman-induced Kerr effect scattering (FRIKES). In the work of Shim *et al.*,[54] the FRIKES experiment was performed using a circularly polarized Raman pump and a linearly polarized Stokes field. The FRIKES signal was observed by recording the scattering that transmitted through a linear polarizer set perpendicular to the polarization of the Stokes field. This experiment still observed residual Stokes field which necessitated background removal. In subsequent FRIKES experiments,[55,56] the background removal of the transmitted Stokes field has been performed by keeping a chopper in the Raman pump path, making FRIKES data acquisition analagous to FSRS.

FRIKES has been used to suppress background signals of non-interacting Stokes fields and other polarization sensitive background signals.[55–61] However, outside of the work of Balakrishnan *et al.*[56] and a collection of Fourier-transform time domain experiments,[63–66] FRIKES research has focused on single mode detection when performed in the frequency domain. In addition, the work of Balakrishnan *et al.* observed unexplained dispersive and negative lineshapes in an optically-heterodyne detected FRIKES (OHD-FRIKES) experiment. As most frequency domain FRIKES experiments are currently being treated as OHD-FRIKES experiments,[55,56] further investigation into the anomalous lineshapes is of strong interest if the polarization sensitive technique is to be applied in future frequency domain studies.

By performing an OHD-FRIKES experiment and treating the data acquisition identically to FSRS experiments, we determine the functional dependence of OHD-FRIKES lineshapes on Raman pump ellipticity. In a FSRS experiment data is typically collected in a gain measurement:

$$I_{\text{FSRS}} = \frac{I_{\text{Stokes, pump on}} - I_{\text{background}}}{I_{\text{Stokes, pump off}} - I_{\text{background}}} \tag{4.1}$$

where the Stokes field covers the frequency domain of interest relative to the Raman pump, and the background intensity is a measure of any homodyne signal component (normal Raman scattering, fluorescence, etc.). Thus, FSRS spectral lineshapes are very similar to those seen in spontaneous Raman scattering (see Fig. 4.1), provided the experiments are performed far from molecular resonance.[144]

The observed OHD-FRIKES intensity as a function of Raman pump ellipticity (ϕ) can be expressed as:[145,146]

$$\frac{I_{\perp}(\omega_{St})}{I(\omega_{St})I^2(\omega_{pu})} = 9(\chi^{NR})^2 \times \left[\frac{(-\omega_R - (\omega_{St} - \omega_{pu}) + \Delta(1-\rho))^2 cos^4(2\phi)}{(-\omega_R - (\omega_{St} - \omega_{pu}))^2 + \Gamma^2} + \frac{(\Gamma cos^2(2\phi) + \Delta(1-3\rho) sin(2\phi))^2}{(-\omega_R - (\omega_{St} - \omega_{pu}))^2 + \Gamma^2}\right]. \tag{4.2}$$

In Eq. 4.2, the overall background amplitude is given by the nonresonant frequency independent Kerr effect contribution, χ^{NR}, which is modulated in amplitude by the *cos* and *sin* functions of ϕ. In addition, ω_R and Γ are the Raman frequency and linewidth, Δ is the resonance parameter, and ρ is the depolarization ratio:[145,146]

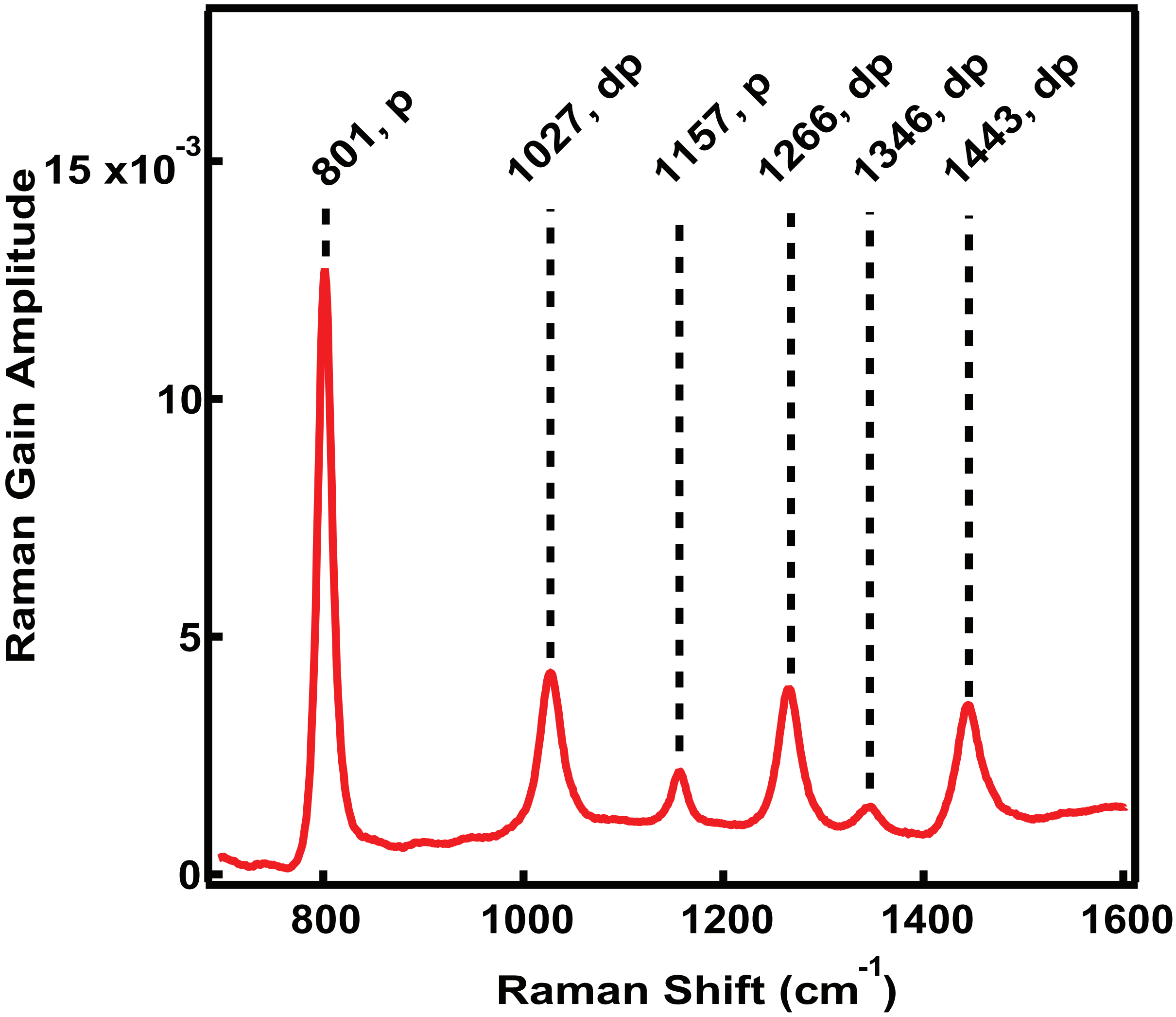

Figure 4.1. FSRS spectrum of cyclohexane with frequency and vibrational mode polarization (dp = depolarized, p = polarized) labels. Figure reproduced with permission from Ref. 62. Copyright 2016 Optical Society of America.

$$\Delta = N(\alpha_{11}^{R})^2/48hc\chi^{NR} \tag{4.3}$$

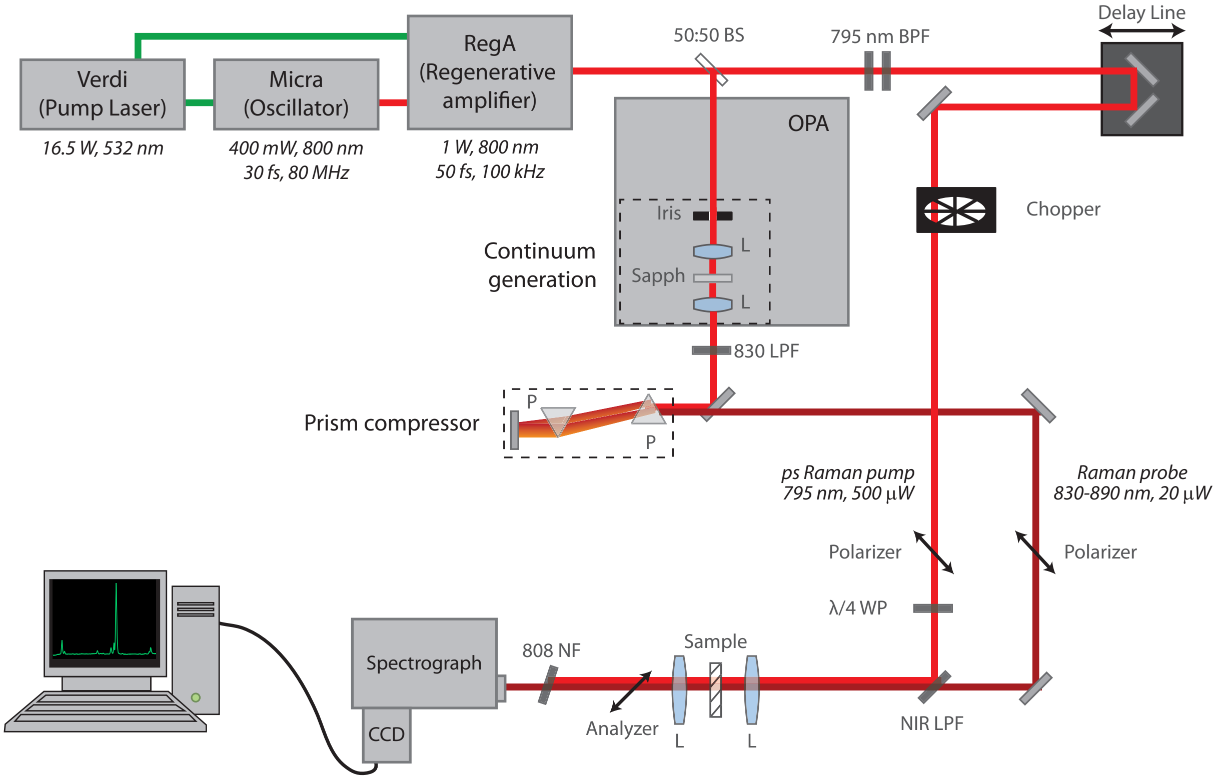

Figure 4.2. Experimental setup for FSRS and OHD-FRIKES. Figure reproduced with permission from Ref. 62. Copyright 2016 Optical Society of America.

where α_{11}^R is the diagonal Raman tensor element, N is the number of oscillators, and hc is the product of Planck's constant with the speed of light.

Thus to understand the dependence of the lineshape on Raman pump ellipticity, one needs to map out the OHD-FRIKES intensity dependence on ϕ. These are the exact experiments we have performed herein, and compared to simulated spectra from Eq. 4.2 where all parameters are derived from previous experimental data.[142,143]

4.3. Experimental Details

To perform the FSRS and OHD-FRIKES experiments we used a spectrometer as shown in Fig. 4.2.

Briefly, the 1 W, 800 nm output of a 100 kHz regenerative amplifier (Coherent RegA) is split into two paths for the FSRS experiment. Approximately 500 mW of the amplified output is used to generate a picosecond bandwidth Raman pump field by passing through two identical angle tuned bandpass filters (CVI optics) at 795 nm. A portion of the remainder of the amplified output is used for white light continuum generation in a sapphire plate which is then temporally compressed by a prism pair. The compressed continuum is then filtered using a set of short- and long-pass filters to create a Stokes field in the spectral region of interest. Pulses are then overlapped spatiotemporally in a collinear geometry in a 2 mm cell. The pump pulse is mechanically chopped so that sequential pump-on and pump-off spectra are obtained in a home-built LabView program. OHD-FRIKES signal is detected using a spectrograph (Princeton Instruments SP2538) and CCD (PIXIS:100F). Average powers were 500 μW and 20 μW for the Raman pump and Stokes fields respectively. Each experimental OHD-FRIKES spectrum shown has a total acquisition time of 100 seconds.

To control the polarization of both the Raman pump and Stokes fields, thin film linear polarizers and waveplates were used before recombining and focusing into the sample. In the Raman pump field, the linear polarizer removes any residual non-desirable polarization components before passing through a quarter waveplate to create an elliptical field. To find the setting of most circular polarized light, a linear polarizer was placed in the sample position then the quarter waveplate was optimized to have minimized power fluctuations across 2π rotation of the analyzer at the sample. The Stokes field also passes through a thin film linear polarizer before the sample, then a high quality double Glan-Taylor calcite polarizer set to a perpendicular polarization of the Stokes field for extinction of >1000:1. The residual Stokes field intensity after the analyzer serves as the local oscillator for the optical heterodyning measured. As there is a portion of space between the two calcite blocks, effectively creating an air-space etalon, having higher extinction after the sample comes at the expense of interference fringes as observed in Fig. 4.6.

Using this spectrometer, the pump ellipticity was mapped by rotating a quarter waveplate in 5 degree increments over a full 2π radians. All experimental and simulated data in Figs. 4.3-4.5 have had the modulating background given by the electronic Kerr-effect contribution flattened to better represent the changes in lineshape. The complete OHD-FRIKES data set is displayed in Fig. 4.3.

4.4. Results and Discussion

From Fig. 4.3, it is apparent that the relative intensities of the vibrational modes track with the degree of depolarization (ρ) to the vibrational mode. Specifically, highly polarized vibrational modes (801 and 1157 cm^{-1}) track while depolarized vibrational modes (1026, 1266, 1444 cm^{-1}) track together.

Focusing on just the 801 cm^{-1} mode, one can clearly see the π periodicity in Fig. 4.3.

To compare to Fig. 4.4, we simulate Eq. 4.2 with experimentally determined values[142] for χ^{NR}, ρ, α_{11}^{R} and Γ across ϕ ranging from $0-2\pi$. For all simulations performed in this paper $\omega_{pu} = 12578.61$ cm^{-1}, $\omega_{St} = \omega_{pu} - \omega_R$, and $\chi^{NR} = 4.8 \times 10^{-14}$ esu. All vibrational mode dependent properties including Raman linewidth (Γ), depolarization ratio (ρ), and

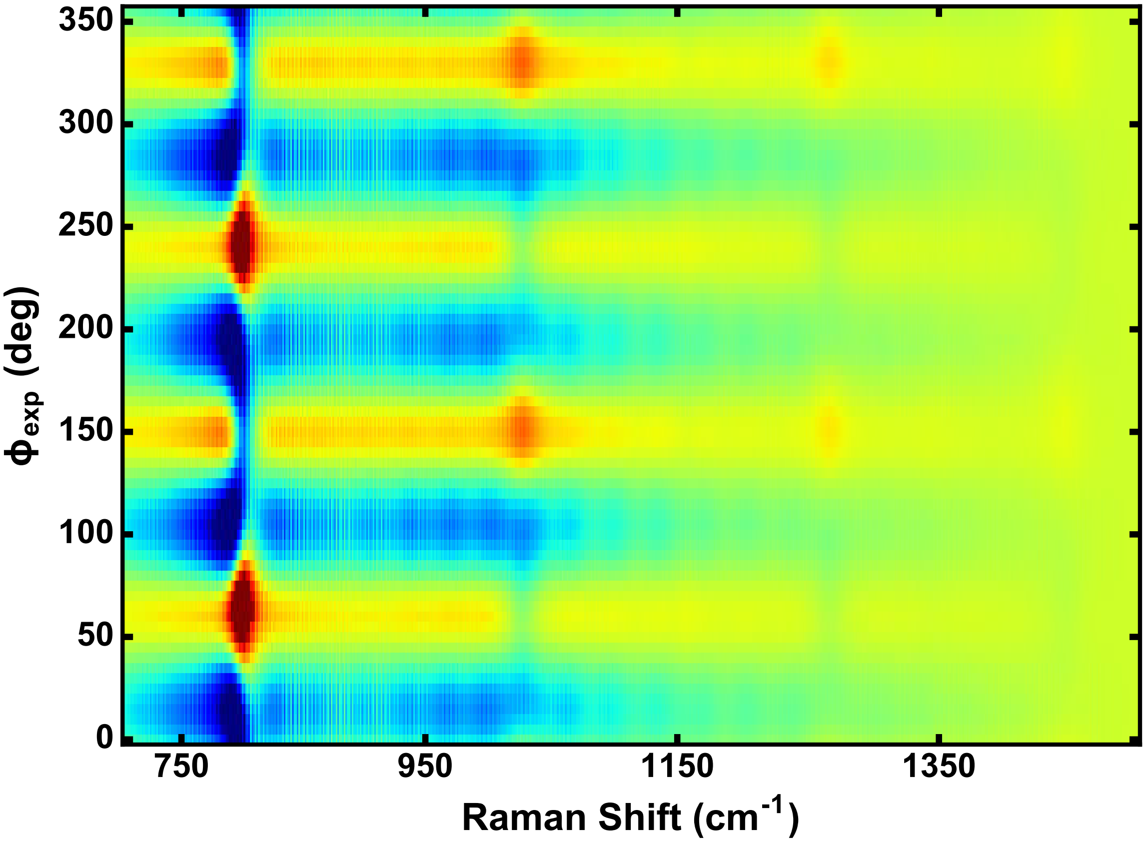

Figure 4.3. Multiplex experimental data mapping the OHD-FRIKES intensity of cyclohexane as a function of Raman pump ellipticity. All data is positive valued. Red indicates positive deviation from baseline, blue indicates negative deviation from baseline. Figure reproduced with permission from Ref. 62. Copyright 2016 Optical Society of America.

Raman tensor element (α_{11}^R) were used from the literature.[142] Fig. 4.5 shows the resulting simulation, displaying identical periodicity and dispersive character.

The anomalous behavior observed at ϕ = 135, 315 is seen as a discontinuous value of the lineshape at perfectly circularly polarized light. As waveplates display strong wavelength dependent phase retardance, perfect circular polarization for broadband pulses is typically unobtainable.

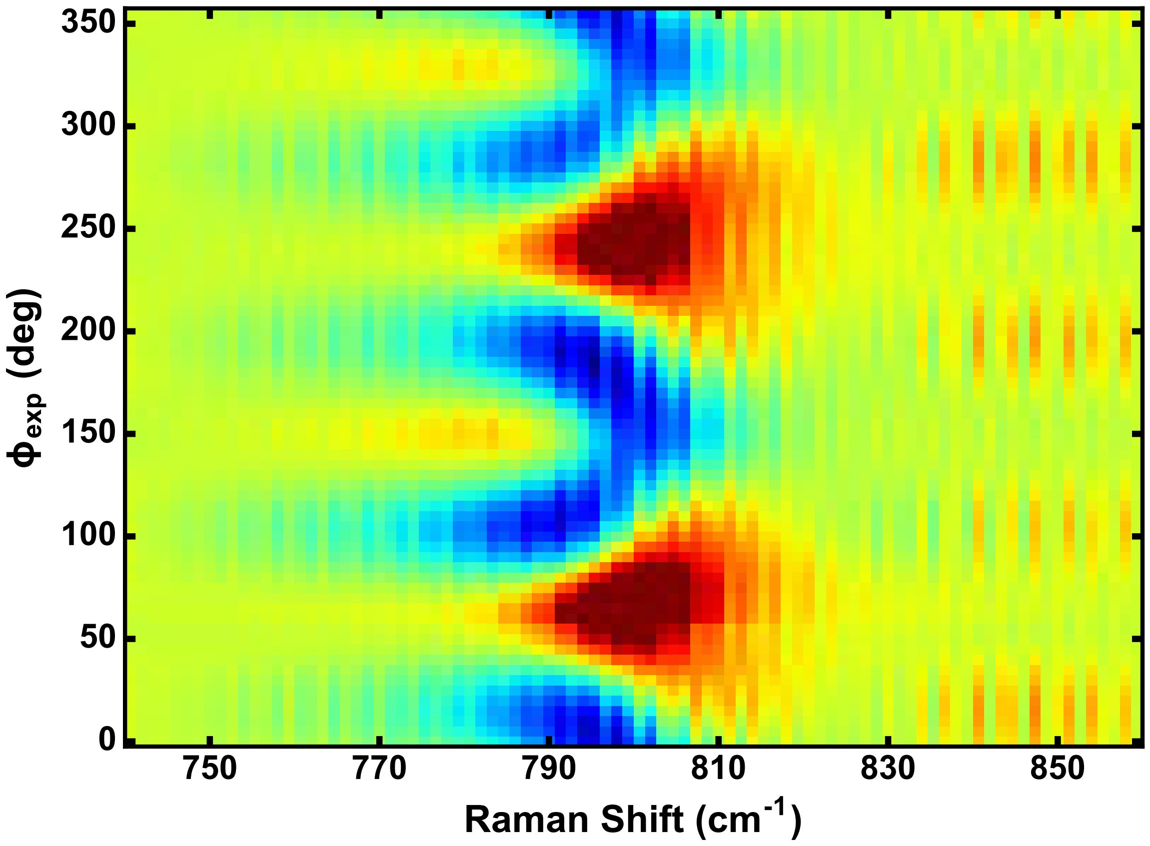

Figure 4.4. Experimental data mapping the OHD-FRIKES intensity of the 801 cm^{-1} mode of cyclohexane as a function of Raman pump ellipticity. All data is positive valued. Red indicates positive deviation from baseline, blue indicates negative deviation from baseline. Fringes in the data along the Raman shift axis correspond to grating resolution. No smoothing was performed in this axis. Figure reproduced with permission from Ref. 62. Copyright 2016 Optical Society of America.

To examine the behavior of the individual vibrational modes we plot slices of the 2D mapping experiment and theoretical calculations in Figs. 4.6 and 4.7, respectively.

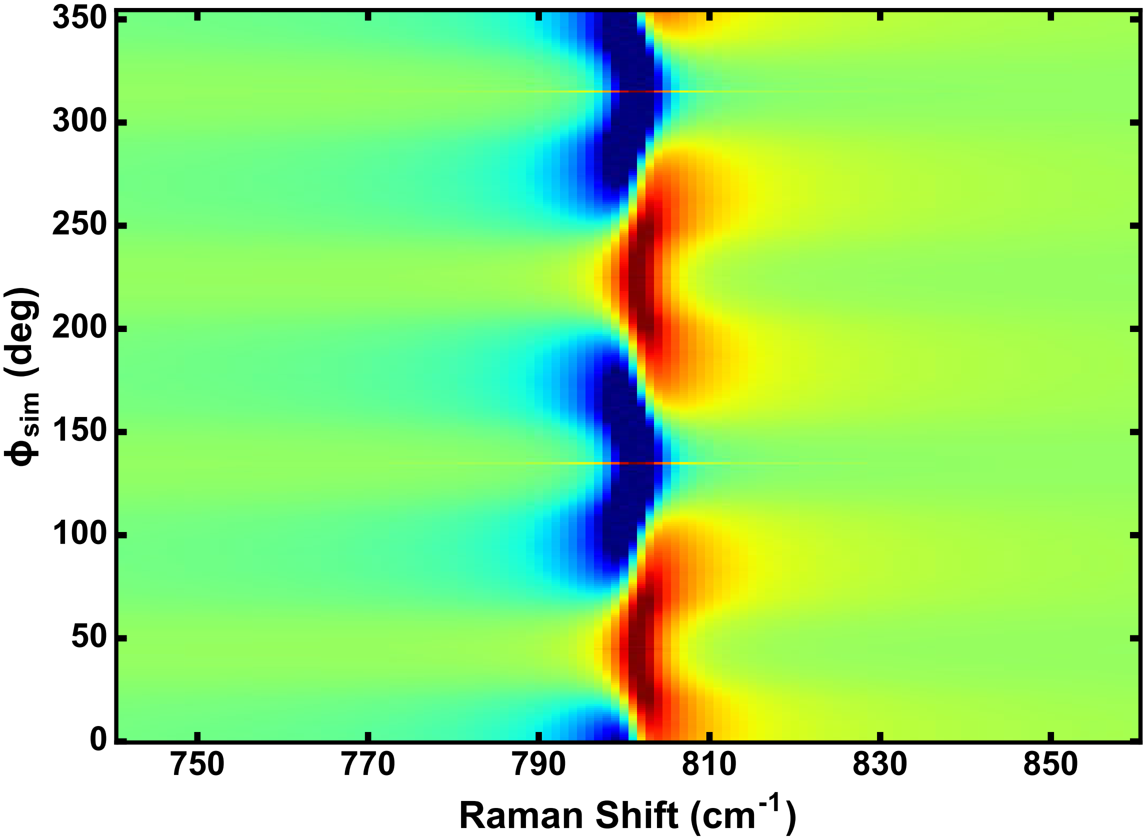

Figure 4.5. Simulated data mapping the OHD-FRIKES intensity of the 801 cm^{-1} mode of cyclohexane as a function of Raman pump ellipticity. All simulated data is positive valued. Red indicates positive deviation from baseline, blue indicates negative deviation from baseline. The anomalous behavior seen at $\phi = 135$ and 315 occurs due to nonphysical limits in Eq. 4.2. Figure reproduced with permission from Ref. 62. Copyright 2016 Optical Society of America.

As evident by the agreement in Figs. 4.6 and 4.7, the experimental OHD-FRIKES spectra of cyclohexane are well reproduced by simulation of Eq. 4.2. Explicitly, the simulations show strong agreement on two points:

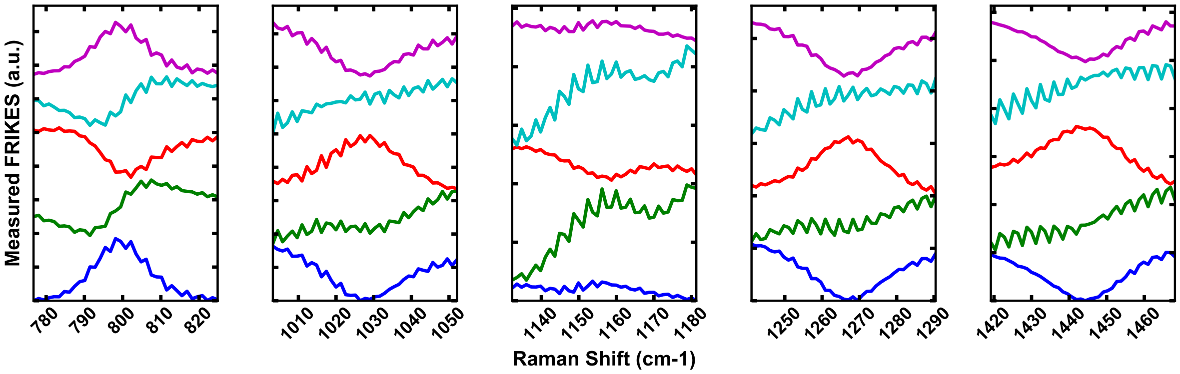

Figure 4.6. Experimental data of cyclohexane OHD-FRIKES lineshapes displayed as function of set Raman pump ellipticities. Blue, green, red, cyan, and magenta traces correspond to quarter waveplate settings of $\phi = 45$, 90, 135, 180, and 225 degrees; respectively. Figure reproduced with permission from Ref. 62. Copyright 2016 Optical Society of America.

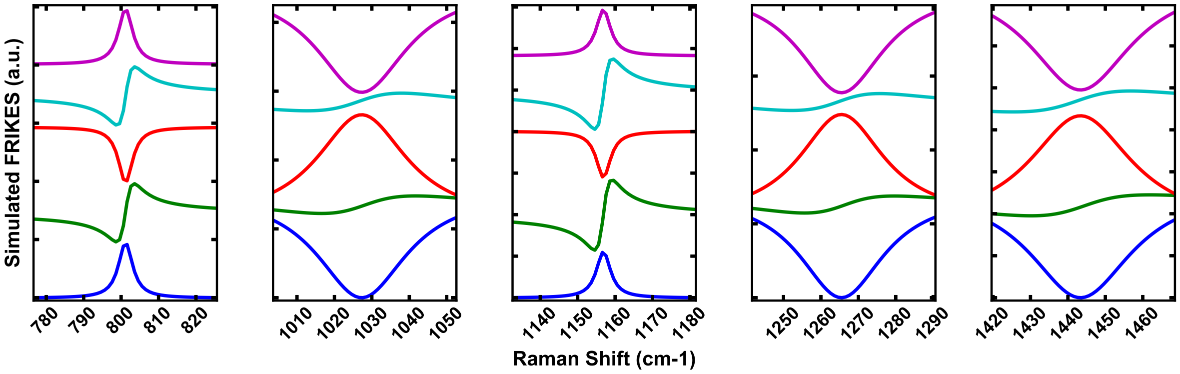

Figure 4.7. Theoretical data of cyclohexane OHD-FRIKES lineshapes displayed as function of set Raman pump ellipticities. Blue, green, red, cyan, and magenta traces correspond to quarter waveplate settings of $\phi = 44$, 89, 134, 179, and 224 degrees; respectively. Line slices were obtained at the specified values to avoid nonphysical limits of Eq. 4.2. Figure reproduced with permission from Ref. 62. Copyright 2016 Optical Society of America.

(1) Accurate sign of positive or negative Lorentzian lineshapes at circularly polarized waveplate settings (45, 135, and 225 degrees) reproducing the opposite trend of sign between highly polarized and depolarized vibrational modes.

(2) Correct phase of dispersive lineshapes at elliptically polarized positions of the quarter waveplate (90 and 180 degrees) for each vibrational mode, including the stronger dispersive character of highly polarized vibrational modes at 801 and 1157 cm^{-1}.

However, it should be noted that the linewidths in the simulated spectra for the polarized modes are much narrower than observed experimentally. This is likely due to the broader bandwidth of the Raman pump used here than that used in the RP-CARS experiment used for simulation parameters.[142]

These results discussed herein suggest that the lineshapes in OHD-FRIKES are highly dependent on Raman pump ellipticity and vibrational mode character, particularly the value of the depolarization ratio. One interesting point, is that the previous work of Shim *et al.*[54] showed only positive Lorentzian lineshapes. However, it was noted extensively in a more recent study by Balakrishnan *et al.*[56] that solvent OHD-FRIKES lineshapes were highly dependent on the Raman pump ellipticity.

4.5. Conclusion

The experiments and simulations shown here suggest that OHD-FRIKES in a multiplex experiment, like the one demonstrated herein, can be a sensitive probe of vibrational polarization. By coupling OHD-FRIKES with time resolution dynamics from ultrafast spectroscopy, biological and materials systems that undergo large scale ordering changes can be probed. Of particular interest to biology are intrinsically disordered proteins (IDPs).[147] IDPs include alpha-synucleins, $\alpha\beta$, and tau proteins all of which exhibit fibril formation indicative of Alzheimer's disease. From a materials perspective, the kinetics of supramolecular materials built from small molecule building blocks can be elucidated by tracking the vibrational polarization.[148] Due to OHD-FRIKES sensitivity to vibrational mode polarization, it is well situated to complement and perhaps improve on current vibrational optical activity techniques for studying large scale structural changes.

4.6. Supplementary Information: OHD-SEFRIKES

4.6.1. Abstract

The coupling of molecules and plasmons has resulted in the new and exciting fields of plasmonically-enhanced and plasmonically-enabled chemistry. While steady-state measurements of molecule-plasmon systems can show results of chemical events they lack the time resolution necessary for mechanistic insight of plasmonically-influenced chemistry. To understand these new classes of chemical events, plasmonically-enhanced coherent Raman scattering is ideal for initiating and tracking ultrafast chemical events. Surface-enhanced femtosecond stimulated Raman scattering (SE-FSRS) is a plasmonically-enhanced coherent Raman scatter with high spectral and temporal resolution. Improvements to SE-FSRS will allow for higher SNR acquisitions and thus better tracking of plasmonically-influenced chemical events. To this end, polarization sensitive excitation and detection methods have been explored.*

4.6.2. Experimental Methods

Using the apparatus shown in Fig. 4.2, a study of OHD-SEFRIKES was performed to examine the possibility of boosting the SNR of existing SE-FSRS experiments.[72,98]

---

*This section was not published in Ref. 62, but was presented as a poster at the 2015 Time-Resolved Vibrational Spectroscopy Conference in Madison, WI.

Colloidals AuNPs functionalized with BPE and silica coated were studied using the pulses shown in Fig. 4.2, specifically 25 μW of Raman pump and 10 μW of Raman probe. The Glan-Taylor polarizer used behind the sample (analyzer) was optimized in real time for maximum SNR. The optimization of the analyzer is a complex experimental parameter that is balancing the effects of extinction in the local oscillator, rejection of background nonresonant Kerr signal, and isolation of vibrationally-resonant SEFRIKES signal.[57,149]

To determine the improvement the FRIKES approach has on SE-FSRS, quantitative comparisons were made between the SNR of the SE-FSRS and (OHD)-SEFRIKES spectra obtained. The noise was defined as the standard deviation of the fit baseline shown in Fig. 4.8 while the signal was defined as the fitted amplitude of the Fano lineshape equation (Eq. 4.4) for the peaks indicated at 1200 and 1008 cm^{-1}.

$$f(\omega) = A \times \left(\frac{\left(q + \frac{\omega-\omega_0}{\Gamma/2}\right)^2}{1 + \left(\frac{\omega-\omega_0}{\Gamma/2}\right)^2} \right) \tag{4.4}$$

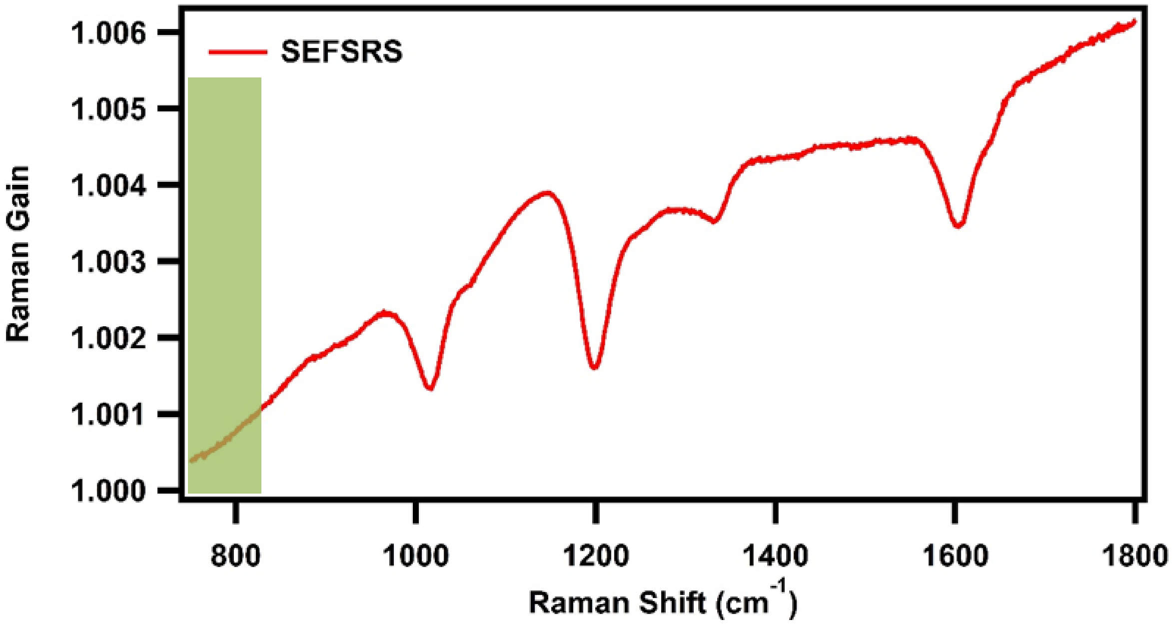

Figure 4.8. SE-FSRS of the BPE NT's used in the OHD-SEFRIKES experiment. Shaded green denotes the location where standardized deviation of baseline is calculated for noise for both SE-FSRS and (OHD)-SEFRIKES. Signal was defined as the fitted amplitude of the Fano lineshape.

4.6.3. Results

First showing the results of the most well-controlled SEFRIKES experiment, with minimal local oscillator intensity, Fig. 4.9. In this experiment, the SEFRIKES polarization control allowed for an increase in SNR of the 1008 and 1200 cm^{-1} modes by factors of 1.38 and 1.68, respectively.

After real time optimization of the analyzer and quarter-waveplate controlling ellipticity in the Raman pump a maximum SNR was obtained as seen in Fig. 4.10. In this experiment, the optimal polarization control for excitation and detection allowed for an increase in SNR of the 1008 and 1200 cm^{-1} modes by factors of 3.98 and 4.70, respectively for OHD-SEFRIKES over SE-FSRS.

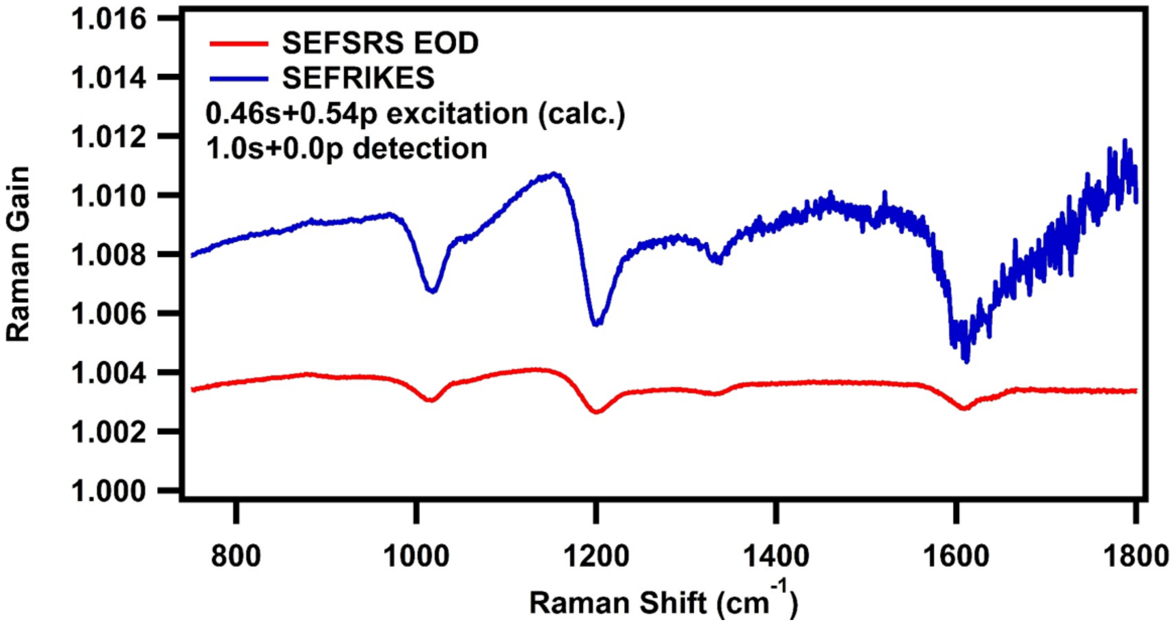

Figure 4.9. Comparison of SEFRIKES (blue) to SE-FSRS (red) at identical excitation powers and acquisition times. Raman pump polarization and analyzer polarization settings are displayed in the sublegend.

4.6.4. Conclusions

While the initial results are promising, showing a $\sim 4\times$ increase of SNR compared to equivalent power SE-FSRS experiments, further experimentation was not as successful due to lack of reproducibility. We believe that the OHD-SEFRIKES experiment may be viable and more reproducible if individual aggregates are interrogated and possibly if purposely asymmetric plasmonic particle aggregates are used as the surface-enhancing substrate.[150–152] However, even with the use of chiral plasmonic substrates we wish to remind the community that while potatoes may have chirality, they do not have handedness.[153,154]

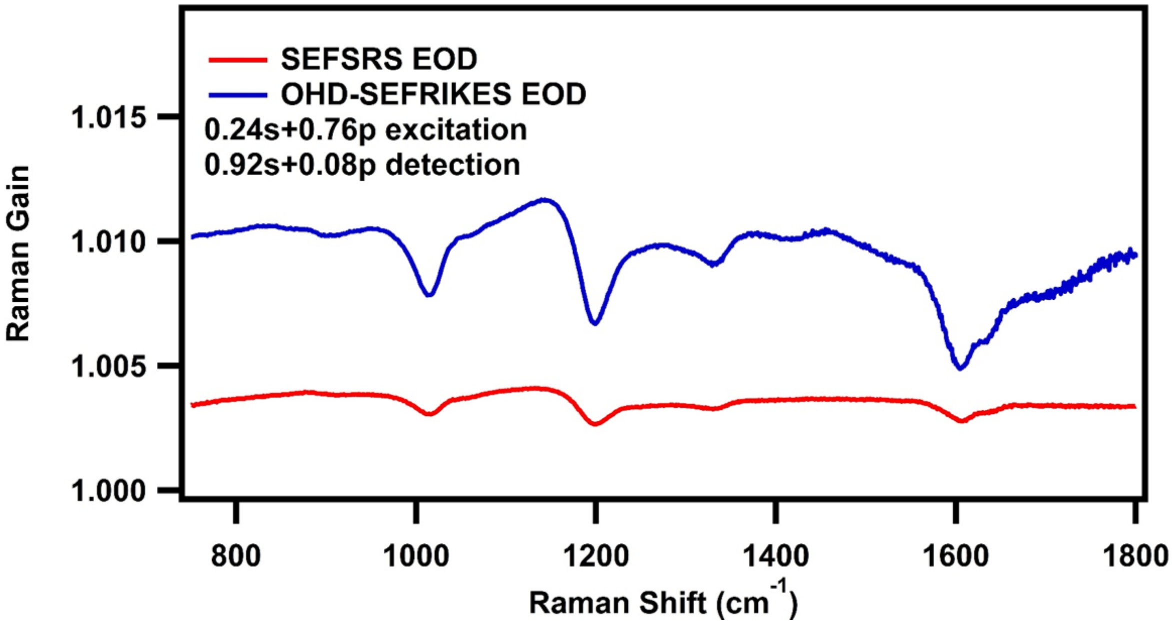

Figure 4.10. Comparison of OHD-SEFRIKES (blue) to SE-FSRS (red) at identical excitation powers and acquisition times. Raman pump polarization and analyzer polarization settings are displayed in the sublegend.

CHAPTER 5

Improving Surface-Enhanced Femtosecond Stimulated Raman Scattering Spectrometers

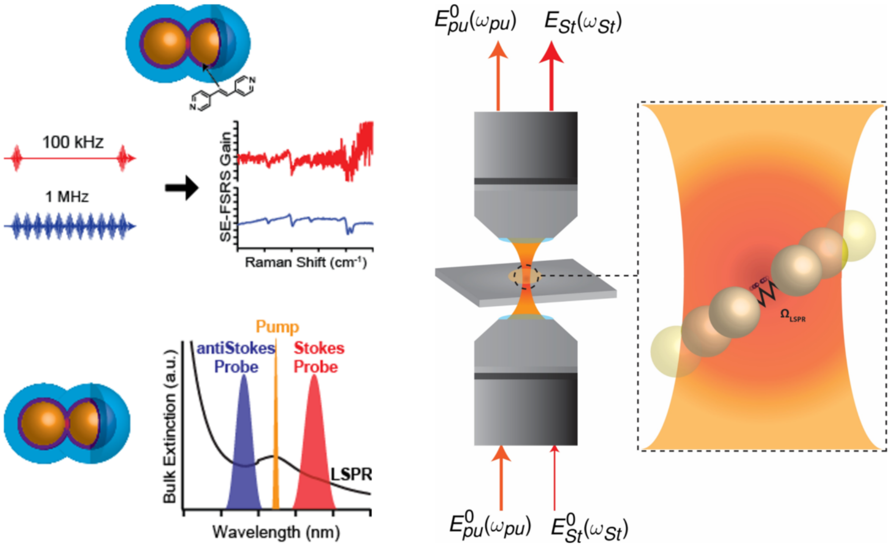

The work performed in this chapter was done in collaboration with Drs. Lauren Buchanan, Natalie Gruenke, Bogdan Negru, and Ms. Hannah Mayhew.

5.1. Abstract

Surface-enhanced femtosecond stimulated Raman scattering (SE-FSRS) is a spectroscopic technique that utilizes the plasmonic enhancement of optical fields via surface-enhanced Raman scattering (SERS) with the broadband, multiplex vibrational spectroscopy of femtosecond stimulated Raman scattering (FSRS). SE-FSRS has shown promise for bringing extraordinary time and frequency resolution to SERS analytes. However, continued improvement is essential to maximizing the potential of this spectroscopy. This chapter details the efforts to improve and expand the SE-FSRS technique by multiple strategies. The first section describes improvements on the first 100 kHz SE-FSRS spectrometer by improving the excitation geometry and suppressing competing nonlinear effects. The second section demonstrates SE-FSRS at higher repetition rates by using a new 1 MHz SE-FSRS spectrometer. The third section is an analysis of the SE-FSRS lineshape dependence on excitation wavelength and plasmon resonance. Finally, the last section covers progress towards single-aggregate SE-FSRS (SA-SE-FSRS). We conclude with a brief discussion of future directions in experimental SE-FSRS.

5.2. Improving 100 kHz Surface-Enhanced Femtosecond Stimulated Raman Spectrometers by Removing Cross-Phase Modulation

5.2.1. Abstract

The previous successes of surface-enhanced femtosecond stimulated Raman scattering (SE-FSRS) demonstrated a new analytical technique incorporating both surface-enhanced Raman scattering (SERS) with femtosecond stimulated Raman scattering (FSRS). However, dispersive lineshapes, broad backgrounds, and weak overall signals pushed for improvements on the SE-FSRS spectrometer used in previous work. A few different directions to improve the technique have been pursued, including polarization control in the form of femtosecond Raman-induced Kerr-effect scattering (FRIKES) (see Chapter 4). This section discusses work on improving the optical detection in SE-FSRS by using a collinear experimental geometry not used in initial studies.

5.2.2. Introduction

Surface-enhanced femtosecond stimulated Raman scattering (SE-FSRS) has been a succesful analytical technique that combines the effects of stimulated Raman scattering (SRS) with surface-enhanced Raman scattering (SERS).[72,98] Previous studies used a noncollinear geometry for overlapping the Raman pump with the Raman probe in the sample then lecting the transmitted Raman probe field to a CCD camera and spectrometer. This approach is not ideal, as a noncollinear overlap of beams in the sample minimizes the effective overlap and thus the path length in the generation of the signal (Eq. 5.1):[26,155]

$$I_{FSRS} = a \times \sigma_R \times l \times N \times I_{RP} \tag{5.1}$$

where, the intensity of the FSRS signal (I_{FSRS}), or stimulated Raman activity, is linear with respect to a collection of analyte-independent physical constants (a), the analyte total Raman scattering cross-section (σ_R), path length (l), analyte concentration (N), and Raman pump power (I_{RP}).

5.2.3. Experimental Methods

To improve on the previous studies, we used a collinear geometry, maximizing the path length in Eq. 5.1. While this increases the FSRS signal, it also allows for a competing process called cross-phase modulation (XPM). XPM arises as a Kerr effect in a medium. Effectively, XPM is described as the change in the optical phase of a 'weak' beam perturbed by the interaction of a 'strong' beam in a nonlinear medium. The nonlinear medium contains a nonlinear index of refraction which allows for the change in optical phase of the 'weak' beam, in FSRS this is observed by the Raman pump changing the optical phase of the Raman probe. When observing XPM dispersed by a spectrometer onto a CCD one typically sees rapidly changing background lineshapes for broadband fields, like that used in a Raman probe field.

To minimize the effects of XPM, we used a XPM-suppresion module with the previously used 100 kHz spectrometer (Fig. 5.1). The XPM-suppresion module consisted of a computer audio speaker playing broadband white noise (Fig. 5.2) duct-taped to a retroreflector in the Raman pump path. The broadband white noise was the most effective means of removing effects of XPM.

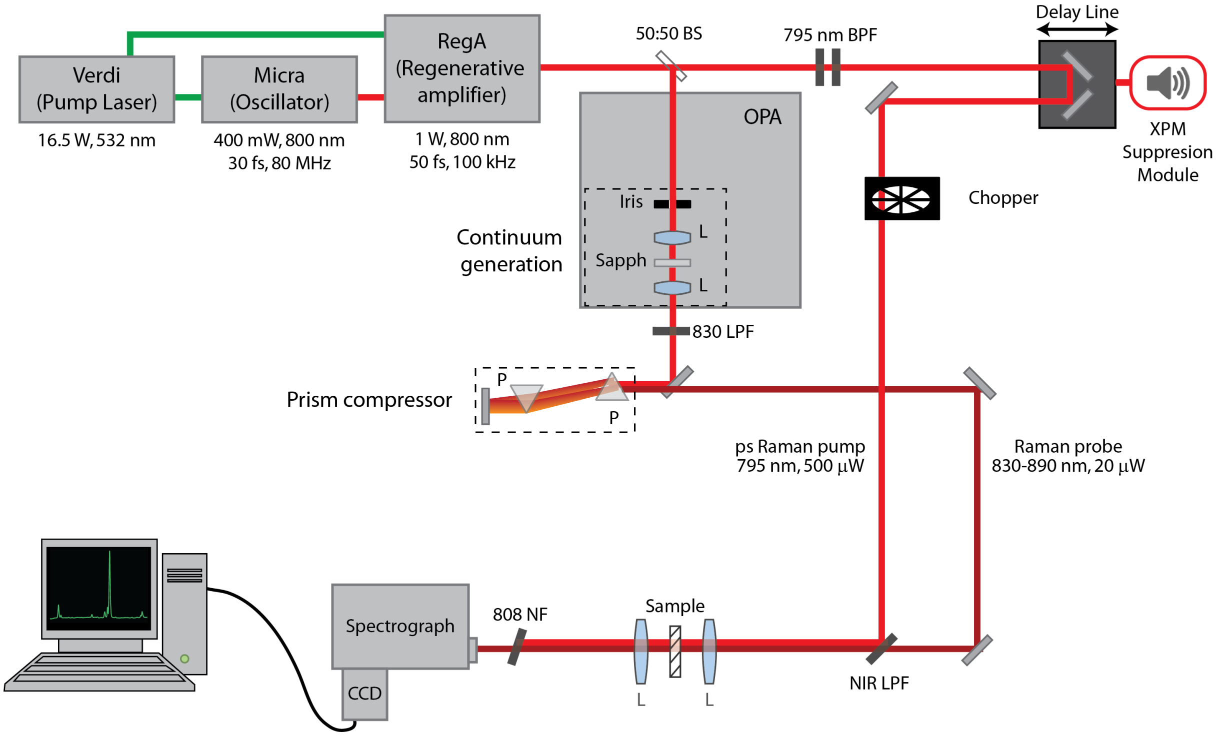

Figure 5.1. Schematic of the 100 kHz laser system described in previous literature.[72,98] Abbreviations: beam splitter (BS), bandpass filter (BPF), cross-phase modulation (XPM), optical parametric amplifier (OPA), sapphire (Sapph), lens (L), longpass filter (LPF), prism (P), notch filter (NF), charge-coupled device (CCD).

5.2.4. Results

Using the XPM-suppression module with the previous 100 kHz FSRS system resulted in marked improvement on collinear FSRS (Fig. 5.3) of CHX. The background seen in Fig. 5.3 could be minimized/optimized in real time by changing the amplitude of the white noise. After successful usage of the XPM-suppression module for FSRS of CHX, the same methodology was implemented for SE-FSRS samples at much lower excitation powers (25 μW Raman pump, 10 μW Raman probe), seen in Fig. 5.4.

In comparison to FSRS, use of the XPM-suppresion module in SE-FSRS provides a smaller improvement. The baseline is improved slightly near the 1400-1600 cm^{-1} region

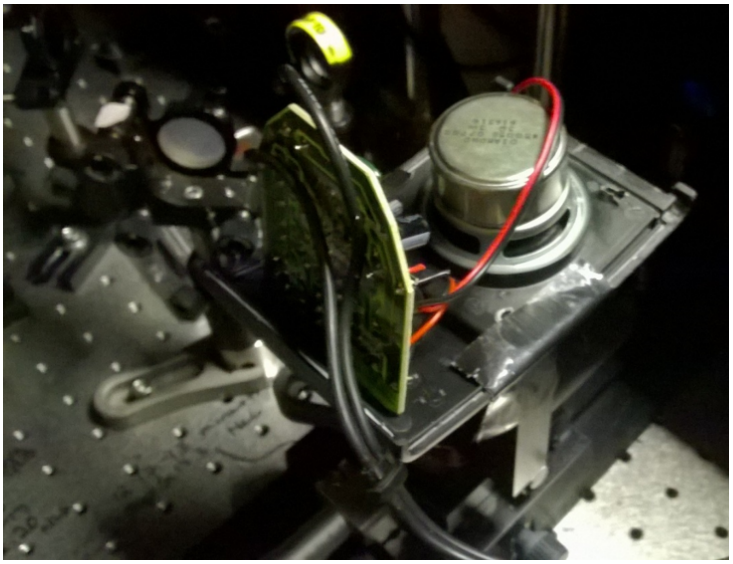

Figure 5.2. To eliminate XPM, an XPM-suppression module consisting of an audio speaker playing broadband white noise was attached (via duct tape) to a retroreflector in the Raman pump path.

and the strong 1600 and 1640 modes are better resolved in SE-FSRS when using the XPM-suppression module. The lack of improvement is due to the lower Raman pump pulse energy used compared to the FSRS experiment shown in Fig. 5.3, 5 nJ/pulse in FSRS vs. 250 pJ/pulse in SE-FSRS.

5.2.5. Conclusion

In conclusion, using XPM-suppression with the 100 kHz system is highly-beneficial for FSRS. However, the benefit is minimal for SE-FSRS. This is likely due to the lower Raman pump pulse energies used in SE-FSRS so the dominant background fluctuations observed experimentally are not from XPM but other field interactions with the plasmonic particles as discussed in Chapter 3.

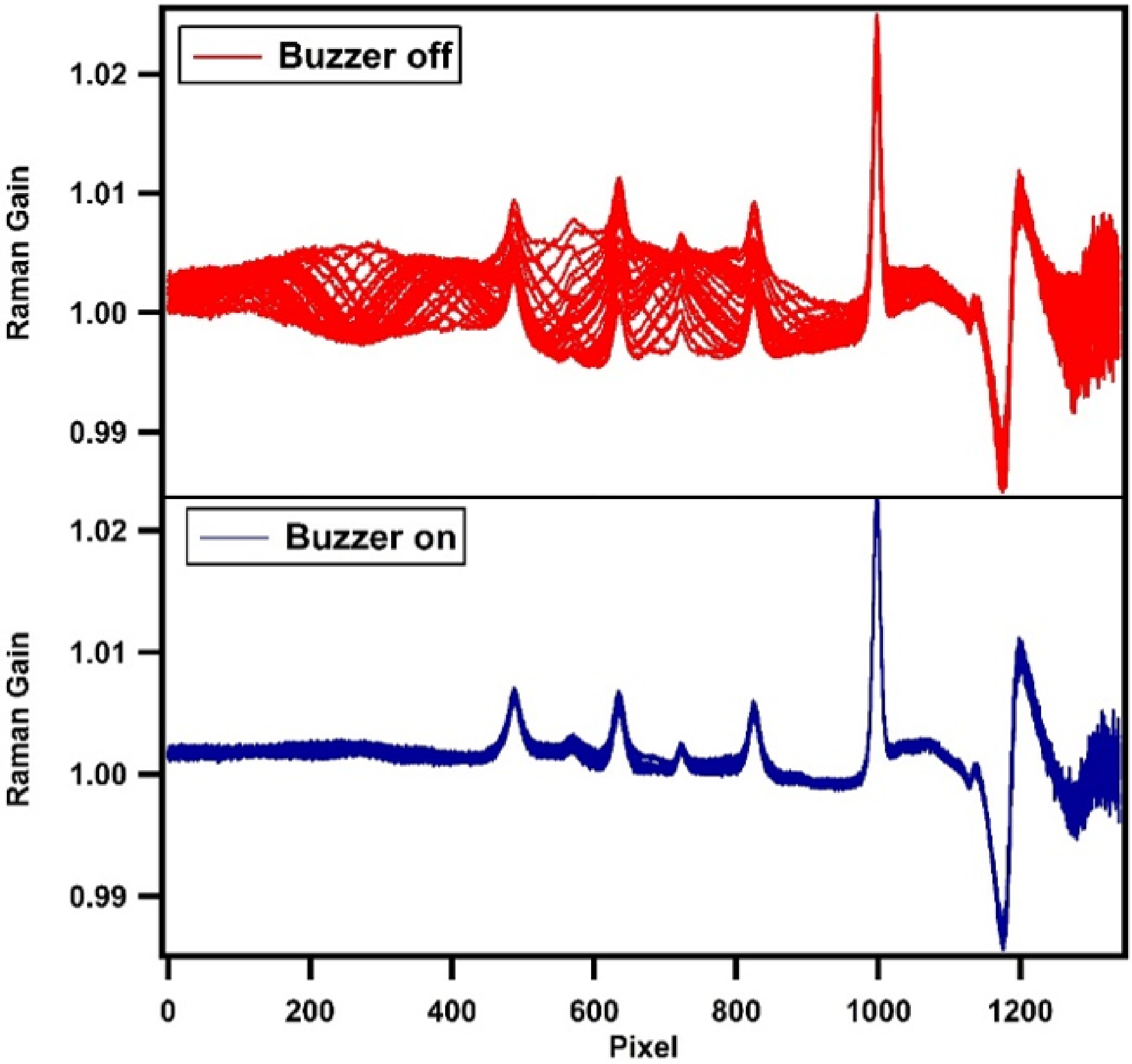

Figure 5.3. By using the XPM-suppression method marked improvement is obtained in collinear FSRS. (Top) In red, twenty sequentially obtained collinear FSRS spectra are plotted. (Bottom) In blue, twenty sequentially obtained collinear FSRS spectra with XPM-suppression are plotted. The baseline in the non-XPM-suppressed spectra contains broad, rapidly fluctuating backgrounds that obscure vibrational features. Using the broadband white noise of the XPM-suppresion module sufficiently perturbs the overlap in the sample between pump and probe such that the destructive interference of XPM with RRS(I) is minimized.

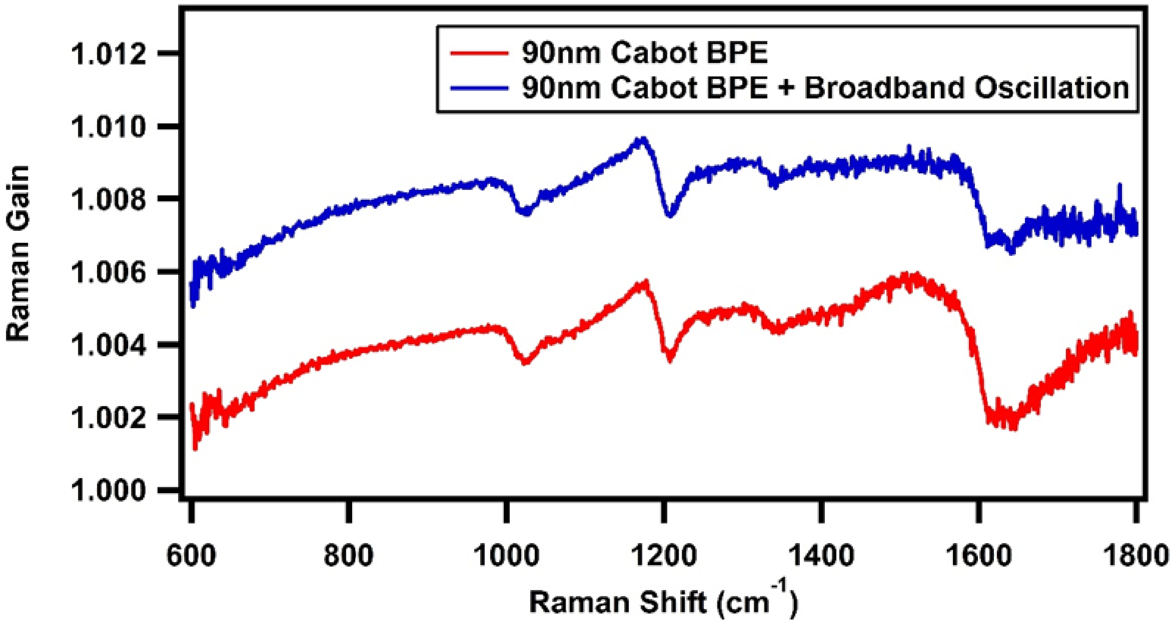

Figure 5.4. In comparison, use of the XPM-suppresion module in SE-FSRS provides a smaller improvement. Some improvement is observed (blue) with the speaker on as evident by the resolution of the 1600 and 1640 peaks compared to the lower red spectrum, but overall the difference is minimal. The lack of improvement is due to the lower Raman pump pulse energy used compared to the FSRS experiment shown in Fig. 5.3.

5.3. Surface-Enhanced Femtosecond Stimulated Raman Spectroscopy at 1 MHz Repetition Rates

5.3.1. Abstract

Surface-enhanced femtosecond stimulated Raman spectroscopy (SE-FSRS) is an ultrafast Raman technique that combines the sensitivity of surface-enhanced Raman scattering with the temporal resolution of femtosecond stimulated Raman spectroscopy (FSRS).* Here, we present the first successful implementation of SE-FSRS using a 1 MHz amplified femtosecond laser system. We compare SE-FSRS and FSRS spectra measured at 1 MHz and 100 kHz using both equal pump average powers and equal pump energies to demonstrate that higher repetition rates allow spectra with higher signal-to-noise ratios to be obtained at lower pulse energies, a significant advance in the implementation of SE-FSRS. The ability to use lower pulse energies significantly mitigates sample damage that results from plasmonic enhancement of high-energy ultrafast pulses. As a result of the improvements to SE-FSRS developed in this report, we believe that SE-FSRS is now poised to become a powerful tool for studying the dynamics of plasmonic materials and adsorbates thereon.

5.3.2. Introduction

Chemical reactions are described by the motion of atoms as systems evolve from reactants to products. Molecular vibrations, the basis for these atomic motions, thus underlie chemical reaction dynamics. Femtosecond stimulated Raman spectroscopy (FSRS), one

---

*This section has been reproduced with permission from Ref. 99. Copyright 2016 American Chemical Society.

of a family of coherent Raman spectroscopies (CRS) that can track molecular vibrations in the time and frequency domain, has emerged as a powerful technique for studying chemical dynamics.[34,36,155] FSRS is remarkable in its ability to acquire complete vibrational spectra with simultaneous high temporal (10-100 fs) and spectral (5-20 cm^{-1}) resolution, allowing molecular dynamics to be monitored on their most fundamental time scales. FSRS has been applied successfully to a wide variety of chemical and biological systems.[37,42,45]

Generally, Raman spectroscopies are sensitivity limited in their application. Since the cross-sections for nonresonant Raman scattering are of order 10^{-29} - 10^{-30} cm^2 sr^{-1} molecule^{-1}, typically one is restricted to highly concentrated systems. To this end, the Van Duyne group has developed surface-enhanced femtosecond stimulated Raman spectroscopy (SE-FSRS) in colloidal solutions,[72] while the Apkarian and Potma groups have demonstrated time-resolved SE-CARS on dry-mounted individual nanostructures.[75,101,156] These approaches take advantage of the electromagnetic (EM) enhancement of the surface fields to increase the CRS signals. In the first demonstration of SE-FSRS, gold nanoparticle assemblies functionalized with *trans*-1,2-bis(4-pyridyl)-ethylene (BPE), exhibited estimated enhancement factors of 10^4-10^6 over FSRS. Further, it was demonstrated that SE-FSRS spectra contain dispersive rather than Lorentzian lineshapes,[98] the origin of which was recently explored by Schatz *et al.*.[110]

SE-FSRS has the potential to become a versatile tool for studying ultrafast dynamics of coupled molecule-plasmon systems.[23] For example, recent studies have reported improved efficiencies for plasmonically-enhanced photocatalysis and photovoltaic devices but the mechanism of these enhancements is unclear.[157–160] Additionally, SE-FSRS could prove instrumental in understanding the emerging field of plasmon-driven chemistry, which includes such phenomena as the hot-electron-induced dissociation of hydrogen on gold nanoparticles.[161] As coupling between the molecule and the plasmon has no observable effect on lifetimes of the molecular vibrational coherence required to generate signal,[75,92,98] SE-FSRS is exceptionally well suited to studying the role of vibrational excited states in plasmonically-enhanced photochemistry.

Unfortunately, the development of time-resolved (TR) SE-FSRS has been hindered greatly by sample degradation. The combination of high-energy ultrafast pulses and plasmonic enhancement has been shown to result in melting, fusion, or fragmentation of particles.[162–164] Furthermore, coupled nanoparticles can also undergo irreversible aggregation and sintering[165] which eliminate the highly-enhancing hot spots that generate the strongest SERS signals. The gold nanoparticle aggregates used for SE-FSRS were overcoated with silica, an approach shown to improve the thermal, mechanical, and chemical stability of plasmonic substrates.[166–168] However, the SE-FSRS signal obtained of colloidal solutions of these aggregates at 100 kHz still decayed significantly on the timescale of minutes,[72] which hindered attempts to use TR-SE-FSRS to study dynamics. Damage can be mitigated by lowering pulse energies; however, improved sample longevity comes at the cost of decreased signal intensity, leading to longer data acquisition times for equivalent signal-to-noise ratios (SNR).

5.3.3. Experimental

Here, we present the first ground-state SE-FSRS spectra obtained at 1 MHz repetition rates. This repetition rate is ten times greater than previously published SE-FSRS experiments and three orders of magnitude greater than typical 1 kHz FSRS experiments, although FSRS studies at repetition rates as high as 80 MHz have been reported.[60,169,170] We compare ground-state SE-FSRS and FSRS spectra obtained at both 100 kHz and 1 MHz to illustrate the advantages of implementing SE-FSRS at high repetition rates. While the 100 kHz system has been described previously,[72] the 1 MHz system is a new SE-FSRS apparatus. The 1 MHz system, shown in Fig. 5.9, is based on an Yb-doped fiber oscillator/amplifier (Clark-MXR Impulse). The beam diameters of the Raman pump (795 nm, 1 ps) and stimulating probe (approximately 825-950 nm, 30 fs) beams at the sample are adjusted to be ∼55 μm on both systems. Spectra are collected using a Princeton Instruments PIXIS 400BR CCD array. Due to the size of the CCD array, the data collection rate is limited to 500 Hz. Variable pump average powers of 5-500 μW and probe average powers of 0.5-1 μW are used on both systems. The probe powers were chosen to maximize dynamic range filling of the CCD camera, thus reducing shot noise in the collected spectra. Unless otherwise indicated, all spectra are averaged for 30 minutes. FSRS spectra are presented for cyclohexane (CHX), while SE-FSRS spectra are shown for the gold nanoparticle assemblies used in previous SE-FSRS studies.[72,98] The nanoparticle assemblies consist of approximately 95 nm gold cores aggregated with BPE and subsequently overcoated with silica (Fig. 5.10). A more detailed description of both systems and other experimental considerations is given in the Supporting Information.

5.3.4. Results

First, we compare FSRS and SE-FSRS spectra taken on each system with identical pump and probe average powers. The FSRS spectra of CHX shown in Fig. 5.5A were measured using 500 μW of Raman pump and 0.5 μW of probe. The spectrum obtained at 100 kHz has approximately 13.5x greater gain than the one obtained at 1 MHz. In FSRS, Raman gain scales with the peak pump intensity (I_{pump}):

$$RG = \frac{I_{pump-on}}{I_{pump-off}} = e^{a\sigma_R c z I_{pump}} \sim 1 + a\sigma_R c z I_{pump} \tag{5.2}$$

where a is a collection of physical parameters, σ_R is the total Raman scattering cross-section, c is the sample concentration, and z is the sample path length.[155] Since the gain coefficient is generally small, the FSRS signal scales linearly with the peak intensity of the pump. While it has been demonstrated that the SE-FSRS signals saturate at high pump intensities, likely due to degradation of the samples,[72] the following experiments are performed within the linear regime. While experimental conditions were matched carefully between the two systems, small differences in spatial or temporal overlap can result in slightly different signal strengths. Thus, the difference in Raman gain in Fig. 5.5A matches expectations as the pump pulse energy at 100 kHz is 10x greater than at 1 MHz for equal average powers. The SE-FSRS signals obtained from the BPE nanoparticle assemblies exhibit an identical pump power dependence (Fig. 5.5B). Both spectra were obtained with 50 μW (50 pJ/pulse at 1 MHz; 500 pJ/pulse at 100 kHz) of Raman pump and 1 μW (1 pJ/pulse at 1 MHz; 10 pJ/pulse at 100 kHz) of probe. As with FSRS, the ratio of the SE-FSRS gains between the two systems does not exactly match that predicted by Eq. 5.2; in Fig. 5.5B, gains at 100 kHz are approximately 16x greater gain than those obtained at 1 MHz. In fact, this trend was observed across all data collected. To compensate for experimental variations between the two systems, an average empirical correction factor of 0.66 is applied to the 100 kHz SNR values for both FSRS and SE-FSRS in the following sections.

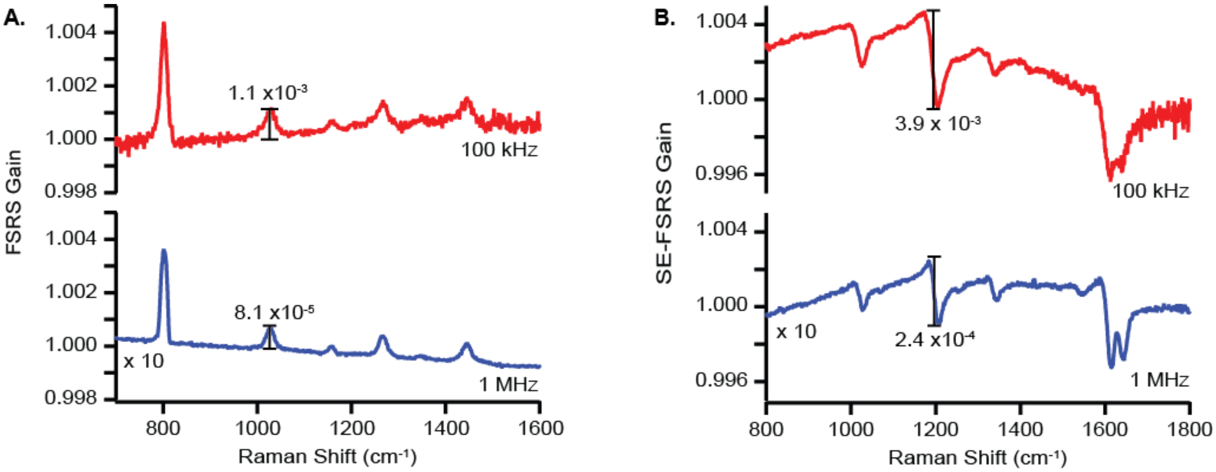

Figure 5.5. FSRS and SE-FSRS obtained with equal pump average powers. (A) FSRS spectra of CHX obtained with 500 μW of Raman pump at 100 kHz (red) and 1 MHz (blue). (B) SE-FSRS spectra of BPE nanoparticle assemblies obtained with 50 μW of Raman pump at 100 kHz (red) and 1 MHz (blue). Both repetition rates yield the FSRS and SE-FSRS spectra with roughly equivalent SNR in the spectral region of 1000-1200 cm^{-1}, but the corrected signal strengths are approximately 10x higher at 100 kHz than at 1 MHz. The gains of the 1028 cm^{-1} peak of CHX and the 1200 cm^{-1} peak of BPE are labeled. Figure reproduced with permission from Ref. 99. Copyright 2016 American Chemical Society.

To determine the SNR ratio for each SE-FSRS spectrum, we fit the averaged spectrum to a sum of Fano lineshape functions[120] superimposed on a broad cubic background, as first implemented in earlier SE-FSRS reports.[98] Each individual vibrational resonance was fit to the function:

$$f(\omega) = A\left(\frac{\left(q + \frac{\omega-\omega_0}{\Gamma/2}\right)^2}{1 + \left(\frac{\omega-\omega_0}{\Gamma/2}\right)^2}\right) \tag{5.3}$$

where A represents the amplitude of the peak, q is the Fano asymmetry parameter that describes the dispersivity of the peak, Γ is the line width, and ω_0 is the frequency of the molecular vibration. The SNR is defined for a particular peak, i, as the amplitude of the peak divided by the root-mean-square (RMS) value of the noise across the bandwidth of the signal peak.

$$SNR_i = \frac{A_i}{RMS_i} \tag{5.4}$$

The RMS of the noise is calculated from the RMS of the residuals from the Fano fit across the width of the peak. For FSRS spectra, SNR is calculated in a similar manner except each peak is fit to a Lorentzian lineshape rather than a Fano lineshape. It is important to note that the noise level across each spectrum is highly dependent on the spectral characteristics of the probe (Fig. 5.11). As a result, the 1 MHz spectra have a near constant level of noise across the entire spectral region, while the 100 kHz spectra exhibit the lowest noise in the 1000-1200 cm^{-1} region and rapidly increasing noise towards higher frequencies where reduced filling of the pixels increases the shot noise. Thus, we will compare the SNR for FSRS at the 1028 cm^{-1} band of CHX and the SNR for SE-FSRS at the 1200 cm^{-1} band of BPE where both systems produce the lowest noise.

After 30 minutes of averaging, the FSRS spectra of CHX (Fig. 5.5A) exhibits a SNR of 12.5 at the 1028 cm^{-1} mode for the spectrum obtained at 1 MHz and a SNR of 20 for the spectrum obtained at 100 kHz. When the 100 kHz SNR is scaled by an empirical correction factor of 0.66, it matches that obtained at 1 MHz. Likewise, the SE-FSRS spectra of the BPE nanoparticle assemblies (Fig. 5.5B) exhibit a SNR of 24 for the spectrum obtained at 100 kHz. Thus, despite an order of magnitude difference in signal strength between the spectra collected at each repetition rate, the spectra have equivalent SNR ratios. This is not the expected result as the 100 kHz system has 10x more intense signals than the 1 MHz system but should only have $\sqrt{10}$ times greater noise due to the difference in repetition rate. The cause of this discrepancy will be discussed below.

Next, we compare FSRS and SE-FSRS spectra obtained on each system with equal pump pulse energies, rather than average powers. The FSRS spectra of cyclohexane shown in Fig. 5.6A were measured using 50 μW of Raman pump on the 100 kHz system or 500 μW on the 1 MHz system. Thus, the pump pulse energy was 500 pJ/pulse for both cases. Meanwhile, the probe average power was left at 0.5 μW for both systems; this power was chosen because Raman gain is invariant with probe intensity (see Eq. 5.2) and using the same average power allowed for equal dynamic range filling of the camera on both systems. While the FSRS spectra have approximately equal gain at both repetition rates, but they exhibit a stark difference in noise. The SE-FSRS spectra of the BPE nanoparticle assemblies (Fig. 5.6B) were both obtained using Raman pump pulse energies of 50 pJ/pulse (an average power of 5 μW on the 100 kHz system and 50 μW on the 1 MHz system), while holding the probe power at 1 μW. As with FSRS, the SE-FSRS gains are approximately equivalent for both spectra, but the SNR ratios are dramatically different. As with the comparison performed at equal average powers, an empirical correction factor of 0.66 is required to compare the spectra; the 100 kHz signals are on average 1.5 times stronger than those obtained at 1 MHz.

After 30 minutes of averaging, the FSRS spectrum of CHX obtained at 100 kHz (Fig. 5.6A) exhibits a SNR of 1.9 at the 1026 cm^{-1} mode. When scaled by the empirical correction factor of 0.66, the SNR is 1.3. This is approximately 10x lower than the SNR of 12 obtained at 1 MHz. Likewise, the SE-FSRS spectrum of the BPE nanoparticle assemblies obtained at 100 kHz (Fig. 5.6B) exhibits a corrected SNR of 2.7 at the 1200

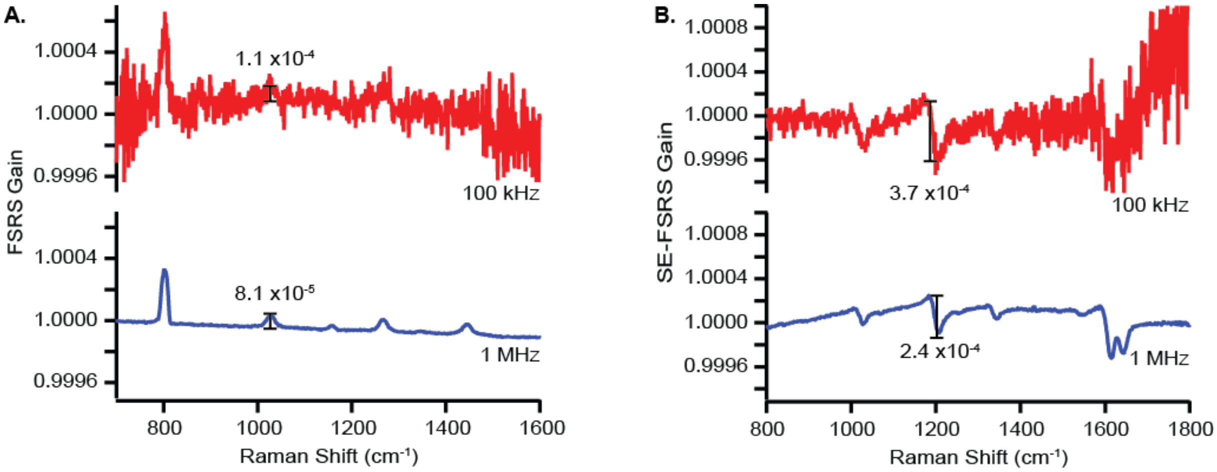

Figure 5.6. FSRS and SE-FSRS spectra obtained with equal pump pulse energies. (A) FSRS spectra of cyclohexane obtained with 500 pJ/pulse of Raman pump at 100 kHz (red) and 1 MHz (blue). (B) SE-FSRS spectra of BPE nanoparticle assemblies obtained with 50 pJ/pulse of Raman pump at 100 kHz (red) and 1 MHz (blue). Both repetition rates yield similar FSRS and SE-FSRS signal strengths, but the spectra obtained at 100 kHz exhibit approximately 10x greater noise than those obtained at 1 MHz. The gains of the 1028 cm^{-1} peak of CHX and the 1200 cm^{-1} peak of BPE are labeled. Figure reproduced with permission from Ref. 99. Copyright 2016 American Chemical Society.

cm^{-1} mode, which is approximately 10x lower than the SNR of 23 obtained at 1 MHz. As predicted, moving to a higher repetition rate system allows SE-FSRS and FSRS spectra to be collected at lower pulse energies with higher SNR than possible using lower repetition rates.

However, the observed improvement in SNR as a function of repetition rate does not match expectations. Signal averaging dictates that the SNR should increase by a factor of $\sqrt{10}$ when collecting signals generated by 10x as many pulses, while we observe a factor of 10 improvement. To uncover the source of this discrepancy, we first examine how SNR scales as a function of signal averaging on each table.

The spectra presented in Figs. 5.5 and 5.6, which represent 30 minutes of data averaging, were collected as a set of 100 individual scans. Thus, we can average randomized subsets of these 100 scans and plot the SNR as a function of the number of scans being averaged (Fig. 5.7). On the 1 MHz system, the SNR for both FSRS (cyan) and SE-FSRS (navy) scales properly as the $\sqrt{n}$, where n is the number of scans being averaged. However, on the 100 kHz system the SNR deviates significantly from expected $\sqrt{n}$ scaling and appears to remain nearly constant after only 20 scans (∼6 minutes) for both FSRS (red) and SE-FSRS (maroon). In fact, after 100 scans or 30 minutes of averaging, the observed SNR is 3 3.5 times smaller than the theoretical value. This difference exactly accounts for the discrepancy in SNR values between the two systems discussed in the previous paragraph. In an attempt to isolate the cause of the empirically asymptotic SNR of the 100 kHz system, we exchanged all data collection electronics between systems including CCD cameras, choppers, and digital delay generators; however, the collected data (not shown) exhibited the same dependence of SNR on the number of scans being averaged.

To determine whether the noise on the 100 kHz system could be read-out noise limited rather than shot noise limited, which would cause signal averaging to fail, we collected FSRS and SE-FSRS spectra at different acquisition rates ranging from 40 Hz to 1 kHz using a PIXIS 100 F CCD camera that could accommodate higher repetition rates. Once again, the same SNR scaling was observed. Having eliminated all elements of the data collection process as possible culprits, we conclude that the problem must originate with the 100 kHz laser itself. While the source of the signal averaging problem in the 100 kHz system is unresolved, ultimately this does not detract from the results presented in this paper.

The SE-FSRS spectra presented herein were obtained at average powers as low as 1/40th of those used in previously published work, which used hundreds of μW of pump

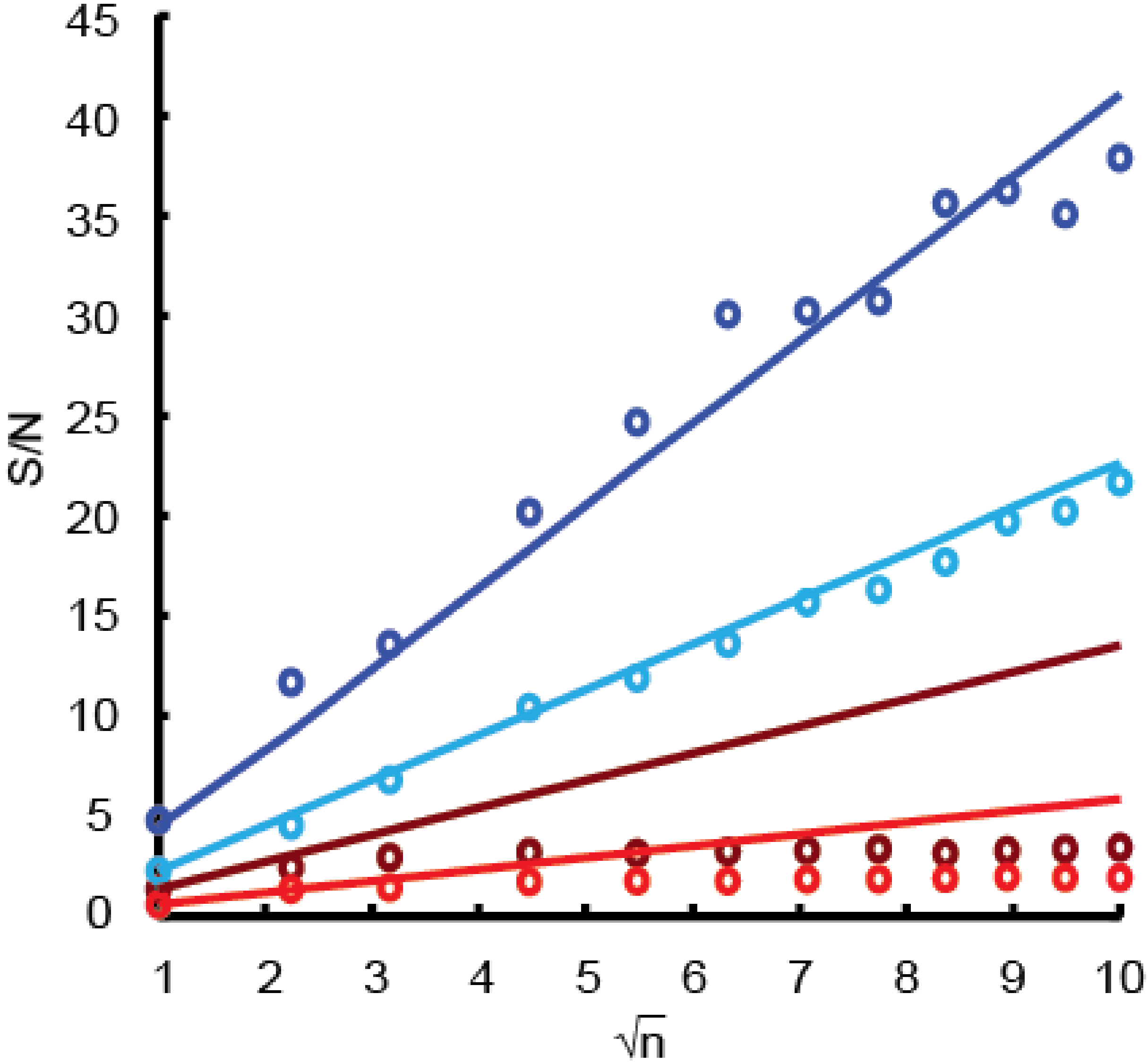

Figure 5.7. FSRS and SE-FSRS signal averaging at 1 MHz and 100 kHz. Plots of SNR (S/N) versus $\sqrt{n}$, where n is the number of scans being averaged. Data is shown for SE-FSRS of BPE nanoparticle assemblies obtained at 1 MHz (navy) and 100 kHz (maroon) and for FSRS of CHX obtained at 1 MHz (cyan) and 100 kHz (red). Experimental data are indicated with markers, while solid lines representing $\sqrt{n}$ scalings are added to guide the eye. Figure reproduced with permission from Ref. 99. Copyright 2016 American Chemical Society.

power on a 100 KHz system.[72] At these powers, half of the SE-FSRS signal was lost after 5 minutes of data collection; extended exposure to pulsed irradiation at high powers resulted in a decrease of the near-infrared extinction of the Au nanoparticle assemblies. These results suggested a destruction of the highly enhancing multi-core particles that contribute most strongly to the SE-FSRS signal. However, any structural changes to the nanoparticles were too small to be observed by TEM on the few nanometer length scale. To probe the extent of sample damage when using high average powers at either 100 kHz or 1 MHz, we measured SE-FSRS spectra for 30 minutes using 500 μW of Raman pump (corresponding to pulse energies of 5 nJ at 100 kHz or 500 pJ at 1 MHz). At this power, the signal at 100 kHz does not increase significantly over the signal obtained using 50 μW (Fig. 5.12);[72] only an 8% increase in signal strength is observed despite an order of magnitude difference in pump power. In contrast, 500 μW at 1 MHz still falls within the linear regime of the pump power dependence of SE-FSRS gain. As a result, the signal magnitudes are now comparable, despite an order of magnitude difference in pulse energies, and the spectra display improved SNR at 1 MHz due to increased averaging. In fact, at 500 μW the SNR ratio now exceeds 375 after 30 minutes of averaging. In Fig. 5.8, we show a time evolution of the SE-FSRS gain signal. The signal from the 100 kHz system decreases to less than half of its initial value over the course of 30 minutes, while the signal from the 1 MHz system remains constant. Thus, using a higher repetition rate laser system allows us to collect SE-FSRS at high enough pump powers to achieve optimal gain and SNR without any apparent damage to the samples. Furthermore, at these powers, less than a minute of averaging is sufficient to achieve a SNR of 41 (Fig. 5.13). Hence, the use of higher repetition rate systems reduces the amount of time necessary to collect

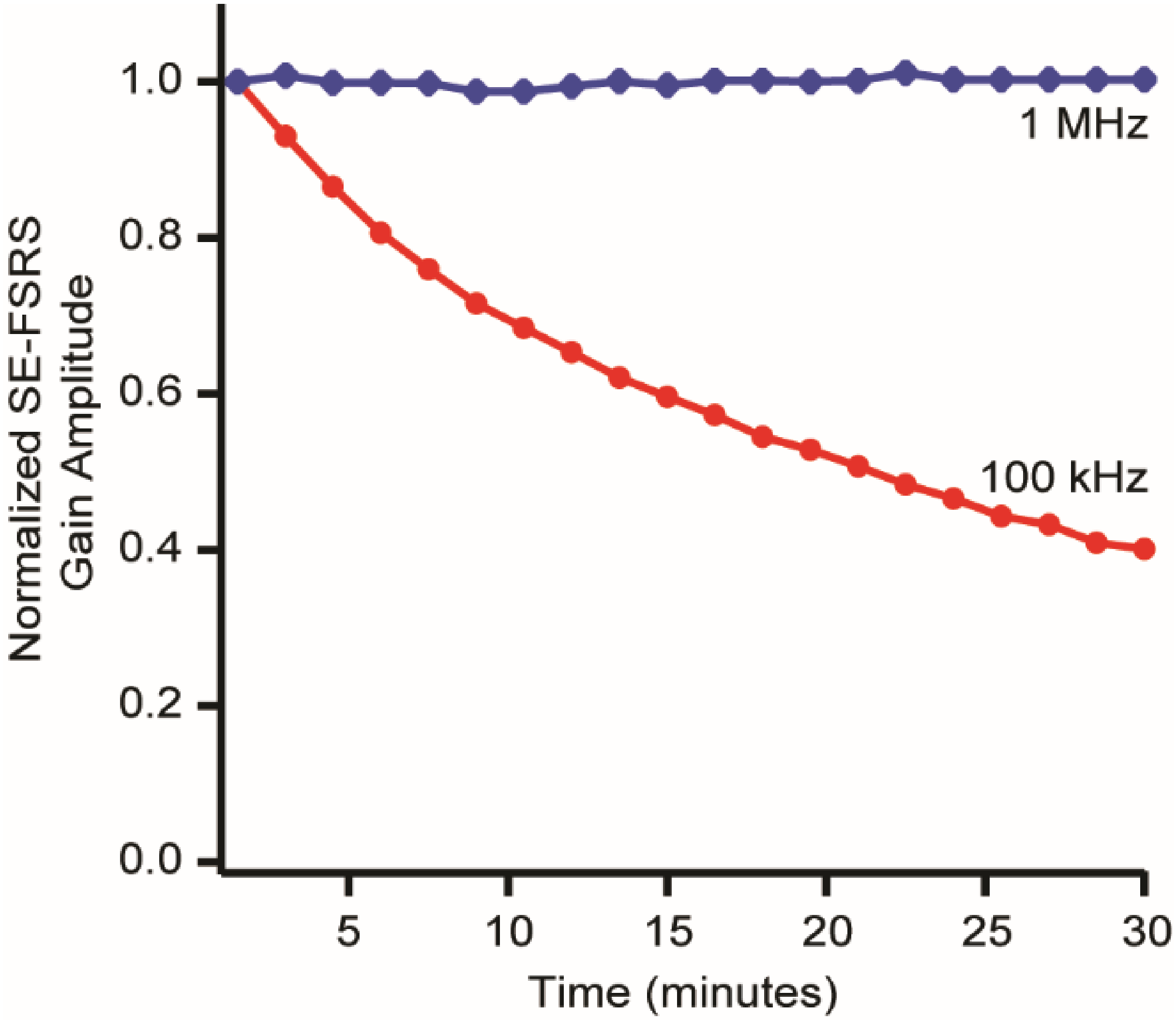

Figure 5.8. Monitoring sample degradation via signal decay in SE-FSRS experiments. While significant loss of SE-FSRS signal is observed on the minute timescale at 100 kHz (red), the signal obtained at 1 MHz (blue) remains constant throughout 30 minutes of data collection. SE-FSRS spectra were collected using 500 μW of pump (corresponding to pulse energies of 5 nJ at 100 kHz or 500 pJ at 1 MHz) and the gain amplitudes are shown for the 1200 cm^{-1} mode, normalized to the initial value for each experiment. The other BPE Raman modes decrease in amplitude at the same rate. Figure reproduced with permission from Ref. 99. Copyright 2016 American Chemical Society.

a well-averaged SE-FSRS spectrum, subsequently reducing the time necessary to collect TR-SE-FSRS data in future experiments.

5.3.5. Conclusion

In summary, we have successfully acquired the first SE-FSRS spectra obtained at 1 MHz repetition rates. We have shown that SE-FSRS, which requires low pulse energies to avoid sample degradation, is better implemented with high repetition rate laser systems. We can now obtain SE-FSRS spectra at 1 MHz with comparable gain as at 100 kHz and with improved SNR ratios. The ability to collect spectra at orders of magnitude lower powers than previous SE-FSRS experiments opens up new classes of plasmonic substrates for use. Up to this point, SE-FSRS measurements have only proved successful on silica-coated nanoparticles like those used in this report. While the silica coating mitigates sample degradation, it also limits the variety of samples that can be used. With the 1 MHz system, SE-FSRS can potentially be applied to a wide range of plasmonic systems, including uncoated colloids and 2D nanosphere lithographic substrates, which will be explored in future experiments. Ultimately, we wish to incorporate time-resolution and use SE-FSRS to study the dynamics of coupled molecule-plasmon systems. TR-FSRS studies generally require significant averaging at a multitude of time steps, which necessitates that samples cannot degrade over the length of the scan. While flowing samples have been used to circumvent sample degradation in non-enhanced FSRS experiments,[45] this approach requires a large amount of sample and is often impractical for use with plasmonic samples that are difficult or expensive to prepare in bulk. At 1 MHz, well-averaged SE-FSRS spectra can be obtained at powers that do not cause damage over the course of 30 minutes, which is sufficient time to conduct a time-dependent study based on analogous FSRS measurements. This represents a significant step towards using SE-FSRS in studies of chemical dynamics. The improved SNR ratio at 1 MHz will further facilitate such efforts as the lower noise floor requires less averaging for small transient signals to be resolved. As a result of the improvements to SE-FSRS developed in this report, we believe that SE-FSRS is poised to become a powerful tool for studying the dynamics of coupled molecule-plasmon systems.

5.3.6. Supplementary Information

1 MHz laser system. The laser system is based on a one-box diode-pumped Yb-doped fiber oscillator/amplifier system (Clark-MXR Impulse). The fundamental output (1 MHz, 1.034 μm, 250 fs, 11 μJ/pulse) is directed into a noncollinear optical parametric amplifier (Clark-MXR iNOPA) where it is split into two beams. Approximately 12% of the fundamental beam is focused into an yttrium aluminum garnet (YAG) plate to generate a broadband white light continuum (WLC) while the other 88% is focused into a type I β-barium borate (BBO) crystal to generate 2.5 W of 532 nm via second harmonic generation (SHG). Half of the WLC is mixed noncollinearly with the SHG in a type I BBO to generate broadband 795 nm light. The 795 nm light is sent through a prism compressor, then directed into a home-built 4f spectral grating filter to narrow the spectral bandwidth and create the Raman pump (795 nm, 1 ps, 3.5 nJ/pulse). The other half of the WLC, after being filtered through an 825 nm longpass filter (86-070, Edmund Optics) and a 950 nm shortpass filter (86-688, Edmund Optics), is sent through a prism compressor to generate the stimulating probe field (825-950 nm, ~30 fs, 2.7 nJ/pulse). A colored glass filter (FGS900, Thorlabs) was placed in the probe path to flatten the probe spectrum (Fig. 5.11), yielding a maximum power of 3 pJ/pulse at the sample. Telescopes with a 50 μm pinhole at the focus are used on both beams to spatially filter the beams and control the focal spot sizes at the sample. The pump and probe beams are focused collinearly onto the samples with a 10 cm focal length lens. The probe beam is recollimated and the Raman pump is removed with an 808 nm stopline filters (NF03-808E-25, Chroma) and an 810 longpass filter (ET810lp, Chroma).

100 kHz laser system. Most of the laser system has been described previously,[72] but modifications were made for this study. As before, an 18 W, 532 nm laser (Coherent Verdi V18) pumps both a Ti:sapph oscillator (Coherent Micra, 80 MHz, 400 mW, 800 nm, 30 fs) and a regenerative amplifier (Coherent RegA 9050, 100 kHz, 1 W, 800 nm, 50 fs). The amplifier is seeded by pulses from the oscillator. The amplifier output is split into two equal parts. One part is directed through two narrow bandpass filters (CVI Laser, F1.5-794.7), generating the Raman pump (795 nm, 1ps, 40 nJ/pulse). 25% of the remaining amplifier output is focused onto a sapphire plate to generate a broadband continuum. 25% of the recollimated continuum is sent through a colored glass filter (RG830, Schott Glass, Thorlabs) and fused silica prisms to generate the stimulating probe field (830-1000 nm, 30 fs, 100 pJ/pulse).

For this study, telescopes with a 50 μm pinhole at the focus are used on both beams to spatially filter the beams and control the focal spot sizes at the sample. The pump and probe beams are focused collinearly onto the samples with a 10 cm focal length lens. The higher energy pulses on this system often create a cross-phase modulation (XPM) that distorts the measured spectra; the effects were minimized by modulating the pump pulse time delay with low frequency vibrations. The beam diameters at the sample are adjusted to be $\sim$55 μm. The probe beam is recollimated and the Raman pump is removed with a series of RG830 and RG1000 filters (Schott Glass, Thorlabs).

Data collection. On each system, the probe and phase-matched (SE-)FSRS signal are sent through a spectrograph (Princeton Instruments Acton SP2300) and focused onto a CCD camera (Princeton Instruments PIXIS 400BR) for self-heterodyned detection. Pump-on and pump-off spectra are collected by chopping the Raman pump at 250 Hz. Thus, 400 laser pulses are accumulated for each readout on the 100 kHz system while 4000 laser pulses are accumulated on the 1 MHz system. Subsequent pump-on and pump-off spectra are divided to provide the background-free stimulated Raman gain spectrum. Individual data sets were acquired for approximately 0.3 minutes and 30 minute scans were used to produce averaged spectra.

SE-FSRS samples. All SE-FSRS experiments were performed on commercially-available nanoparticle assemblies (STA Technologies) consisting of one or more gold cores with a diameter of approximately 90 nm, a sub-monolayer coverage of *trans*-1,2-bis(4-pyridyl)-ethylene (BPE) molecules, and an approximately 60 nm silica shell (Fig. 5.10). SE-FSRS samples were prepared by suspending the nanoparticle assemblies in water and placed in a cuvette with a path length of 2 mm. The optical density of the samples was ∼3.1 at 600 nm, as determined by extinction spectroscopy. The sample was stirred constantly during data acquisition using a magnetic stir bar.

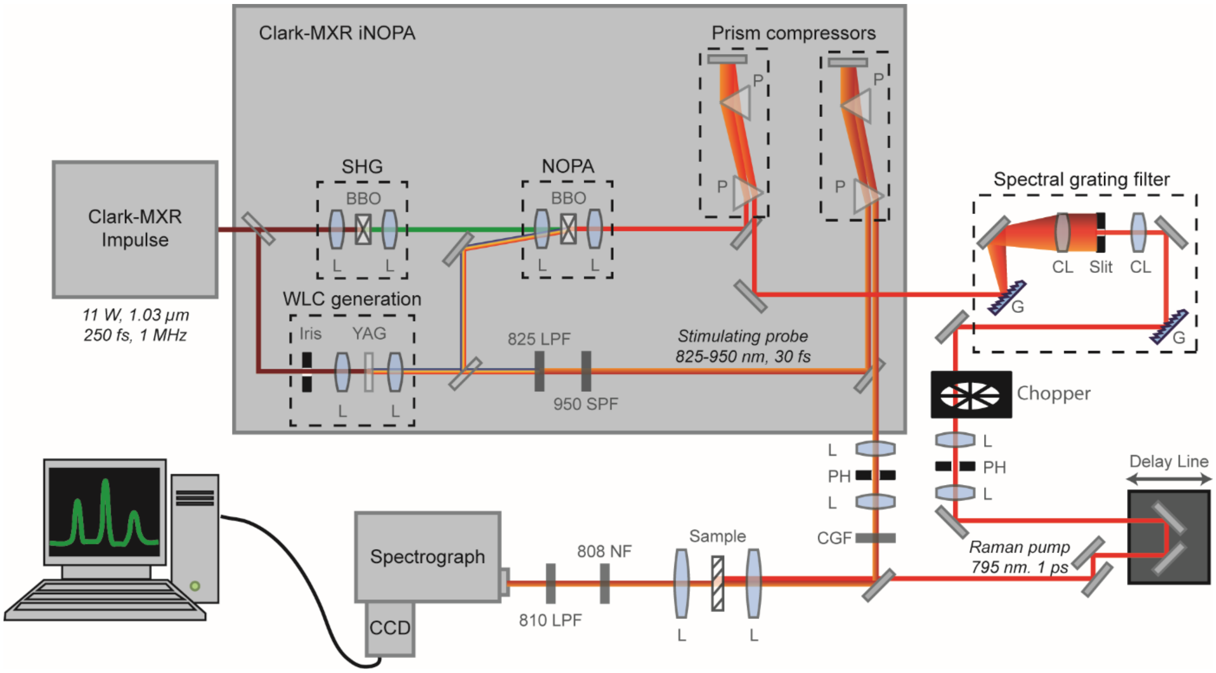

Figure 5.9. Schematic of the 1 MHz laser system. Abbreviations: second harmonic generation (SHG), β-barium borate crystal (BBO), lens (L), white light continuum (WLC), yttrium aluminum garnet (YAG), long pass filter (LPF), short pass filter (SPF), prism (P), grating (G), cylindrical lens (CL), pinhole (PH), colored glass filter (CGF), notch filter (NF). Figure reproduced with permission from Ref. 99. Copyright 2016 American Chemical Society.

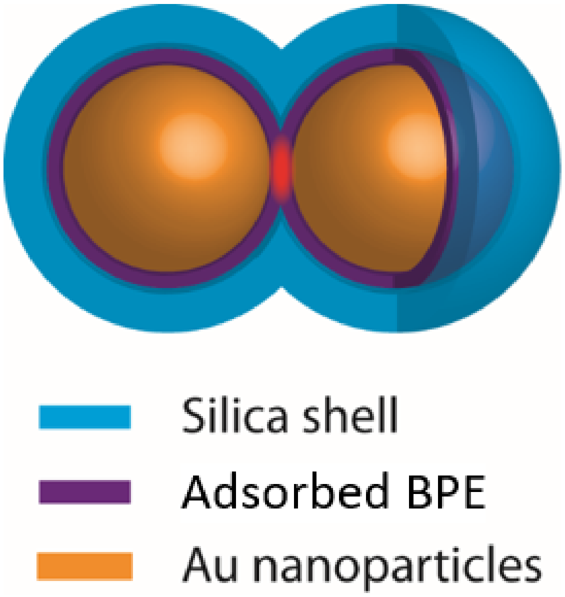

Figure 5.10. Schematic depiction of nanoparticle assemblies. The nanoparticle assemblies consist of gold nanoparticles with an average diameter of 95 nm and a broad (roughly 12%) distribution of individual particles sizes. The gold particles are aggregated with *trans*-1,2-bis(4-pyridyl)-ethylene (BPE) and overcoated with an approximately 63 nm shell. These samples have been characterized previously to contain a range of aggregate sizes ranging for single cores to dimer, trimers, and larger aggregates.[171] Figure reproduced with permission from Ref. 99. Copyright 2016 American Chemical Society.

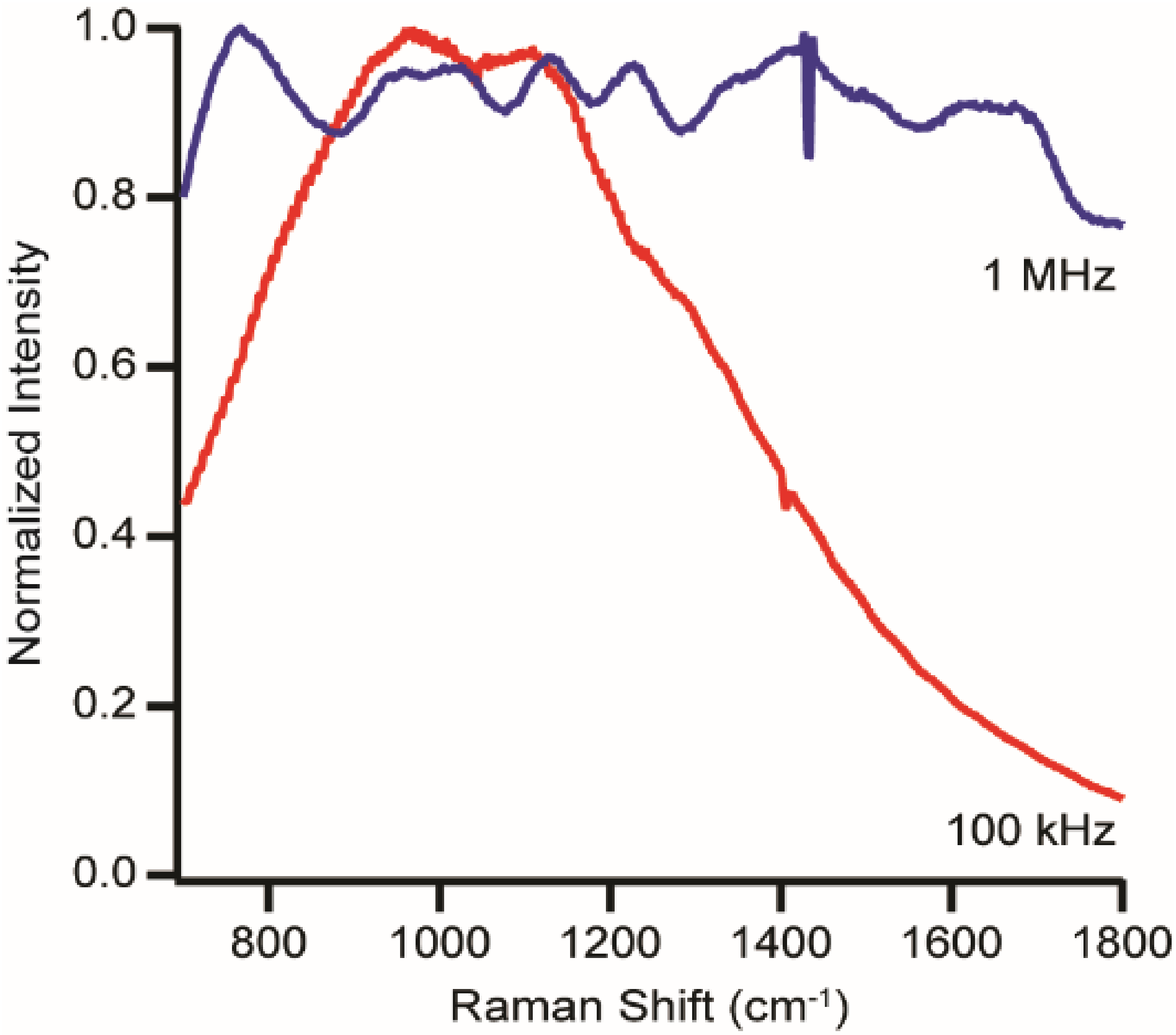

Figure 5.11. Comparison of probe spectra between systems. The 1 MHz system has a flatter probe spectrum with almost constant intensity across the entire spectral window. The 100 kHz system has a peaked probe spectrum, with the highest intensity at wavelengths correlating to Raman shifts of 1000-1200 cm^{-1}. The flatness of the 1 MHz probe spectrum suggests that the pulse is not transform limited. While this does not affect the current study, the chirp will decrease the temporal resolution that can be obtained in future time-resolved SE-FSRS studies. Figure reproduced with permission from Ref. 99. Copyright 2016 American Chemical Society.

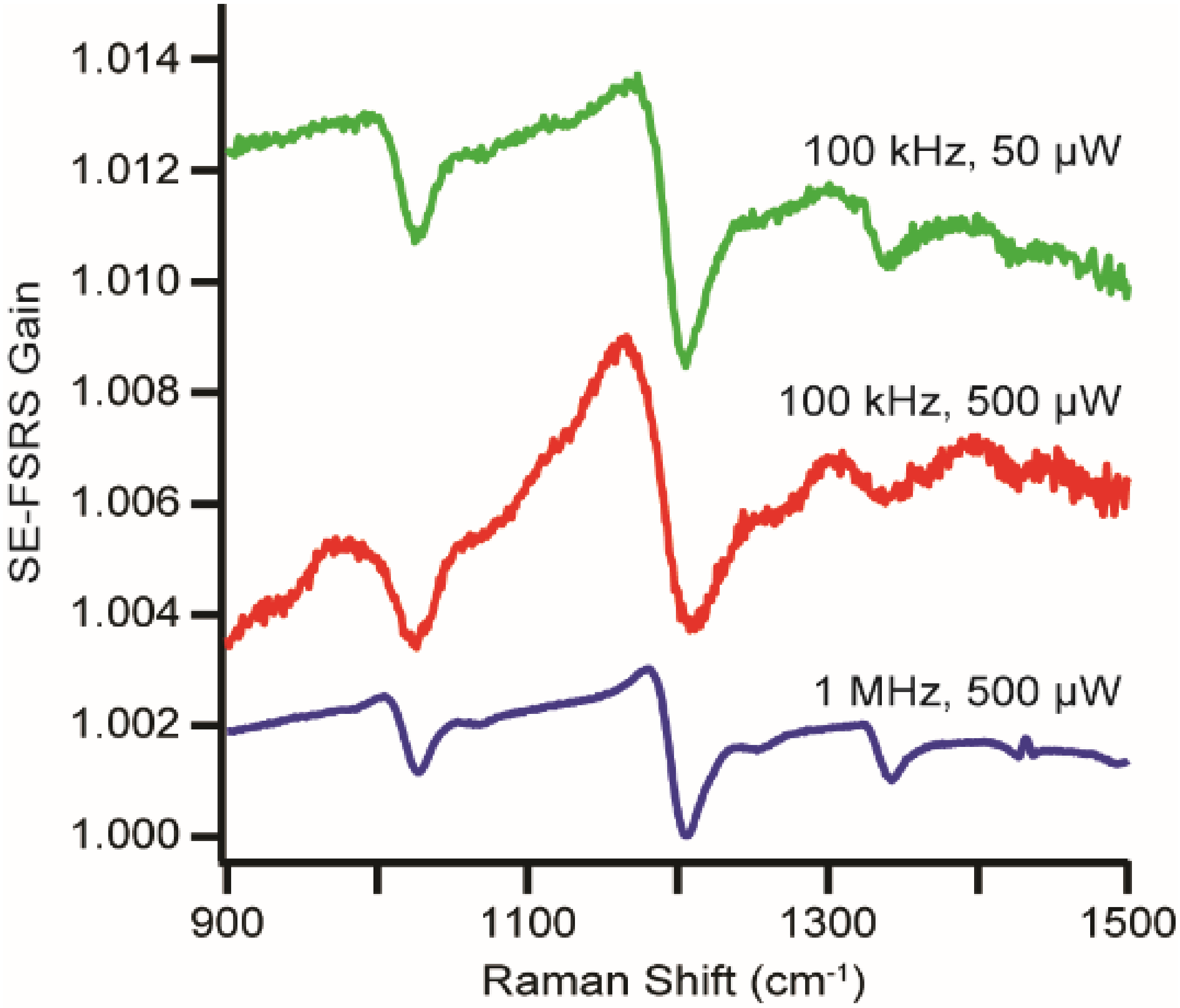

Figure 5.12. SE-FSRS spectra of BPE nanoparticle assemblies collected at high average pump powers. At 100 kHz, the SE-FSRS gain saturates at high pump powers, leading to sublinear dependence of signal on the pump power. The SE-FSRS spectrum collected at 500 μW of pump power exhibits only an 8% increase in signal over the spectrum collected at 50 μW. At 1 MHz, the signal has yet to saturate at 500 μW of pump and is comparable in strength to the 100 kHz system at equal pump powers, with 10x greater SNR. Figure reproduced with permission from Ref. 99. Copyright 2016 American Chemical Society.

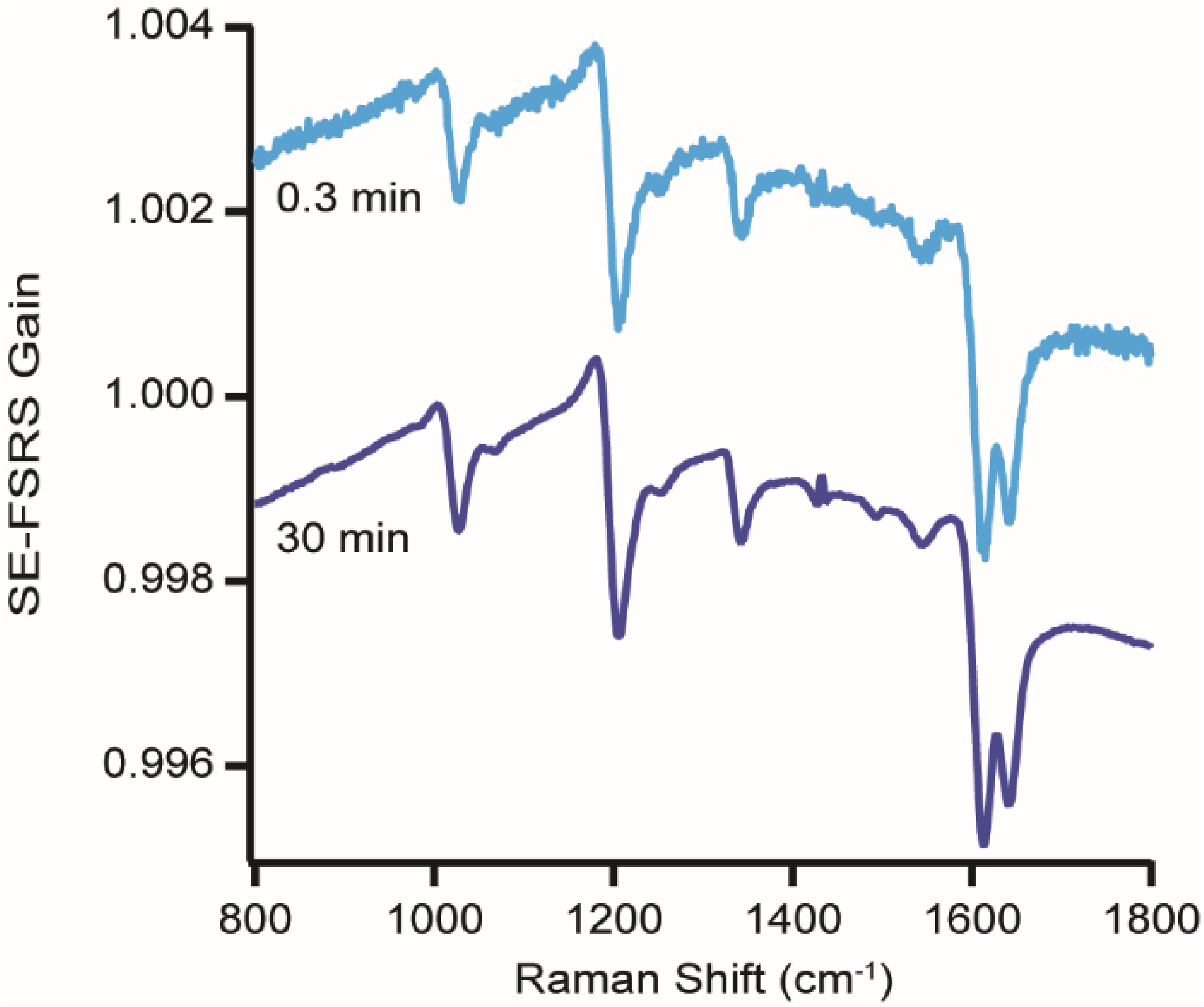

Figure 5.13. High SNR spectra obtainable with short acquisition times. On the 1 MHz system, less than a minute of averaging is required to obtain high SNR SE-FSRS spectra. The SNR at 1200 cm^{-1} is 41 after only 0.3 minutes of averaging (cyan), while it exceeds 375 after 30 minutes of averaging (navy). The quality of the spectra obtainable in such a short time will facilitate the acquisition of time-resolved SE-FSRS data. Figure reproduced with permission from Ref. 99. Copyright 2016 American Chemical Society.

5.4. Studying stimulated Raman gain and loss by wavelength-sampled excitation in surface-enhanced femtosecond stimulated Raman spectroscopy

5.4.1. Abstract

We present the first wavelength-scanned surface-enhanced femtosecond stimulated Raman spectroscopy (SE-FSRS) study, as well as the first observation of anti-Stokes vibrational features in SE-FSRS spectra.[†] We compare stimulated Raman loss (anti-Stokes) and stimulated Raman gain (Stokes) signals at three pump wavelengths chosen to sample different portions of nanoparticle aggregate localized surface plasmon resonances (LSPRs). The SE-FSRS signals exhibit similar signal magnitudes in the SRL or SRG regions of the spectra regardless of Raman pump or probe wavelength. The spectral lineshapes, however, differ dramatically with excitation wavelengths. The observed trends in spectral lineshape show a strong dependence on the relative position of the excitation fields with respect to the plasmon resonance, but do not match predictions from any existing SE-FSRS theory. These results suggest the need for further theoretical efforts with complementary experimental studies of individual aggregates in order to remove the effects of inherent ensemble averaging.

5.4.2. Introduction

Studying the fundamental structural dynamics of bond breakage and formation requires techniques that can characterize deformities of molecular equilibrium structures in time scales corresponding to collective nuclear motion. To investigate the dynamics of bond-breakage and formation, vibrational spectroscopy is ideal as it can directly detect changes

---

[†] This section was reproduced with permission from Ref. 100. Copyright 2017 American Chemical Society.

in molecular structure based on changes in the vibrational spectrum.[30] Characterizing vibrational motion near the limit of the vibrational period can be easily performed using a variety of coherent Raman scattering (CRS) techniques.[26,32] In particular, femtosecond stimulated Raman scattering (FSRS) is a technique that can acquire vibrational spectra across a large frequency window, with simultaneous high temporal (10-100 fs) and spectral (5-20 cm^{-1}) resolutions.[34,37,40]

FSRS is a versatile technique that has been utilized as stimulated Raman gain (SRG),[37] stimulated Raman loss (SRL),[144] with molecular resonance (FSRRS),[144] and with surface-enhancement (SE-FSRS).[72,98,99] When performed off resonance with the analyte molecule, FSRS has the benefit of lineshapes that are directly comparable to spontaneous Raman scattering,[126] a considerable advantage compared to coherent anti-Stokes Raman scattering (CARS) where interference between non-resonant and resonant vibrational terms in the optical susceptibilities lead to dispersive lineshapes and broad backgrounds.[26,67] When performed on resonance, FSRS exhibits dispersive lineshapes that vary as the pump wavelength is scanned through the molecular electronic absorption band.[144] The dispersive signals are attributed to the interference of hot luminescence (HL) and resonance Raman scattering (RRS) pathways upon generating an excited state population. However, even when SE-FSRS is performed far from molecular resonance, dispersive lineshapes are observed.[72,98,99] SE-FSRS lineshapes are strongly dependent on the location of the excitation pulses with respect to the plasmon resonance, as observed in a previous two-point plasmon resonance comparison.[98] In that study, the dispersive lineshapes were attributed to Fano-like coupling between narrowband vibrational coherences and the broadband plasmon resonance. The behavior seen in Frontiera *et al.* was independently reproduced theoretically by two research groups using either a purely quantum mechanical time domain approach, which supports the hypothesis of purely Fano-like coupling as described above,[111] and semiclassical mixed frequency-time domain approach, which proposes that the lineshapes result from the combination of two Fano-like contributions arising from the interference between both the real and imaginary components of the Raman susceptibility and the plasmon resonance.[110]

Our current study examines three points of interest: (1) observe for the first time SRL in SE-FSRS experiments; (2) understand differences in SE-FSRS probe enhancement by comparing signal magnitudes of SRG to SRL; (3) investigate the wavelength dependence of SE-FSRS lineshapes by Raman pump-tuned SRG and SRL experiments. By exploring the three points, we will demonstrate the versatility of plasmonic enhancement in SE-FSRS as applied to a variety of experimental conditions. Moreover, this study will contribute to further understanding of the plasmonic enhancement in SE-FSRS as we can compare experimental results to recent SE-FSRS theoretical predictions.[110,111]

5.4.3. Experimental

Two different molecule-plasmonic nanoparticle assemblies are used in this study: 90 nm Au cores aggregated with 1,2-*trans*-bispyridylethylene (BPE) and 60 nm Au cores aggregated with 4,4'-bipyridine (BPY). The aggregated cores are overcoated with silica (Fig. 5.17). The 90 nm BPE nanoparticle assemblies (BPE90) have been used in several previous SE-FSRS studies[72,98,99] and have been characterized to consist of both monomers and aggregates - including dimers, trimers, and larger clusters.[171] The 60 nm BPY nanoparticle assemblies (BPY60) are analogous to the 60 nm BPE assemblies used in Frontiera

Sample	Signal Type	$\lambda_{pu} = 750nm$	$\lambda_{pu} = 795nm$	$\lambda_{pu} = 840nm$
BPE90	SRG	$\lambda_{pu}, \lambda_{pr} < \lambda_{LSPR}$	$\lambda_{pu}, \lambda_{pr} < \lambda_{LSPR}$	$\lambda_{pu} < \lambda_{LSPR}, \lambda_{pr} \sim \lambda_{LSPR}$
	SRL	$\lambda_{pu}, \lambda_{pr} < \lambda_{LSPR}$	$\lambda_{pu}, \lambda_{pr} < \lambda_{LSPR}$	$\lambda_{pu}, \lambda_{pr} < \lambda_{LSPR}$
BPY60	SRG	$\lambda_{pu}, \lambda_{pr} < \lambda_{LSPR}$	$\lambda_{pu}, \lambda_{pr} < \lambda_{LSPR}$	$\lambda_{pu} < \lambda_{LSPR}, \lambda_{pr} \sim \lambda_{LSPR}$
	SRL	$\lambda_{pu}, \lambda_{pr} < \lambda_{LSPR}$	$\lambda_{pu}, \lambda_{pr} < \lambda_{LSPR}$	$\lambda_{pu}, \lambda_{pr} < \lambda_{LSPR}$

Table 5.1. Summary of experimental conditions for wavelength-sampled SE-FSRS.

et al. except for the difference in reporter molecule;[98] they consist of a similar range of aggregate sizes but with a relatively higher proportion of monomers, although the exact composition was not quantified. Extinction spectra of BPE90 exhibit an aggregate localized surface plasmon resonance (LSPR) near 1000 nm (Fig. 5.15, top), while the aggregate LSPR of BPY60 occurs near 850 nm (Fig. 5.16, top). BPE90 and BPY60 are investigated by SE-FSRS with three distinct Raman pump wavelengths (Pu)750 nm, 795 nm, and 840 nmand the corresponding SRG and SRL signals are obtained using Raman probe fields (Pr) with spectral width sufficient to stimulate vibrational modes from 700 1900 and 700 1900 relative cm^{-1}, respectively. Multiple pump wavelengths were chosen to sample different portions of the aggregate LSPR with SE-FSRS, such that different plasmonic responses to either the pump or probe fields could be interrogated. These conditions include positioning both excitation fields on the rising edge of the aggregate LSPR, both on the falling edge, one on either side, and even both fields far off resonance of the aggregate LSPR. The specific conditions probed are summarized in the Table 5.1 and illustrated schematically in the top portions of Figs. 5.15 and 5.16.

SE-FSRS spectra are collected using a 1 MHz repetition rate system that has been described previously.[99] Briefly, the system consists of a noncollinear optical parametric amplifier (Clark-MXR iNOPA) pumped by a Yb-doped fiber oscillator/amplifier (Clark-MXR Impulse) Fig. 5.18. The NOPA output is sent through a spectral grating filter to narrow the spectral bandwidth and generate the picosecond Raman pump. Residual white light from within the NOPA is filtered using a pair of edge-pass filters to generate the broadband Raman probe. For this study, the wavelength of the pump beam was adjusted by tuning the NOPA and spectral grating filter accordingly, while the probe wavelength range was adjusted by exchanging the edge-pass filters. All SE-FSRS experiments were performed with 320 μW of average pump power (320 pJ pulse energies) and enough probe to reach 50k counts on the charge-coupled device (CCD) camera. The probe power was not rigidly controlled because Raman gain is invariant with probe intensity[40] and maintaining equal dynamic range filling of the camera prevents the SNR variations between data sets. The pump beam is mechanically chopped to collect alternating pump-on and pump-off spectra. As discussed by McAnally *et al.*,[110] the first published SE-FSRS spectra[72,98] were incorrectly phased due to an issue with the chopper; this issue has been corrected and the SE-FSRS spectra presented here are plotted properly as pump-on divided by pump-off. Further experimental details are given in the Supporting Information.

5.4.4. Results

We start by comparing the Stokes and anti-Stokes signals of non-plasmonically enhanced FSRS. Other studies have demonstrated that the anti-Stokes side of the FSRS spectrum is dominated by negative SRL features that are equal in both magnitude and linewidth to the positive SRG features that appear on the Stokes side of the FSRS spectrum.[144,172,173] This serves as a stark contrast with spontaneous Raman experiments, in which the anti-Stokes signals are generally orders of magnitude weaker than the Stokes signals. A theoretical description of FSRS attributes the SRL features to a different set of four-wave mixing processes than those that generate SRG features,[129] a result that explains their equal magnitudes but opposite signs. Our 1 MHz laser system produces lower energy pulses than the 1 kHz systems typically used for FSRS; while this is beneficial for SE-FSRS studies as it mitigates sample degradation,[99] it limits the molecules that we can study without plasmonic enhancement. Thus, we chose to use neat cyclohexane in our comparison of SRG and SRL for non-plasmonically enhanced FSRS as it is a much stronger Raman scatterer than saturated aqueous solutions of either BPE or BPY, the analytes used in our SE-FSRS studies. Fig. 5.14 shows the SRG (red) and SRL (blue) responses of cyclohexane pumped at 795 nm. The spectra were collected using 1.1 mW (1.1 μJ) of Raman pump and are plotted as a function of the absolute value of the Raman shift to show them both on the same scale and facilitate comparison between spectral features. The SRG and SRL responses agree with results from the literature with regards to signal magnitude and sign. This comparison was used at every Raman pump wavelength to ensure that SE-FSRS magnitudes could be compared accurately such that changes in SE-FSRS magnitudes and signs can be assigned to plasmonic influences (Fig. 5.14).

Next, we examine the Stokes and anti-Stokes SE-FSRS signals of BPE90 (Fig. 5.15) pumped at three different wavelengths. When the Raman pump is tuned to 750 nm, it is far off resonance with the aggregate LSPR of BPE90 (Fig. 5.15A, top). As with unenhanced FSRS, the signal magnitudes (Fig. 5.15A, bottom) are nearly identical between SRG (red) and SRL (blue). Precise determination of the signal magnitudes is hampered by the varying dispersivities of the lineshapes. While a previous SE-FSRS study of BPE90

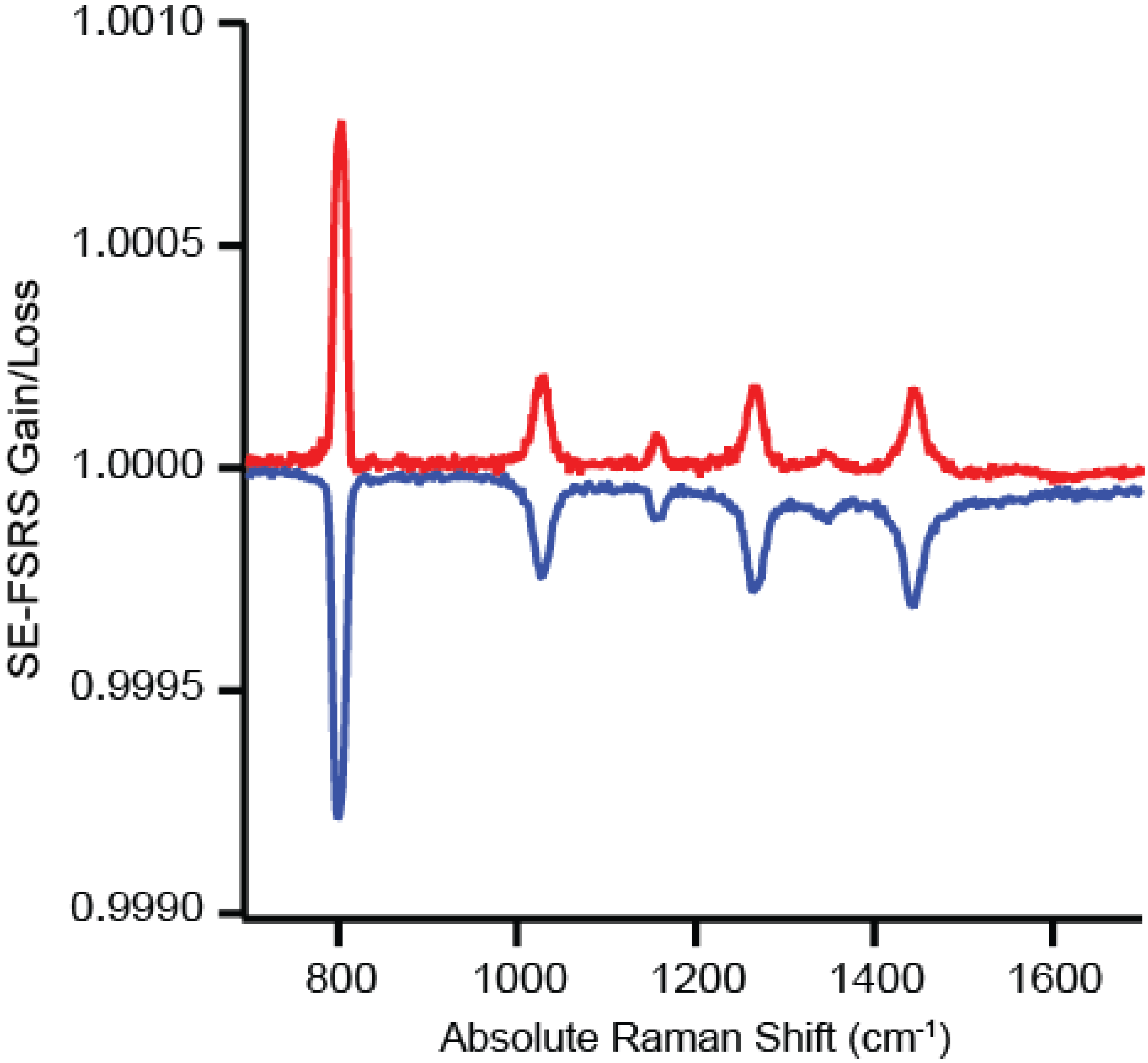

Figure 5.14. FSRS spectra of cyclohexane. The SRG (red) and SRL (blue) spectra, plotted as a function of absolute Raman shift, show signals with equal magnitudes but opposite signs. Figure reproduced with permission from Ref. 100. Copyright 2017 American Chemical Society.

fit the spectral features to Fano lineshapes,[98] the fits are entirely empirical; the linewidth and line asymmetry parameters cannot be uncoupled and the interplay between them additionally affects the fit intensities, leading to multiple solutions when fitting complex spectra with overlapping lineshapes. The lack of a unique fit precludes a more rigorous quantitative comparison of intensity and dispersiveness between spectra in which the lineshapes differ considerably, such as those shown here. The SRG shows highly dispersive lineshapes across all modes, while the SRL has less dispersive lineshapes. It is important to note that, unlike the FSRS spectra of cyclohexane in which 'loss' features are strictly negative and 'gain' features are strictly positive, the dispersivity of the SE-FSRS lineshapes can obscure the interpretation of spectral features as originating from SRL versus SRG without prior knowledge of the excitation conditions. For example, within the Fano lineshape equation, the asymmetry parameter, q, describes the coupling between the narrow vibrational mode and the broad plasmon resonance; the phase of the measured signals depend both on the sign of the molecular signal and the sign of the coupling parameter.[72] If a positive amplitude 'gain' feature and a negative amplitude 'loss' feature experience couplings of equal magnitude but opposite sign, the phases of the resulting spectral features will be the same.

Fig. 5.15B shows the SRG and SRL responses (bottom) of BPE90 to a 795 nm pump, which is closer in wavelength to the aggregate maximum LSPR but still off-resonant (top). Again, the SRG and SRL signals are nearly identical in intensity but display differing dispersivities. The SRL and SRG signals are both highly dispersive, but the SRG lineshapes exhibit a strong frequency-dependent dispersive character between modes. The pair of modes around 1600 cm^{-1} are significantly less dispersive than the modes between 1000 1400 cm^{-1}. Finally, Fig. 5.15C shows the SRG and SRL responses of BPE90 to an 840 nm pump. While still off-resonant with the aggregate LSPR of BPE90, the pump is closer to the resonance than in either of the two prior pump wavelengths. As in the

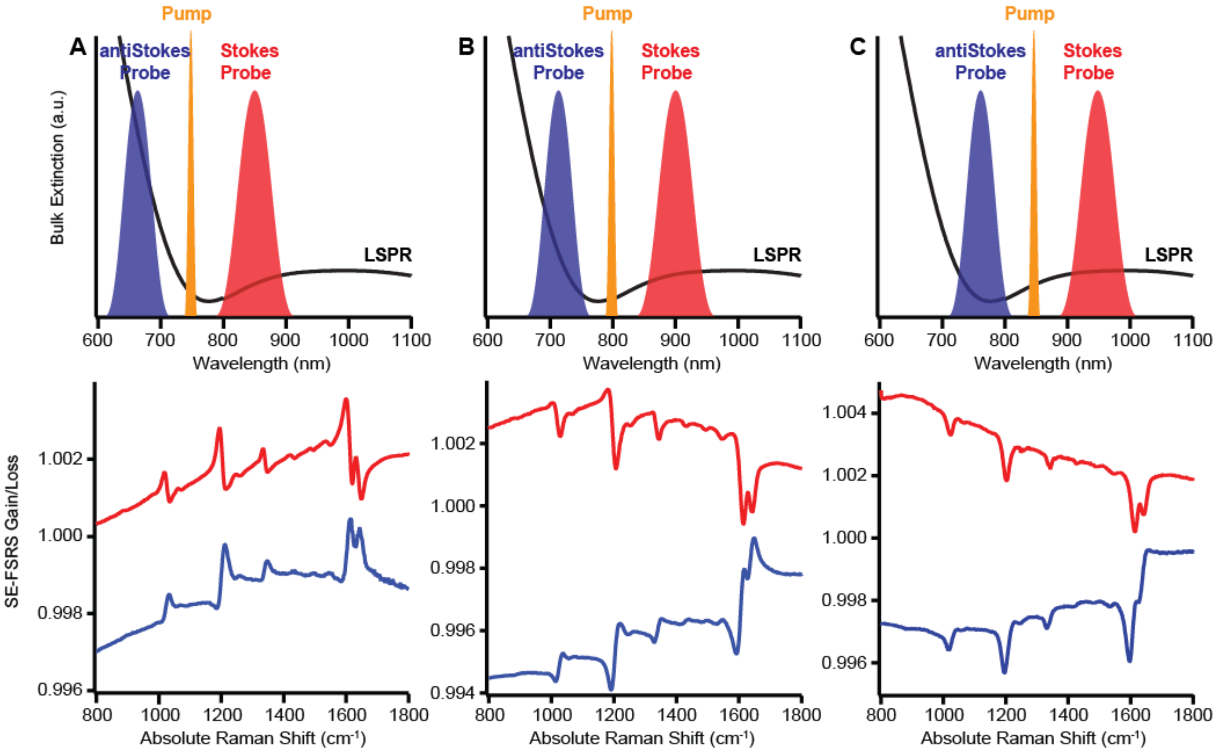

Figure 5.15. SE-FSRS spectra of BPE90 pumped at three wavelengths. Extinction spectra with schematic pump and probe pulses (top) and SE-FSRS spectra (bottom) for BPE90 pumped at 750 nm (A), 800 nm (B), and 840 nm (C). The spectra are plotted as a function of absolute Raman shift, with SRL shown in blue and SRG shown in red. Figure reproduced with permission from Ref. 100. Copyright 2017 American Chemical Society.

previous data sets, the signal magnitudes remain approximately equal between SRG and SRL, while the dispersivities of the lineshapes differ.

To confirm that the trends in signal magnitude and lineshape are not unique to BPE90, we obtained SE-FSRS spectra of BPY60 for the same set of excitation conditions (Fig. 5.16). For each pump wavelength, the SRL and SRG signal magnitudes are nearly identical. The lack of any noticeable difference in intensity is particularly interesting in the case of pumping at 750 nm (Fig. 5.16A), as the probe is resonant with the aggregate LSPR in the SRG experiment but far off resonance in the SRL experiment. Additionally, the

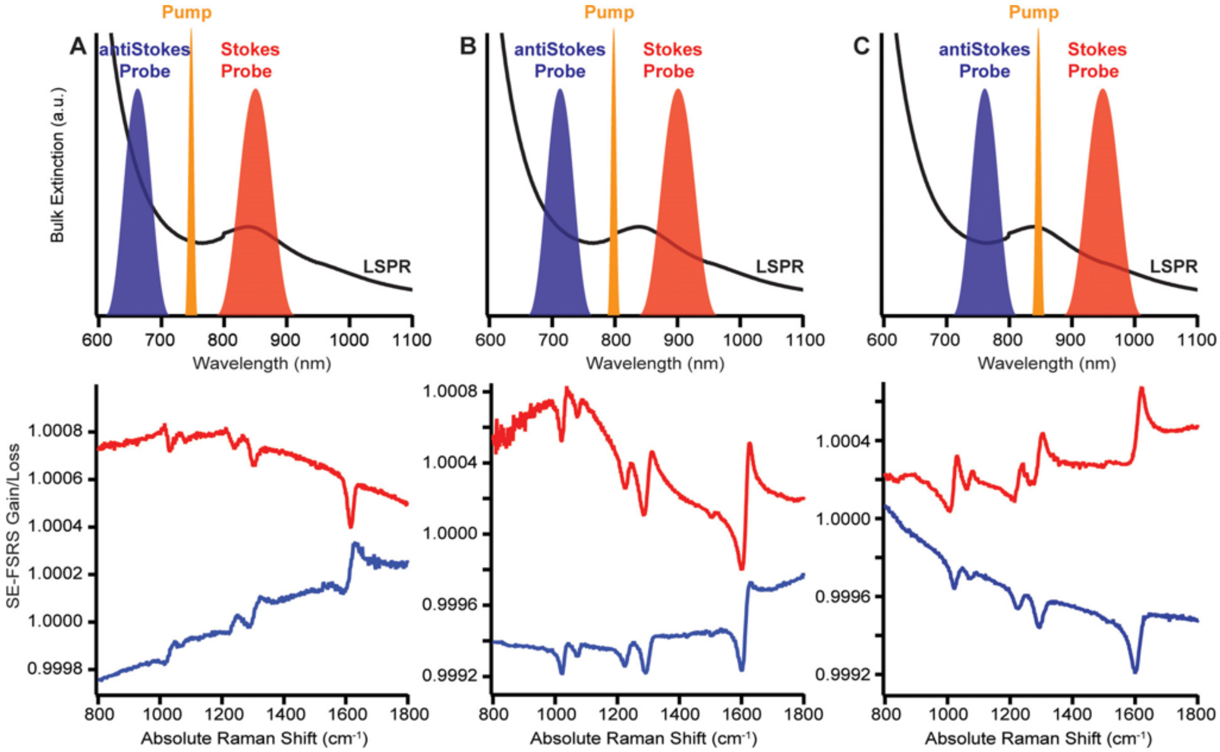

Figure 5.16. SE-FSRS spectra of BPY60 pumped at three wavelengths. Extinction spectra with schematic pump and probe pulses (top) and SE-FSRS spectra (bottom) for BPY60 pumped at 750 nm (A), 800 nm (B), and 840 nm (C). The spectra are plotted as a function of absolute Raman shift, with SRL shown in blue and SRG shown in red. Figure reproduced with permission from Ref. 100. Copyright 2017 American Chemical Society.

SRG exhibits almost no dispersive character while the SRL lineshapes are dispersive. In contrast, when pumped at 800 nm (Fig. 5.16B) the spectral features are more dispersive for SRG than for SRL. Both the SRG and SRL responses appear to become less dispersive when the pump wavelength is further increased to 840 nm (Fig. 5.16C).

Comparing the SE-FSRS spectra collected at all three pump wavelengths, we observe that for BPE90, which has an aggregate LSPR near 1000 nm, both SRG and SRL lineshapes become less dispersive as the wavelength of the Raman pump increases from 750 nm to 840 nm (Fig. 5.15). This is a surprising result as McAnally *et al.* predicts more dispersive lineshapes when the excitation field is closer to the plasmon resonance.[110] Likewise, we see that for SE-FSRS of BPE60, which has an aggregate LSPR near 850 nm, the lineshapes are less dispersive when pumped at 840 nm (Fig. 5.16C) compared to pumping at 795 nm (Fig. 5.16B). As the Stokes probe in the 840 nm pump experiment is 910-1025 nm, this challenges the prediction by Mandal *et al.* that lineshapes should become more dispersive as excitation fields become redder than the plasmon resonance.[111] Instead, we observe a new trend in the lineshapes that has not been suggested by theory. SE-FSRS lineshapes generally appear less dispersive when the probe field occurs a 'flat' region of the LSPR. For this trend to hold, we must also take into account the presence of a monomer LSPR at shorter wavelengths. Thus, the least dispersive lineshapes are observed when the probe field falls within either the maximum of the aggregate LSPR or the dip between the monomer LSPR, while more dispersive lineshapes are observed when the probe field falls on the rising or falling edge of either the monomer or aggregate LSPR. The dependence of the SE-FSRS lineshape on the LSPR slope can even be observed within a single spectrum, such as in the SRG response of BPE90 when pumped at 795 nm (Fig. 5.15B). As mentioned previously, the pair of modes at 1600 cm^{-1} are noticeably less dispersive than the lower energy modes. When we look at how the probe spectrum overlaps the LSPR, we can see that the redder probe wavelengths are nearly on resonance with the aggregate LSPR; these are the wavelengths that correspond to the 1600 cm^{-1} modes.

5.4.5. Conclusion

In summary, we have observed SRL in SE-FSRS experiments for the first time, a step that will allow us to explore the effects of molecular and plasmonic resonances on SE-FSRS signals and determine experimental limitations. By probing molecular resonances at different positions along the aggregate LSPR, these studies can help us understand how the mechanism of plasmonic enhancement in coherent Raman scattering differs from that in spontaneous Raman scattering. While surface enhanced Raman scattering (SERS) experiments see a simple local field enhancement (LFE) of the incoming excitation and incoherently scattered fields, coherent Raman signals exhibit an additional strong dependence on the coherently-driven molecular polarization that interacts with the plasmon resonance.

By examining the SRL and SRG responses for the BPE90 and BPY60 substrates at different pump wavelengths, we can conclude that the dependence of SE-FSRS signal magnitudes on excitation wavelength is either weak or complex. We see nearly identical signal intensities between SRL and SRG for a given pump wavelength, and only small differences in signal intensity between spectra obtained at different pump wavelengths. The weak dependence of plasmonic enhancement on excitation wavelength has also been observed in SERS experiments.[174] While the SE-FSRS lineshapes have a strong dependence on the relative position of the excitation wavelengths with respect to the LSPR, this dependence did not match predictions based on any current SE-FSRS theory. This suggests that current theories are incomplete as demonstrated by the incorrectly predicted amounts of dispersive character either near an LSPR[110] or at wavelengths redder than an LSPR.[111]

Thus, further theoretical efforts are needed and should be aided by the collection of additional experimental data over wider ranges of excitation wavelengths. Both theoretical models were applied to single aggregates;[110,111] the presence of dispersive peaks in the both sets of calculated SE-FSRS spectra suggest that the complex lineshapes observed experimentally are not simply an artifact of the ensemble measurement. However, to better correlate with theoretical results, experimental studies of individual aggregates should be made in order to remove inherent ensemble averaging. Such measurements would also eliminate any possibility that broadband probe pulse is being chirped by propagation through the colloidal sample, potentially creating a phase shift in the stimulating field that could add an additional dispersive element to the measured lineshapes.

5.4.6. Supplementary Information

SE-FSRS samples. All SE-FSRS experiments are performed on commercially-available nanoparticle assemblies provided by STA Technologies consisting of one or more gold cores topped with a sub-monolayer coverage of a reporter molecule and overcoated with a silica shell. One sample (BPE90) consists of gold cores with a diameter of approximately 90 nm aggregated with *trans*-1,2-bis(4-pyridyl)-ethylene (BPE), while the other sample (BPY60) comprises approximately 60 nm gold cores aggregated with 4,4'-bipyridine (BPY) (Fig. 5.17). SE-FSRS samples are prepared by suspending the nanoparticle assemblies in water and placing the colloidal mixture in a cuvette with a path length of 2 mm. The sample is stirred constantly during data acquisition using a magnetic stir bar.

1 MHz laser system. The laser system is summarized in Fig. 5.18. The laser system is based on a one-box diode-pumped Yb-doped fiber oscillator/amplifier system (Clark-MXR Impulse). The fundamental output (1 MHz, 1.034 μm, 250 fs, 11 μJ/pulse) is directed into a noncollinear optical parametric amplifier (Clark-MXR iNOPA) where it is split into two beams. Approximately 12% of the fundamental beam is focused into an yttrium aluminum garnet (YAG) plate to generate a broadband white light continuum (WLC) while the other 88% is focused into a type I β-barium borate (BBO) crystal to generate 2.5 W of 532 nm via second harmonic generation (SHG). Half of the WLC is mixed noncollinearly with the SHG in a type I BBO to generate femtosecond bandwidth 795 nm light. The 795 nm light is sent through a prism compressor, then directed into a home-built 4-f spectral grating filter to narrow the spectral bandwidth and create the Raman pump (795 nm, 1 ps, 3.5 nJ/pulse). The other half of the WLC, after being filtered through an 825 nm longpass filter (86-070, Edmund Optics) and a 950 nm shortpass filter (86-688, Edmund Optics), is sent through a prism compressor to generate the stimulating probe field (825-950 nm, $\sim$30 fs, 2.7 nJ/pulse). A colored glass filter (FGS900, Thorlabs) was placed in the probe path to flatten the probe spectrum, yielding a maximum power of 3 pJ/pulse at the sample. The pump and probe beams are focused collinearly onto the samples with a 10 cm focal length lens. The beam diameters at the sample are adjusted to be $\sim$55 μm. The probe beam is recollimated and the Raman pump is removed with an 808 nm stopline filters (NF03-808E-25, Chroma) and an 810 longpass filter (ET810lp, Chroma).

Data collection. On each system, the probe and phase-matched (SE-)FSRS signal are sent through a spectrograph (Princeton Instruments Acton SP2300) and focused onto

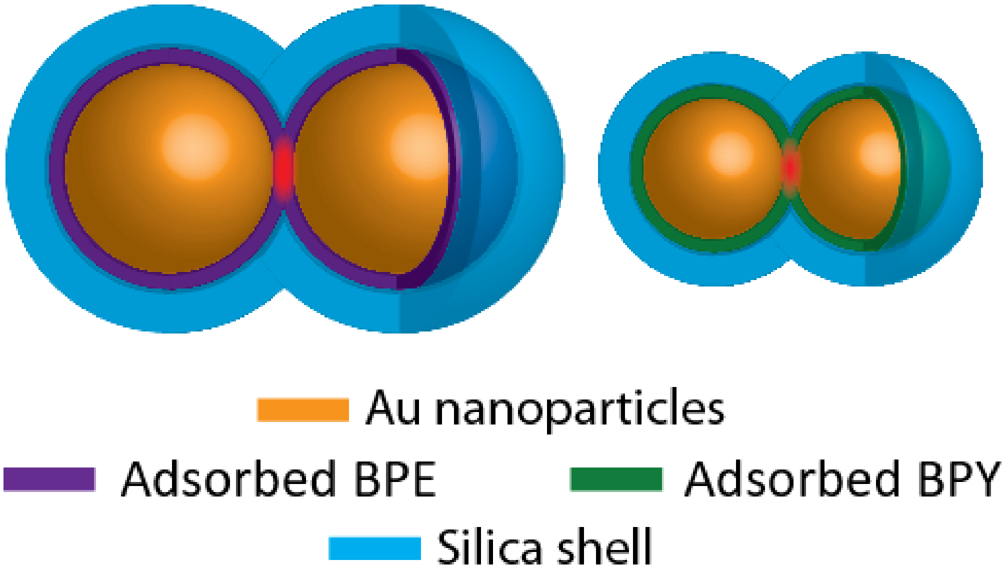

Figure 5.17. The nanoparticle assemblies consist of gold nanoparticles with an average diameter of either 90 nm (left) or 60 nm (right) and a broad (roughly 12%) distribution of individual particles sizes. The 90 nm particles are aggregated with *trans*-1,2-bis(4-pyridyl)-ethylene (BPE) while the 60 nm particles are aggregated with 2,2'-bipyridine (BPY) overcoated with a silica shell. These samples have been characterized previously to contain a range of aggregate sizes ranging for single cores to dimer, trimers, and larger aggregates. Figure reproduced with permission from Ref. 100. Copyright 2017 American Chemical Society.

a CCD camera (Princeton Instruments PIXIS 400BR) for self-heterodyned detection. Pump-on and pump-off spectra are collected by chopping the Raman pump at 250 Hz. Individual data sets were acquired for approximately 0.3 minutes and 30 minute scans were used to produce averaged spectra.

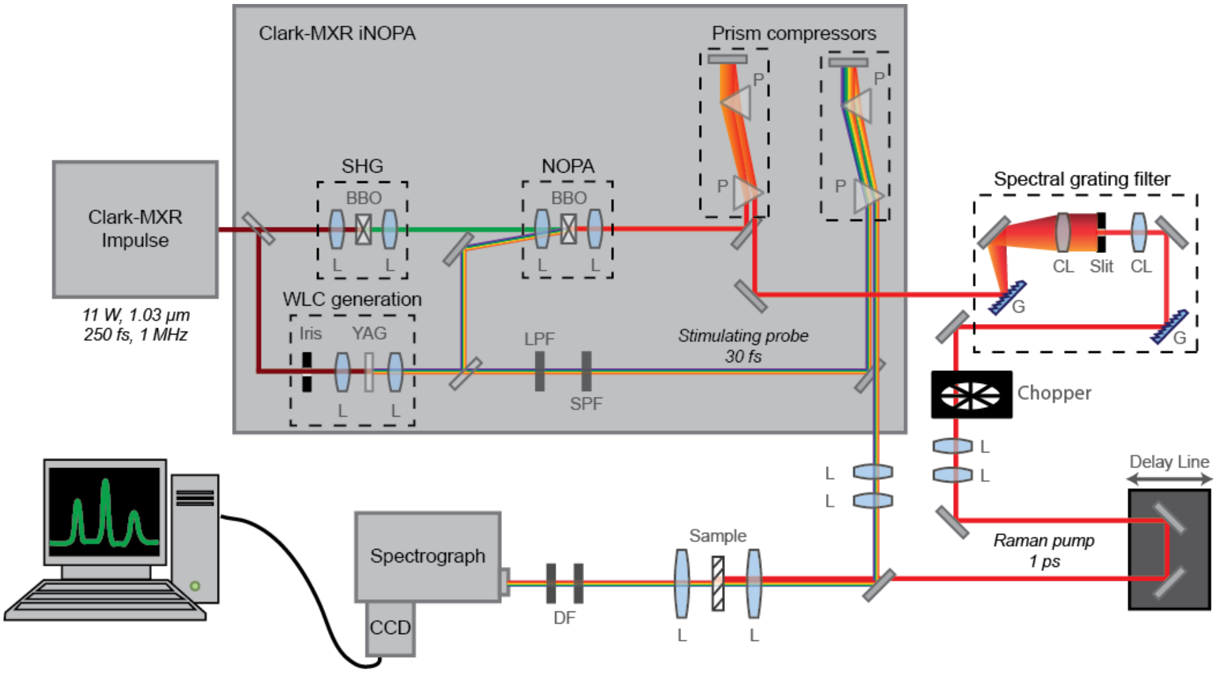

Figure 5.18. Schematic of the 1 MHz laser system. Abbreviations: second harmonic generation (SHG), β-barium borate crystal (BBO), lens (L), white light continuum (WLC), yttrium aluminum garnet (YAG), long pass filter (LPF), short pass filter (SPF), prism (P), grating (G), cylindrical lens (CL), detection filters (DF). Figure reproduced with permission from Ref. 100. Copyright 2017 American Chemical Society.

5.5. Towards Single-Aggregate SE-FSRS

5.5.1. Abstract

Single-aggregate surface-enhanced femtosecond stimulated Raman scattering (SA-SE-FSRS) is a highly desirable analytical technique. SA-SE-FSRS brings together the benefits of SE-FSRS with spatial and molecular localization provided by single-aggregate SERS (SA-SERS) studies. Initial SE-FSRS experiments were promising as they showed a unique coupling of the molecular vibrational modes with the plasmon oscillation. However, this coupling leads to strongly dispersive lineshapes in ensemble measurements. To alleviate this problem, SA-SE-FSRS has the promise to examine individual systems - closer to the systems explored by current theoretical methods. This chapter reports the efforts taken to reach SA-SE-FSRS thus far with suggestions of future directions.

5.5.2. Introduction

Single-aggregate surface-enhanced femtosecond stimulated Raman scattering (SA-SE-FSRS) promises to elucidate the coupling of molecular vibrational modes to the broadband plasmon resonance. Previous SE-FSRS experimental studies were colloidal ensemble measurements[72,98] which brought up suggestions of significant extinction and optical phase retardance.[123,149] Theoretical SE-FSRS papers considered only single aggregate/single plasmon resonance conditions coupled to single molecules.[110,111] To understand the coupling of molecular vibrational modes to the plasmon resonance, single aggregate studies are necessary to better match current SE-FSRS theory.

SA-SE-FSRS was pursued by building a coherent Raman scattering (CRS) microscope (μCRS) with the current 1 MHz SE-FSRS spectrometer (Fig. 5.18).[99,100] This chapter details the progress towards SA-SE-FSRS: observing steady-state coherent anti-Stokes Raman scattering (CARS) and femtosecond stimulated Raman scattering (FSRS) of solvents and solutions of β-carotene.

5.5.3. Experimental Methods

Using the 1 MHz SE-FSRS spectrometer built for previous studies,[99,100] additional optical paths were built for overlapping the Raman pump and probe fields in the focal plane of a microscope. An Olympus IX-3 inverted microscope was used for the optical microscope for spectroscopic measurements (Fig. 5.19). To collect the forward-scattered field that is the optimal phase-matching condition for the signal field, a home-made objective holder was fabricated to collimate excitation and signal fields to send to a CCD camera and spectrometer.

With the high numerical aperture (high-NA) focusing conditions used in the microscope, both CARS and FSRS scattering processes have phase-matching conditions met. In fact, the processes occur simultaneously with CARS generating a stronger signal often used for optimization of the optical alignment (Fig. 5.20).

To align both the Raman pump (also degenerate probe field in CARS) and Raman probe (Stokes field in CARS) spatial alignment is done with observation on a witness CCD camera attached to the auxillary port of the microscope. Temporal alignment is done utilizing $\chi^{(2)}$ signal from sum frequency generation of the Raman pump and probe fields (Fig. 5.21). SFG signals were generated by spatiotemporal overlap of the two beams inside of a type-I BBO crystal in the focal plane of the microscope. Signal is collected

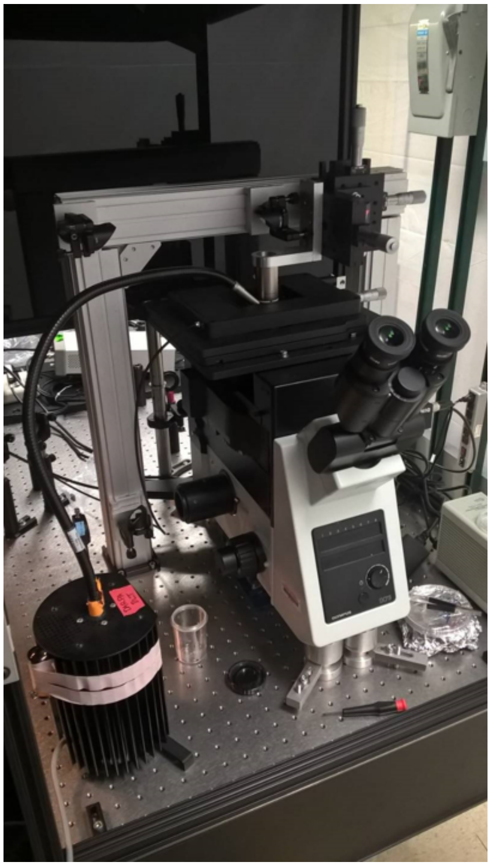

Figure 5.19. Home-made assembly of microscopic FSRS apparatus. The top assembly holds a second microscope objective that is used to collect forward-directed scatter that is then directed towards a CCD camera and spectrometer.

by the top microscope objective seen in Fig. 5.19 and sent to the spectrometer and CCD camera with excitation fields filtered by shortpass filters.

5.5.4. Results

After spatiotemporal alignment of the excitation fields in the microscope forward-scattering CARS and FSRS were collected as shown in Fig. 5.22. The experimental conditions for the solvent spectra collected were 20x excitation/20x collection objectives, 2 mW pump and 1 mW of probe (900 nW of probe for FSRS), with 5 second integration

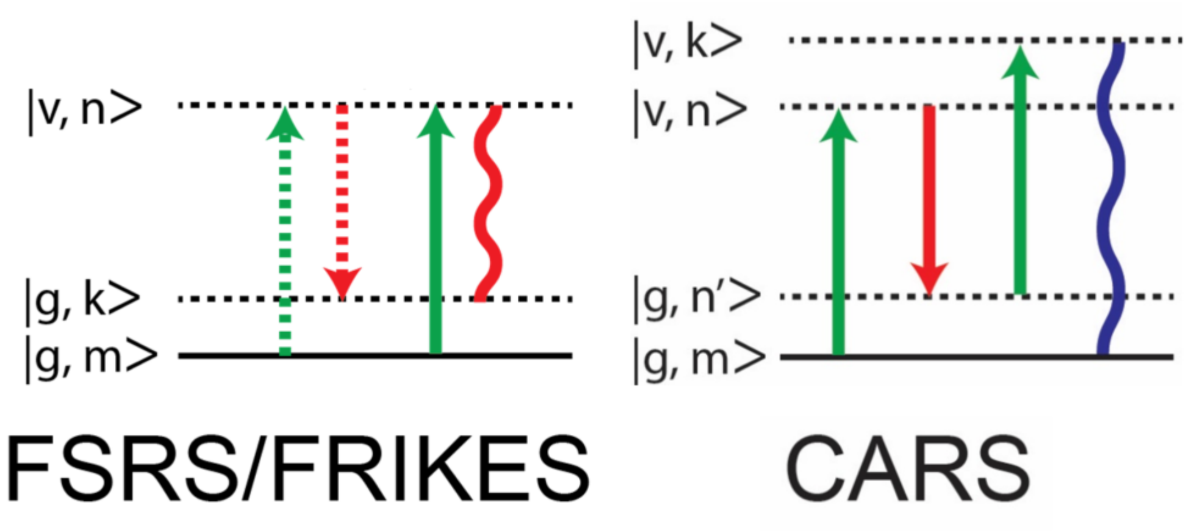

Figure 5.20. Four-wave mixing energy level diagrams (FWMEL) for both FSRS/FRIKES and CARS. The microscope assembly shown in Fig. 5.19 allows for correct phase-matching conditions for both processes.

time for CARS and 120 second integration for FSRS. CARS shows strongly dispersive lineshapes in the solvent modes with a strong background signal. Meanwhile, FSRS demonstrates weaker, but Lorentzian, lineshapes for the solvent vibrational modes. This discrepancy between CARS and FSRS with regards to the strength of signal is a common issue. In fact, even the epidirectional CARS signal was stronger than the FSRS signal regardless of worst optical collection efficiency.

Seen in Fig. 5.23 is the comparison of epi- and forward-scattering CARS of benzene. Excitation conditions were identical to those shown in Fig. 5.22. CARS signal of benzene was strong enough to use for alignment purposes with the signal observable above baseline as early as 0.1 second integration time.

To study more interesting systems by the μCRS microscope, solutions of saturated β-carotene in cyclohexane were analyzed by CARS and FSRS (Figs. 5.24 and 5.25).

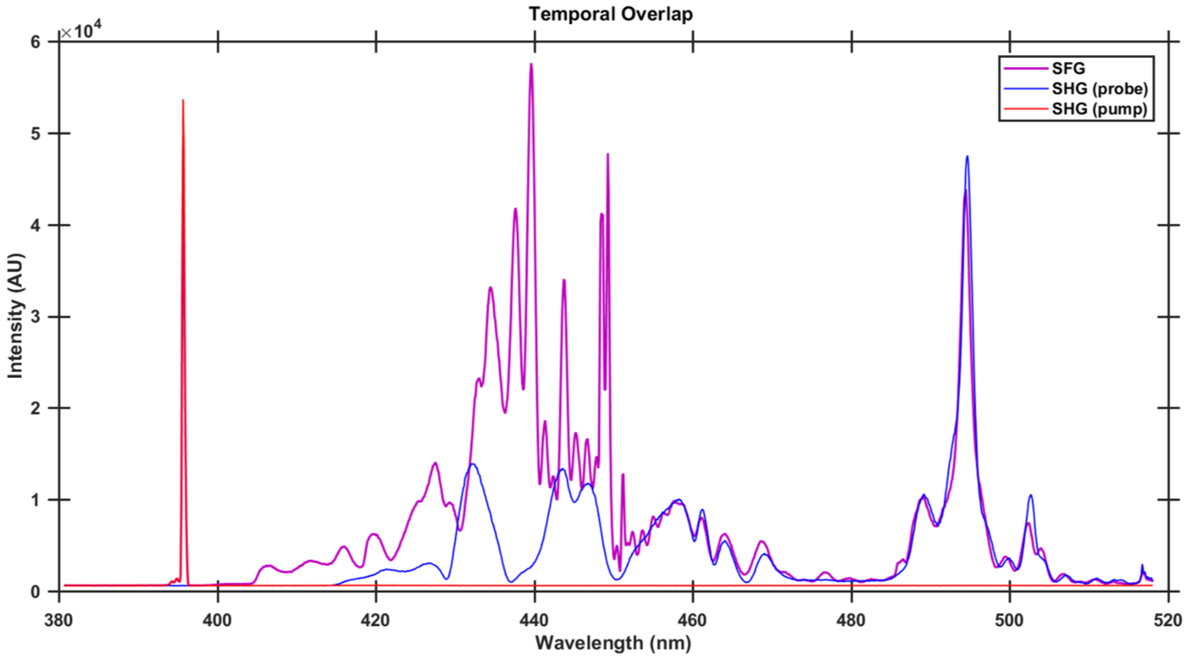

Figure 5.21. Temporal overlap in the microscope is found using SFG in a BBO crystal. SHG of the pump (red) and probe (blue) are observed alongside SFG (purple). SFG across broad wavelength range suggests high spatiotemporal overlap of both the Raman pump and probe in the BBO crystal.

CARS spectra shown in Fig. 5.24 were collected in the forward-direction with 20x excitation and collection objectives. Raman pump was 2 mW of power and Stokes field was 1 mW. 0.5 second integration time was used to record the spectra, with asterisks marking cyclohexane solvent peaks and question marks indicating possible β-carotene vibrational modes (red). The solvent-subtracted spectrum has two modes of β-carotene observable with a strong background interference.

FSRS spectra shown in Fig. 5.25 were collected in the forward-direction with 20x excitation and collection objectives. Raman pump was 2 mW of power and Raman probe field was 900 nW. 90 second integration time was used to record the spectra, with

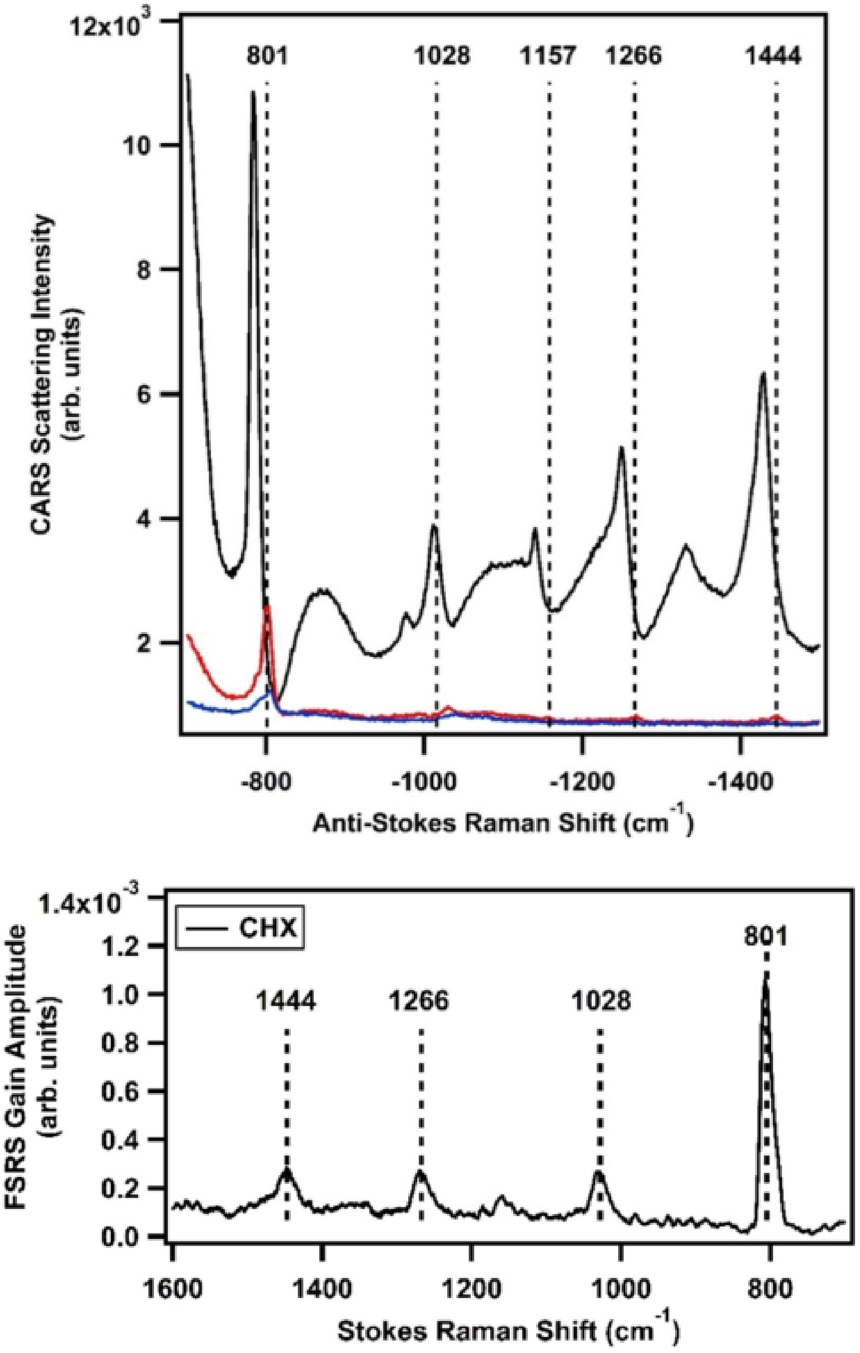

Figure 5.22. (Top) CARS and (bottom) FSRS of cyclohexane obtained using μCRS setup.

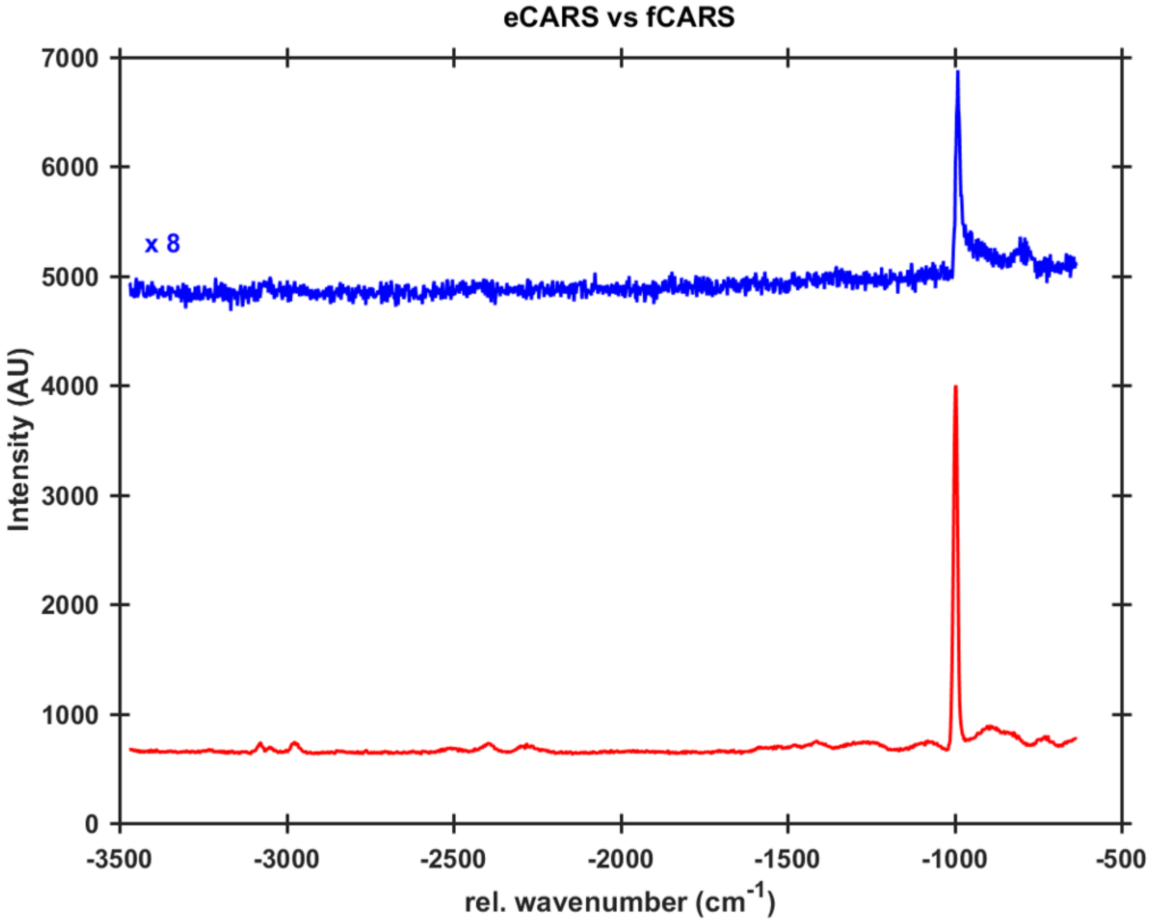

Figure 5.23. Comparison of benzene CARS measured in epi- and forward-direction, blue and red respectively.

asterisks marking cyclohexane solvent peaks and question marks indicating possible β-carotene vibrational modes (red). The solvent-subtracted spectrum has three modes of β-carotene observable with Lorentzian lineshapes and flat background.

After success of the solvent (benzene, cyclohexane) and β-carotene solution CRS experiments, plasmonically-enhanced coherent Raman scattering microspectroscopy (μPECRS) experiments were pursued. The system studied was BPE NT's identical to those used previously[72,98–100] drop-coated and dried on a glass coverslip. As CARS was so much

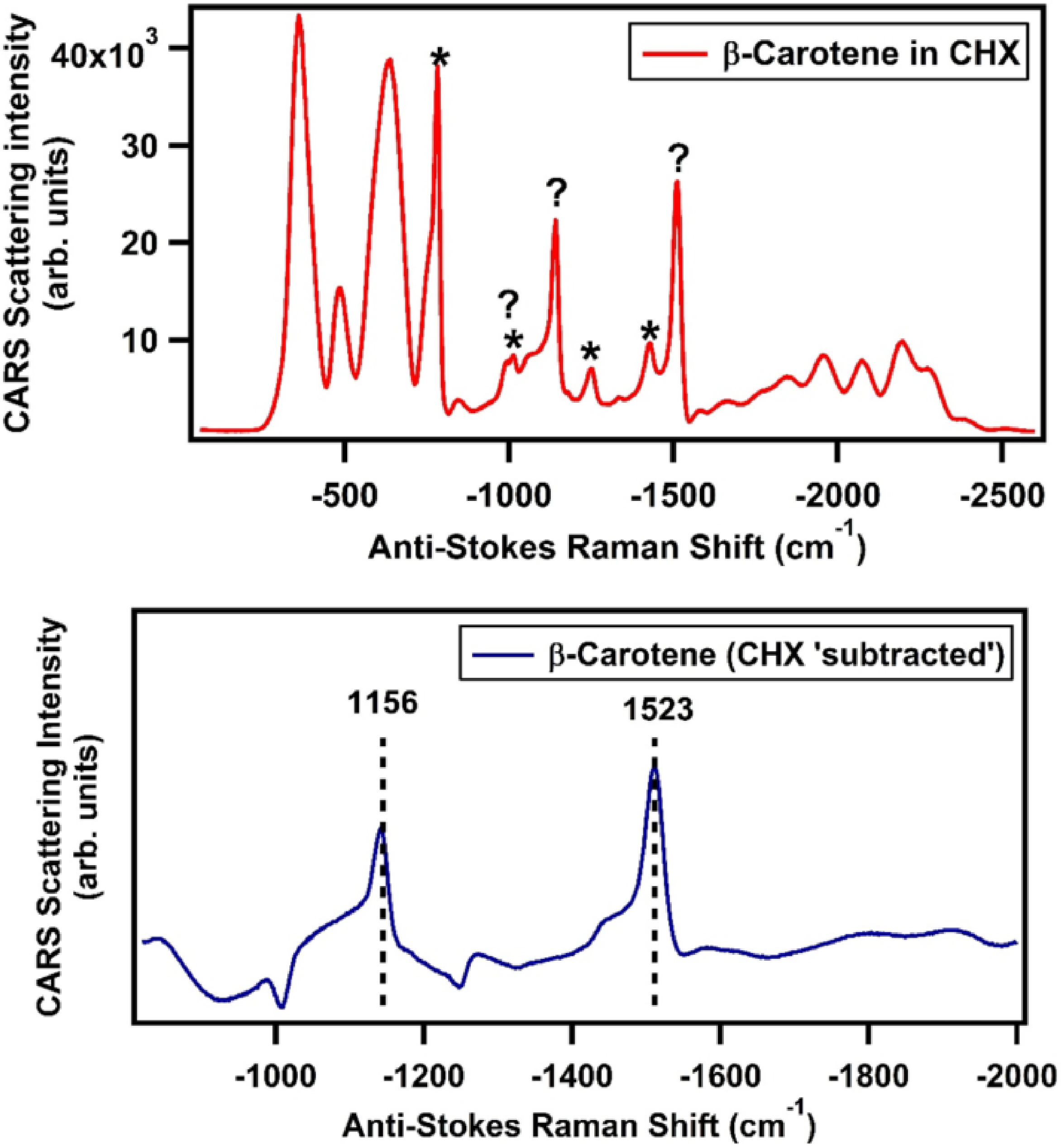

Figure 5.24. CARS of β-carotene in CHX. (Top, red) raw CARS spectrum with solvent-subtraction shown in blue below. Strong nonresonant electronic interference is observed and obscures vibrational lines in the β-carotene spectrum even after solvent subtraction. Solvent peaks are marked with asterisks while potential β-carotene mode assignments are marked with question marks.

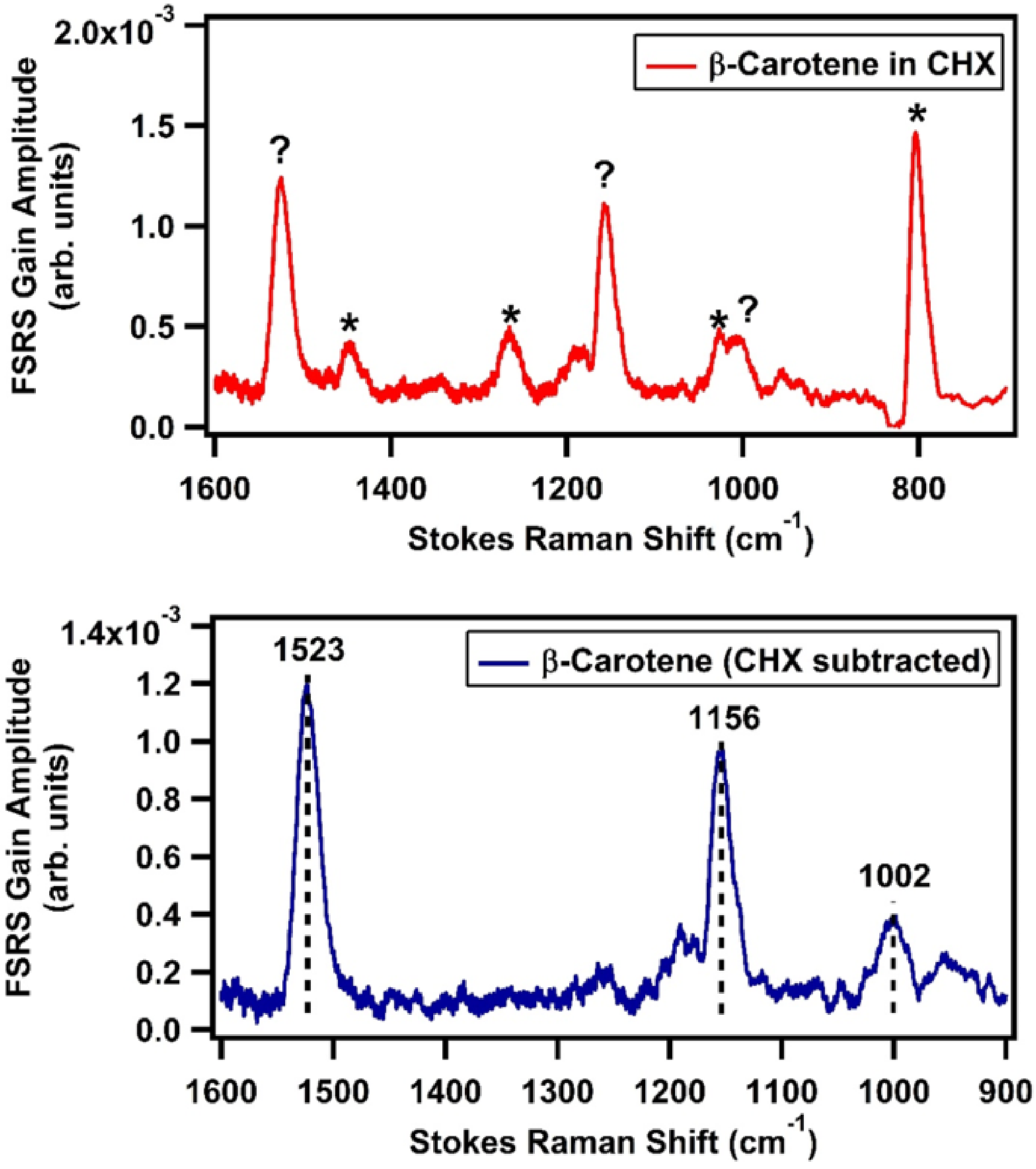

Figure 5.25. FSRS of β-carotene in CHX. (Top, red) raw FSRS spectrum with solvent-subtraction shown in blue below. Solvent peaks are marked with asterisks while potential β-carotene mode assignments are marked with question marks. In comparison to CARS, the vibrational lines of β-carotene are well-resolved and labeled at 1523, 1156, and 1002 cm^{-1}.

stronger of a process, surface-enhanced coherent anti-Stokes scattering (SECARS) was studied first.

Seen in Fig. 5.26, is SECARS of the BPE NT's on a glass coverslip. Experimental conditions were 100x oil objective for excitation, 50x extra-long working distance collection objective, 1.4 mW of Raman pump, 400 μW of Stokes field, and 1 second integration time. To isolate the SECARS signal (Fig. 5.26, black), the Stokes field is blocked and SERS is recorded (Fig. 5.26 in red). The broad background observed in SECARS is intense and destructively interferes with the vibrationally-resonant SECARS signal. In comparison to SERS, the 1600 modes of BPE are more dispersive and ∼50% less intense. Comparison of SECARS to the SERS signal shows an additional ∼2200 cm^{-1} vibrational mode that isn't present in the SERS spectrum. To further study this a time series of SECARS spectra were collected (Fig. 5.27).

As the electronic background from CARS is so much stronger than the vibrational resonances, the waterfall plot shown in Fig. 5.27 is plotted as the natural log of the intensity. Examining the intensities as a function of time shows significant spectral wandering in distinct regions. In the low wavenumber region where electronic background is strong (see Fig. 5.26) there is large amounts of frequency domain movement. At the BPE vibrational resonances the intensity is more stable with minimal wandering (∼1200, 1600, and 1640 cm^{-1}). In addition looking at the ∼2200 cm^{-1} mode seen in Fig. 5.26, the intensity stays stable in the frequency domain. This suggests that a new molecular species is being formed by the intense fields used during the CRS process.

After successful SECARS of drop-coated BPE NT's on glass coverslip SE-FSRS was pursued. Unfortunately, no signal has been obtained for this type of sample. Further

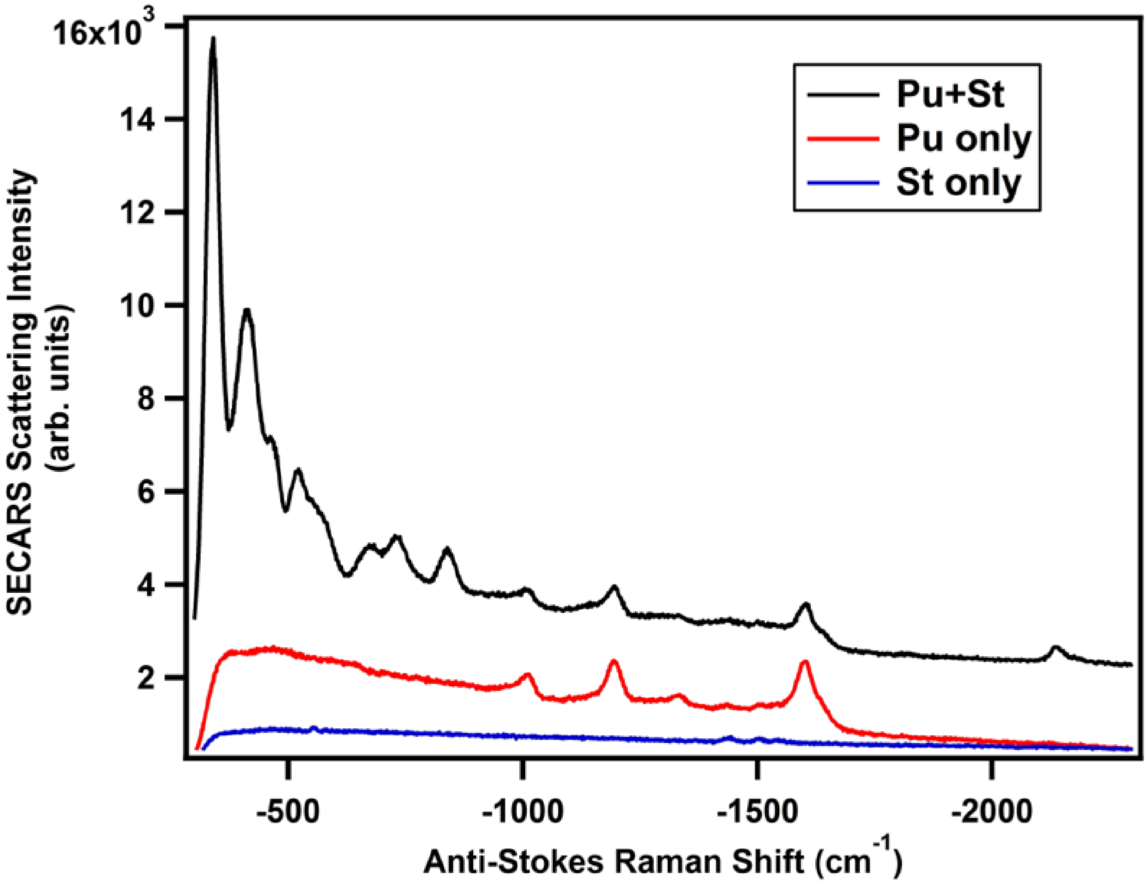

Figure 5.26. (Black) SECARS of BPE NT's dried on a glass coverslip. Comparison of the SECARS spectrum to SERS (red) and Stokes field background (blue) shows strong non-resonant electronic background destructively interfering with the vibrationally resonant signal.

work with individual aggregates drop-coated on a TEM grid has also been unsuccessful. Further experimentation is needed for understanding the difficulties of SA-SE-FSRS so that the isolation of a single plasmon resonance with the molecular vibrational modes can be achieved.

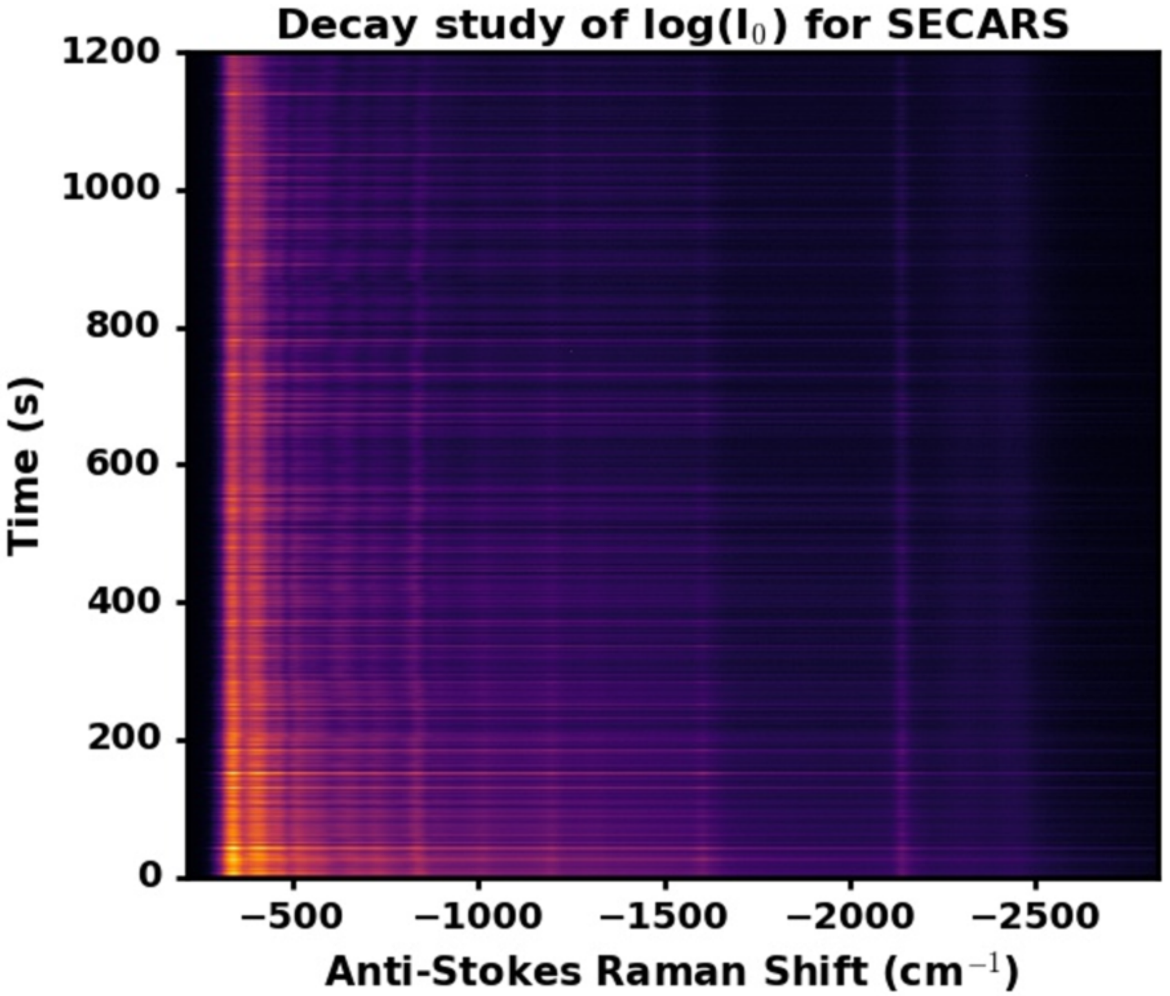

Figure 5.27. Decay of the SECARS signal from Fig. 5.26 plotted for twenty minutes. The vibrational resonances remain strong without frequency wandering while nonresonant contributions show wandering. A strong mode near 2200 cm^{-1} suggests formation of a new molecule in the nanoparticle junction observed by SECARS.

5.5.5. Conclusion and Future Directions

In conclusion, SA-SE-FSRS is an experiment that is still full of potential - yet unrealized. Based on the description of work performed herein and work from close collaborators new directions need to be taken. A few ideas that have been discussed but not yet implemented:

(1) Step back from broadband, multiplex, SA-SE-FSRS and work on single mode SA-SE-SRS. This is an experiment that can be done with an 80 MHz oscillator (or cw system) allowing for extremely fast modulation, lock-in amplifier detection, and near shot-noise level system. This approach is being used by colleagues in the CaSTL research center yet has only seen strong background metal luminescence.[175]

(2) To try to isolate the vibrationally-resonant signal in an SA-SE-FSRS, additional modulation techniques can be adopted. The most promising would be to use a combination of the SA-SE-SRS technique described above with frequency-modulated FSRS (FM-FSRS).[176]

(3) Finally, the last new approach would be to not do SA-SE-FSRS. One of the key issues is that theory doesn't understand how to deal with a plasmonically-enhanced self-heterodyned local oscillator. To get a handle on the way plasmonic enhancement of local oscillators work, a simultaneous heterodyned/homodyned SA-SECARS experiment can be performed. This experiment would be best done with sweeping a picosecond bandwidth pulse to get the full vibrational lineshape to take advantage of the lower SNR attainable.

Thus, SA-SE-FSRS is an experiment that, while not yet successful, has new approaches to explore. There are really two directions to pursue: one a more theoretical-driven avenue (understanding heterodyne detection/local oscillators in plasmonic samples), the other simply optimization of the experimental parameter space for detecting stimulated SRS in plasmonic assemblies.

5.6. Conclusion

SE-FSRS is a technique that has advanced greatly from initial reports.[72,98] Early papers used a 100 kHz Ti:sapph system to study ensemble colloidal gold nanoparticles with BPE adsorbed to the surface as a Raman reporter molecule. The first paper saw that the FSRS process occuring near a plasmonic surface observed dispersive lineshapes attributed to Fano interference of the molecular sharp vibrational resonances coupling to the broad plasmon resonance.[72] This result was very unexpected as off-resonant FSRS normally reproduces Lorentzian NRS lineshapes.[144] Studying the dependence of the dispersive lineshape character on plasmon resonance was the focus of the second SE-FSRS paper.[98] This paper showed that for identical excitation conditions and molecule the SE-FSRS lineshapes showed a π-phase shift.

After a dormant period, SE-FSRS has had revitalized interest.[99,100,110,111,123,149,177] Recent papers have expanded the knowledge of SE-FSRS from both experimental[99,100,149] and theoretical perspectives.[110,111,123,177] Experimental progress has focused on optimizing the SE-FSRS technique by increasing the repetition rate,[99] balancing the effects of extinction and enhancement,[149] and exploring the efficiency of SRL in SE-FSRS.[100] While experiments are progressing the efficiency and SNR of SE-FSRS, theory has focused on explaining the dispersive lineshapes observed experimentally. Mandal *et al.* explained the dispersive lineshapes by proposing a destructive interference of a stimulated plasmon resonance emission with the heterodyned SE-FSRS signal.[111] McAnally *et al.* developed a semiclassical coupled-wave equations framework for the Fano lineshapes observed experimentally. Both theoretical approaches proposed new ideas for how plasmonic enhancement works in SE-FSRS, but make incorrect predictions related to the Raman pump wavelength dependence in SE-FSRS.[100] These discrepancies has driven the need for both new experiments and new theory.

SA-SE-FSRS is an experimental approach that aims to remove the ensemble averaging from SE-FSRS experiments. Similar to work done in SECARS,[75,101] SA-SE-FSRS is an experiment that is closer to the theoretical models used in previous work.[110,111] However, the SA-SE-FSRS experiment has numerous difficulties related to the SNR of a single-aggregate stimulated Raman response. Collaborative efforts are underway to isolate vibrationally-resonant SE-FSRS response from the electronic metal response. Alongside new experimental approaches, theory is working to bring together ideas between Mandal *et al.* and McAnally *et al.*, particularly with the concepts of stimulated plasmon emission mixing with a complex local field effect (LFE). To fully realize the capabilities of SE-FSRS, a combination of theory and experimental work is essential for understanding how to best use the limited plasmonic enhancement in SE-FSRS with chemical problems that necessitate the use of coherent Raman scattering.

CHAPTER 6

Quantitative Determination of the Differential Raman Scattering Cross-Sections of Glucose by Femtosecond Stimulated Raman Scattering

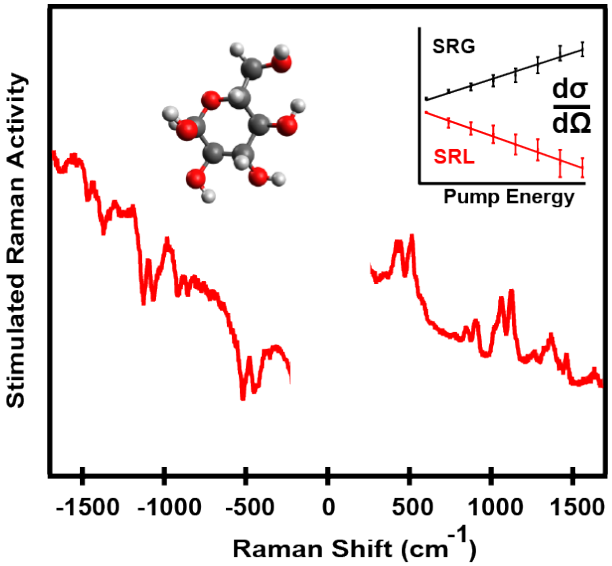

This chapter has been reproduced with permission from Ref. 173 . Copyright 2017 American Chemical Society.

6.1. Abstract

Femtosecond stimulated Raman spectroscopy (FSRS) is a vibrational spectroscopy technique that has been used in a wide variety of applications: from transient vibrational signature tracking to amplifying weak normal Raman scattering signals. Presented in this chapter is an application of FSRS to quantify the differential Raman scattering cross-sections (DRSCs) of glucose. In using FSRS to determine the DRSCs of multiple glucose vibrational modes, we demonstrate the applicability of both stimulated Raman loss (SRL) spectroscopy and stimulated Raman gain (SRG) FSRS. Using the two analogous FSRS techniques, SRG and SRL, we determine that the DRSCs of glucose excited at 514.5 nm range from a low of $5.0 \pm 1.1 \times 10^{-30}$ to a high of $8.9 \pm 0.9 \times 10^{-30}$ cm^2 $\mathrm{molecule}^{-1}$ sr^{-1}. This work establishes both the compatibility of SRL for measuring DRSCs and values for the DRSC of multiple vibrational modes of glucose.

6.2. Introduction

An accurate value for the Raman scattering cross-section of an analyte is a requirement for assessing the likelihood of success for a proposed measurement. As the Raman scattering cross-section describes the scattering activity of an analyte, it is easy to compare the utility of different Raman scattering techniques for observing an analyte. While the Raman scattering cross-section is an important property, it can be quite difficult to measure using normal Raman scattering (NRS), which measures the differential Raman scattering cross-section (DRSC) by comparison with a standard.[178,179]

An alternative approach to using NRS for measuring Raman scattering cross-sections is to use stimulated Raman scattering.[155] Femtosecond stimulated Raman scattering (FSRS) is the implementation that will be used here. FSRS has numerous advantages over NRS for measuring DRSCs: including being a self-referencing technique to remove instrument response from grating and camera efficiencies, removing ambiguities of solid angle scattering collection in NRS due to FSRS being a coherent scattering process, and increased Raman scattering efficiency over NRS by coherent processes. In comparing FSRS to NRS, it is important to note that the DRSC is an intrinsic molecular property. The boost in Raman scattering efficiency from FSRS compared to NRS is due to the collection of coherent oscillators emitting Raman shifted photons in a stimulated manner from the driven macroscopic polarization in FSRS compared to the incoherent oscillators spontaneously emitting Raman shifted photons in NRS.

Ground state, or non-transient FSRS, has been used to measure the Raman scattering cross-sections for a variety of analytes, including resonant dye molecules.[54,180,181] FSRS as a vibrational spectroscopy technique has been used extensively for measuring transient vibrational features of photoexcited species when coupled with a photoexcitation, or actinic, pulse.[34,37] However, the stimulated Raman process in itself is useful as the coherent Raman process boosts the Raman scattering efficiency compared to NRS. FSRS can be performed as either a stimulated Raman gain (SRG) or a stimulated Raman loss (SRL) process.[144,182] As FSRS cross-section measurements have been shown to be identical to NRS measurements, the more highly efficient FSRS measurements are helpful for weakly scattering systems. An important analyte that falls into this category is glucose.

Glucose is the most important molecule in the metabolic chain. The concentration of glucose is a key diagnostic quantity for many metabolic disorders, most notably diabetes.[183] The importance of glucose has led to many researchers attempting to quantify glucose concentration *in vivo* using Raman scattering techniques,[184–186] including by SRS microscopy.[187] As NRS studies of glucose showed very weak scattering,[188,189] surface-enhanced Raman scattering (SERS)[184,185] and coherent Raman scattering techniques[186,187] were used to enhance the low overall NRS signal (shown in Fig. 6.8).

Unfortunately previous research[184,185] either cites a literature value of the DRSC that references unpublished and non-peer reviewed data for the DRSC of the 1126 cm^{-1} mode of glucose,[178,190] or simply omits the exact value. To resolve this issue, we utilize FSRS to quantitatively determine its DSRCs using both SRL and SRG simultaneously.

To measure a FSRS signal, a chopper is frequently employed to modulate the Raman pump field. Modulation of the Raman pump field, when synced with a camera, measures sequential Raman pump-on and Raman pump-off intensities of the Raman probe field as shown in Eq. 6.1.[155]

$$I_{FSRS} = \frac{(I_{probe})_{pump-on}}{(I_{probe})_{pump-off}} \tag{6.1}$$

As the stimulated Raman activity only occurs when both the Raman pump and probe fields are coincident in time and space inside the sample, measuring the ratio allows for extraction of the FSRS intensity. The FSRS signal being proportional to a ratio of intensities makes the technique well-suited for measuring optical properties as instrument response issues related to grating and detector efficiencies are normalized.[155,178,179]

The signal intensity in FSRS can be approximated as shown in Eq. 6.2[155]

$$I_{FSRS} = a \times \sigma_R \times l \times N \times I_{RP} \tag{6.2}$$

where, the intensity of the FSRS signal ($\mathrm{I_{FSRS}}$), or stimulated Raman activity, is linear with respect to a collection of analyte-independent physical constants (a), the analyte total Raman scattering cross-section (σ_R), path length (l), analyte concentration (N), and Raman pump power ($\mathrm{I_{RP}}$). Thus, performing a study of the stimulated Raman activity as a function of Raman pump power can isolate the analyte total Raman scattering cross-section along with a collection of controllable physical constants.

While FSRS provides information about the total Raman scattering cross-section, the more commonly referenced fundamental Raman scattering property is the DRSC. To measure an absolute DRSC of an analyte, tightly controlled experimental conditions including polarization and geometry need to be used.[178,179,191,192] Alternatively, the same physical information can be obtained by measuring the Raman scattering properties of an analyte in reference to a known absolute DRSC.[178,179,193]

There are important motivations for the use of FSRS over NRS in the approach taken herein. While the self-referencing for grating and camera instrumental responses that are intrinsic to FSRS are helpful, these same properties exist when performing the relative DRSC experiment in NRS. However, FSRS has the advantage over NRS still as it (1) allows for a more complete collection of signal photons compared to the isotropic scatter of NRS and (2) takes advantage of the multiple field-matter interactions in coherent Raman scattering to more efficiently create signal photons in the probe field compared to spontaneously emitted signal photons from NRS.

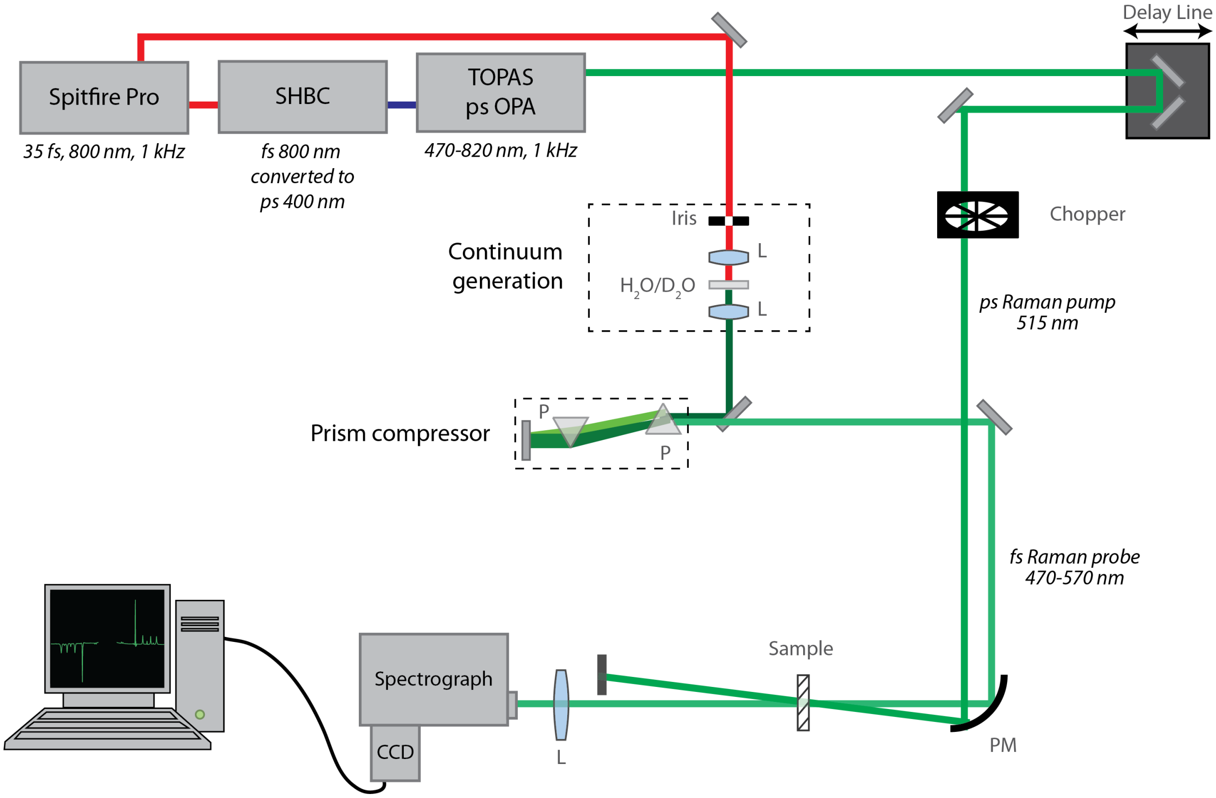

Figure 6.1. Experimental FSRS setup for measuring DRSCs of glucose consisting of an amplified Ti:sapph laser system, a second harmonic bandwidth compressor (SHBC), a tunable picosecond optical parametric amplifier (TOPAS), curved mirrors (CM), prisms (P), lens (L), parabolic mirror (PM), spectrograph, and CCD camera. Figure reproduced with permission from Ref. 173. Copyright 2017 American Chemical Society.

6.3. Experimental Details

To measure the relative DRSCs of glucose, we use an approach similar to that used previously.[54,180,181] However, unlike the previous studies, we use a sufficiently broad continuum that overlaps the Raman pump on both the Stokes and anti-Stokes frequencies simultaneously, dispersing the full SRG and SRL spectra on the CCD. Briefly, the concept is that by using FSRS the stimulated Raman activity as a function of Raman pump power can be determined, fit in a linear regime, and compared to a known standard.

A 1 kHz Ti:sapph system (Spitfire Pro, Spectra Physics), described previously,[42] was used for this experiment (Fig. 6.1). Specifically, < 35 mW of the fundamental was directed through a prism compressor, along a manual stage, and into a 50:50 mixture of H2O/D2O in a 5 mm cuvette for continuum generation, creating the chirped Raman probe (470-570 nm), which was determined to be < 100 fs at a single frequency and $\sim$500 fs across the entire frequency range. Approximately 1.5 W was split from the fundamental to pump a second harmonic bandwidth compressor (SHBC, Light Conversion), which creates an intense 400 nm picosecond bandwidth pulse that pumped a commercial tuneable optical parametric amplifier (TOPAS-400-WL, Light Conversion). The TOPAS was tuned to an output center wavelength of 514.5 nm ($\sim$0.7 ps), creating a Raman pump that matches the literature values for DRSCs of glucose and cyclohexane used in the present study.[178,192] The Raman probe was overlapped temporally with the Raman pump, chopped at 125 Hz, then both were focused into the sample (2 mm quartz cuvette) by a parabolic mirror. The transmitted Raman probe containing the stimulated Raman activity was focused into a spectrograph (Triax 180, Horiba Jobin Yvon), dispersed using a 1200 gv/mm grating, and recorded as differential optical density (ΔOD) on a CCD camera (PIXIS 100B, Princeton Instruments) using home-built LabView programming. The spectral resolution of the experiment was determined to be sub-20 cm^{-1} based on fitting solvent modes near the glucose modes of interest (See Supporting Information Fig. 6.7, Table 6.3). Using this system, FSRS spectra of 1 M aqueous glucose and neat cyclohexane were obtained in triplicate at Raman pump pulse energies of 0.2-1.6 μJ/pulse with 2-minute acquisition times per spectrum.

Individual FSRS spectra of glucose showing the simultaneous SRL and SRG stimulated Raman activity at the highest (1.6 μJ/pulse) and lowest (0.2 μJ/pulse) Raman pump energies are displayed in Fig. 6.2. The increasing background near the Raman pump is attributed to cross-phase modulation.[155] The decision to display Raman pump energy instead of Raman pump power was made to allow for easier conversion when considering higher repetition rate laser systems. As will be seen in Eq. 6.3, there is no functional difference between measuring a stimulated Raman activity as a function of Raman pump power or energy because the relevant parameter is a ratio in which repetition rate dependencies are removed.

The method of measuring the DRSC indirectly can be adapted to the total Raman scattering cross-sections measured in FSRS (see Supporting Information Eqs. 6.4-6.11) by incorporating the effects of the linear Raman scattering depolarization ratio:[179]

$$\frac{d\sigma_{R,glu}}{d\Omega} = \left(\frac{1+\rho_{R,glu}}{1+2\rho_{R,glu}}\right)\left(\frac{1+2\rho_{R,chx}}{1+\rho_{R,chx}}\right)\left(\frac{m_{glu}}{m_{chx}}\right)\left(\frac{N_{chx}}{N_{glu}}\right)\frac{d\sigma_{R,chx}}{d\Omega} \tag{6.3}$$

Eq. 6.3 shows that the relative DRSCs of glucose (glu) with respect to cyclohexane (chx) can be measured by using the linear Raman scattering depolarization ratios (obtained from Ref. 189), the concentrations of glucose and cyclohexane, a known value of the absolute DRSC of cyclohexane, and the ratio of the linear fits of stimulated Raman activity with respect to Raman pump power or energy. This method is in contrast to the process of directly measuring the total cross-section which requires knowledge of the total spectral photon flux a quantity that is exceedingly difficult to measure accurately across the broad spectral range used in the current experiment.[40]

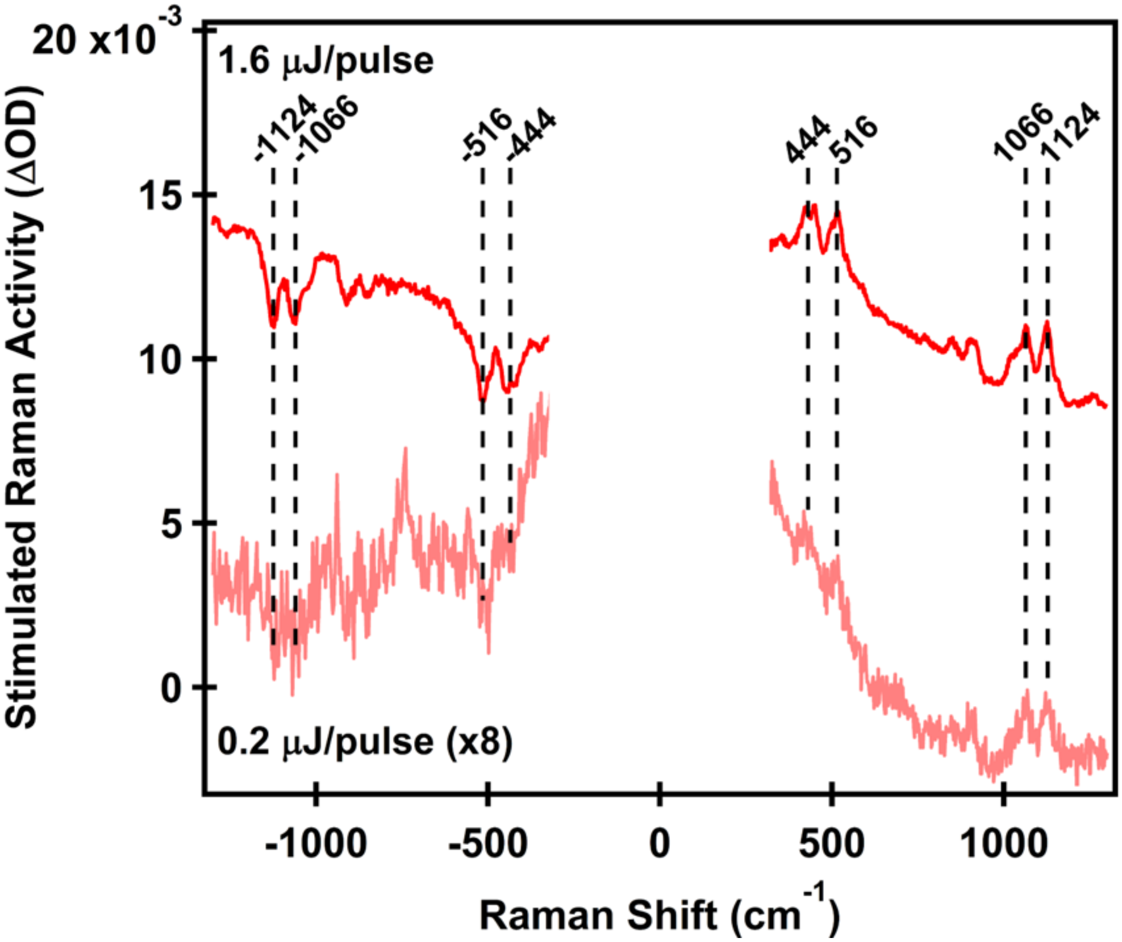

Figure 6.2. FSRS spectra of the lowest (0.2 μJ/pulse) and highest (1.6 μJ/pulse) Raman pump energies of the linear Raman pump regime used in the experimental determination of the DRSCs of glucose. Labeled peaks have DRSCs determined by use of Eq. 6.3 and are reported in Table 6.1. Spectra have been shifted vertically for clarity. Figure reproduced with permission from Ref. 173. Copyright 2017 American Chemical Society.

6.4. Results and Discussion

Using the FSRS apparatus shown in Fig. 6.1, we obtained the integrated stimulated Raman activity as a function of Raman pump energy. Fitting the Raman pump energy dependence for each vibrational mode of interest in glucose (444, 516, 1066, 1124 cm^{-1}) linear fits were obtained for both SRL and SRG (see Supporting Information Fig. 6.5).

Molecule	ν_{exp}(cm^{-1})	$d\sigma/d\Omega$ (cm^2 molecule^{-1} sr^{-1} $\times 10^{-30}$)
Glucose[a]	444 (SRL)	6.5 ± 0.6
	444 (SRG)	6.1 ± 0.9
	516 (SRL)	8.9 ± 0.9
	516 (SRG)	5.9 ± 1.0
	1066 (SRL)	5.0 ± 1.1
	1066 (SRG)	5.3 ± 0.5
	1124 (SRL)	6.4 ± 0.5
	1124 (SRG)	6.3 ± 0.8
Glucose[178]	1126	5.6
Cyclohexane[192]	802	5.2

Table 6.1. Results of the study performed herein[a], along with literature values for glucose[178] and cyclohexane.[192]

The range of Raman pump pulse energies used was verified to provide linear response in the stimulated Raman activity for both SRL and SRG in the reference neat cyclohexane system (see Supporting Information Fig. 6.6).

In Table 6.1, we summarize the results of the DRSCs obtained by SRL and SRG for glucose along with values of the DRSCs for the 1126 cm^{-1} (1124 cm^{-1} in current study) mode of glucose and the 802 cm^{-1} (801 cm^{-1} in current study) mode of cyclohexane; all were obtained with Raman pump wavelengths of 514.5 nm.

From the results in Table 6.1, the DRSCs of glucose vary between 5.0×10^{-30} cm^2 molecule^{-1} sr^{-1} and 8.9×10^{-30} cm^2 molecule^{-1} sr^{-1} for the 444, 516, 1066, and 1124 cm^{-1} vibrational modes. The literature value[178] of 5.6×10^{-30} cm^2 molecule^{-1} sr^{-1} is an unsubstantiated value18 that we confirm with the present experimental work, and expand to further vibrational modes of interest. The DRSC discrepancy for the 516 cm^{-1} mode is likely due to differing backgrounds near the mode when comparing the SRL and SRG sides as seen in Fig. 6.2. The results summarized in Table 6.1 do raise an important question: why is glucose so difficult to observe by Raman scattering if the DRSC of glucose is so similar to cyclohexane?[184,185,187] To answer that question, we examine calculated DRSCs for both cyclohexane and glucose using density functional theory (DFT).[135]

Examining Figs. 6.3 and 6.4, the difference in empirically observed Raman scattering intensity can be traced to the relatively complicated vibrational manifold of glucose compared to cyclohexane. In glucose, the peaks nominally labeled as 444, 516, 1066, and 1124 cm^{-1} are in reality convoluted spectra of multiple vibrational modes. Meanwhile in cyclohexane, the Raman spectrum is dominated by fewer overall vibrational modes. Thus when comparing the two molecules and their Raman scattering activity, an important point to consider is the broader distribution of vibrational modes present in the single peaks of glucose compared to cyclohexane. To further complicate the Raman spectrum of glucose in aqueous solutions is the effect of inhomogenous line broadening due to a combination of multiple conformations and hydrogen bonding.[186,194–196] The effects of multiple vibrational modes contained in single peaks of glucose, multiple conformations, and hydrogen bonding effectively widen the peaks making them less distinguishable relative to cyclohexane.

6.5. Conclusions

In conclusion, we demonstrate for the first time the applicability of SRL for measuring DRSCs of weakly scattering analytes. SRL has been considered for many theoretical considerations and has been demonstrated to have the highest possible stimulated Raman activity.[129,172,197] However, this is the first study to show the applicability of SRL for

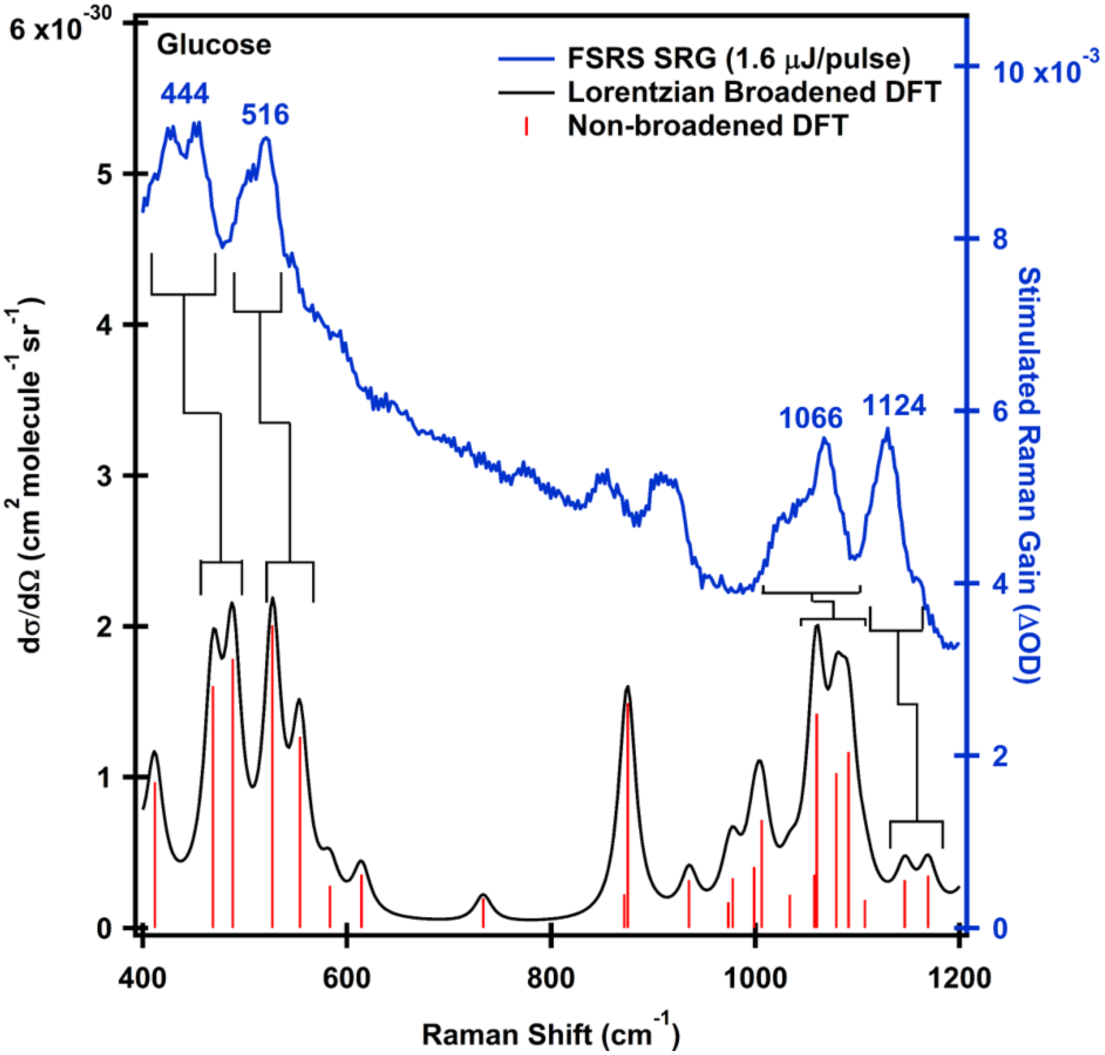

Figure 6.3. Comparison of FSRS SRG (blue) to DFT calculated (black and red) Raman scattering spectra for glucose using gas-phase geometry (see Supporting Information for details on calculations). The bracketed regions are to guide the eye for comparisons between experimental and calculated spectra. Figure reproduced with permission from Ref. 173. Copyright 2017 American Chemical Society.

DRSC measurements. For the presented case of glucose, we have determined the DRSC to be in line with previously reported, but unsubstantiated, values for the 1124 cm^{-1}

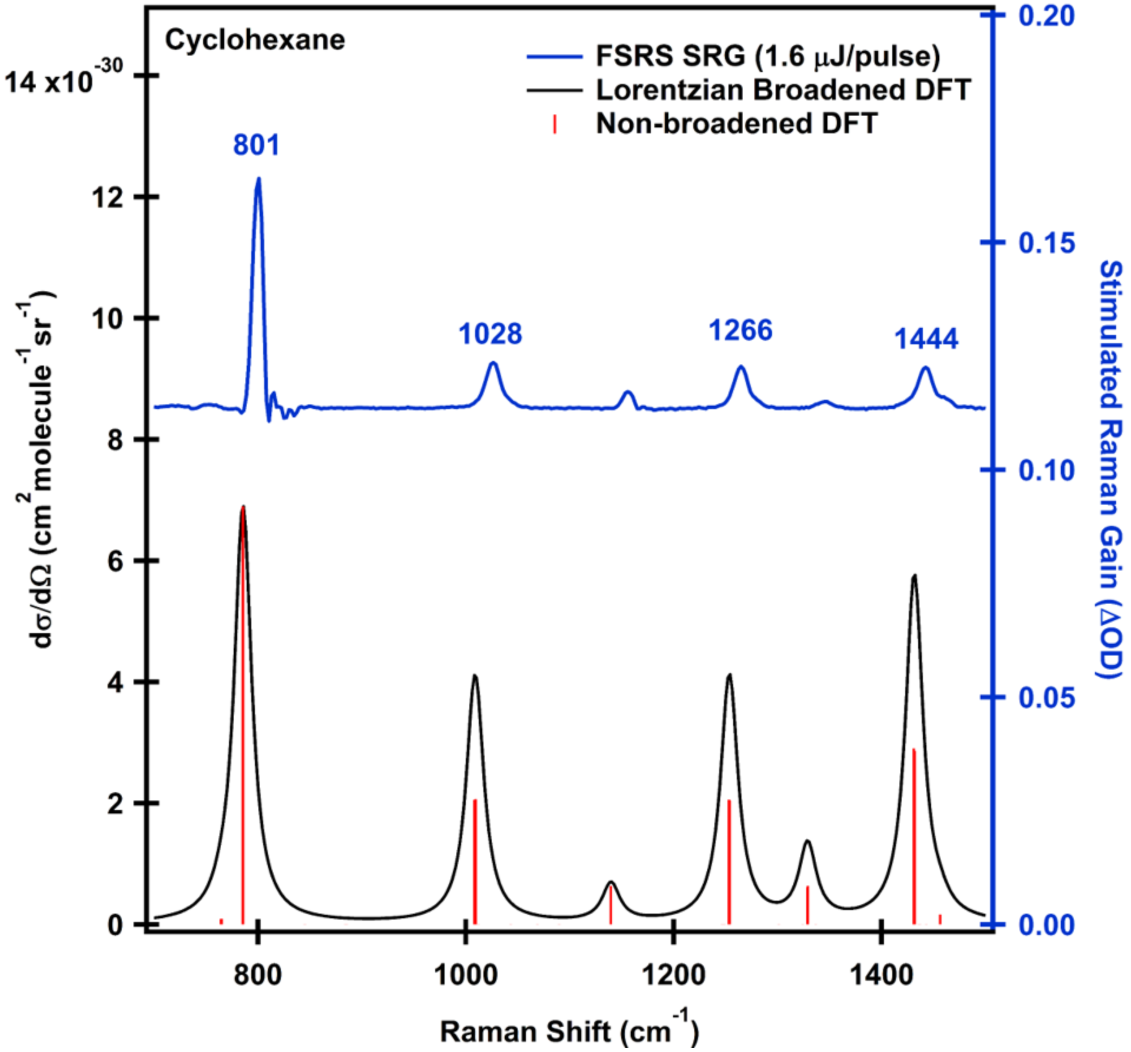

Figure 6.4. Comparison of FSRS SRG (blue) to DFT calculated (black and red) Raman scattering spectra for cyclohexane using gas-phase geometry. Figure reproduced with permission from Ref. 173. Copyright 2017 American Chemical Society.

mode of glucose. The generality of using either SRL or SRG for measuring DRSCs is highly advantageous as it allows for flexibility in experimental system constraints from laser equipment to wavelength dependent extinction effects.

6.6. Supplementary Information

- Figure 6.5: Linear plots of glucose integrated stimulated Raman activity vs. pulse energy
- Figure 6.6: Linear plot of cyclohexane integrated stimulated Raman activity vs. pulse energy
- Table 6.2: Linear Raman scattering depolarization ratio values used in calculation of differential Raman scattering cross-sections
- Equations 6.4-6.11: Derivation of Eq. 6.3 in manuscript
- Equations 6.12-6.16: Details of DFT calculations for differential Raman scattering cross-sections for glucose and cyclohexane
- Figure 6.7: Determining experimental FSRS linewidth resolution with toluene
- Table 6.3: FWHM of fitted peaks in Fig. 6.7.
- Figure 6.8: Normal Raman scattering spectrum of 1 M aqueous glucose

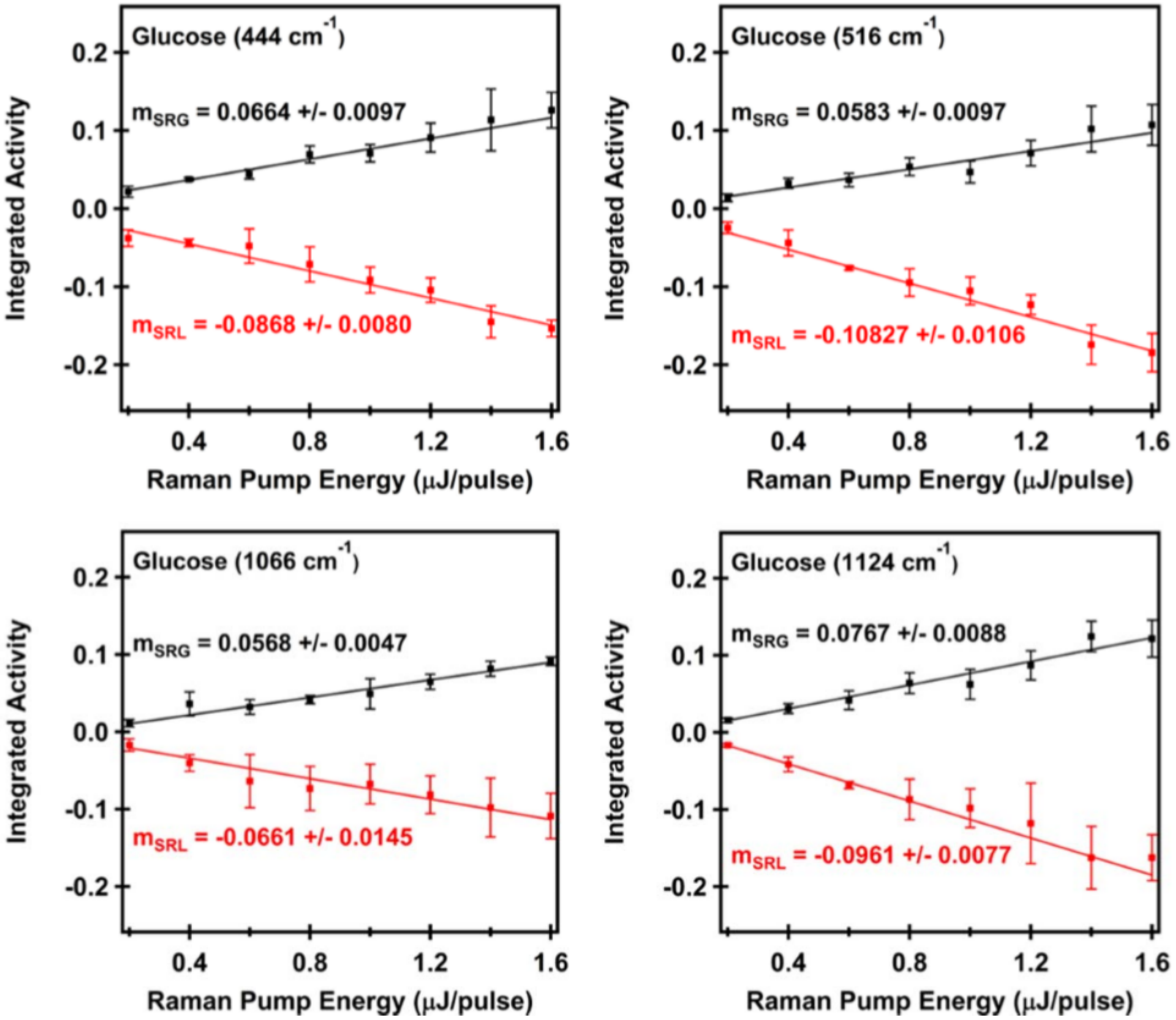

Figure 6.5. Experimental plots of integrated stimulated Raman activity for four vibrational modes of glucose. Stimulated Raman loss (SRL) and stimulated Raman gain (SRG) are shown in red and black, respectively. The markers indicate the average integrated differential optical density (stimulated Raman activity) for three measurements with standard deviation at the indicated Raman pump power. Each vibrational spectrum was fit using a sum of Lorentzians with separate cubic backgrounds for the Stokes and anti-Stokes regions. The data sets were then analyzed using a weighted-linear regression to determine slopes and standard deviation that includes error due to the standard deviation at each average integrated differential optical density. Figure reproduced with permission from Ref. 173. Copyright 2017 American Chemical Society.

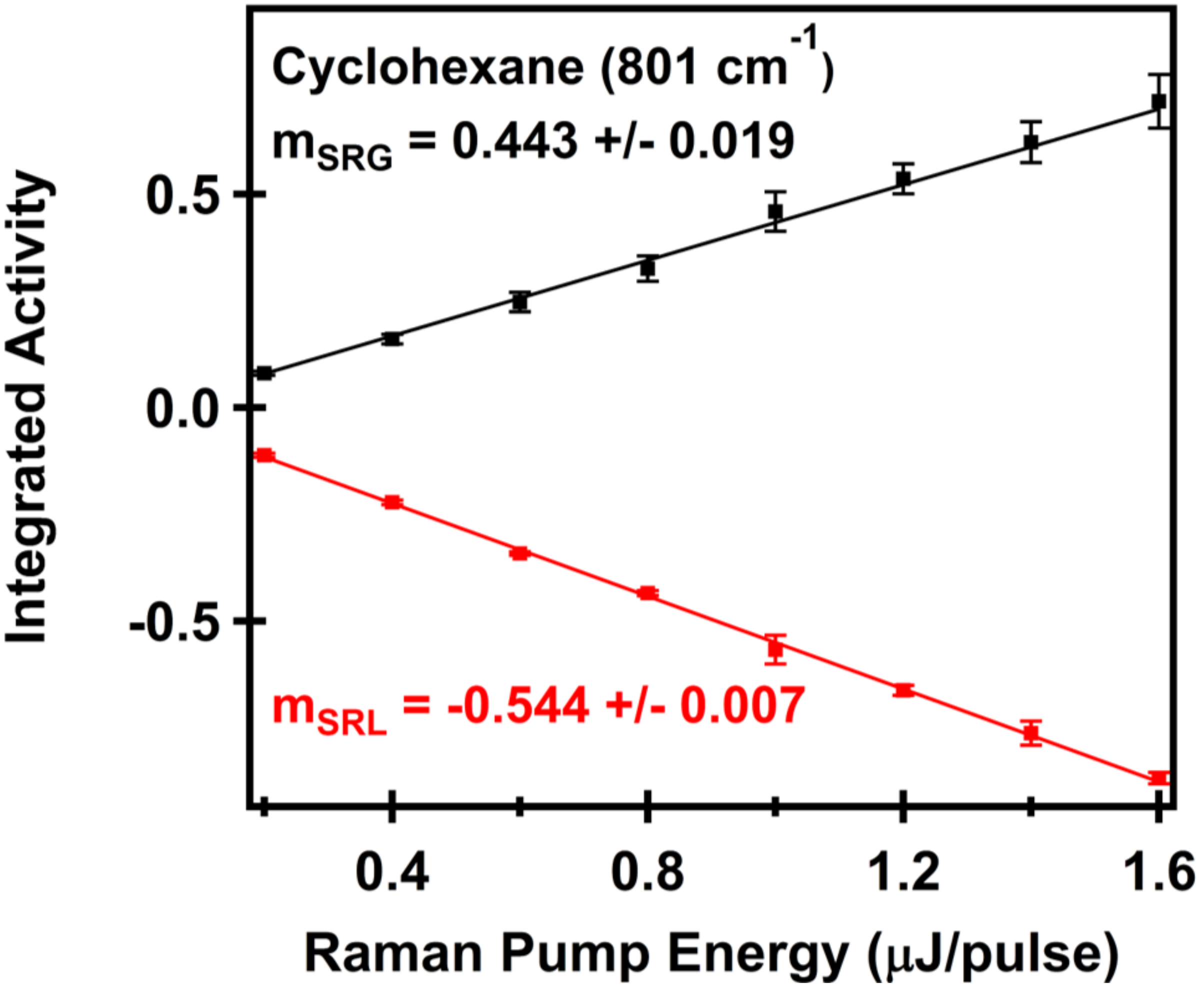

Figure 6.6. Experimental plot of stimulated Raman activity for the reference 801 cm^{-1} vibrational mode of neat cyclohexane. SRL and SRG are shown in red and black, respectively. The markers indicate the average integrated differential optical density (stimulated Raman activity) for three measurements with standard deviation at the indicated Raman pump power. Each vibrational spectrum was fit using a Lorentzian with separate linear backgrounds for the Stokes and anti-Stokes regions. The data sets were then analyzed using a weighted-linear regression to determine slopes and standard deviation that includes error due to the standard deviation at each average integrated differential optical density. Figure reproduced with permission from Ref. 173. Copyright 2017 American Chemical Society.

Molecule	ν_{exp}(cm^{-1})	ρ_R
Cyclohexane[a]	801	0.04 ± 0.01
Glucose[b]	444	0.30
	516	0.14
	1066	0.27
	1124	0.61

Table 6.2. Linear Raman scattering depolarization ratio (ρ_R) values for (a) cyclohexane[142] and (b) glucose[189] used in calculation of differential Raman scattering cross-sections in Eq. 6.3 of manuscript. No errors were reported in the glucose depolarization ratio values from Ref. 189. As the values for the glucose linear Raman scattering depolarization ratios are only reported to two significant figures with no associated error, we have reported our DRSCs in Table 6.1 of the manuscript to two significant figures.

To obtain a relative DRSC from the measured FSRS signal we need to consider the linearization of the FSRS signal and how the total Raman scattering cross-section is related to the DRSC.

First a key assumption in determining the total Raman scattering cross-section from FSRS data is that you are in a linear regime for the stimulated Raman activity as a function of the Raman pump power.[54,180,181] This linear relationship is given by Eq. 6.4:

$$I_{FSRS} = a \times \sigma_R \times l \times N \times I_{RP} \tag{6.4}$$

where the FSRS intensity is linearly proportional to a collection of analyte-independent physical constants (a), the analyte total Raman scattering cross-section (σ_R), path length (l), analyte concentration (N), and Raman pump power ($\mathrm{I_{RP}}$).

Alternatively, we could show the linearized relationship of the FSRS signal as a simple linear expression:

$$I_{FSRS} = m \times I_{RP} \tag{6.5}$$

where m is a collection of both analyte and non-analyte dependent constants, and can be obtained by linear regression of the stimulated Raman activity as a function of Raman pump energy.

To relate the total Raman scattering cross-section measured in FSRS to the DRSC we use Eq. 6.6:[179]

$$\sigma_R = \frac{8\pi}{3} \frac{1 + 2\rho_R}{1 + \rho_R} \frac{d\sigma_R}{d\Omega} \tag{6.6}$$

Thus to convert from the total Raman scattering cross-section (σ_R) to the DRSC $\left(\frac{d\sigma_R}{d\Omega}\right)$ we need to include the linear depolarization ratio (ρ_R) for the vibrational mode in question.

In previous FSRS studies,[54,180,181] relative total Raman scattering cross-sections are obtained by using a reference total Raman scattering cross-section (or converting a literature DRSC to a total Raman scattering cross-section using Eq. 6.6), measuring the FSRS intensity of an analyte at a Raman pump power in a linear regime for the reference molecule, then using Eq. 6.7:

$$(\sigma_R)_{Sample} = \left(\frac{I_{FSRS,Sample}}{I_{FSRS,Ref}}\right)\left(\frac{N_{Ref}}{N_{Sample}}\right)(\sigma_R)_{Ref} \tag{6.7}$$

However, taking the linearization approximation of the FSRS signal a step further, we can determine the DRSC for an analyte if the linear depolarization ratio is known or measured.

Starting with the ratio of FSRS intensities for a sample and reference:

$$\frac{I_{FSRS,Sample}}{I_{FSRS,Ref}} = \frac{a \times \sigma_{R,Sample} \times l \times N_{Sample} \times I_{RP}}{a \times \sigma_{R,Ref} \times l \times N_{Ref} \times I_{RP}} = \frac{m_{Sample}}{m_{Ref}} \tag{6.8}$$

$$\frac{m_{Sample}}{m_{Ref}} = \frac{\sigma_{R,Sample} \times N_{Sample}}{\sigma_{R,Ref} \times N_{Ref}} \tag{6.9}$$

Then using Eq. 6.6 in Eq. 6.9, we can relate the relative slopes of the FSRS intensities to the DRSCs of the reference and sample analyte:

$$\frac{m_{Sample}}{m_{Ref}} = \left(\frac{1+2\rho_R}{1+\rho_R}\right)_{Sample} \left(\frac{d\sigma_R}{d\Omega}\right)_{Sample} \frac{N_{Sample}}{N_{Ref}} \left(\frac{1+\rho_R}{1+2\rho_R}\right)_{Ref} \left(\frac{d\sigma_R}{d\Omega}\right)^{-1}_{Sample} \tag{6.10}$$

And thus the general form of Eq. 6.3 of the manuscript is obtained, relating the relative FSRS intensities measured in a linear approximation to the DRSCs:

$$\left(\frac{d\sigma_R}{d\Omega}\right)_{Sample} = \left(\frac{1+\rho_R}{1+2\rho_R}\right)_{Sample} \left(\frac{1+2\rho_R}{1+\rho_R}\right)_{Ref} \left(\frac{m_{Sample}}{m_{Ref}}\right) \left(\frac{N_{Ref}}{N_{Sample}}\right) \left(\frac{d\sigma_R}{d\Omega}\right)_{Ref} \tag{6.11}$$

An advantageous property of the current work and derivation is that any improvement on the reference values for the reference DRSC or the sample and reference linear depolarization ratios can quickly be used to obtain more accurate sample DRSC values. In addition, the factor containing the depolarization ratios in Eq. 6.11 (Eq. 6.3 in manuscript) can only vary from 0.5 to 0.636 across the full range of $\rho = 0$ vs. $\rho = 0.75$. This small possible variance in the factor leads to a maximum percent difference of $\sim 24\%$.

Differential Raman scattering cross-sections were computed using the frequency dependent AORESPONSE module of Amsterdam Density Functional theory with the BP86 functional and TZ2P basis set.[135] The calculated polarizability derivatives were converted to differential Raman scattering cross-sections by the following equation:[136]

$$\frac{d\sigma_P}{d\Omega} = \frac{\pi^2}{\epsilon_0^2}(\omega - \omega_P)^4 \frac{h}{8\pi^2 c\omega_P} S_P \left[45\left(1 - e^{\frac{-hc\omega_P}{k_B T}}\right)\right]^{-1} \tag{6.12}$$

Where $\frac{d\sigma_P}{d\Omega}$ is the differential Raman scattering cross-section of the p^{th} vibrational mode, ϵ_0 is the vacuum permittivity, ω_P is the frequency of the p^{th} vibrational mode, ω is the frequency of the incident laser field (514.5 nm in presented work), h is Planck's constant, c is the speed of light, k_B is the Boltzmann constant, T is temperature (300 K in presented work), and S_P is the scattering factor for the p^{th} vibrational mode.

The scattering factor gives the overall Raman activity of the vibration and is composed of the isotropic and anisotropic polarizabilities:

$$S_P = 45\alpha_P'^2 + 7\gamma_P'^2 \tag{6.13}$$

Where $\alpha_P'^2$ is the square of the isotropic polarizability and $\gamma_P'^2$ is the anisotropic polarizability.

Specifically, the isotropic polarizability is defined as:

$$\alpha_P' = \frac{1}{3}\left(\left(\frac{d\alpha_P}{dQ}\right)_{xx} + \left(\frac{d\alpha_P}{dQ}\right)_{yy} + \left(\frac{d\alpha_P}{dQ}\right)_{zz}\right) \tag{6.14}$$

While the anisotropic polarizability is defined as:

$$\gamma_P'^2 = \frac{1}{2}\left[\left(\left(\frac{d\alpha_P}{dQ}\right)_{xx} - \left(\frac{d\alpha_P}{dQ}\right)_{yy}\right)^2 + \left(\left(\frac{d\alpha_P}{dQ}\right)_{xx} - \left(\frac{d\alpha_P}{dQ}\right)_{zz}\right)^2 + \left(\left(\frac{d\alpha_P}{dQ}\right)_{yy} - \left(\frac{d\alpha_P}{dQ}\right)_{zz}\right)^2 + 6\left(\left(\frac{d\alpha_P}{dQ}\right)^2_{xy} + \left(\frac{d\alpha_P}{dQ}\right)^2_{xz} + \left(\frac{d\alpha_P}{dQ}\right)^2_{yz}\right)\right] \tag{6.15}$$

To compensate for the lack of dielectric medium for the gas-phase molecule DRSCs calculated in Eq. 6.12, we introduce a local field correction (L) given by:

$$L = \left(\frac{n^2+2}{3}\right)^4 \tag{6.16}$$

where n is the refractive index of the liquid.[193] For cyclohexane the refractive index of cyclohexane is used ($n = 1.43$) and for glucose the refractive index of water is used ($n = 1.34$), resulting in $L = 3.29$ and $L = 2.53$ for cyclohexane and glucose, respectively.

For final comparison to experimental data, the DRSCs resulting from Eq. 6.12 were multiplied by the appropriate local field correction and broadened to a Lorentzian with FWHM of 20 cm^{-1}.

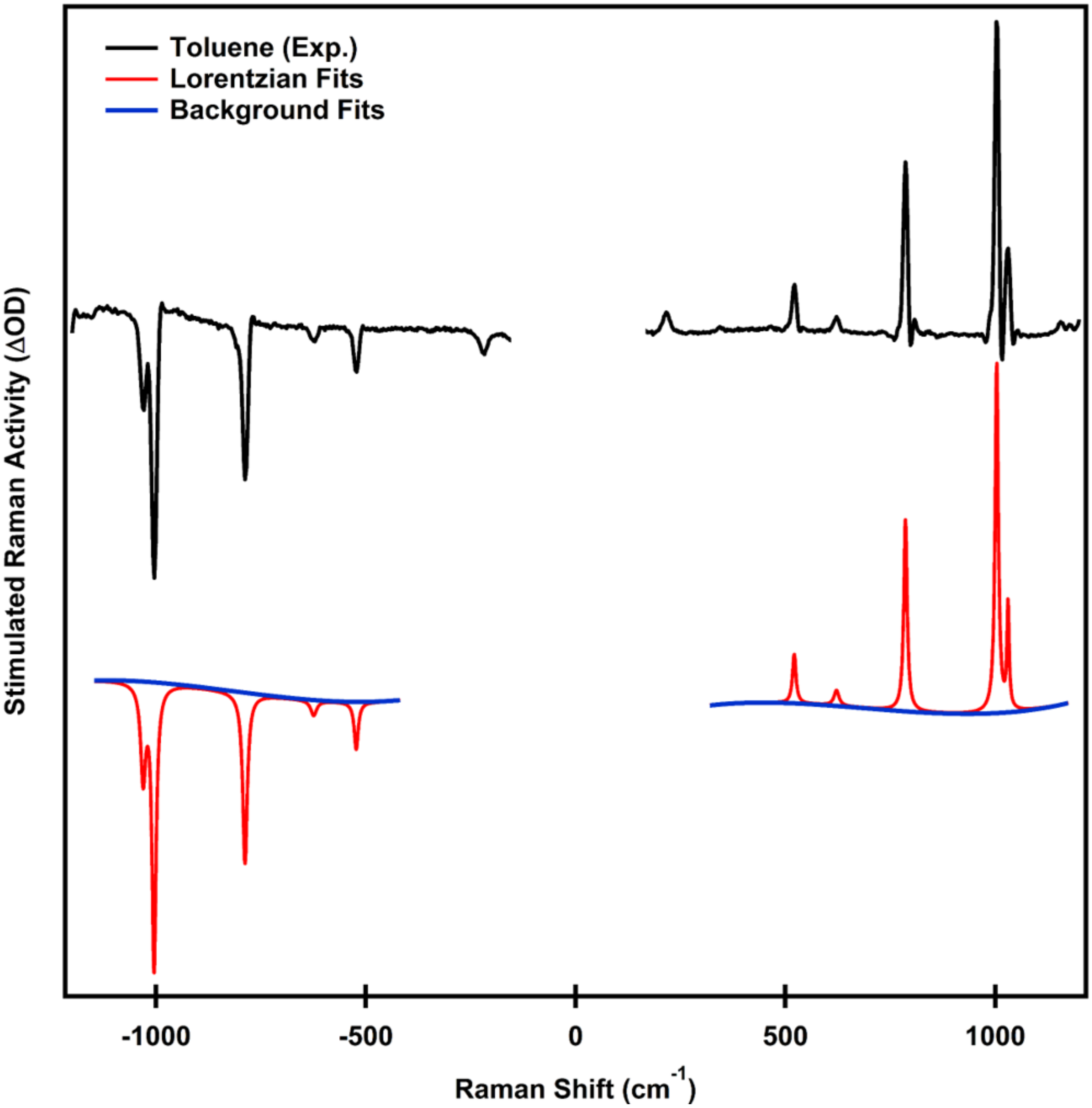

Figure 6.7. Determining the linewidths resolvable in the FSRS apparatus used for the glucose measurements. In the figure, FSRS spectra of neat toluene taken with 1.6 μJ/pulse (black) is shown along with the Lorentzian fits (red) and the cubic backgrounds (blue). The peak position and FWHM are shown in Table 6.3. Figure reproduced with permission from Ref. 173. Copyright 2017 American Chemical Society.

ν_{fit} (cm^{-1})	FWHM (cm^{-1})
-1030.8 ± 0.4	14.0 ± 1.4
-1004.7 ± 0.1	11.8 ± 0.4
-787.9 ± 0.2	13.2 ± 0.7
-624.3 ± 2.7	16.5 ± 8.9
-522.9 ± 0.7	11.3 ± 2.2
521.1 ± 0.7	9.7 ± 2.1
621.9 ± 2.6	14.2 ± 8.2
786.2 ± 0.2	9.5 ± 0.5
1003.7 ± 0.1	9.0 ± 0.3
1030.7 ± 0.3	6.1 ± 0.7

Table 6.3. Peak position and FWHM of fitted toluene spectrum from Fig. 6.7. The fitted FWHM of the toluene Raman modes confirm a sub-20 cm^{-1} spectral resolution to the experiment. The narrower linewidths in the SRG side is attributed to the chirp of the probe pulse resulting in a slight variation in the relative timing of the Raman pump and probe pulses across the frequency domain of the probe pulse.[130]

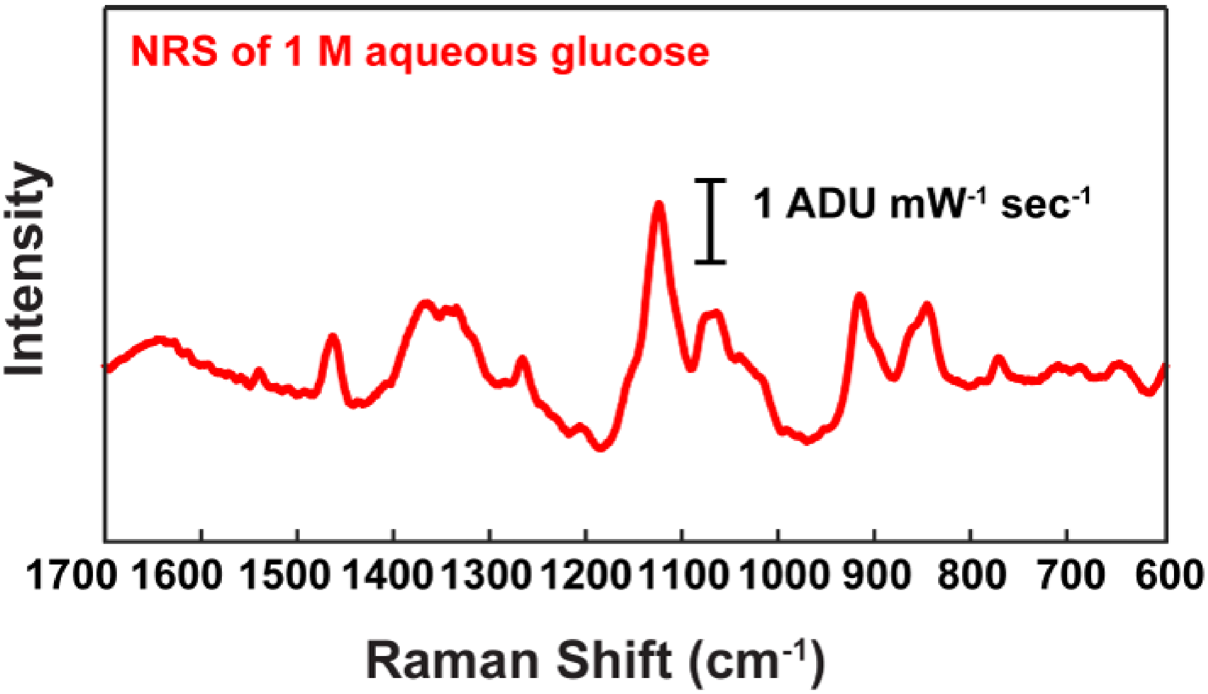

Figure 6.8. Normal Raman scattering (NRS) spectrum of 1 M aqueous glucose. NRS spectrum was collected using 12 mW of 785 nm continuous wave excitation laser through a 20x dry objective for a 60 second acquisition. Figure reproduced with permission from Ref. 173. Copyright 2017 American Chemical Society.

APPENDIX A

Original Research Proposal: Controlling charge transfer plasmons for infrared nanoantennae

A.1. Statement of Objectives

Plasmonic materials have extraordinary properties that have led to advances in near-field optics,[198] constructive (and destructive) interference in optical spectroscopies,[23,110] and new chemical applications.[3] [*] All of these advances are due to the large light-matter (photon-electron) coupling on the surface of the plasmonic materials, the largest in nature.[2] By intelligent engineering of plasmonic materials on the nanoscale, localized surface plasmon resonances (LSPRs) can be manufactured to couple with specific wavelengths of light. In addition to the LSPR of a single nanoparticle, many other plasmon resonances can occur when multiple plasmonic particles interact.[199] The interaction of multiple particles to create novel resonances leads to broader tunability than that achieved by single particles alone.[200,201]

The reality of continuously tunable plasmonic materials from the near-infrared (NIR, ~0.8-1.4 μm) through shortwave infrared (SWIR, 1.4-3 μm) to the midwave-infrared (MWIR, 3-8 μm) has proven to be difficult using single nanoparticle aggregates of

---

[*] This proposal was submitted as a 2017 National Research Council Research Associateship Proposal that was funded with a score of 92/100 but declined by M.O. McAnally.

traditional plasmonic materials.[201] Having continuously tunable plasmonic resonances from the NIR to MWIR is advantageous for numerous optical applications and light-driven chemical applications including plasmonically-enhanced optical spectroscopies (ie: surface-enhanced Raman scattering (SERS)),[8,23] and plasmon-enhanced photocatalyic water splitting.[3,202–204] While we are interested in learning general design principles for plasmon resonance tuning across the full NIR-MWIR spectrum (Fig. A.1), we are particularly interested in exploiting resonances in the NIR-SWIR to introduce new disruptive technology near telecommunication wavelengths (1.26-1.675 μm).

To study the tunability of plasmonic materials across the broad wavelength range spanning NIR to MWIR, we propose to use and control a variety of plasmonic modes in gold nanorods (AuNRs). In addition to the LSPR, bonding dipole plasmon (BDP) and charge transfer plasmon (CTP) modes will be exploited. The work of Fontana *et al.* has demonstrated the utility of AuNRs as ideal building block materials for tuning optical properties of the plasmonic material across a broad range (Fig. A.2).[200] The research efforts in this proposal will provide fundamental understanding of the femtosecond time scale evolution of the welding process, where the nanoscopic junctions transition from capacitive to conductive, allowing us to adjust the width and resonant frequency of the plasmon resonance over a decade of wavelengths (Fig. A.2).

A.2. Research Effort

To fully realize the utility of AuNRs for disruptive technologies in the infrared three distinct research directions, described as work packages (WP), will be taken. The first

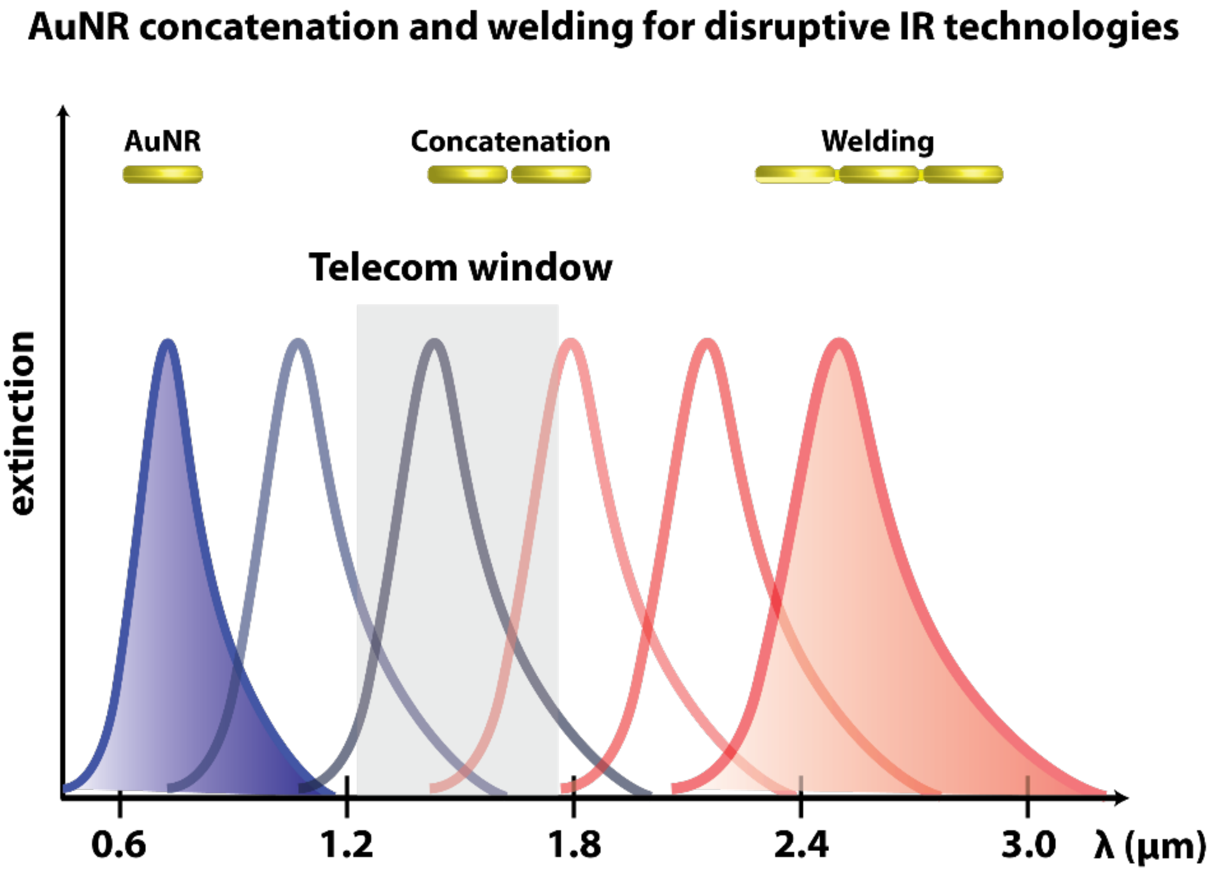

Figure A.1. Using techniques from Fontana *et al.* broadly tunable plasmonic material technologies from the NIR to MWIR wavelengths will be created. The key is to use a combination of robust AuNR building blocks that can be concatenated together to create bonding dipole plasmon (BDP) modes and then further welded to create charge transfer plasmon (CTP) modes. Using these techniques, a combination of LSPR, BDP, and CTP plasmonic modes will provide full tunability.

work package (WP1) focuses on understanding the current techniques of AuNR concatenation and light-driven welding for formation of BDP and CTP plasmonic modes (Fig. A.4), at more fundamental levels by new experimental approaches.[200,201] By explicitly measuring and modeling the process depicted in Fig. A.4 using ultrafast spectroscopic techniques and finite element method (FEM) simulations, we will gain new insight into

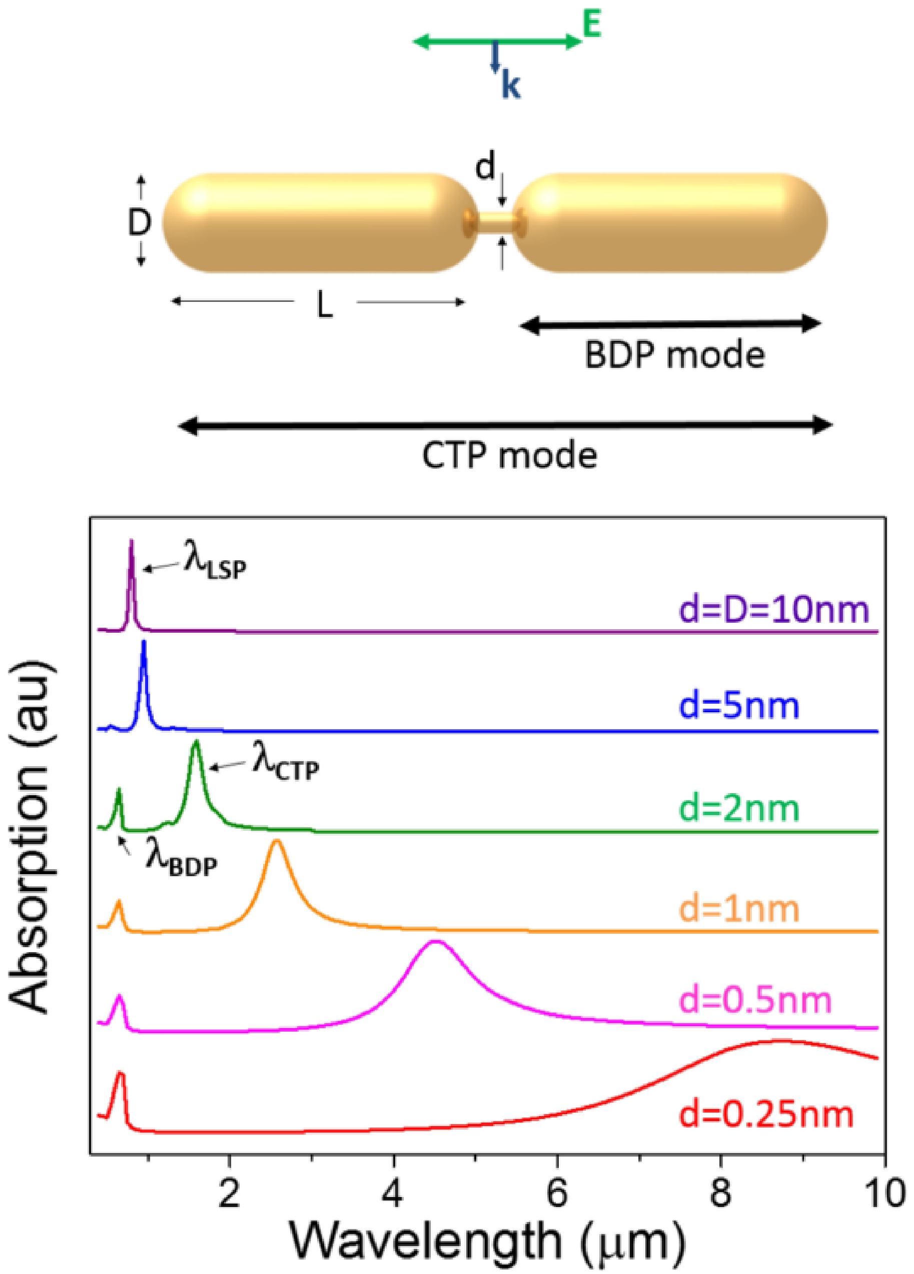

Figure A.2. (Top) Schematic of a AuNR dimer structure of aspect ratio L/D and separation of d. (Bottom) Three-dimensional finite element method (FEM) simulations of absorption spectra for different AuNR dimer system parameters. Figure reproduced with permission from Ref. 200. Copyright 2014 American Institute of Physics.

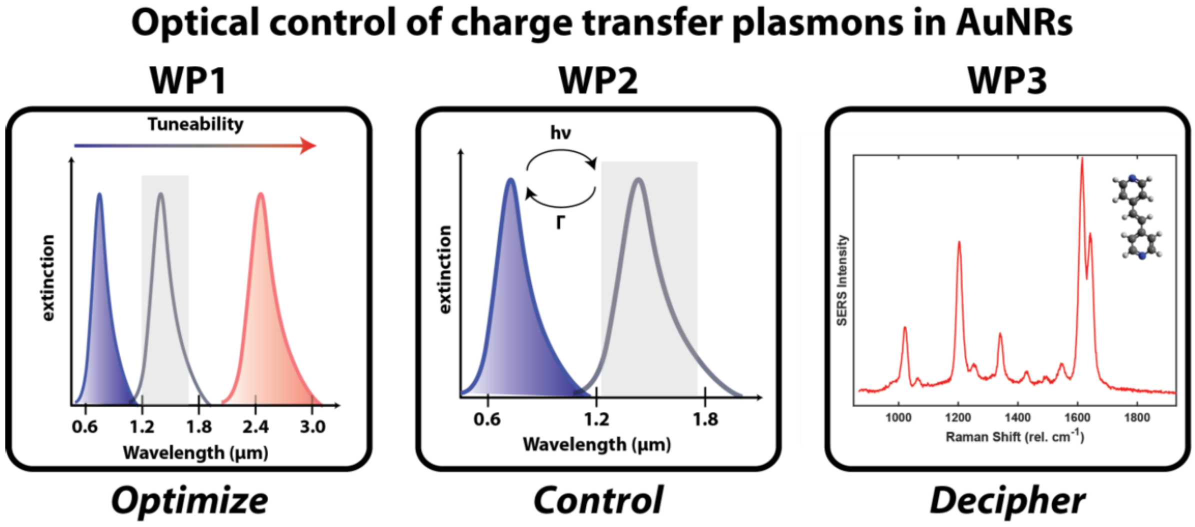

Figure A.3. The research effort will be comprised of three separate work packages (WP). WP1 focuses on the optimization of AuNR plasmonic extinction tunability. WP2 will develop methods of photoswitching (hν) of AuNR assemblies for making transient (Γ) plasmonic resonances in the telecommunications spectrum. Finally, WP3 explores the nanoscopic molecular rearrangement occurring during concatenation and welding of the AuNRs by transient SERS measurements.

how to this process can be dynamically controlled. The WP2 expands on knowledge obtained in the investigation of WP1 to create photoswitchable plasmonic materials that can have reversible extinction properties in the telecommunications band of the NIR-SWIR. WP3 attempts to gain fundamental understanding of the molecular and nanoparticle rearrangement occurring during concatenation and welding at the nanoscopic scale using SERS.

A.2.1. WP1

In WP1, we will understand and control the concatenation and welding process in AuNRs. In optimizing the tunability of AuNR concatenation and welding for creating plasmon resonances throughout the NIR-MWIR spectrum we will essentially control the

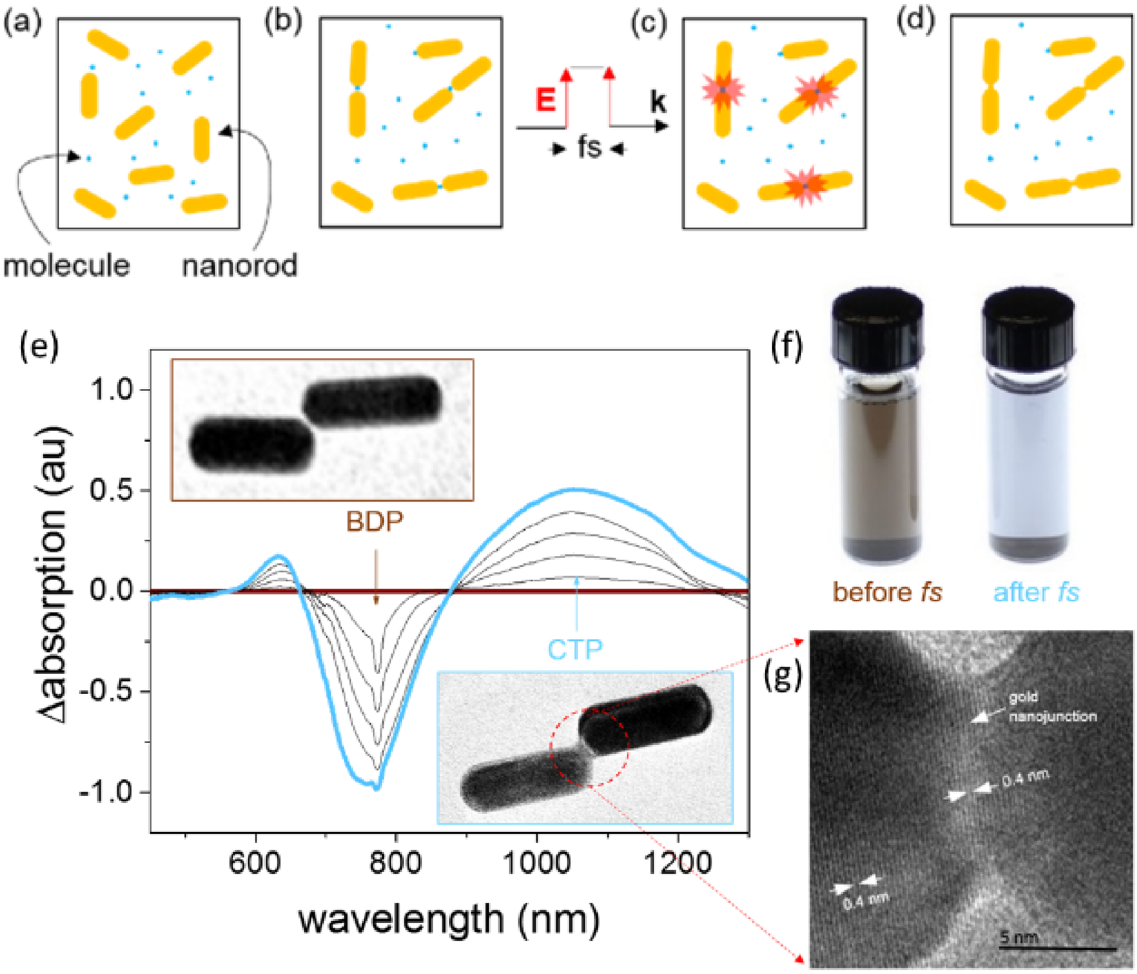

Figure A.4. AuNRs (a) with molecular linkers spontaneously concatenate (b) creating BDP modes (e). By femtosecond laser irradiation, the concatenated AuNRs weld, creating CTP modes (e). (g) High resolution TEM (HRTEM) images show the collapse of the nanoparticle gap and presence of a conductive Au channel. Figure reproduced with permission from Ref. 201. Copyright 2016 American Chemical Society.

flow of charge at optical frequencies through the nanojunction. While AuNR syntheses have been optimized and studied for numerous years;[205,206] for the studies performed herein we will use a new cutting edge synthetic technique that allows for more control of

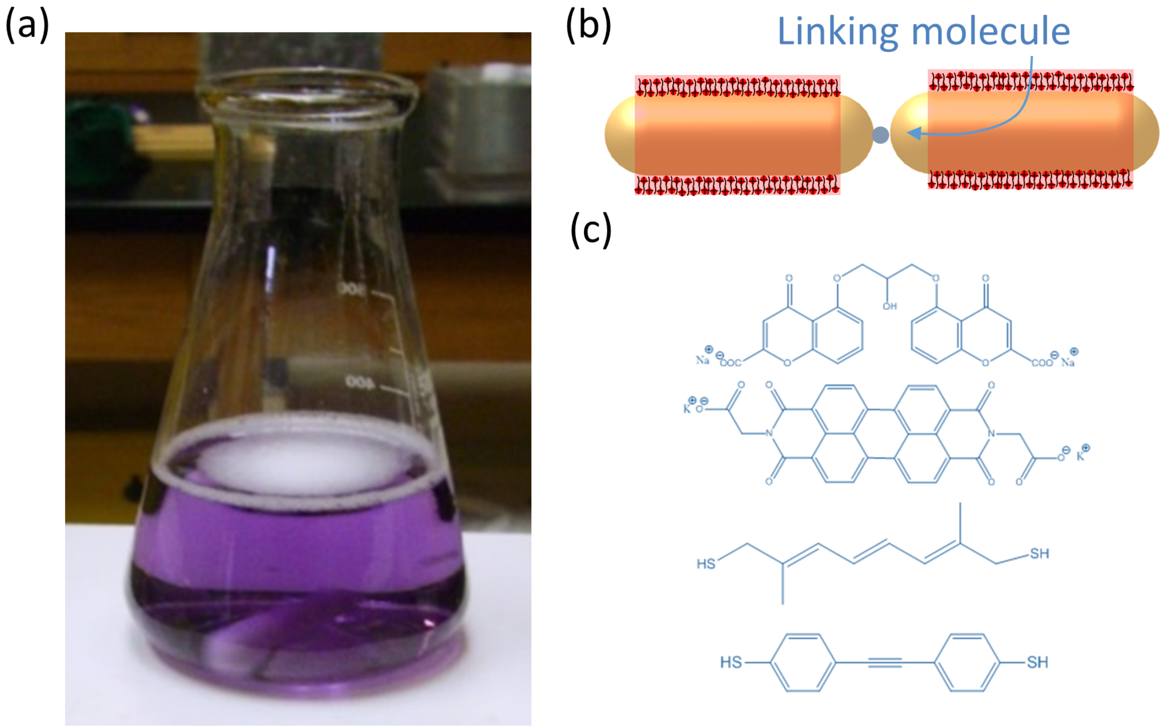

Figure A.5. (a) Image of flask containing AuNRs created by the Park *et al.* synthetic procedure.[207] (b) Schematic of molecular linker molecules aiding concatenation of AuNRs. (c) Potential molecular analytes to be used for concatenation and transient SERS tracking.

the surface chemistry on the AuNR (Fig. A.5).[207]

Using the AuNR systems diagramed in Fig. A.5, we will investigate the synthetic and photophysical parameter space in AuNR concatenation and welding. To map the parameter space, we will systematically vary AuNR aspect ratios, linker molecules, and laser excitation parameters (fluence, wavelength, pulse width, and polarization) while watching the transient plasmonic response in a pump-probe (transient absorption, TA)

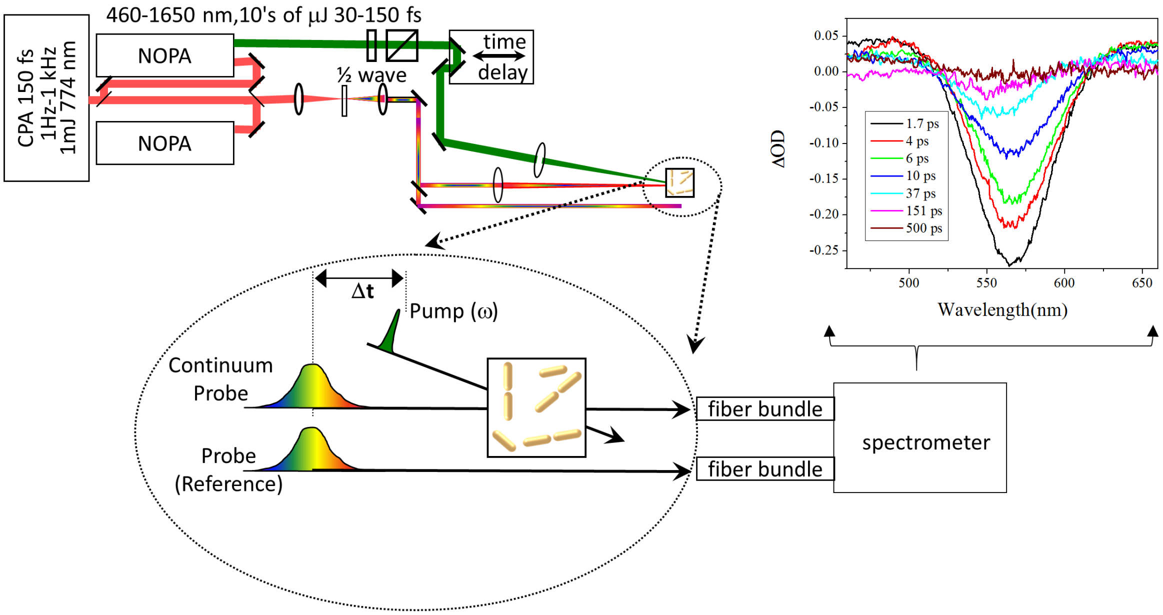

Figure A.6. Transient absorption laser system to be used for monitoring the plasmonic response of AuNRs being concatenated and welded by pump excitation. The system consists of a chirp-pulsed amplifier (CPA)-pumped noncollinear optical parametric amplifier (NOPA) for generating the pump and probe beams needed in transient absorption (TA). TA data will be collected using fiber coupled detection with separate reference channel collection for high signal-to-noise differential optical density spectra.

laser setup (Fig. A.6).

The TA system shown in Fig. A.6 will be an essential equipment in this proposal. As the laser parameters are tuned with respect to AuNR system variables, a full parameter space will be mapped out. Optimization of the AuNR concatenation and subsequent welding (Fig. A.4) will lead to design principles for more stable and reproducible plasmonic systems in the NIR-SWIR to be utilized in WP2.

A.2.2. WP2

Using the same optical system in WP1, WP2 focuses on controlling the presence of plasmonic modes in the telecommunications window of the NIR-SWIR. A method of modulating the gap without irreversible change is to excite the phonon modes of the AuNRs.[205] Exciting the phonon modes of the AuNR will transiently modulate the gap distance between the particles resulting in a transient plasmonic response (Fig. A.7).

As opposed to the irreversible change of plasmon resonance explored in WP1, WP2 builds on the parameter space knowledge gained by the TA experiments of WP1 to push the system to the brink of irreversible change. Using the combination of concatenation and welding with the AuNR systems will bring the system to a plasmon resonance near a desired window in the telecommunications range. Then using excitation provided by the pump field in the TA experiment shown in Fig. A.6 phonon excitation will create the small modulation needed to adjust the final plasmonic property. As suggested in the FEM analyses displayed in Fig. A.2 the final plasmonic properties are highly dependent on the gap distance, where angstrom level displacements can result in hundreds of nanometer shifts to the plasmon resonance. This proposed work in WP2 can result in directly applicable, switchable, disruptive IR technologies using these AuNR systems.

A.2.3. WP3

WP3 will explore the molecular scale origin of CTP creating by welding. Previous LSPR studies that examined the changing plasmon regimes in spherical Au nanoparticles[208] and measured transient SERS spectra of molecular analytes embedded between spherical Au

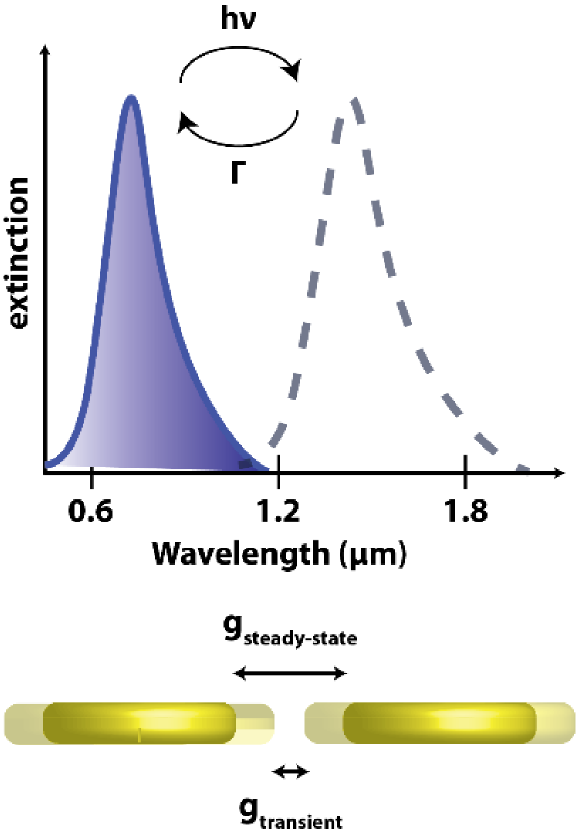

Figure A.7. To create photoswitchable plasmonic resonances the AuNR systems will be driven through careful concatenation and welding to a steady-state gap distance (g) producing a stable plasmon resonance. By photoexciting (hν) phonon modes in the AuNRs, a transient g is introduced, which will give a short-lived plasmon resonance in red-shifted frequencies. The AuNRs phonon modes decay and relax (Γ) to the steady-state resonance.

nanoparticles[140,209] suggest that there are interesting dynamics to be observed in molecular vibrational spectroscopy during the formation of a CTP. In WP3, we will directly measure the SERS response of molecular linkers (Fig. A.5) involved in AuNR concatenation during creation of CTP modes using the laser system described in WP1 and WP2 (Fig. A.8).

The laser shown in Fig. A.6 will be used in a different mode for WP3 compared to WP1 and WP2. In these experiments, we will use a broadband femtosecond pulse (typically the probe for TA) as a pump and t_0 excitation for welding to initiate. Then, the AuNRs will

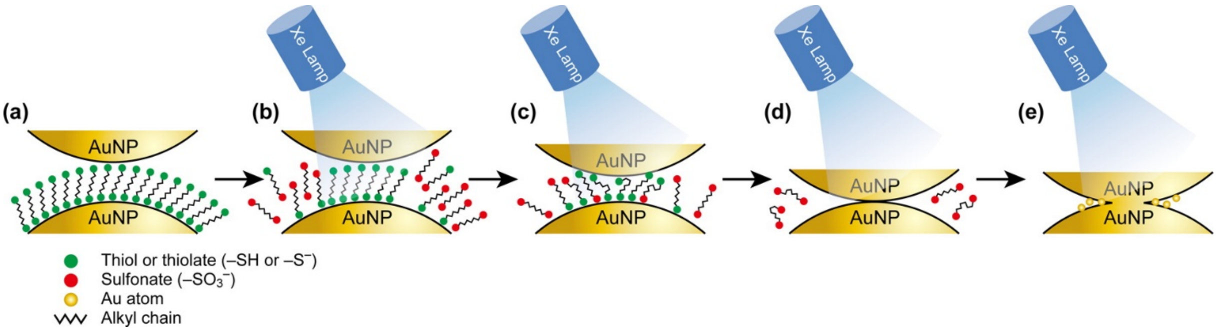

Figure A.8. As the AuNRs with molecular linkers are excited by broadband light (Xe Lamp in Ref. 208, broadband probe field in WP3) the AuNRs weld. Starting from just concatenated AuNRs (a) light excitation drives AuNRs to weld (b-e). During the welding process, the molecular linkers will be strongly influenced by optical confinement, electrons tunneling in formation of the CTP, and strong perturbations on the molecular equilibrium geometry. Figure reproduced with permission from Ref. 208.

be interrogated during different amounts of completed welding by a picosecond bandwidth pulse for measuring a transient SERS response. By varying the time separation of the pulses and fluence of the t_0 pulse, transient SERS spectra can be obtained that illustrate the changing environment sampled by the molecule in the nanoscale. Using the time-resolved SERS measurement of the liner molecules will provide a two-handle approach (transient SERS and TA) to understanding the physics of optical control of plasmon resonances in AuNRs.

A.3. Experimental Results, Significance, Application

The work described herein will provide significant improvement in current disruptive IR technologies using plasmonic materials. Each WP contains results which will further advancement of goals for the Office of Naval Research (ONR) and the general scientific community. Specifically, the proposed work leverages and amplifies current 6.1 and 6.2 programs being supported by NRL, ONR, and at the N2N6 level. The results of WP1, optimization of AuNR concatenation and welding for tunability from NIR-MWIR, will provide impactful design principles for widespread use of AuNR technology in designing plasmonic materials. WP2 results provide a technical approach that is directly applicable to interests of the ONR and general national security interests for switchable disruptive IR technologies. Finally, WP3 gives a fundamental molecular identification to chemistry happening at the nanoscale. Using a transient SERS approach will elucidate mechanisms of BDP and CTP plasmon mode formation. The following Gantt chart (Table A.1) describes the projected evolution of the research effort in terms of milestones (M), deliverables (D), conference presentations, and public outreach.

As each WP is connected, significant overlap of the schedule is expected. However, each WP contains independent milestones and deliverables that will be disseminated to professional and general audiences as appropriate in conferences and scientific outreach, respectively. The conferences listed in the Gantt chart were chosen specifically to reach audiences that would be most likely to adapt the research efforts described in this proposal in their own research. The Materials Research Society (MRS) conference is a broad scientific conference with researchers in many fields using materials for different applications. The Gordon Research Conference (GRC) on Vibrational Spectroscopy was chosen as a more focused conference to discuss the work as it will engage many academic researchers in a closer environment allowing for more detailed discussions and higher yield for technique adoption.

In addition, the applicant is a co-chair for the next Gordon Research Seminar on Vibrational Spectroscopy, which caters exclusively to graduate students and young postdoctoral researchers: providing an opportunity for recruiting more talented researchers

Month	1-3	4-6	7-9	10-12	13-16	17-20	21-24
WP1	🟧	🟧	🟧				
M1 - Build fs-TA 1 kHz system for tracking phonon oscillations in AuNRs to verify setup	🟧						
M2 - Obtain data for fs-TA of the AuNR systems observing the growth of a CTP		🟧					
D1 - Write technical paper on optimziation of the welding technique for CTP in AuNRs			🟧				
WP2			🟦	🟦	🟦		
M3 - Improve the control of CTP by phonon modulation using the 1 kHz system			🟦	🟦			
D2 - Write technical paper on the optimization of controlled CTP in NIR-SWIR				🟦	🟦		
WP3					🟥	🟥	🟥
M4 - Obtain data for transient SERS of molecular linkers involved in CTP of AuNRs					🟥	🟥	
D3 - Write paper on the correlation of transient SERS with CTP formation						🟥	🟥
Conference Presentations			MRS		GRC		
Engagement with General Public	PEPP		PEPP		PEPP		PEPP

Table A.1. Gantt chart showing project schedule of the research effort described in this proposal. Each work package (WP) has milestones (M) and deliverables (D) to verify progress of the project. In addition, specific conferences will be attended including the Materials Research Society (MRS) conference and the Gordon Research Conference (GRC) on Vibrational Spectroscopy. Scientific engagement with a general audience will be done through the Department of the Navys Personal Excellence Partnership Program (PEPP).

to national and federal laboratories and research centers. Finally, continuing the public outreach performed graduate studies, the applicant will participate in the Personal Excellence Partnership Program (PEPP) facilitated by the Department of the Navy. PEPP provides an opportunity to mentor younger scientific minds in local public schools.

A.4. Conclusion

This proposal provides a description of new work to be performed in controllably creating disruptive IR technologies using AuNRs as building blocks for optical manipulation. Each WP has clearly delineated goals and accomplishments that are of high general scientific and national security interests. It is anticipated that this work will have significant intellectual merit in addition to the broad impacts, particularly in the proposed three-step approach. In going from optimization, to control, and finally understanding of the CTP from macroscopic observable of extinction to kinetics of transient molecular response; unprecedented knowledge of AuNR response will be determined.

APPENDIX B

Calculated Surface-Enhanced Raman Spectra of Atomic Layer Deposition Precursors

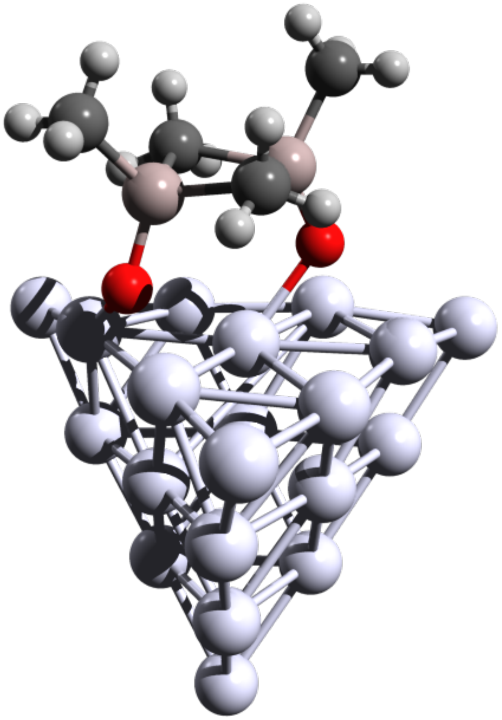

DFT-optimized structure of TMA dimer on Ag_{20} cluster.

B.1. Abstract

This section details the electronic structure calculations performed in support of papers published on determining the structure of atomic layer deposition (ALD) precursors on AgFONs.[210–212] ALD is a robust deposition technique that has been used to fabricate a variety of thin films and nanostructures from pure metals,[213] metal oxides,[214,215] metal nitrides,[216] and metal sulfides.[217] While ALD is commonly thought of as creating uniform, pinhole-free layers; this isn't true until multiple cycles of the ALD process have completed. Before uniform growth is achieved, island growth and individual species adsorption dominates. Therefore, in recent studies by the Van Duyne group,[210–212] SERS was used during early growth cycles to observe the vibrational spectra of adsorbed species on the AgFON surface. To understand and identify molecular species present in alumina deposition, electronic structure calculations of the Raman scattering spectra for potential analytes were simulated.

B.2. Gas-Phase Trimethylaluminum Raman Scattering Calculations

In the first of three papers,[210] electronic structure calculations were performed to help assign vibrational modes observed in the differential SERS spectra of trimethylaluminum (TMA) deposited on AgFONs.[*] The electronic structure calculations determined the gas-phase Raman of the dimer and monomer TMA species *in vacuo*.

Electronic structure calculations presented in this work have been performed with the Amsterdam Density Functional (ADF) computational chemistry package.[135] Full geometry optimization, frequency, and polarizability calculations for isolated monomer and

---

[*] This section has been reproduced with permission from Ref. 210 . Copyright 2016 American Chemical Society.

dimer TMA complexes were completed using the Becke-Perdew (BP86) generalized gradient approximation (GGA) exchange correlation functional and a triple-ζ polarized (TZP) Slater orbital basis set.

Static Raman polarizabilities (ω=0) were calculated in the RESPONSE package by two-point numerical differentiation using the RAMANRANGE keyword. Raman scattering intensities were determined by the scattering factor: $45\alpha_j'^2 + 7\gamma_j'^2$, where α_j' and $\gamma_j'^2$ are the isotropic and anisotropic polarizability tensors with respect to the j^{th} vibrational mode. The Raman intensity for each vibrational mode were broadened to a Lorentzian lineshape with full-width at half-maximum (FWHM) of 10 cm^{-1} for comparison to experimental data. Optimized structures and Raman scattering spectra are displayed in Figs. B.1-B.2 and B.3, respectively.

B.3. Silver Cluster-Trimethylaluminum Raman Scattering Calculations

In the second of three papers,[211] electronic structure calculations were performed to help assign vibrational modes observed in the differential SERS spectra of trimethylaluminum (TMA) deposited on AgFONs to help in understanding the distance dependence of SERS.[†] These electronic structure calculations determined the Raman of the adsorbed dimer and monomer TMA species on Ag_{20} and Ag_{19} clusters.

Electronic structure calculations presented in this work have been performed with the Amsterdam Density Functional (ADF) computational chemistry package.[135] Full geometry optimization, frequency, and polarizability calculations for surface bound monomer

---

[†] This section has been reproduced with permission from Ref. 211 . Copyright 2016 American Chemical Society.

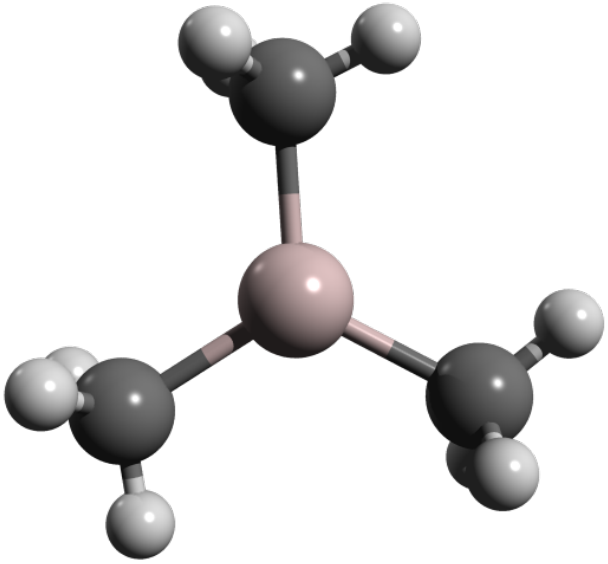

Figure B.1. Optimized gas-phase TMA monomer. Figure reproduced with permission from Ref. 210 . Copyright 2016 American Chemical Society.

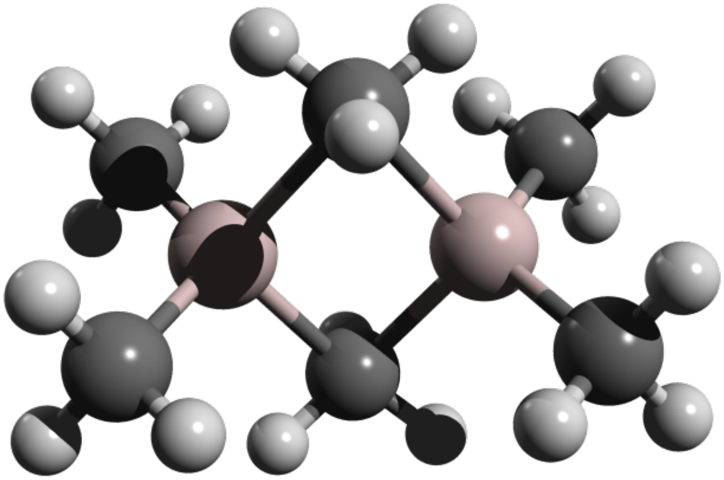

Figure B.2. Optimized gas-phase TMA dimer. Figure reproduced with permission from Ref. 210 . Copyright 2016 American Chemical Society.

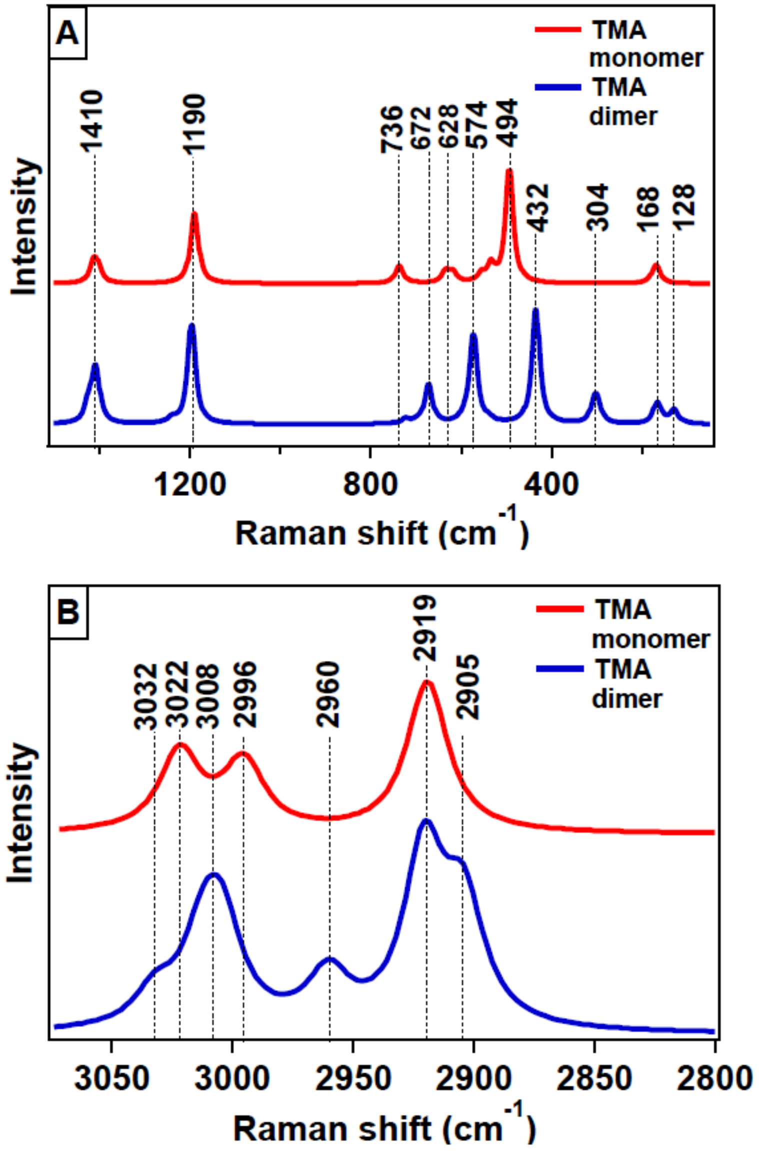

Figure B.3. Gas-phase Raman of optimized monomer and dimer TMA molecules in the low (A) and high (B) wavenumber regions. Figure reproduced with permission from Ref. 210 . Copyright 2016 American Chemical Society.

bound to the surface through two oxygen atoms with a bridging methylene group between the aluminum atoms.

Static Raman polarizabilities (ω=0) were calculated in the RESPONSE package by two-point numerical differentiation using the RAMANRANGE keyword. Raman scattering intensities were determined by Eq. B.1:

$$\frac{d\sigma_j}{d\Omega} = \frac{\pi^2}{\epsilon_0^2}(\omega - \omega_j)^4 \frac{h}{8\pi^2 c\omega_j} S_j \left[45\left(1 - e^{\frac{-hc\omega_j}{k_B T}}\right)\right]^{-1} \tag{B.1}$$

where ω is the frequency of the incident laser field, ω_j is the frequency of the j^{th} vibrational mode, and the scattering factor (S) is: $45\alpha_j'^2 + 7\gamma_j'^2$, where α_j' and $\gamma_j'^2$ are the isotropic and anisotropic polarizability tensors with respect to the j^{th} vibrational mode. The Raman intensity for each vibrational mode were broadened to a Lorentzian line shape with full-width at half-maximum (FWHM) of 10 cm^{-1} for comparison to experimental data. Optimized structures and Raman scattering spectra are displayed in Fig. B.4.

B.4. Silver Cluster-DMACl Raman Scattering Calculations

In the final of three papers,[212] electronic structure calculations were performed to help assign vibrational modes observed in the differential SERS spectra of both trimethylaluminum (TMA) and dimethylaluminum chloride (DMACl) deposited on AgFONs to help in understanding the orientation of ALD precursors on the AgFON surface.[‡] These electronic structure calculations determined the assignment of Raman modes for both the TMA and DMACl SERS spectra.

[‡] This section has been reproduced with permission from Ref. 212 . Copyright 2017 American Chemical Society.

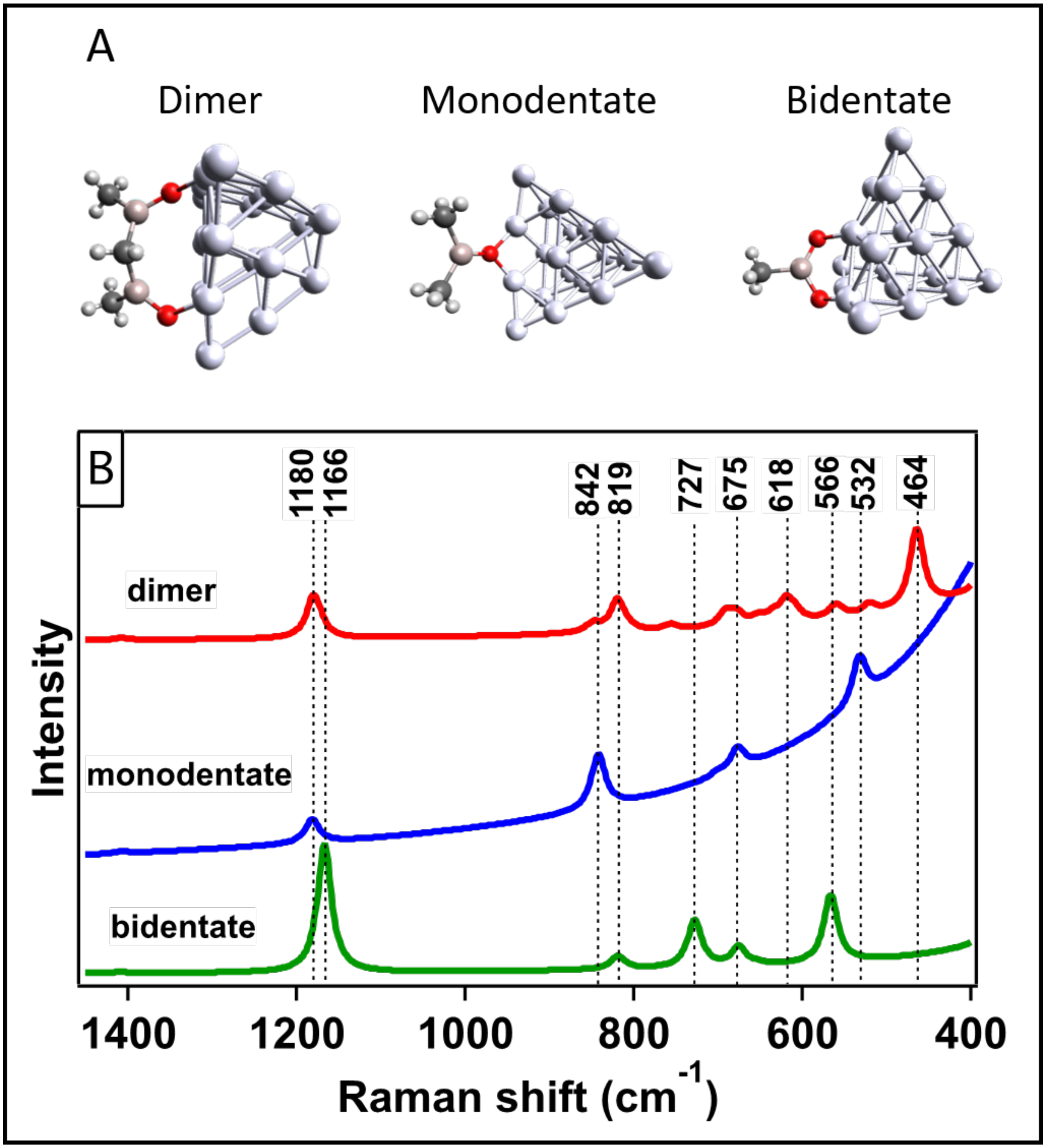

Figure B.4. Optimized cluster models (A) for the TMA dimer-Ag_{19}, TMA monomer monodentate-Ag_{20}, and TMA monomer bidentate-Ag_{20} systems along with the associated SERS simulations (B). Figure adapted with permission from Ref. 211. Copyright 2016 American Chemical Society.

Electronic structure calculations presented in this work have been performed with the Amsterdam density functional (ADF) computational chemistry package.[135] Full geometry optimization, frequency, and polarizability calculations for surface bound monomer (both mono- and bidentate) and dimer TMA and DMACl complexes on Ag_{20} clusters were completed using the Becke-Perdew (BP86) generalized gradient approximation (GGA) exchange correlation functional and a triple-ζ polarized (TZP) Slater orbital basis set.

Static Raman polarizabilities (ω=0) were calculated in the RESPONSE package by two-point numerical differentiation using the RAMANRANGE keyword. Raman scattering intensities were determined by Eq. B.1 with lineshapes simulated using 532 nm excitation and 298 K with a Lorentzian broadening FWHM of 20 cm^{-1} for comparison to experimental data.

Optimized structures and Raman scattering spectra are displayed in Figs. B.5 and B.6.

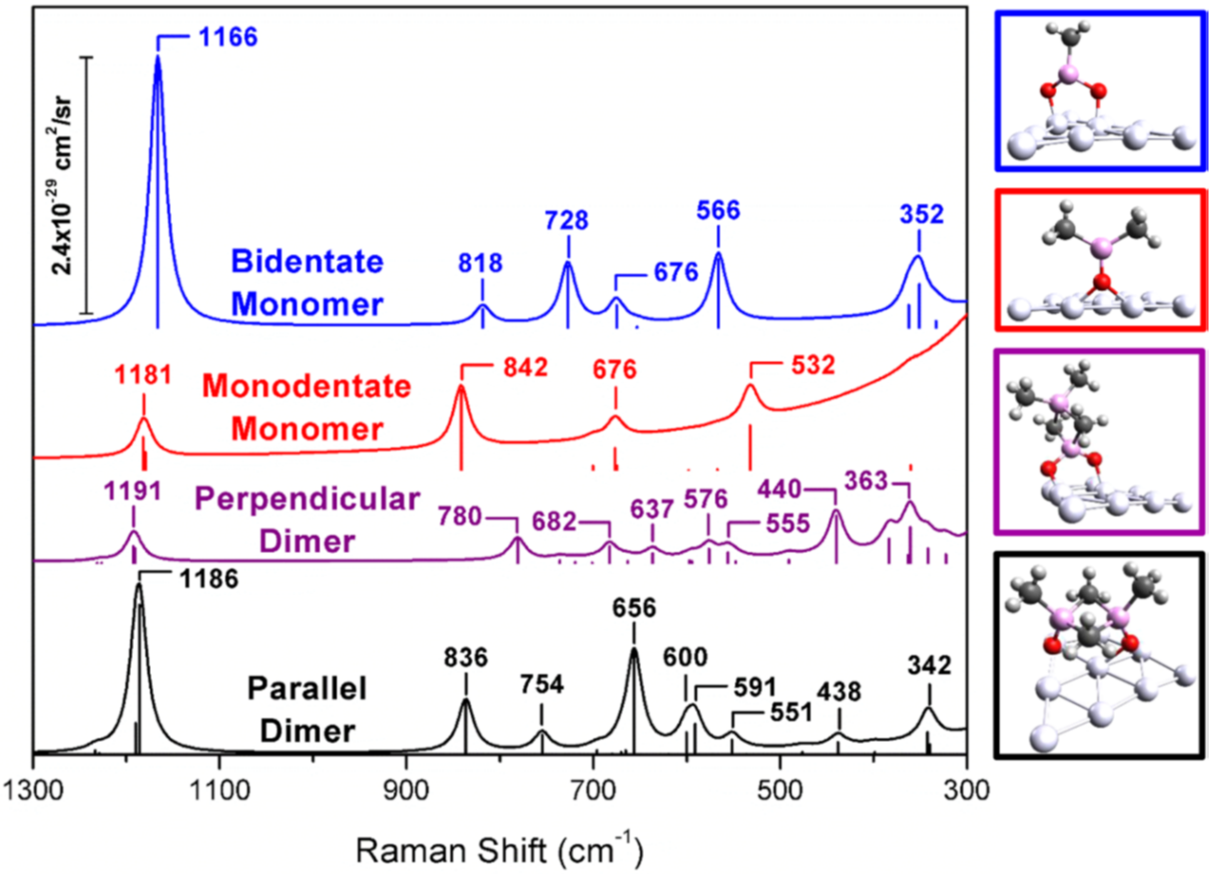

Figure B.5. DFT-calculated Raman spectra (at 298 K) in the low wavenumber region (1300 - 300 cm^{-1}) of TMA surface species (parallel dimer (black), perpendicular dimer (purple), monodentate (red), and bidentate (blue)), with corresponding molecular structures. This figure adapted with permission from Ref. 212. Copyright 2017 American Chemical Society.

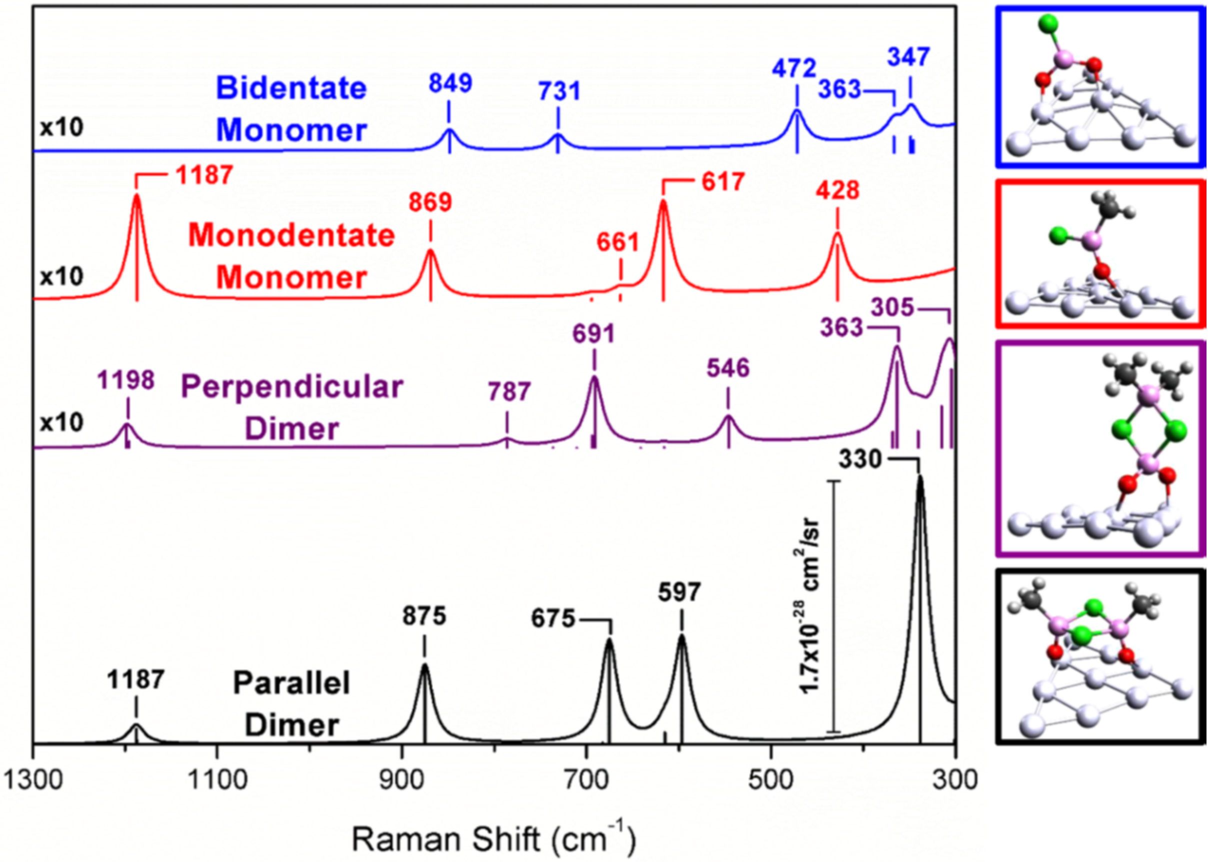

Figure B.6. DFT-calculated Raman spectra (at 298 K) in the low wavenumber region (1300 - 300 cm^{-1}) of DMACl surface species (parallel dimer (black), perpendicular dimer (purple), monodentate (red), and bidentate (blue)), with corresponding molecular structures. The perpendicular dimer, monodentate, and bidentate spectra are magnified (×10) for clarity of comparison. This figure adapted with permission from Ref. 212. Copyright 2017 American Chemical Society.

APPENDIX C

Electronic Structure Calculations of Various Spectroscopic Analytes

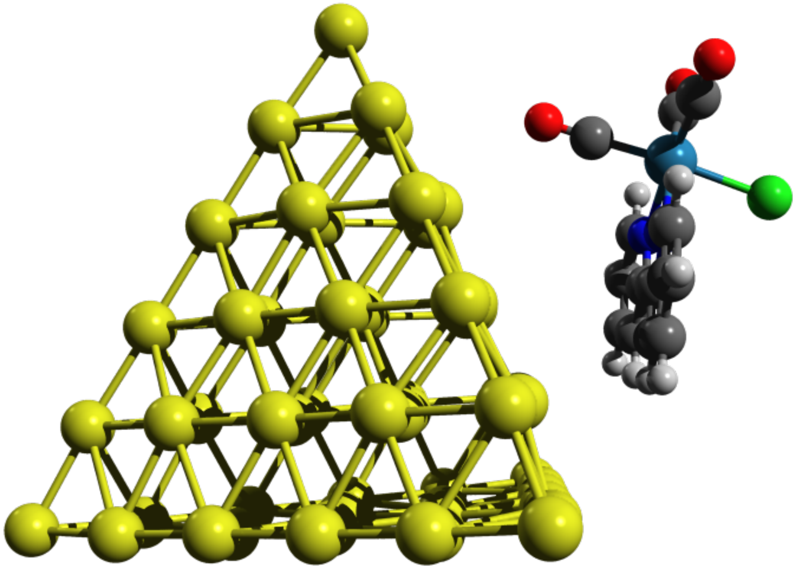

DFT-optimized structure of $Re(bpy)(CO)_3Cl$ on Au_{56} cluster.

C.1. Static Raman Scattering of Bipyridine Isotopologues in Neutral and Anionic States

As eluded to earlier, plasmonic chemistry is a very promising field of research that primarily utilizes the plasmonic substrate as a source of charge carriers for reductive/oxidative chemistry of molecules near a surface.[3] An early target for observing plasmonic chemistry in the Van Duyne group utilized the BPE nanotags used in earlier studies by the group.[72,98,99,110,174,218]

The new experiments performed in this study utilized a “two-color”, “pump-probe” cw laser scheme to interrogate individual 4,4’-bipyridine aggregated AuNPs (BPY-NT’s).[218,219] Briefly, a 532 nm cw laser pumps a BPY-NT which then is probed by SERS using a 785 nm cw laser. Conceptually, the working idea is that the intense 532 nm light (∼10x more intense than the 785 nm probe) induces charge carriers in the nanoparticle to migrate to the surface in some relaxation process from the plasmon oscillation. These carriers can then hop from the nanoparticle surface to the LUMO (or HOMO in case of oxidation) of the adsorbed molecule. To aid in deciphering SERS spectra taken in this experiment, electronic structure calculations were performed on the BPY system: neutral and anionic for both the d_0 and d_8 isotopologues.

DFT calculations were performed for both BPY-d_0 (Fig. C.1) and BPY-d_8 (Fig. C.2) anions using CAM-B3LYP in the 6-311+G** basis set in the Q-CHEM 4.3 computational chemistry package.[220] The CAM-B3LYP functional was selected for comparison against experimental spectra because of its long-range corrected behavior, which is of particular

---

The research described in this section was done in collaboration with Emily Sprague-Klein, Bogdan Negru, and Dmitry Zhdanov.

Mode Assignment	Neutral BPY-*d0*	Neutral BPY-*d8*	Radical BPY-*d0*	Radical BPY-*d8*
Symmetric C-H bending (HCCCCH)	851	851	869	869
Symmetric C-H bending (HCNCH)	960	960	942	942
Asymmetric C=C stretch, ring deformation	1033	1002	1089	1050
Symmetric ring-linking C-C stretch	1332	1245	-	-
Asymmetric ring deformation	-	-	1299	1270
Asymmetric ring stretch	-	-	1391	1413?
C=C-N stretch	-	-	1479	1491?
Symmetric ring stretch	1563	1485	1556	1495
C-N ring stretch	1683	1654	1682	1655

Table C.1. Tentative vibrational mode assignments for simulated Raman scattering spectra for the BPY-*d0* and BPY-*d8* neutral and radical species.

importance desirable when modeling properties of charged molecular species. Optimizations were performed on the neutral and radical anionic species followed by frequency analyses and two-point numeric differentiation of the polarizability to obtain static polarizability derivatives. The differential Raman scattering cross-sections $\left(\frac{d\sigma}{d\Omega}\right)$ were calculated according to the following equation:

$$\frac{d\sigma}{d\Omega} = \frac{\pi^2}{\epsilon_0^2}\left(\omega - \omega_p\right)^4 \frac{h}{8\pi c\omega_p}\left(S_p\right)\left[45(1 - e^{-\frac{hc\omega_p}{k_B T}})\right]^{-1} \tag{C.1}$$

where S_p represents the Raman activity for the p^{th} vibrational mode (ω_p) and the remainder of the expression contains the fourth order dependence of scattering on frequency and the thermal Boltzmann distribution.[136] An excitation of 12738.85 cm^{-1} was used, corresponding to a 785 nm excitation and temperature was assumed to be 298 K. All theoretical spectra were broadened to Lorentzian lineshapes with FWHM of 20 cm^{-1} for comparison to experiment (Fig. C.3).

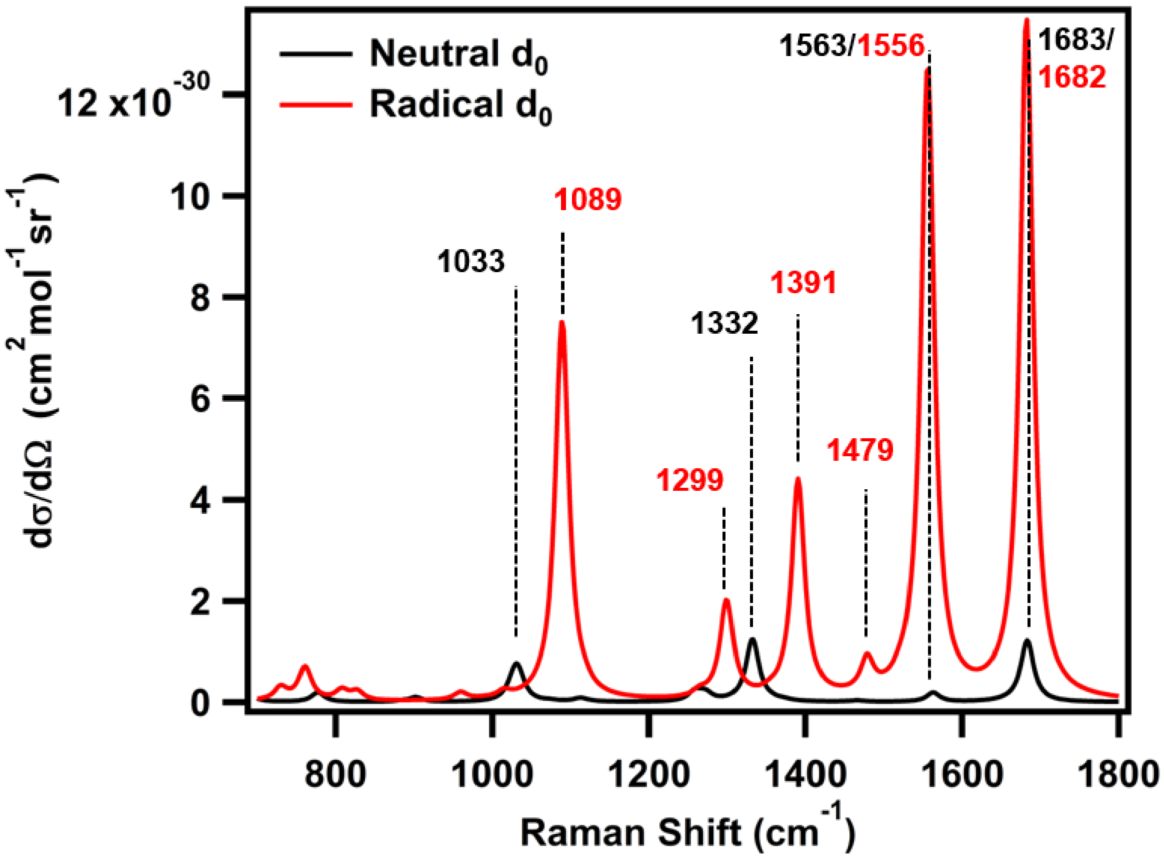

Figure C.1. Calculated Raman scattering of the BPY-d_0 neutral (black) and radical anion (red) species.

The simulated Raman spectra shown in Figs. C.1-C.2 show striking similarity to the transient SERS data shown in Fig. C.3. However, many modes are not seen simultaneously in both the theory and experiment. This is a discrepancy that is still being analyzed, but one likely explanation is that there is a multitude of mechanisms occuring during acquisition of transient SERS. The electronic structure calculations performed herein only consider a gas-phase molecule. A likely scenario is that both the neutral and radical species are present in the probe volume, and are sampling different binding geometries.

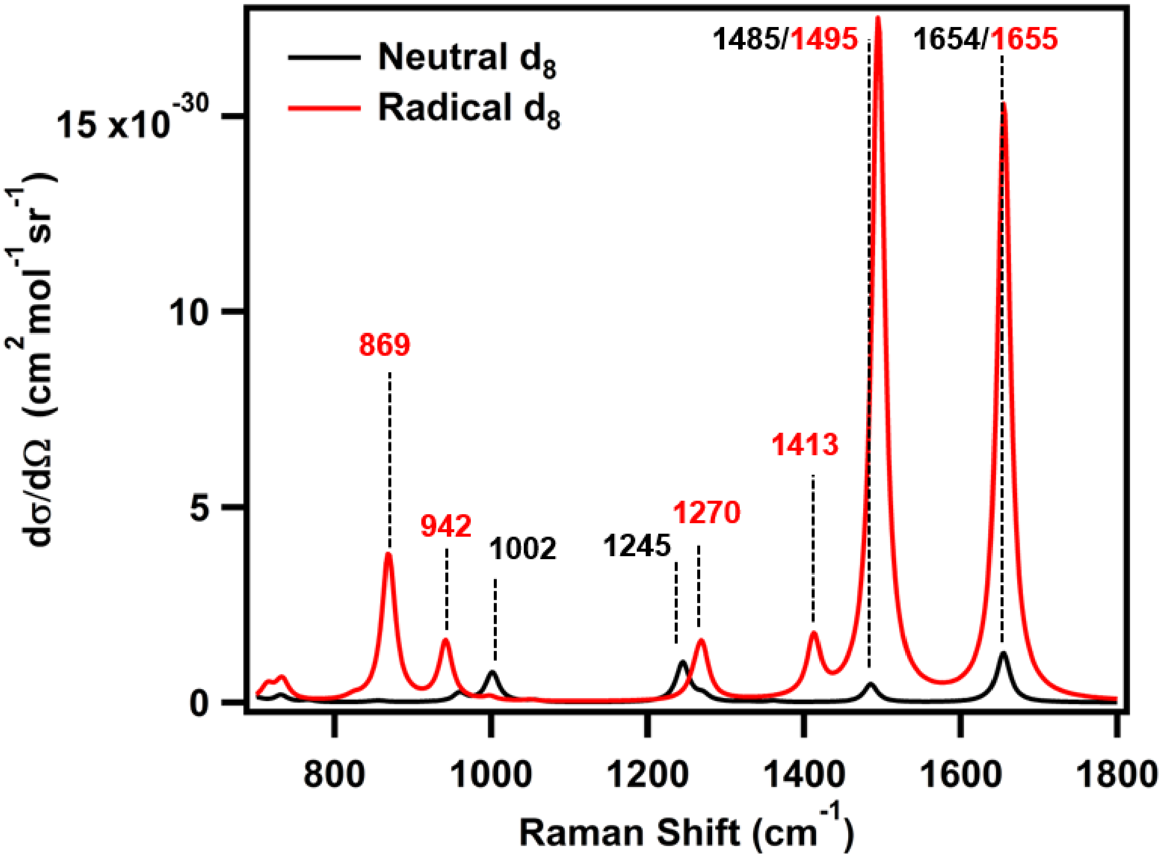

Figure C.2. Calculated Raman scattering of the BPY-d_8 neutral (black) and radical anion (red) species.

The different geometries of the BPY species on the Au surface will result in shifting vibrational frequencies. While this work is preliminary, it suggests that BPY is an excellent reporter molecule for plasmonic chemistry.

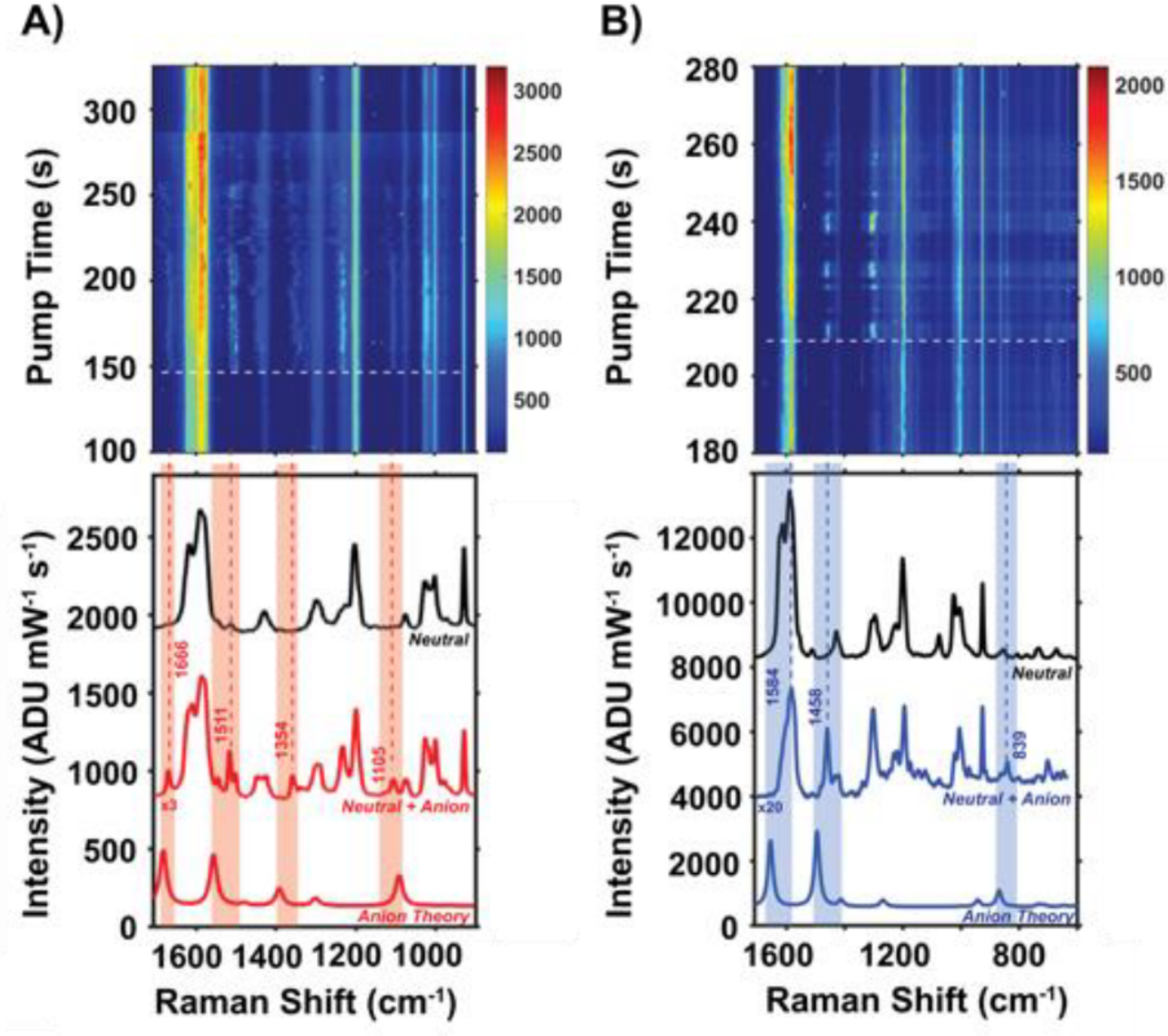

Figure C.3. Representative anion events for both BPY-d_0 and BPY-d_8. (A) Top waterfall plot depicts time-dependent SERS data as a function of optical pump time. Anion modes appear beginning at 148 seconds, indicated by white dotted line. Bottom plot shows neutral spectrum for a BPY-d_0 + BPY-d_8 nanosphere assembly (black). Mid-spectrum depicts contribution from neutral molecules plus BPY-d_0 anion modes that appear (red). Bottom spectrum shows open-shell DFT (CAM-B3LYP) calculation for radical BPY-d_0 anion. (B) Waterfall plot from a differing nanosphere assembly that shows a preference for BPY-d_8 anionic behavior, with anion activity appearing at 209 seconds of pump time. Top spectrum in lower plot consists of neutral molecules only (black), mid-spectrum is neutral plus BPY-d_8 anion modes, and bottom spectrum is open-shell DFT (CAM-B3LYP) calculated BPY-d_8 anion modes.

C.2. Static Raman Scattering of Carbon Dioxide Reducing Rhenium Complexes on Gold Clusters

Building on the plasmonic chemistry theme discussed earlier in this appendix, another molecule has gained significant traction as a target for plasmonically-enhanced CO_2 reduction: $Re(bpy)(CO)_3Cl$.

CO_2 reduction is a chemical process with significant interest for industrial applications, particularly as a precursor for Fischer-Tropsch cycle to create alkanes.[221–223] However, this is an energy intensive and kinetically complicated reaction. As an approach to providing higher energy electrons for reduction, interaction of CO_2 with plasmonic substrates has been pursued.[3,202–204]

$Re(bpy)(CO)_3Cl$, has been explored significantly from an electrochemical standpoint.[224–227] The general thought is that the Cl ligand can be displaced via reduction or oxidation, allowing for binding of CO_2 and subsequent reduction.[228] Based on previous success with the reduction of BPY molecules, the rhenium system was a logical target for observing plasmonic chemistry via SERS. To aid in assignment and deciphering experimental spectra, electronic structure calculations were used.

Electronic structure calculations in support of SERS experiments were performed with the Amsterdam Density Functional (ADF) computational chemistry package.[135] Full geometry optimization, frequency, and polarizability calculations for surface bound $Re(bpy)(CO)_3Cl$ on Au_{20} and Au_{56}, $Re(bpy)(CO)_4^+$, and $Re(bpy)(CO)_3CO_2$ using the Becke-Perdew (BP86) generalized gradient approximation (GGA) exchange correlation

---

The research described in this section was done in collaboration with Tyler Ueltschi, Hannah Mayhew, and Emily Sprague-Klein.

functional and a triple-ζ polarized (TZP) Slater orbital basis set with zeroth order regular approximation (ZORA).

Static Raman polarizabilities (ω=0) were calculated in the RESPONSE package by two-point numerical differentiation using the RAMANRANGE keyword. Raman scattering intensities were determined by Eq. C.2:

$$\frac{d\sigma_j}{d\Omega} = \frac{\pi^2}{\epsilon_0^2}(\omega - \omega_j)^4 \frac{h}{8\pi^2 c\omega_j} S_j \left[45\left(1 - e^{\frac{-hc\omega_j}{k_B T}}\right)\right]^{-1} \tag{C.2}$$

where ω is the frequency of the incident laser field, ω_j is the frequency of the j^{th} vibrational mode, and the scattering factor (S) is: $45\alpha_j^{'2} + 7\gamma_j^{'2}$, where $\alpha_j^{'}$ and $\gamma_j^{'2}$ are the isotropic and anisotropic polarizability tensors with respect to the j^{th} vibrational mode. The Raman intensity for each vibrational mode were broadened to a Lorentzian lineshape with full-width at half-maximum (FWHM) of 10 cm^{-1} for comparison to experimental data.

Shown in Fig. C.4 is a comparison of solution-phase NRS, solid NRS, SERS, and calculated SERS of the Re(bpy)(CO)$_3$Cl on a Au$_{20}$ cluster (Fig. C.5).

However as seen in Fig. C.4, there are unexplained modes near 2155 cm^{-1} in the SERS spectrum that are not present in either NRS or the theory from the structure in Fig. C.5. Therefore, we explored three alternatives: (1) combination of cluster edges effects (due to the large size of the molecule relative to the cluster face) and the orientation of the Cl being at the cluster, (2) possibility of Cl ligand dissociation and a CO ligand binding to the Re center resulting in a Re(bpy)(CO)$_4^+$ structure, and (3) Cl ligand dissociation and a CO$_2$ binding to the Re center resulting in a Re(bpy)(CO)$_3$CO$_2^-$ structures.

Based on the results of Figs. C.6-C.8, a couple of conclusions about the SERS observed in Fig. C.4. The theory used in initial comparisons, while agreeing well with the NRS,

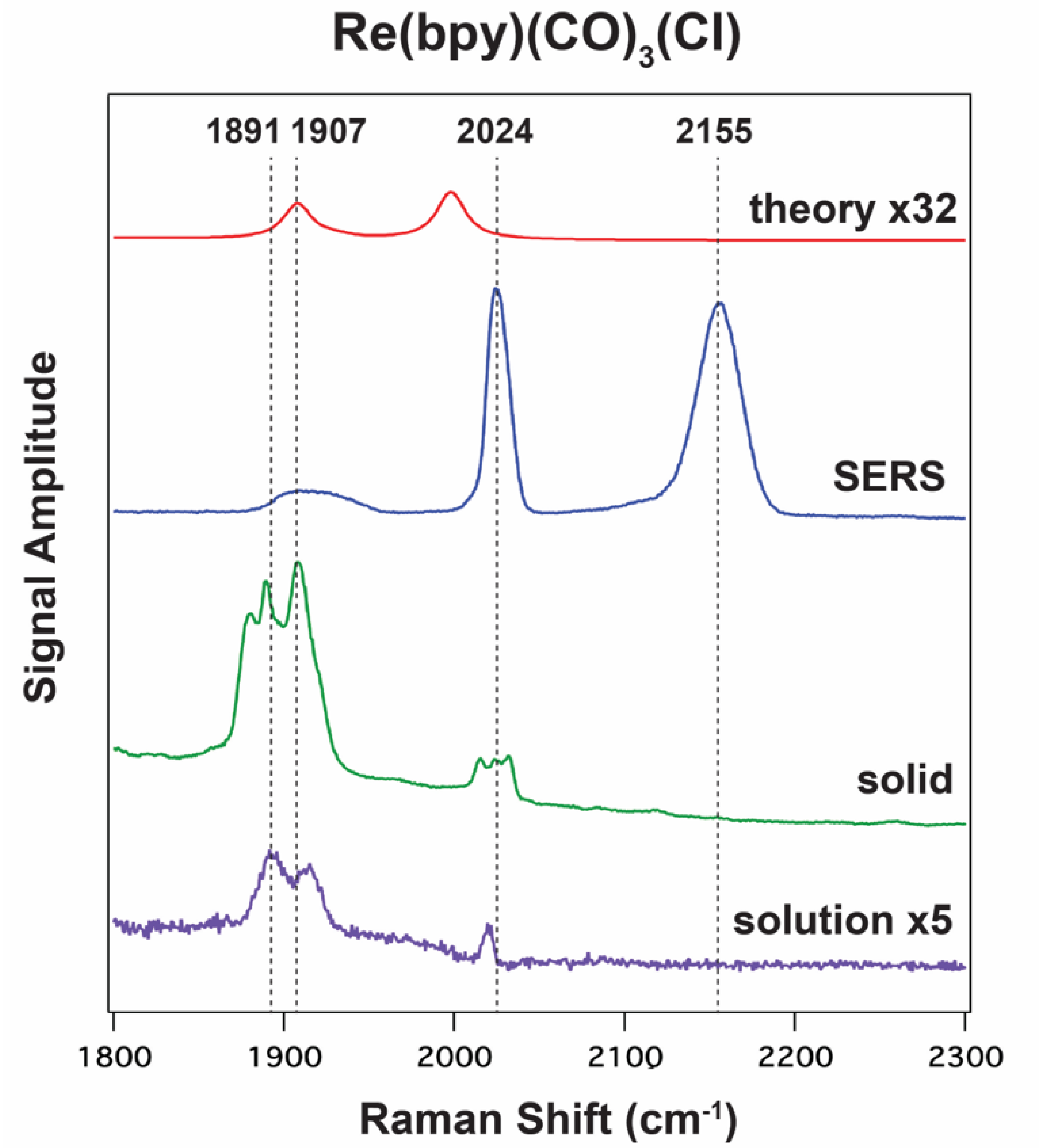

Figure C.4. Comparison of solution-phase NRS, solid NRS, SERS, and DFT-calculated SERS of the Re(bpy)(CO)$_3$Cl system.

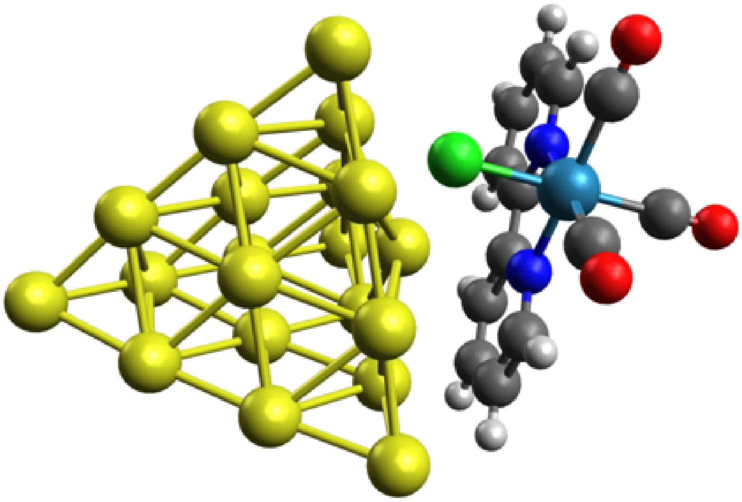

Figure C.5. Geometry used for DFT-calculated SERS of the Re(bpy)(CO)$_3$Cl system in Fig. C.4.

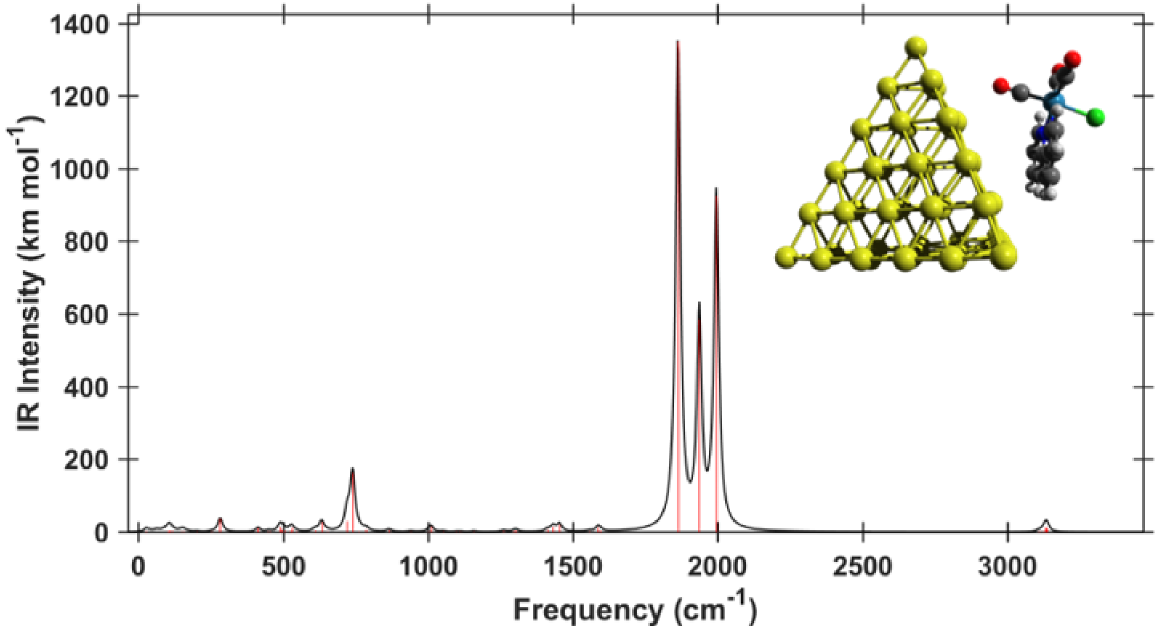

Figure C.6. Normal mode analysis of optimized Re(bpy)(CO)$_3$Cl @ Au$_{56}$ cluster.

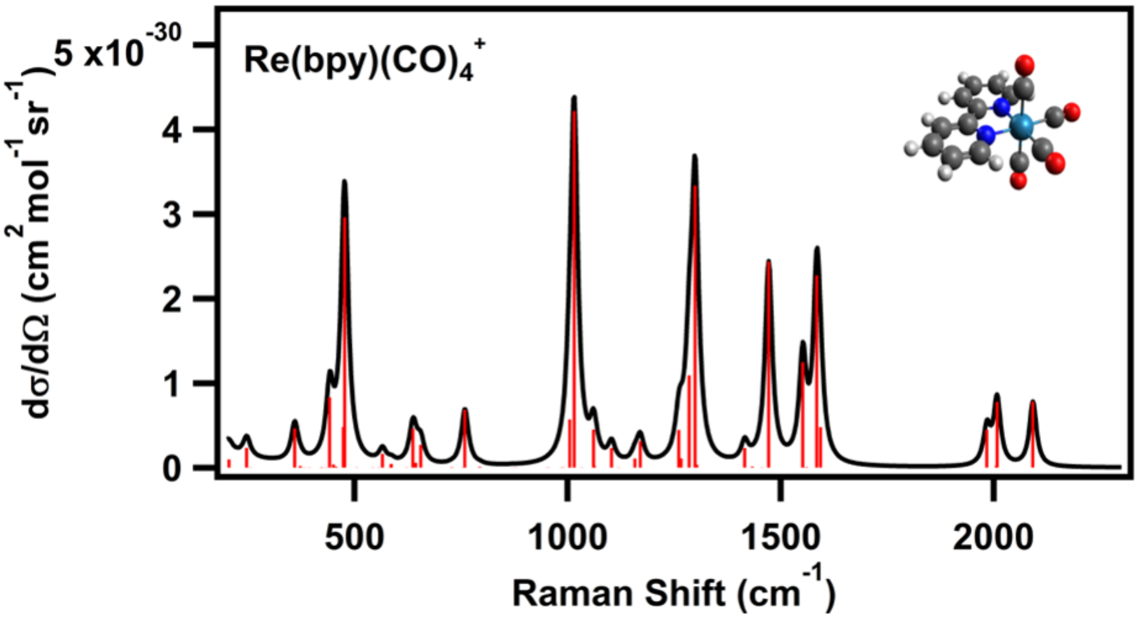

Figure C.7. Raman scattering of gas-phase Re(bpy)$(CO)_4^+$ structure.

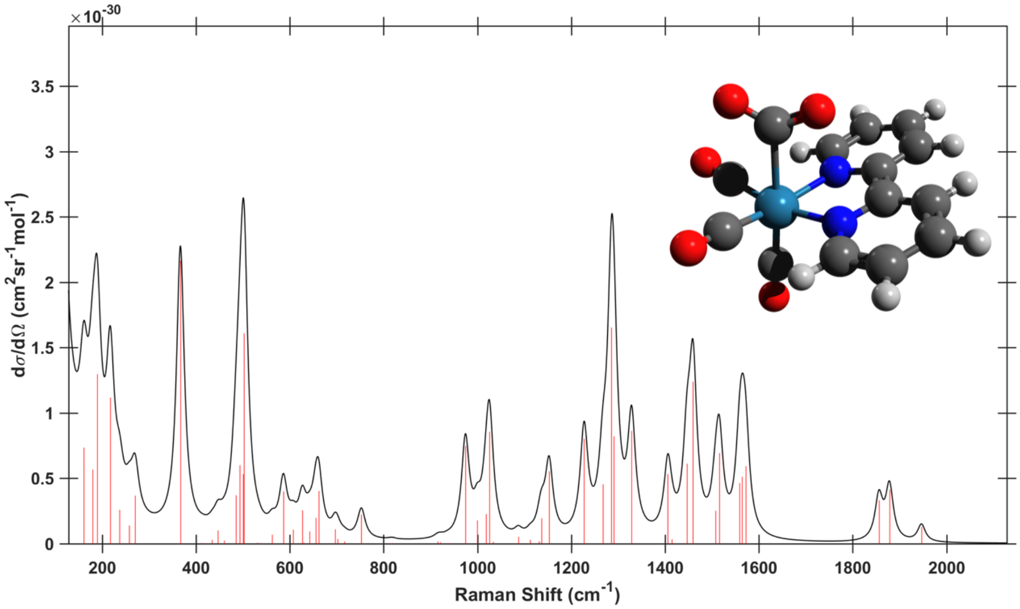

Figure C.8. Raman scattering of gas-phase Re(bpy)$(CO)_3CO_2^-$ structure.

doesn't compare well to the SERS measurement. This is possibly due to loss of Cl and binding of either a CO or CO_2 ligand to the Re center. The possibility of the cluster size effects appears to be negligible based on the normal mode analysis shown in Fig. C.6. The comparison of the SERS spectra with theoretical predictions suggests that the molecular system is losing Cl during the aggregation of the AuNPs in the SERS process. To further study this effect, electrochemical controlled SERS would be illuminating for studying both the electrochemistry and vibrational spectroscopy *in situ*.

APPENDIX D

Surface-Enhanced Ramen Raman Scattering

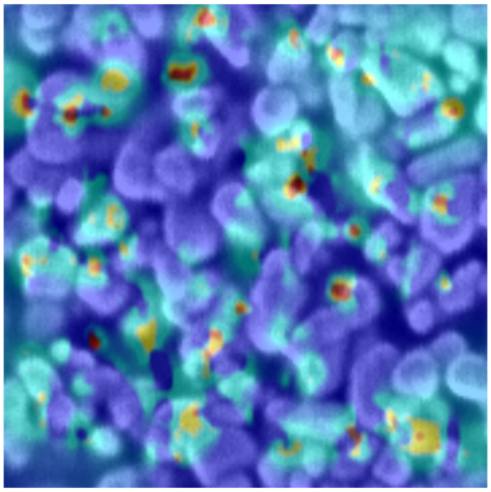

Overlay of FEM simulation on SEM image of Surface-Enhanced Ramen Raman Scattering Substrate.

D.1. Introduction

Surface-enhanced Raman scattering (SERS) is a powerful vibrational spectroscopy for identification of molecular species near plasmonic surfaces.[8,9] However a common issue in the SERS, and to some extent the greater Raman scattering literature, is a predisposition to confuse Raman with Ramen. This issue has appeared numerous times in presentations by undergraduate students, likely due to their familiarity with the cheap Ramen noodle dishes, but also has been present in peer-reviewed studies.[229–232] In an effort to resolve this discrepancy, numerous members of the Van Duyne group unified to create the world's first Surface-Enhanced Ramen Raman Scattering (SERRS) substrate. This effort culminated in a public demonstration of SERRS efficiency compared to commercial fiber based substrates at the 71st birthday celebration of Richard P. Van Duyne.

D.2. Experimental Methods

To make a SERRS substrate, Nissan-brand Cup Noodles were purchased in Spicy Chile Chicken flavor. The noodles were minimally altered for substrate fabrication. A Kimwipe was used to gently remove excess chile chicken salt and spice before taping into a home-built thermal deposition chamber described previously.[233]

Ag was deposited without spinning at a rate of 2 Å/sec for a total thickness 130 nm as measured by a quartz crystal microbalance. After deposition, two SERRS substrates were created. One substrate was immediately dosed with 30 μL of 60 mMol ethanolic BPE solution. Then both substrates were left open to atmosphere for a week.

This work was done in collaboration with Anne-Isabelle Henry, Yinsheng Guo, Ryan Hackler, and Craig Chapman.

SERS measurements were performed both in the Van Duyne research lab using an inverted optical microscope system and an in-field portable Raman spectrometer.

Microscope experiments were performed focusing a 532 nm cw laser through a 40x dry objective. SERS and control NRS spectra were collected with 290 μW of power for 60 second acquisitions. Figs. D.1 and D.2 show comparison of SERRS and NRS of BPE on the metal functionalized and non-functionalized noodles respectively.

Density functional theory (DFT) calculations were performed in the Amsterdam Density Functional theory package[135] using the BP86 exchange functional in the TZP basis set. Finite-difference time-domain (FDTD) simulations were performed in Lumerical (Lumerical Solutions, Inc.).[234]

In-field experiments were performed with a Metrohm Instant Raman Analyzer (Mira). Experimental in-field SERRS data was graciously collected by Professor/amateur experimentalist George C. Schatz for both the SERRS substrates created herein and commercial 3D SERS substrates.[235] Comparison between the two substrates is shown in Fig. D.3.

D.3. Results and Discussion

Based on the surprisingly intense SERS spectra observed in D.1, further investigation of the SERRS substrate was performed using scanning electron microscopy (SEM) and FDTD simulations.

Shown in Fig. D.4 is an SEM image of the SERRS substrate surface. Instead of a roughened Ag metal layer growing on the noodle as expected based on the deposition procedure, well-packed and uniform Ag nanoparticles are formed across the noodle surface. These interesting surface features were further explored by FDTD simulations (Fig. D.5).

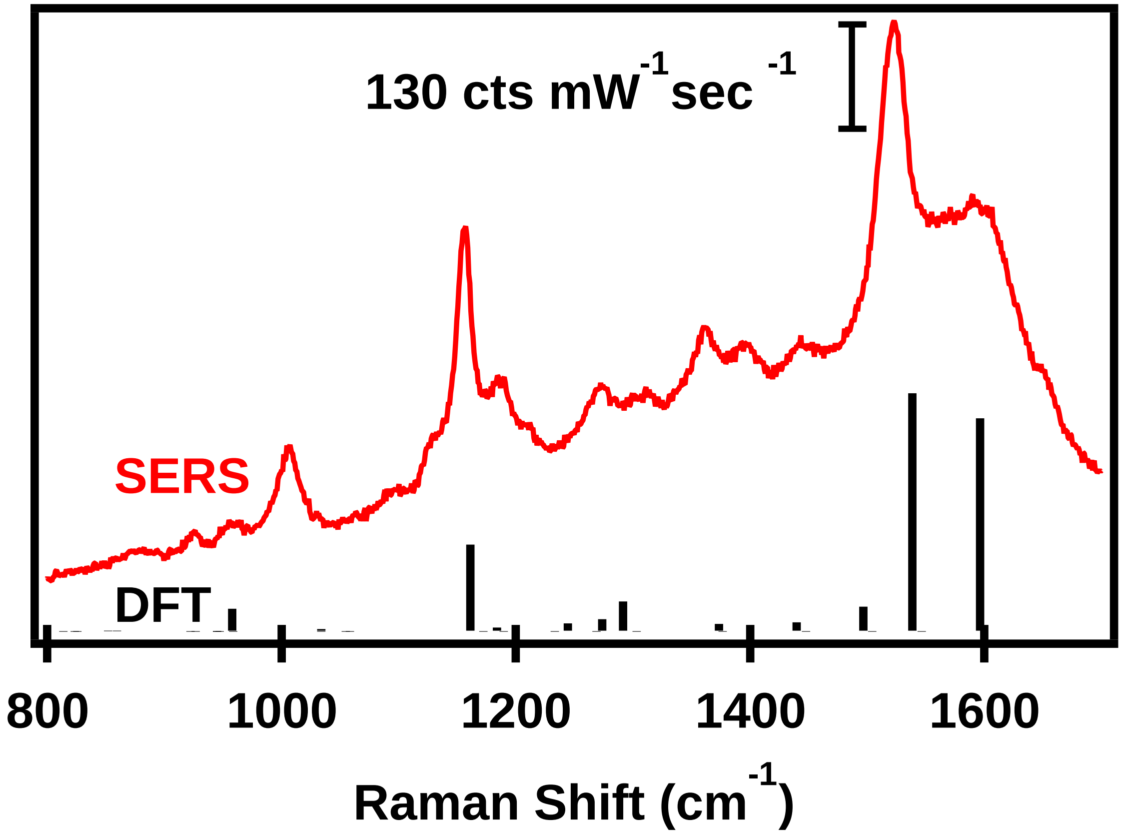

Figure D.1. Comparison of calculated and experimental BPE SERS from the SERRS substrate.

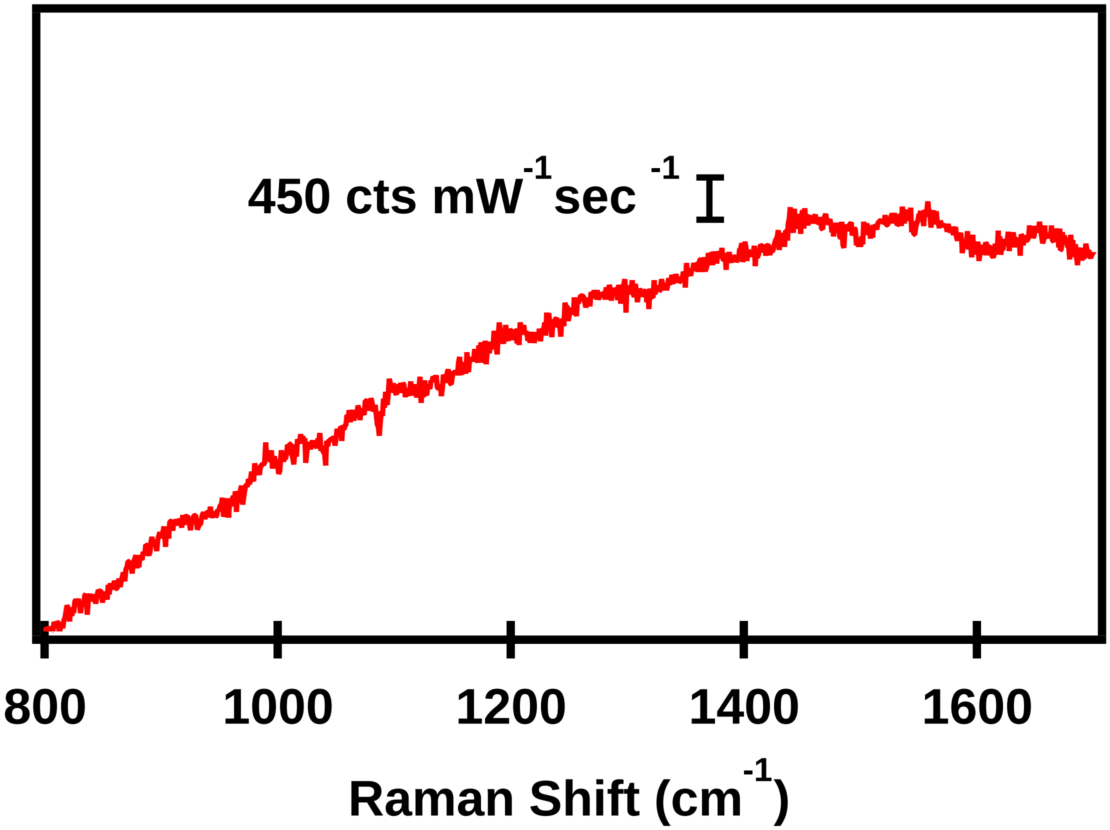

Figure D.2. Control NRS of BPE on Ramen noodle showing only background fluorescence.

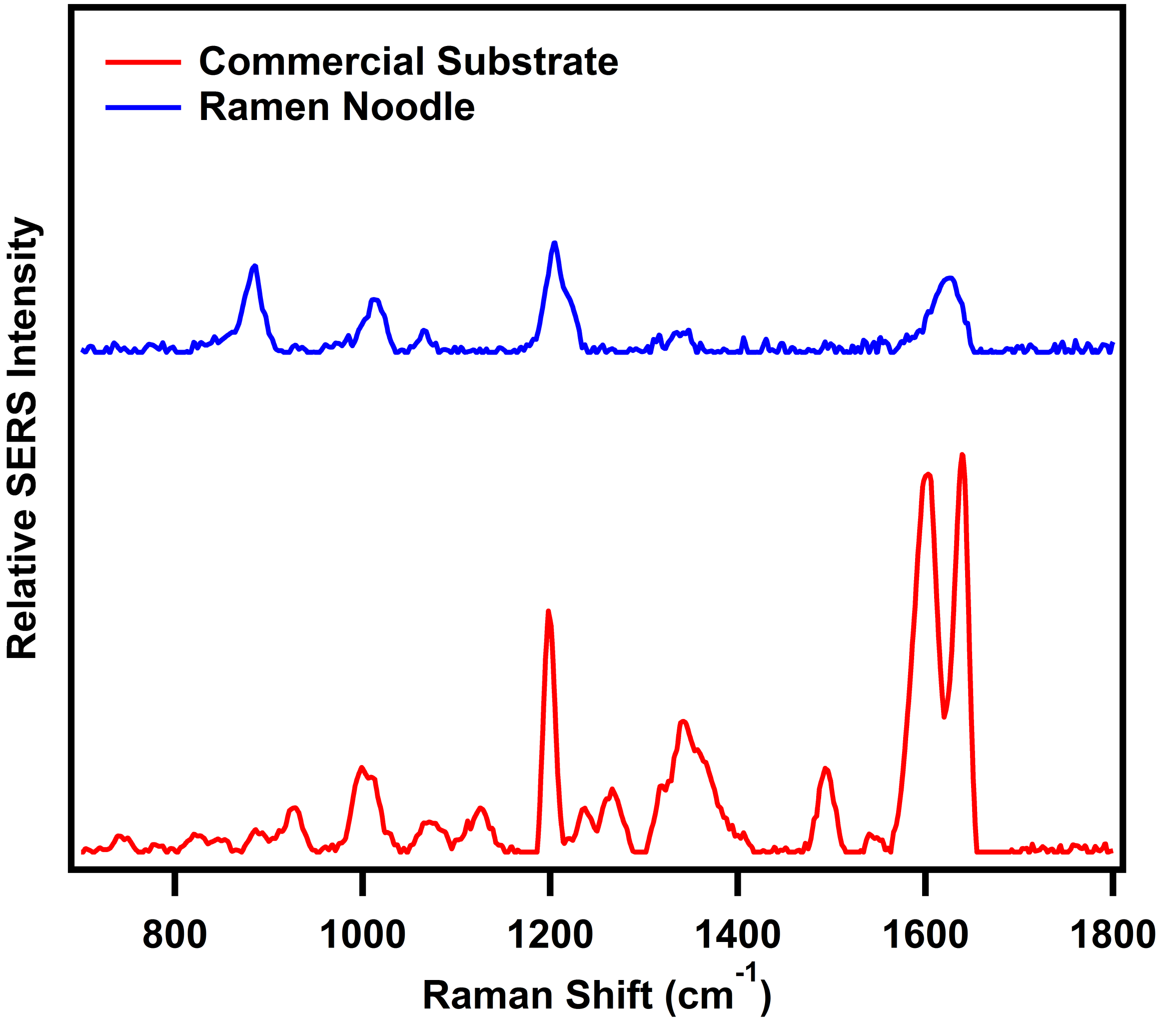

Figure D.3. Comparison of BPE SERS from a functionalized Ramen noodle and commercial substrate.

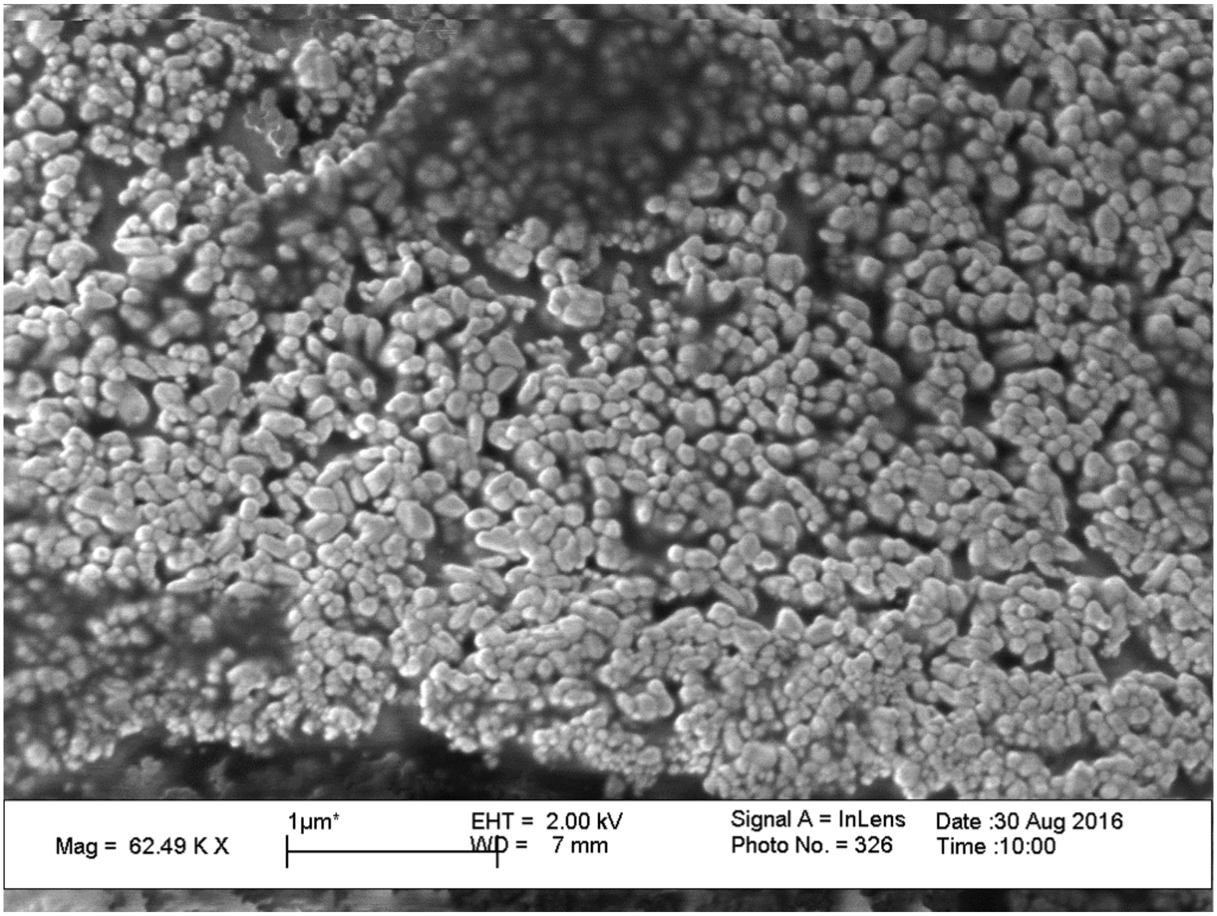

Figure D.4. SEM image of the SERRS substrate.

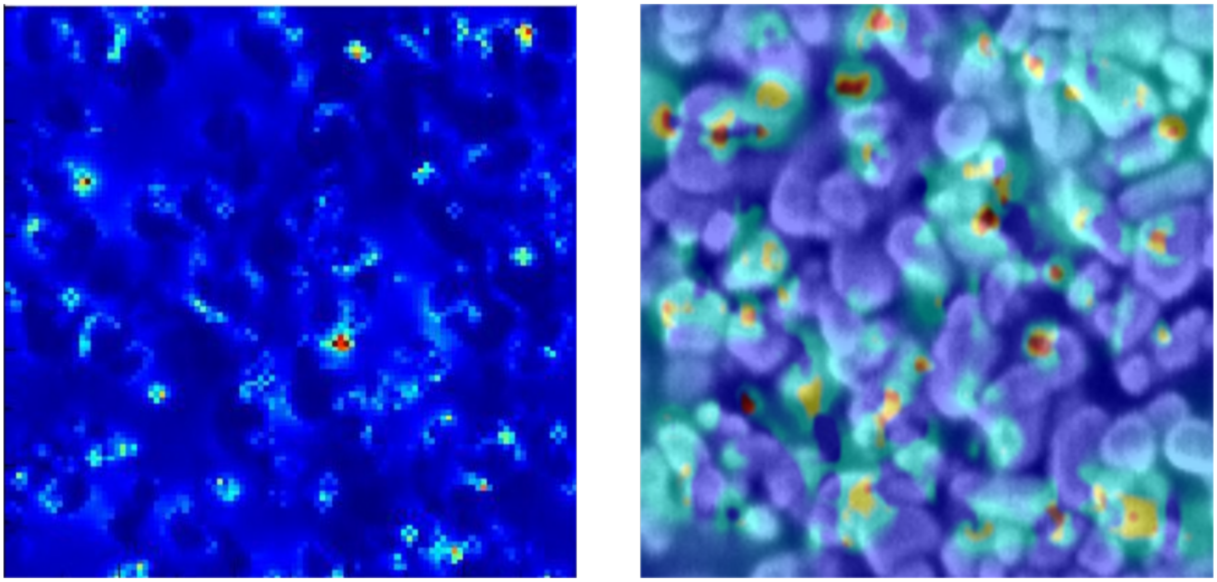

Figure D.5. (Left) FDTD simulation peformed on a 1 μm × μm section of Ag-coated SERRS substrate taken from SEM image (Fig. D.4) Field enhancement has a 10 nm resolution. Shown is the response to an incident field polarized along the horizontal direction of the sample evaluated at 450 nm. (Right) Overlay of FDTD simulation with the SEM image showing the SERS hot spots in the SERRS substrate.

D.4. Conclusion

Noodle-based substrates, including Ramen noodles, are a viable option for SERS substrates. The SERRS demonstrated in the herein study exemplifies the diverse variety of templates researchers can use for further device optimization - potentially towards edible SERS substrates. The surprisingly intense SERS spectra observed are explained by the presence of well-packed and uniform nanoparticle formation across the noodle surface as observed by SEM imaging. The FDTD simulations verify that the interparticle distance and particle size leads to intense electromagnetic hot spots providing the observed SERS intensity that is under an order of magnitude weaker than highly developed commercial substrates (D.3). This work suggests further study into carbohydrate-based SERS substrates in addition to surface-enhanced resonance Ramen Raman scattering (SERRRS).

APPENDIX E

Native Electron Capture Dissociation Characterizes Iron-Binding Channels in Horse Spleen Ferritin

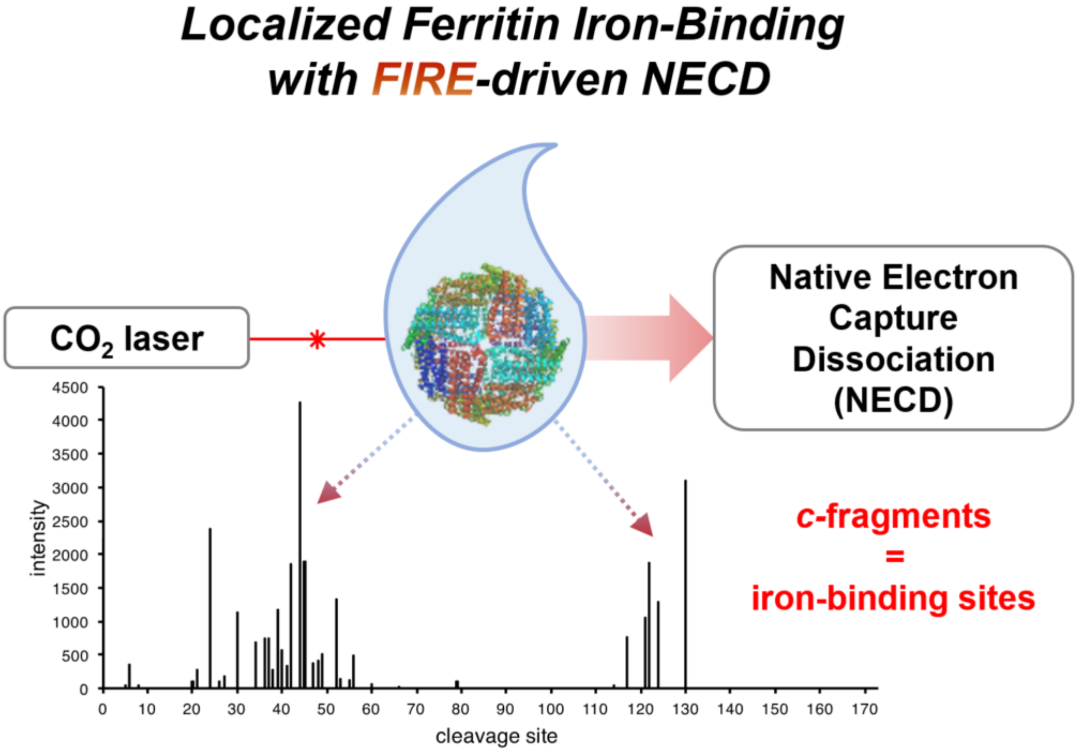

This section has been reproduced with permission from Ref. 236. Copyright 2017 American Chemical Society.

E.1. Abstract

Native electron capture dissociation (NECD) is a process during which proteins undergo fragmentation similar to that from radical dissociation methods, but without the addition of exogenous electrons. However, after three initial reports of NECD from the cytochrome *c* dimer complex, no further evidence of the effect has been published. Here, we report NECD behavior from ferritin, a 24-meric protein complex, ∼20-fold larger than the previously studied cytochrome *c* dimer. Application of front-end infrared excitation (FIRE) in conjunction with low- and high-m/z quadrupole isolation and collisionally activated dissociation (CAD) provides new insights into the NECD mechanism, showing that activation of the intact complex in either the electrospray droplet or the gas phase can produce *c*-fragments with asymmetrically partitioned net charges. Similar to the previously reported results on cytochrome *c*, these fragments appear to form near residues that non-covalently interact with iron atoms. By mapping the location of backbone cleavages onto the crystal structure, we are able to characterize two distinct iron binding channels that facilitate iron ion transport from the cytosol to the core of the complex. The resulting pathways, in good agreement with previously reported results for iron binding in model systems, provide the first direct mapping of iron binding sites in mammalian ferritin from an endogenous sample.

E.2. Introduction

Interest in native mass spectrometry for characterization of biologically relevant macromolecular assemblies has exploded in recent years,[237] with great insights provided for both soluble[238,239] and integral membrane complexes.[240,241] Gas-phase fragmentation of these complexes by electron-based and collision-based dissociation techniques allows for unprecedented characterization of primary and higher-order structures.[242–246] Of these, native electron capture dissociation (NECD), first introduced in 2003 by Breuker and McLafferty, proved both unexpected and useful for the elucidation of the heme-binding and gas-phase unfolding of the dimeric species of cytochrome *c*.[247,248] However, finding examples of this effect on other macromolecular complexes has proven elusive, and the underlying mechanism has not been investigated further.

NECD is a fragmentation process that occurs during ion transfer through a heated capillary in native electrospray ionization (nESI) of an iron-containing protein complex. Covalent bond cleavage near residues in contact with the heme results in apparent complementary *c*- and *y*-fragment ions.[249] Changes in higher-order complex structure (*e.g.* unfolding) can perturb the heme-protein interactions, causing variation in the formation of NECD products. By analyzing changes in these fragment ion yields, it was possible to study the early gas-phase unfolding of cytochrome *c*,[248] and even the early partitioning of protons onto the dimer ions.[250] Unfortunately, despite great promise for NECD as a technique for protein characterization, no further studies of the effect, either theoretical or experimental, have since been reported.

Here, we extend the use of NECD to the ∼490 kDa 24-mer ferritin, a protein complex known to store up to 4500 Fe atoms.[251] Unlike the previously-studied cytochrome *c* dimer, ferritin does not contain a covalently bound heme group, instead using a di-iron site to catalytically convert soluble Fe(II) to an inorganic mineral similar to ferrihydrate (composed of Fe(III), oxygen, and small amounts of phosphate) which is stored in the core of the protein complex.[252–255] Iron ions are channeled through subunit helices[253] and protein nanocage pores[256,257] and stored in the central cavity for future cellular use.[258,259] Ferritin from mammalian tissues is made up of different proportions of the L (liver)- and H (heart)-chain, with the H-chain providing catalytic activity and the L-chain implicated in structural stability and cavity mineralization.[260–262] The present work analyzed horse spleen holo-ferritin, which is made up of ∼90% L-chain.

E.3. Experimental Methods

Ferritin from horse spleen and cytochrome *c* from horse heart (Sigma) were desalted with 100 kDa and 10 kDa molecular weight cutoff filters, respectively, into 150 mM ammonium acetate at slightly acidic pH (∼5.6 - 7.0). Samples were diluted to a final concentration of 2 μM (ferritin) and 100 μM (cytochrome *c*) for the intact complex and sprayed using a custom-built nanospray source as described previously.[263,264]

All mass spectrometry measurements were performed on a Q-Exactive HF (Thermo Scientific) modified to allow for high-m/z ion transfer and quadrupole isolation.[242] Spectra were acquired at a resolving power of 120000 (at 200 m/z), with the exception of the ferritin MS^1, which was acquired at 7500 resolving power (at 200 m/z), and smoothed for more accurate mass determination. The mass error presented here represents the standard deviation of the masses determined from the apex of each charge state peak, and therefore indicates the precision of the measurement. NECD fragment ions from ferritin were collected as two separate spectra, one at higher energy in the collision cell for fragments from sites 6-79, and one at lower energy for fragments from sites 114-130. Data analysis was performed with Xtract (Thermo Scientific) and mMass[265] software and graphical fragment maps were created with Prosight Lite.[266] All intensity values used for the determination of weighted-average charges were normalized by charge to account for the detection bias in the Orbitrap mass analyzer.

Front-end infrared excitation (FIRE) experiments used a 20 W continuous-wave CO_2 laser (Synrad Firestar v20). The laser was attenuated with a 1.0 optical density (O.D.) nickel-coated zinc selenide neutral density filter (NDF), then aligned unfocused to the inlet capillary with protected gold mirrors. An average power of 1.2 W was used for FIRE experiments.

Safety Considerations Vigilance and proper protective equipment should be used when handling ferritin, cytochrome *c*, and any other sample from a biological source. Additionally, the high-voltage in the electrospray source can cause dangerous electrical shocks when not properly shielded. Finally, proper eye protection should be worn when using a CO_2 or any other laser, especially as pointing it at the highly reflective front end of an instrument may cause unpredictable scattering.

E.4. Results and Discussion

Horse spleen ferritin was desalted and characterized by native top down mass spectrometry (nTDMS)[242,267] (Fig. E.1). The MS^1 spectrum (Fig. E.1a) indicated the presence of the intact complex with a mass of 490380 ± 59 Da, consistent with the $L_{22}H_2$ complex and a ∼9500 Da iron oxide mineral. Broad spectral peaks (FWHM of ∼3000 Da) were likely caused by polydispersity in the core mass, but may also indicate small molecule adduction common with nTDMS.[268] Source collisional activation produced peaks at lower m/z (Fig. E.1b, isotopically resolved) corresponding in mass to the ejected ferritin L-chain, with the previously-reported[267] cysteine methyl-disulfide modification at near complete stoichiometry. The observed signal is at a much (∼6-fold) higher charge state than would be predicted from a symmetric charge partitioning during monomer ejection, indicating that it undergoes asymmetric charge partitioning.[269,270]

In addition to ejected monomer, several fragment ions were observed and clearly resolved in the MS^2 spectrum (Fig. E.1b, inset). Closer examination of these species revealed that they did not correspond to the traditional *b*- and *y*-fragments generated from threshold dissociation,[271] but were instead consistent with the mass of *c*-fragment ions. In conjunction with fragment ions observed from a spectrum acquired at higher collision energy, products from cleaving 37 L-chain backbone sites were characterized (Fig. E.1c). On the other hand, isolation and fragmentation of a single charge state of the ejected monomer produced only *b*- and *y*-fragments (Fig. E.5). No evidence for the intact or fragmented H-chain was observed.

The observation of *c*-fragments is characteristic of radical fragmentation processes such as electron capture or electron transfer dissociation (ETD).[272,273] However, here no exogenous electrons were added or transferred. Instead, the formation of these products recalls the heme-mediated intramolecular electron transfer and fragmentation, of NECD.[247,248,250] Unlike the original reports of NECD on the cytochrome *c* dimer, the ∼20-fold larger ferritin complex does not contain a heme group, and no complementary *y*-fragment ions were observed. Therefore, in order to confirm that the *c*-type cleavage products were from NECD, it was necessary to better characterize the mechanism driving the fragment formation in ferritin.

First, we confirmed the identity of the observed *c*-fragments by quadrupole-isolating and using collisionally-activated dissociation (CAD) to characterize the 5+ charge state

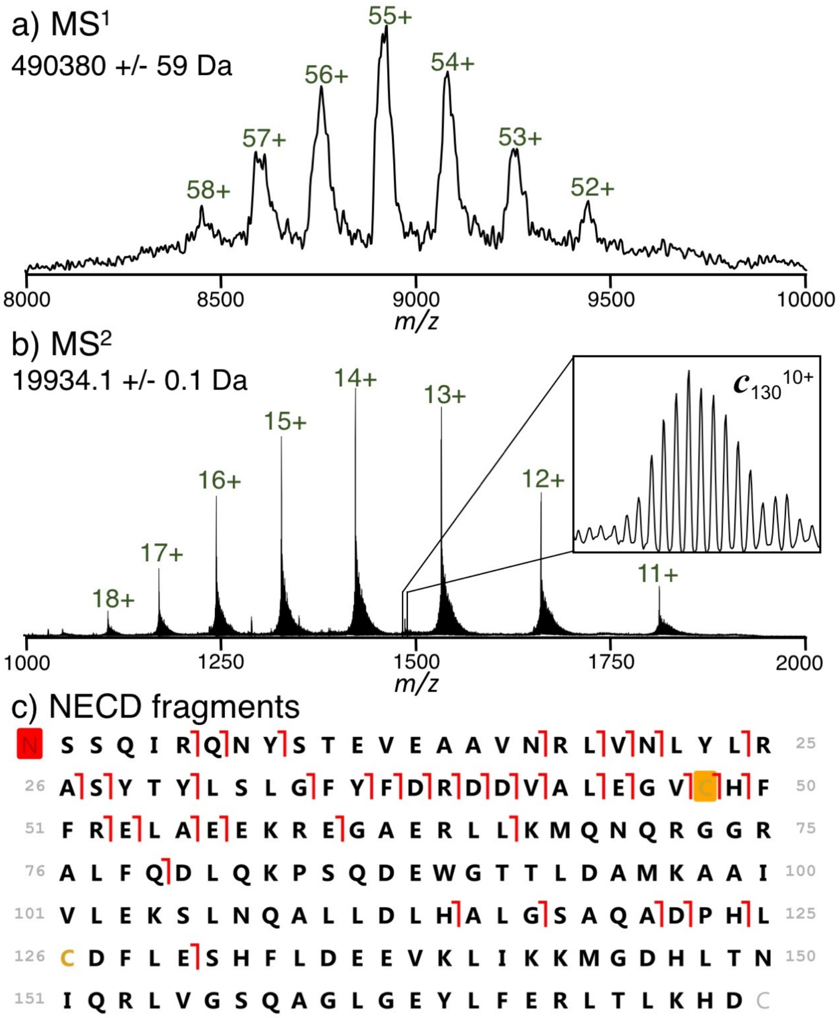

Figure E.1. Analysis of ferritin by native top-down mass spectrometry. The MS^1 spectrum (a) exhibits broad peaks corresponding to the mass of the intact 24-mer. After gas-phase activation in the source region, the intact L-chain is ejected along with *c*-fragments (MS^2, b). Mapping the fragment ions onto the protein sequence (c) shows peptide bond cleavage at 37 unique sites, with cleavages from sites 5-79 determined using higher-energy conditions, and those from sites >113 determined using lower-energy conditions. The red box on the N-terminus corresponds to an acetylation, the orange box to a cysteine methyl disulfide modification. Figure reproduced with permission from Ref. 236. Copyright 2017 American Chemical Society.

of c_{44}, the most abundant NECD product (Fig. E.2). CAD produced *b*- and *y*-fragments originating from 50% of all peptide bonds present in the c_{44} precursor, including seven y-fragments corresponding (<5 ppm) to the mass of the sequence with a C-terminal amide. The *y*-fragments in this MS^3 experiment contain the mass of the 'ragged end' of the original NECD cleavage, which is characteristic of a *c*-fragment. Other NECD fragments were insufficiently abundant to perform a similar characterization, but were consistent in mass with *c*-fragments. Thus, we were able to exclude other potential factors (*e.g.* unexpected adducts and modifications) that may have confounded the mass values and confirm the presence of *c*-fragments in the spectrum with high confidence.

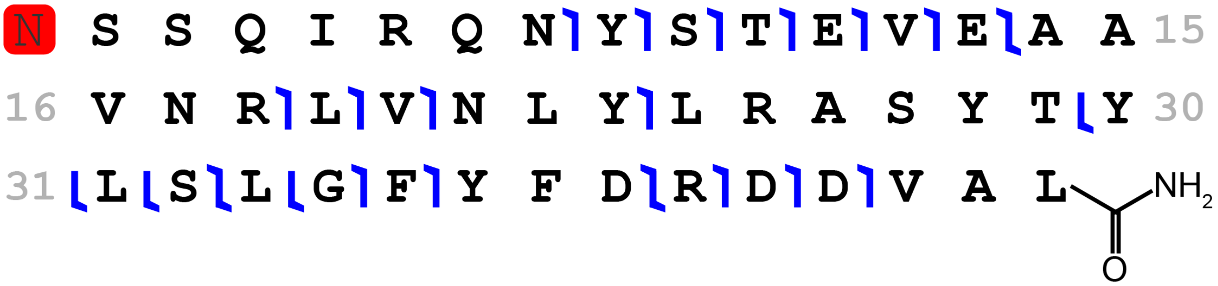

Figure E.2. Isolation and CAD fragments provide unambiguous characterization of the NECD-produced c_{44} 5+ fragment ion. The C-terminal amide corresponds to the 'ragged end' of the original NECD cleavage (after tautomerization), which is characteristic of a *c*-fragment and not hydrolysis. Figure reproduced with permission from Ref. 236. Copyright 2017 American Chemical Society.

However, while NECD products from cytochrome *c* were shown to form primarily in the source region of the instrument,[247] the location where NECD of ferritin occurs remained more ambiguous. Isolation and collisional activation of the intact ferritin complex gave clear evidence of NECD (Fig. E.6), albeit at a lower efficiency. This is in contrast with isolation and fragmentation of the ejected monomer (Fig. E.5), which produced no *c*-fragments. Therefore, both cytochrome *c* and ferritin require the intact complex to fragment. However, unlike cytochrome *c*, ferritin can evidently form NECD fragments in the gas phase, after quadrupole isolation. The apparent discrepancy between NECD of these two systems could be due to significant water solvation of the ferritin ions even after transfer to the gas phase. Additionally, it is possible that fragment ions are being formed in the source region, but are only separated after activation in the gas phase.[274]

In order to examine whether ferritin NECD fragmentation can also occur in the source region, we used a 20 W CO_2 continuous-wave laser aligned with the inlet capillary of the mass spectrometer in a method termed front-end infrared excitation (FIRE) (experimental setup, Fig. E.7). In order to better characterize the effects of FIRE, we used a 100 μM solution of cytochrome *c*, as its NECD behavior has been extensively characterized previously.[247,248,250] Application of FIRE produced NECD (both *c*- and *y*-fragments) of cytochrome *c* dimer species at inlet capillary temperatures low enough not to produce fragments without laser irradiation (Fig. E.8). Using the additional precision of the distance dependence of the FIRE experiment when compared to the traditional heating with the inlet capillary, we correlated the relative signal of the major NECD peak ($y_{55}{}^{5+}$) with the distance between the laser and nESI spray tip (Fig. E.9). The intensity dropped drastically between 2 mm and 3 mm, indicating that FIRE has little effect on nESI droplets after they have been sufficiently desolvated. Misalignment of the laser so that it only irradiated the droplet pathway between the nESI tip and the inlet capillary also drove NECD (Fig. E.10), providing further evidence that FIRE affects the droplets most just after they leave the nESI nozzle. Because application of FIRE to ferritin also produced NECD fragments (Fig. E.11), we can conclude that this process occurs in the nESI droplet as well.

As reported previously for NECD[250] and ETD[275] fragments of cytochrome *c* dimer, ferritin *c*-fragments also undergo asymmetric charge partitioning, as is evident from the great decrease in m/z between the precursor and its product ions (from >8000 to 1000-2000, respectively, Figs. E.1a,b). Plotting the average charge of each NECD fragment with respect to cleavage site indicates a relatively high level of charge density in the fragment ions, with discrete steps corresponding to the locations of arginine residues (Fig. E.3a). In comparison, CAD fragments from the isolated 14+ ejected monomer (overall weighted-average charge of ejected monomers = 13.93) exhibited a similar distribution of charge states also repeating the discreet jumps in charge at arginines 18, 26 and 39 (Fig. E.3a). The overall similarity in charge between the NECD and CAD fragments indicates that the protons have partitioned to analogous locations after the fragments have been ejected from the intact complex.

While the overall charge state of a fragment is a good measure of charge density, we use the asymmetric charge partitioning factor (ACPF) to determine the full magnitude of charge partitioning for products of different mass.[275] The ACPF indicates the fold change between how much charge an ejected subunit has when compared to how much it would have upon symmetric charge partitioning. Thus, a symmetric charge partitioning would correspond to an ACPF of 1, whereas higher values indicate an increasing magnitude of the effect. Plotting the ACPF values of observed NECD fragments (with two or more charges) with respect to their cleavage sites shows that the magnitude of asymmetric charge partitioning remained relatively constant with respect to fragment size (Fig. E.3b). Surprisingly, only two fragments partitioned less than the ejected monomer (ACPF = 6.1); the overall average ACPF was 7.2. Therefore, the NECD fragments are not only

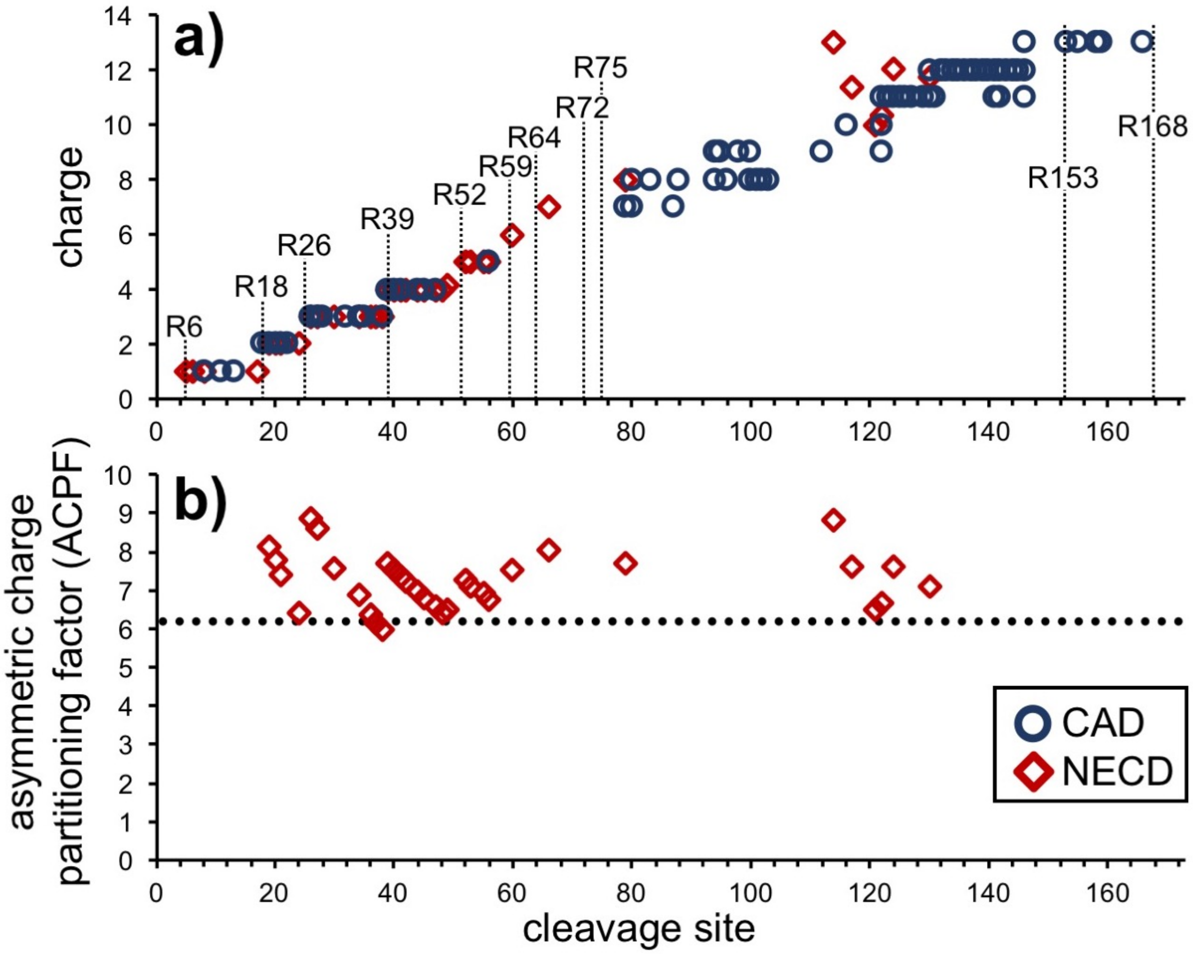

Figure E.3. Charge distribution observed in ferritin fragment ions. (a) The observed charge states of *c*-type fragments from NECD fragmentation of the intact complex and the *b*- and *y*-type fragments from CAD of the 14+ ejected monomer exhibit many of the same discrete steps. In order to plot them on the same axis as the N-terminal fragments, the charge of *y*-fragments is displayed as the difference 14 observed charge. The locations of the eleven arginine residues in ferritin are marked, as they often correlate with increases in charge. (b) The asymmetric charge partitioning factor (ACPF) is displayed for each of the observed NECD fragments with two or more charges. While there is no noticeable change in the ACPF for larger fragments, all but two partition more asymmetrically than the ejected monomer (dotted line at ACPF = 6.1). Figure reproduced with permission from Ref. 236. Copyright 2017 American Chemical Society.

undergoing asymmetric charge partitioning, but are doing it more so than even the ejected monomer.

The *c*-fragments observed from ferritin have many of the same characteristics as those found previously for NECD from cytochrome *c*. Therefore, because previous work on NECD has shown that fragment formation only occurs near residues that interact with the iron-bearing heme group, the location of fragments in ferritin too should be dependent on iron-side chain interactions. However, cleavages occur between two residues, so any given cleavage site could indicate up to two individual iron-binding interactions. The assignment of residues to cleavage sites can be simplified because not all amino acids are likely to coordinate to iron, and were therefore excluded from assignment.

Plotting the yields of *c*-fragment ions with respect to their location on the protein sequence (Fig. E.4a) exhibits two regions of major fragmentation: sites 34-49 and 117-130. High-intensity fragmentation from these regions strongly indicates iron-binding interactions. The first, 34-49, corresponds to a loop-pocket region (Fig. E.4b), which is a cavity in the protein cage hypothesized to be involved in the release of iron atoms into the cell.[255,276] The second, located on a three-fold axis in the cage structure (Fig. E.4c) has been implicated in the uptake of soluble Fe^{2+} prior to deposition in the inner iron core.[255,276] Previous studies to characterize these regions have relied on over-expressed systems and alternate metals; NECD provides the first direct mapping of iron interactions on a mammalian system from an endogenous sample.

Surprisingly, little fragmentation was observed around the catalytically-active residues 53-63 and 135-140. However, only the H-chain is considered catalytically active.[261] Thus,

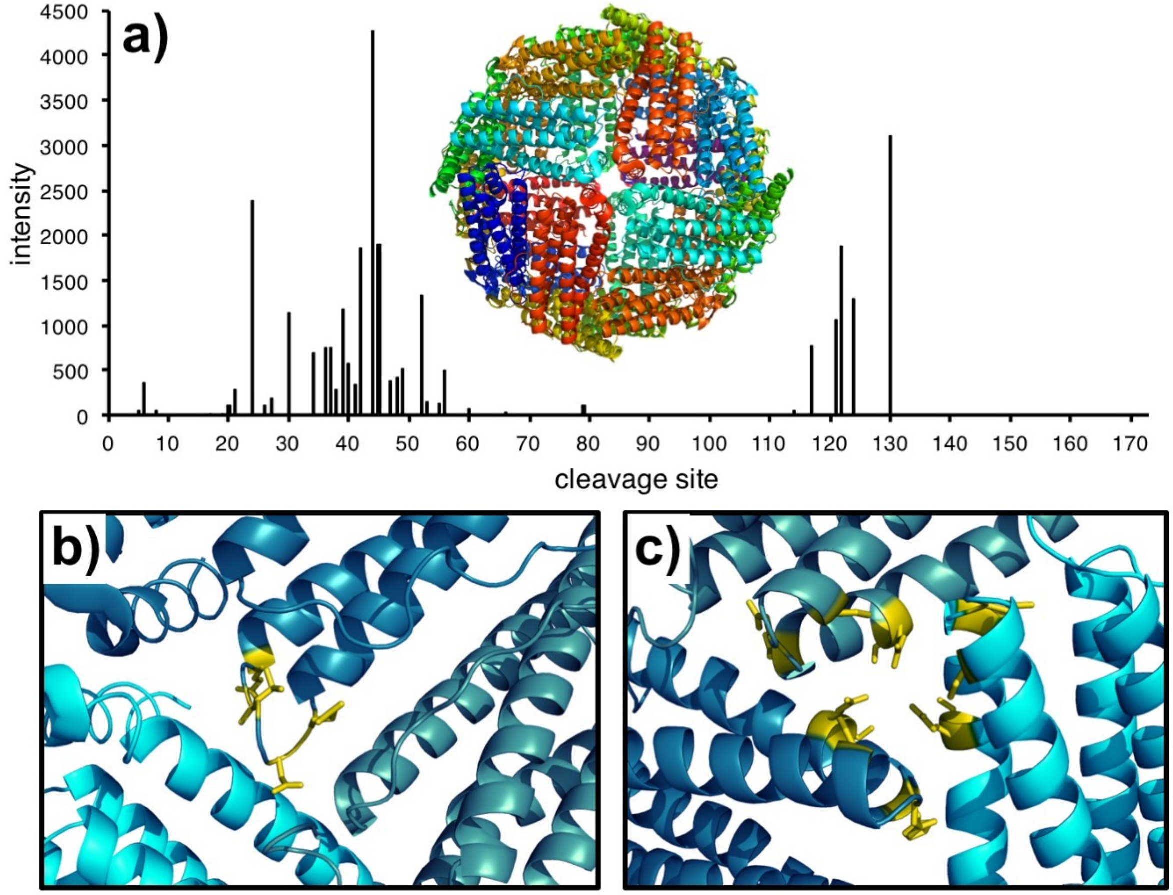

Figure E.4. The yields of *c*-fragment ions plotted with respect to their cleavage site (a) with the crystal structure of ferritin (PDB:1IER) indicating the difference in subunits. Mapping abundant fragments onto the crystal structure for sites 43-53 (b) indicates that the cleavages are centered in the helix-loop region. Fragments from sites 114-130 (c) instead indicate cleavages from the three-fold axis pore regions. Figure reproduced with permission from Ref. 236. Copyright 2017 American Chemical Society.

NECD fragments, which are observed exclusively from the L-chain, cannot be directly correlated to di-iron site oxidation of soluble Fe^{2+}. Additionally, activation of apoferritin from horse spleen, which contains no iron oxide mineral produced many similar *c*-fragments (Fig. E.12), suggesting that the effect cannot be attributed to the core. However, a recent study by Carmona *et al.* has shown that the light chain of horse ferritin is critical for the transfer of an electron across the boundary of the ferritin cage.[277] The apparent dependence of ferritin NECD on electron transfer brings it in line with the electron-transport protein cytochrome *c*, and could explain why NECD is not observed from other systems.

Despite the strong correlation between ferritin NECD fragment ions and iron-binding channels, how the iron ions can generate radical-type fragment ions is not completely clear. However, with the improved fragment ion characterization presented here we propose a potential mechanism for NECD in ferritin. In the first step, a subunit partially unfolds, driving a similar proton transfer process to that predicted for monomer ejection.[278,279] This step explains the 'stepped' appearance of charge distribution in NECD fragment ions (Fig. E.3a), as the protons are no longer mobilized and have already been distributed prior to cleavage. While most of the subunit monomer has un-folded, the stronger iron-mediated protein-protein interactions are maintained. With increasing energy, these interactions are finally broken, transferring an electron from complexed iron and cleaving the monomers peptide bond.

E.5. Conclusion

Native electron capture dissociation promised to be a powerful new technique for elucidating iron binding interactions when it was first presented in 2003, however, no systems beyond the original cytochrome *c* dimer have since been described.[247,248,250] Here, we demonstrate application of this method to the ∼500 kDa protein complex ferritin. Leveraging information from FIRE-assisted dissociation and gas-phase isolation/dissociation techniques, we show that the resulting fragments are indeed NECD type *c*-fragments, undergo asymmetric charge partitioning, and can be formed in the electrospray droplet or in the gas phase upon collisional or infrared activation. The formation of NECD products, postulated here to be liberated from previously-unfolded CAD monomers, could be further probed with future experiments using electron capture dissociation, which has been used to monitor structural changes in other gaseous protein complexes.[280]

When mapped on the crystal structure, prevalent NECD fragments indicated significant iron binding at the loop-pocket and three-fold axis regions. These residues are not implicated in the catalytic process of ferritin, but instead correspond to channels which mediate iron ion transport in and out of the protein cage. Future applications of NECD could therefore probe the migration of iron and potentially other metals through the ferritin protein cage, and would require orders-of-magnitude less sample than crystallography experiments. While the applicability of NECD remains limited to two protein complexes, its precise readout of iron affinitive sites provides a high potential for the targeted analysis of perturbations in iron binding systems.

E.6. Supplementary Information

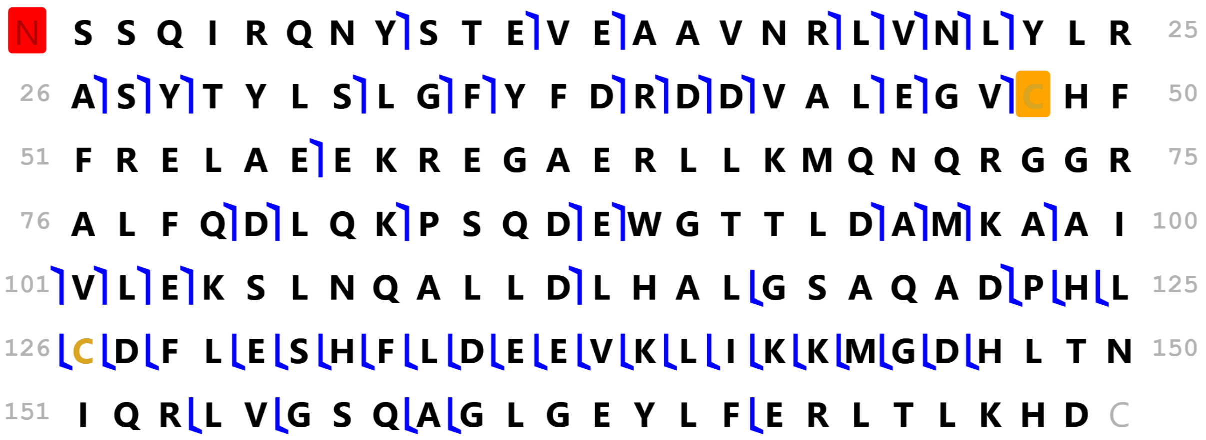

Figure E.5. Graphical fragment map representation of fragment ions formed from isolation and CAD dissociation of the 14+ ejected ferritin monomer. Only *b*- and *y*-type fragment ions were detected. The red square corresponds to an N-terminal acetylation modification and the orange square corresponds to a cysteine methyl disulfide modification. Figure reproduced with permission from Ref. 236. Copyright 2017 American Chemical Society.

Figure E.6. Evidence of NECD *c*-fragments from isolation and activation of the intact ferritin complex. The products must therefore be formed after quadrupole isolation. Figure reproduced with permission from Ref. 236. Copyright 2017 American Chemical Society.

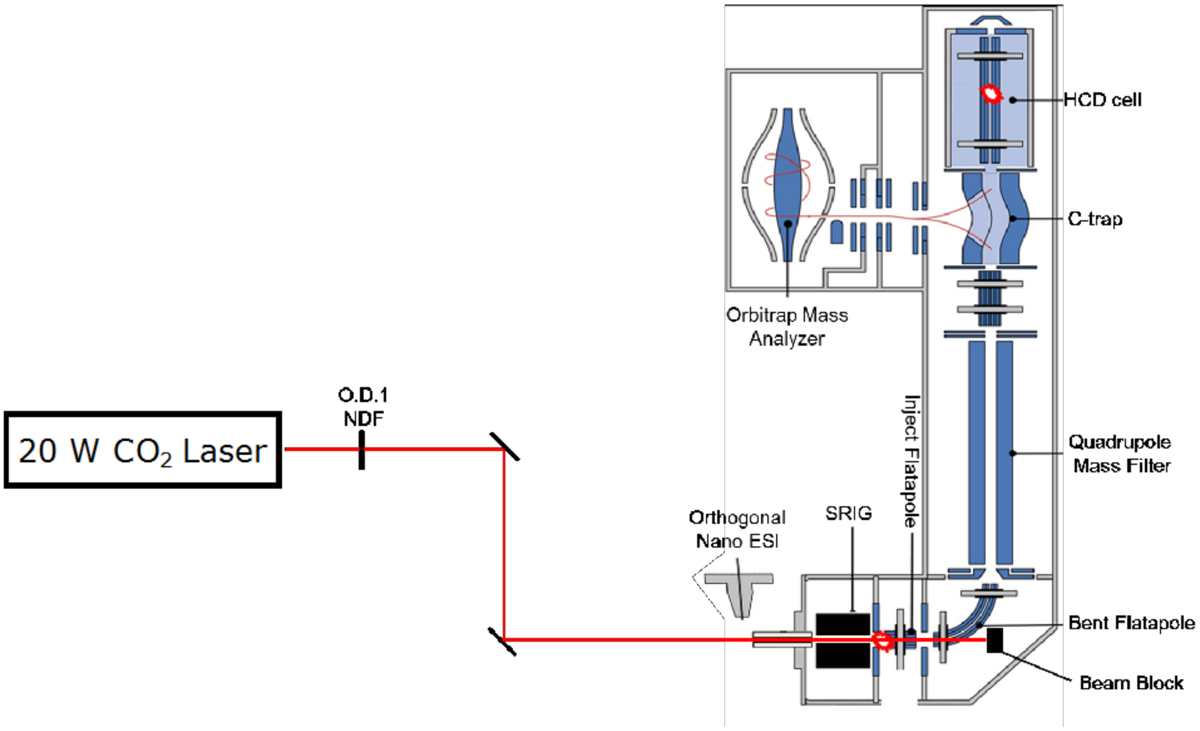

Figure E.7. Experimental setup for front-end infrared excitation (FIRE). The laser is aligned collinearly through the inlet capillary of the instrument, and blocked by a beam block placed behind the bent flatapole. The MS-portion of this figure was modified from Ref. 241. Figure reproduced with permission from Ref. 236. Copyright 2017 American Chemical Society.


N G D V E K G K K I F V Q K C A Q C H T V E K G G K 25
26 H K T G P N L H G L F G R K T G Q A P G F T Y T D 50
51 A N K N K G I T W K E E T L M E Y L E N P K K Y I 75
76 P G T K M I F A G I K K K T E R E D L I A Y L K K 100
101 A T N E C

Figure E.8. Fragment map showing the NECD *c*- and complementary *y*-type cleavage products of cytochrome *c* upon laser activation by FIRE. The orange box corresponds to the mass shift caused by the covalent heme binding (+615.1695 Da), which is also bound to Cys-17. No fragments were observed without laser activation (data not shown). Figure reproduced with permission from Ref. 236. Copyright 2017 American Chemical Society.

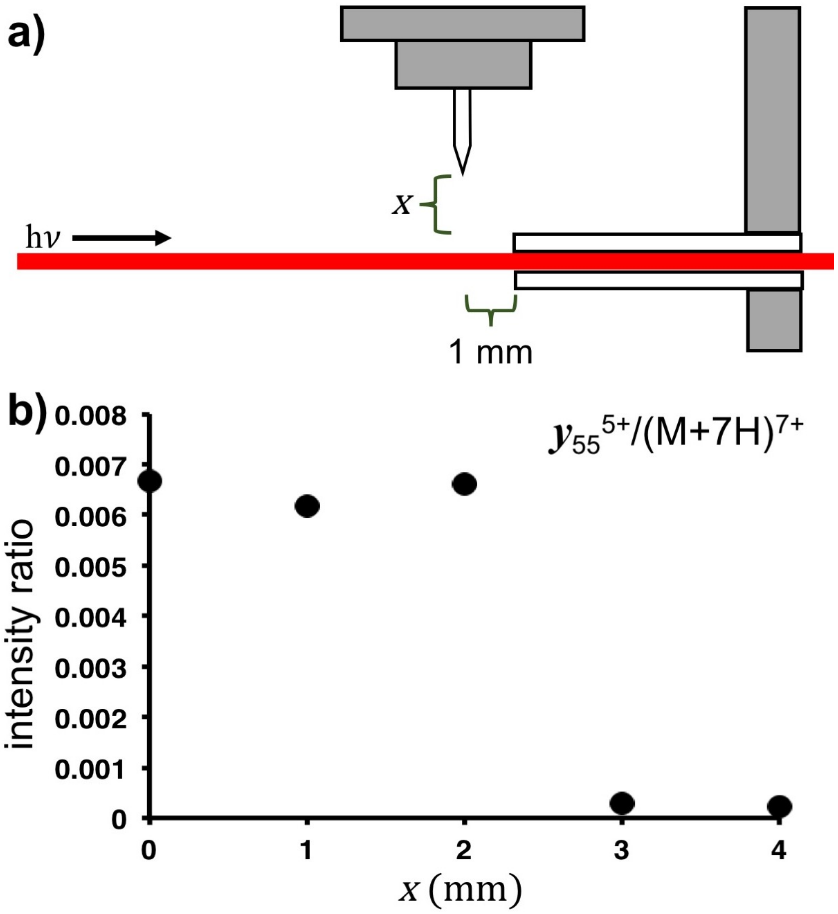

Figure E.9. (a) Experimental schematic of the FIRE setup highlighting the distance parameters used; x is the variable tip-laser distance. (b) The relative ratio of the y_{55} 5+ compared to the 7+ molecular ion of cytochrome *c* at varying electrospray emitter distances. The y_{55} fragment is an abundant NECD product, its intensity after normalization to the molecular ion is used to indicate NECD cleavage. Figure reproduced with permission from Ref. 236. Copyright 2017 American Chemical Society.

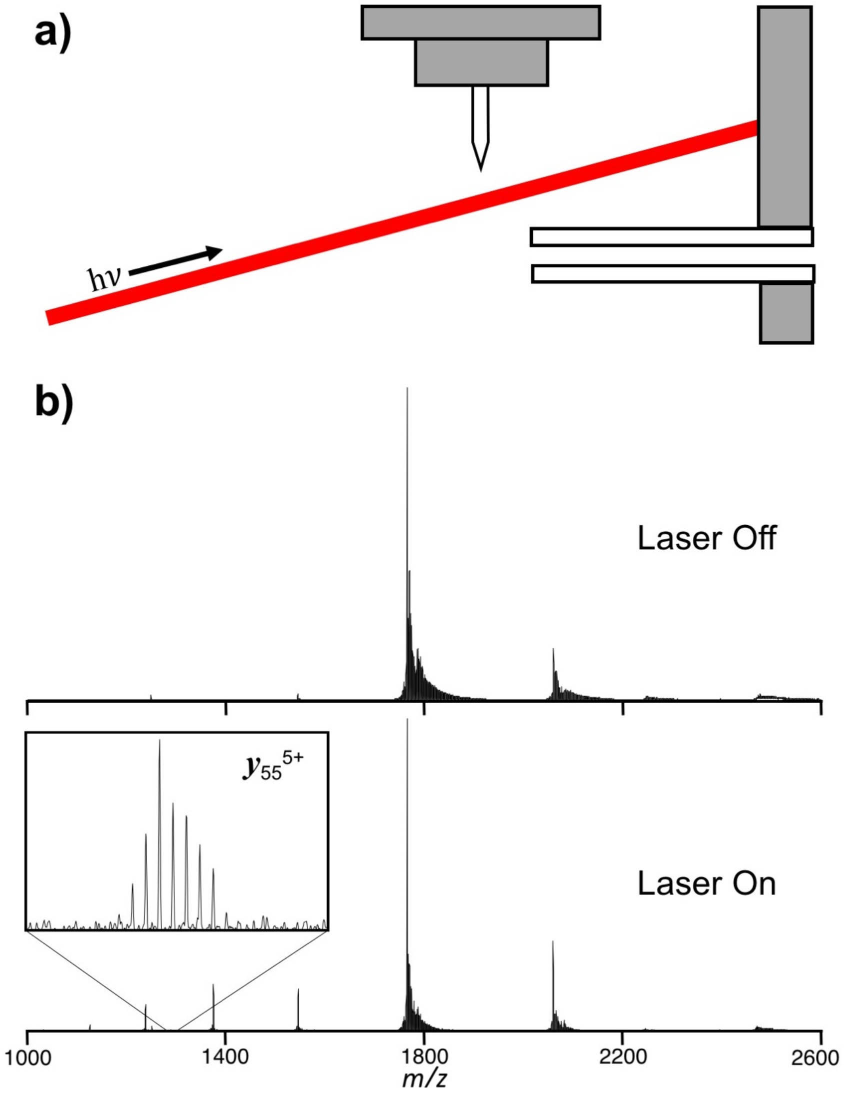

Figure E.10. (a) Experimental schematic of the intentionally misaligned FIRE setup. (b) Spectra of cytochrome *c* with the laser off (top) and on (bottom). Laser irradiation with FIRE produced evidence of higher-charged monomers and NECD fragmentation, despite only overlapping with the sample just after exit from the electrospray tip. Thus, the majority of ion activation from FIRE occurs in the droplet. Figure reproduced with permission from Ref. 236. Copyright 2017 American Chemical Society.

Figure E.11. Fragment map of ferritin activated by FIRE exhibiting *c*-fragments. Figure reproduced with permission from Ref. 236. Copyright 2017 American Chemical Society.

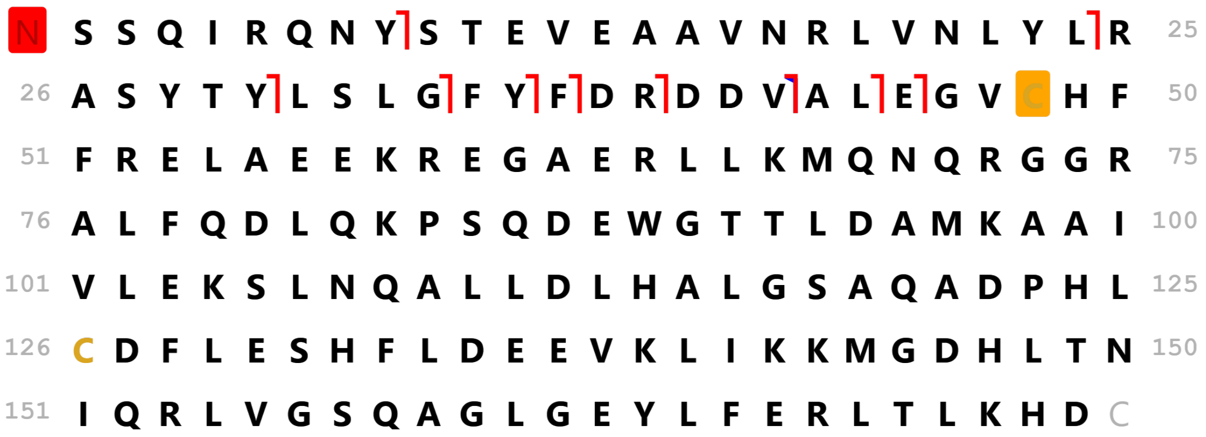

Figure E.12. Activation of the apo-form of horse spleen ferritin produced similar *c*-fragments to the holo-form, suggesting that the iron mineral core is not implicated in NECD. Figure reproduced with permission from Ref. 236. Copyright 2017 American Chemical Society.

References

[1] Willets, K. A.; Van Duyne, R. P. *Annual Review of Physical Chemistry* **2007**, *58*, 267–297.

[2] Bohren, C. F.; Huffman, D. R. *Absorption and Scattering of Light by Small Particles*; Wiley-VCH Verlag GmbH, 1998.

[3] Christopher, P.; Moskovits, M. *Annual Review of Physical Chemistry* **2017**, *68*, 379–398.

[4] Jeanmaire, D. L.; Van Duyne, R. P. *Journal of Electroanalytical Chemistry and Interfacial Electrochemistry* **1977**, *84*, 1–20.

[5] Sharma, B.; Frontiera, R. R.; Henry, A.-I.; Ringe, E.; Van Duyne, R. P. *Materials Today* **2012**, *15*, 16–25.

[6] Moskovits, M. *Reviews of Modern Physics* **1985**, *57*, 783–826.

[7] Zrimsek, A. B.; Chiang, N.; Mattei, M.; Zaleski, S.; McAnally, M. O.; Chapman, C. T.; Henry, A.-I.; Schatz, G. C.; Van Duyne, R. P. *Chemical Reviews* **2016**, *117*, 7583–7613.

[8] Stiles, P. L.; Dieringer, J. A.; Shah, N. C.; Van Duyne, R. P. *Annual Review of Analytical Chemistry* **2008**, *1*, 601–626.

[9] Schatz, G. C.; Van Duyne, R. P. *Handbook of Vibrational Spectroscopy*; Wiley Online Library, 2002; pp 1–16.

[10] Schatz, G. C.; Young, M. A.; Van Duyne, R. P. In *Surface-Enhanced Raman Scattering - Physics and Applications, Topics in Applied Physics*; Kneipp, K., Moskovits, M., Kneipp, H., Eds.; Springer, 2006; Vol. 103; Chapter 2, pp 19–46.

[11] Ding, S.-Y.; You, E.-M.; Tian, Z.-Q.; Moskovits, M. *Chemical Society Reviews* **2017**,

[12] Lombardi, J. R.; Birke, R. L. *The Journal of Physical Chemistry C* **2008**, *112*, 5605–5617.

[13] Kambhampati, P.; Child, C.; Foster, M. C.; Campion, A. *The Journal of Chemical Physics* **1998**, *108*, 5013–5026.

[14] Le Ru, E. C.; Meyer, M.; Etchegoin, P. G. *The Journal of Physical Chemistry B* **2006**, *110*, 1944–1948.

[15] Dieringer, J. A.; Lettan, R. B.; Scheidt, K. A.; Van Duyne, R. P. *Journal of the American Chemical Society* **2007**, *129*, 16249–16256.

[16] Zrimsek, A. B.; Wong, N. L.; Van Duyne, R. P. *The Journal of Physical Chemistry C* **2016**, *120*, 5133–5142.

[17] Chulhai, D. V.; Hu, Z.; Moore, J. E.; Chen, X.; Jensen, L. *Annual Review of Physical Chemistry* **2016**, *67*, 541–564.

[18] Moore, J. E.; Morton, S. M.; Jensen, L. *The Journal of Physical Chemistry Letters* **2012**, *3*, 2470–2475.

[19] Valley, N.; Jensen, L.; Autschbach, J.; Schatz, G. C. *The Journal of Chemical Physics* **2010**, *133*, 054103.

[20] Morton, S. M.; Jensen, L. *Journal of the American Chemical Society* **2009**, *131*, 4090–4098.

[21] Morton, S. M.; Ewusi-Annan, E.; Jensen, L. *Physical Chemistry Chemical Physics* **2009**, *11*, 7424–7429.

[22] Pozzi, E. A.; Goubert, G.; Chiang, N.; Jiang, N.; Chapman, C. T.; McAnally, M. O.; Henry, A.-I.; Seideman, T.; Schatz, G. C.; Hersam, M. C.; Van Duyne, R. P. *Chemical Reviews* **2016**, *117*, 4961–4982.

[23] Gruenke, N. L.; Cardinal, M. F.; McAnally, M. O.; Frontiera, R. R.; Schatz, G. C.; Van Duyne, R. P. *Chemical Society Reviews* **2016**,

[24] Moskovits, M. *Journal of Raman Spectroscopy* **2005**, *36*, 485–496.

[25] Cardinal, M. F.; Vander Ende, E.; Hackler, R. A.; McAnally, M. O.; Stair, P. C.; Schatz, G. C.; Van Duyne, R. P. *Chemical Society Reviews* **2017**, *46*, 3886–3903.

[26] Mukamel, S. *Principles of nonlinear optical spectroscopy*; Oxford University Press, New York, NY, 1999.

[27] Shen, Y.-R. *The principles of nonlinear optics*; Wiley-Interscience: New York, 1984.

[28] Boyd, R. W. *Nonlinear optics*; Academic Press: San Diego, 2003.

[29] Eesley, G. L. *Journal of Quantitative Spectroscopy and Radiative Transfer* **1979**, *22*, 507–576.

[30] Fleming, G. *Chemical applications of ultrafast spectroscopy*; Oxford University Press, New York, NY, 1986.

[31] Potma, E. O.; Mukamel, S. In *Coherent Raman Scattering Microscopy*; Cheng, J.-X., Xie, X. S., Eds.; CRC Press/Taylor & Francis Group, LLC, 2013; Chapter 1, pp 3–42.

[32] Prince, R. C.; Frontiera, R. R.; Potma, E. O. *Chemical Reviews* **2016**, *117*, 5070–5094.

[33] Kukura, P.; Yoon, S.; Mathies, R. A. *Analytical Chemistry* **2006**, *78*, 5952–5959.

[34] Kukura, P.; McCamant, D. W.; Mathies, R. A. *Annual Review of Physical Chemistry* **2007**, *58*, 461–488.

[35] Frontiera, R. R.; Mathies, R. A. *Laser & Photonics Reviews* **2011**, *5*, 102–113.

[36] Dietze, D. R.; Mathies, R. A. *ChemPhysChem* **2016**, *17*, 1224–1251.

[37] Kukura, P.; McCamant, D. W.; Yoon, S.; Wandschneider, D. B.; Mathies, R. A. *Science* **2005**, *310*, 1006–1009.

[38] McCamant, D. W.; Kukura, P.; Mathies, R. A. *The Journal of Physical Chemistry B* **2005**, *109*, 10449–10457.

[39] Dasgupta, J.; Frontiera, R. R.; Taylor, K. C.; Lagarias, J. C.; Mathies, R. A. *Proceedings of the National Academy of Sciences* **2009**, *106*, 1784–1789.

[40] McCamant, D. W.; Kukura, P.; Mathies, R. A. *Applied Spectroscopy* **2003**, *57*, 1317–1323.

[41] Frontiera, R. R.; Dasgupta, J.; Mathies, R. A. *Journal of the American Chemical Society* **2009**, *131*, 15630–15632.

[42] Brown, K. E.; Veldkamp, B. S.; Co, D. T.; Wasielewski, M. R. *The Journal of Physical Chemistry Letters* **2012**, *3*, 2362–6.

[43] Provencher, F.; Brub, N.; Parker, A. W.; Greetham, G. M.; Towrie, M.; Hellmann, C.; Ct, M.; Stingelin, N.; Silva, C.; Hayes, S. C. *Nature Communications* **2014**, *5*, 4288.

[44] Yu, W.; Donohoo-Vallett, P. J.; Zhou, J.; Bragg, A. E. *The Journal of Chemical Physics* **2014**, *141*, 044201.

[45] Fang, C.; Frontiera, R. R.; Tran, R.; Mathies, R. A. *Nature* **2009**, *462*, 200–204.

[46] Yoon, S.; Kukura, P.; Stuart, C. M.; Mathies, R. A. *Molecular Physics* **2006**, *104*, 1275–1282.

[47] Ploetz, E.; Gellner, M.; Schütz, M.; Marx, B.; Schlücker, S.; Gilch, P. Surface Enhancement in Femtosecond Stimulated Raman Scattering. American Institute of Physics Conference Series. 2010; pp 88–89.

[48] Heiman, D.; Hellwarth, R. W.; Levenson, M. D.; Martin, G. *Physical Review Letters* **1976**, *36*, 189–192.

[49] McMorrow, D.; Lotshaw, W. T.; Kenney-Wallace, G. A. *Chemical Physics Letters* **1988**, *145*, 309–314.

[50] Borysow, J.; Taylor, R.; Keto, J. *Optics Communications* **1988**, *68*, 80–86.

[51] Borysow, J.; Taylor, R.; Keto, J. *Journal of Raman Spectroscopy* **1989**, *20*, 203–208.

[52] Klenerman, D.; Gerrard, D. L.; Herman, H.; Macpherson, M. T. *Chemical Physics Letters* **1990**, *168*, 579–583.

[53] Klenerman, D. *Optics Letters* **1991**, *16*, 838–839.

[54] Shim, S.; Mathies, R. A. *Journal of Raman Spectroscopy* **2008**, *39*, 1526–1530.

[55] Bachler, B. R.; Fermann, M. E.; Ogilvie, J. P. *Optics Express* **2012**, *20*, 835–844.

[56] Balakrishnan, G.; Soldatova, A. V.; Reid, P. J.; Spiro, T. G. *Journal of the American Chemical Society* **2014**, *136*, 8746–8754.

[57] Freudiger, C. W.; Roe, M. B. J.; Zhang, X.; Saar, B. G.; Min, W.; Xie, X. S. *Journal of Physical Chemistry B* **2011**, *115*, 5574–5581.

[58] Kumar, V.; Casella, M.; Molotokaite, E.; Gatti, D.; Kukura, P.; Manzoni, C.; Polli, D.; Marangoni, M.; Cerullo, G. *Physical Review A* **2012**, *86*, 053810.

[59] Ideguchi, T.; Bernhardt, B.; Guelachvili, G.; Hänsch, T. W.; Picqué, N. *Optics Letters* **2012**, *37*, 4498–4500.

[60] Dobner, S.; Groß, P.; Fallnich, C. *Journal of Chemical Physics* **2013**, *138*, 244201.

[61] Kumar, V.; Coluccelli, N.; Cassinerio, M.; Celebrano, M.; Nunn, A.; Levrero, M.; Scopigno, T.; Marangoni, M. *Journal of Raman Spectroscopy* **2014**, *46*, 109–116.

[62] McAnally, M. O.; Guo, Y.; Balakrishnan, G.; Schatz, G. C.; Van Duyne, R. P. *Optics Letters* **2016**, *41*, 5357–5360.

[63] Shirota, H.; Fujisawa, T.; Fukazawa, H.; Nishikawa, K. *Bulletin of the Chemical Society of Japan* **2009**, *82*, 1347–1366.

[64] Zhong, Q.; Fourkas, J. T. *The Journal of Physical Chemistry B* **2008**, *112*, 15529–15539.

[65] Castner, E.; Maroncelli, M. *Journal of Molecular Liquids* **1998**, *77*, 1–36.

[66] Lotshaw, W. T.; McMorrow, D.; Thantu, N.; Melinger, J. S.; Kitchenham, R. *Journal of Raman Spectroscopy* **1995**, *26*, 571–583.

[67] Evans, C. L.; Xie, X. S. *Annual Review of Analytical Chemistry* **2008**, *1*, 883–909.

[68] Cheng, J.-X.; Xie, X. S. *Journal of Physical Chemistry B* **2004**, *108*, 827–840.

[69] Potma, E. O.; De Boeij, W. P.; Wiersma, D. A. *Journal of the Optical Society of America B* **2000**, *17*, 1678–1684.

[70] Piatkowski, L.; Hugall, J. T.; Van Hulst, N. F. *Nature Photonics* **2014**, *8*, 589–591.

[71] Chen, C. K.; de Castro, A. R. B.; Shen, Y. R.; DeMartini, F. *Physical Review Letters* **1979**, *43*, 946–949.

[72] Frontiera, R. R.; Henry, A.-I.; Gruenke, N. L.; Van Duyne, R. P. *The Journal of Physical Chemistry Letters* **2011**, *2*, 1199–1203.

[73] Du, J.; Harra, J.; Virkki, M.; Mäkelä, J. M.; Leng, Y.; Kauranen, M.; Kobayashi, T. *Scientific Reports* **2016**, *6*.

[74] Maker, P.; Terhune, R. *Physical Review* **1965**, *137*, A801.

[75] Yampolsky, S.; Fishman, D. A.; Dey, S.; Hulkko, E.; Banik, M.; Potma, E. O.; Apkarian, V. A. *Nature Photonics* **2014**, *8*, 650–656.

[76] Zhang, Y.; Zhen, Y.-R.; Neumann, O.; Day, J. K.; Nordlander, P.; Halas, N. J. *Nature Communications* **2014**, *5*, 4424.

[77] Koo, T.-W.; Chan, S.; Berlin, A. A. *Optics Letters* **2005**, *30*, 1024–1026.

[78] Liang, E.; Weippert, A.; Funk, J.-M.; Materny, A.; Kiefer, W. *Chemical Physics Letters* **1994**, *227*, 115–120.

[79] Lee, P.; Meisel, D. *The Journal of Physical Chemistry* **1982**, *86*, 3391–3395.

[80] Zumbusch, A.; Holtom, G. R.; Xie, X. S. *Physical Review Letters* **1999**, *82*, 4142.

[81] Cheng, J.-X. X.; Book, L. D.; Xie, X. S. *Optics Letters* **2001**, *26*, 1341–1343.

[82] Ichimura, T.; Hayazawa, N.; Hashimoto, M.; Inouye, Y.; Kawata, S. *Journal of Raman Spectroscopy* **2003**, *34*, 651–654.

[83] Fang, Y.; Seong, N.-H.; Dlott, D. D. *Science* **2008**, *321*, 388–392.

[84] Schlucker, S.; Salehi, M.; Bergner, G.; Schutz, M.; Strobel, P.; Marx, A.; Petersen, I.; Dietzek, B.; Popp, J. *Analytical Chemistry* **2011**, *83*, 7081–7085.

[85] Addison, C. J.; Konorov, S. O.; Brolo, A. G.; Blades, M. W.; Turner, R. F. *The Journal of Physical Chemistry C* **2009**, *113*, 3586–3592.

[86] Steuwe, C.; Kaminski, C. F.; Baumberg, J. J.; Mahajan, S. *Nano Letters* **2011**, *11*, 5339–5343.

[87] Chew, H.; Wang, D. S.; Kerker, M. *Journal of the Optical Society of America B* **1984**, *1*, 56–66.

[88] Parkhill, J. A.; Rappoport, D.; Aspuru-Guzik, A. *The Journal of Physical Chemistry Letters* **2011**, *2*, 1849–1854.

[89] Hua, X.; Voronine, D. V.; Ballmann, C. W.; Sinyukov, A. M.; Sokolov, A. V.; Scully, M. O. *Physical Review A* **2014**, *89*, 43841.

[90] Voronine, D. V.; Sinyukov, A. M.; Hua, X.; Munusamy, E.; Ariunbold, G.; Sokolov, A. V.; Scully, M. O. *Journal of Modern Optics* **2015**, *62*, 90–96.

[91] Moad, A. J.; Simpson, G. J. *The Journal of Physical Chemistry A* **2005**, *109*, 1316–1323.

[92] Voronine, D. V.; Sinyukov, A. M.; Hua, X.; Wang, K.; Jha, P. K.; Munusamy, E.; Wheeler, S. E.; Welch, G.; Sokolov, A. V.; Scully, M. O. *Scientific Reports* **2012**, *2*, 891.

[93] Scully, M.; Kattawar, G.; Lucht, R.; Opatrnỳ, T.; Pilloff, H.; Rebane, A.; Sokolov, A.; Zubairy, M. *Proceedings of the National Academy of Sciences* **2002**, *99*, 10994–11001.

[94] Ichimura, T.; Hayazawa, N.; Hashimoto, M.; Inouye, Y.; Kawata, S. *Physical Review Letters* **2004**, *92*, 220801.

[95] Ichimura, T.; Hayazawa, N.; Hashimoto, M.; Inouye, Y.; Kawata, S. *Applied Physics Letters* **2004**, *84*, 1768–1770.

[96] Hayazawa, N.; Ichimura, T.; Hashimoto, M.; Inouye, Y.; Kawata, S. *Journal of Applied Physics* **2004**, *95*, 2676–2681.

[97] Furusawa, K.; Hayazawa, N.; Catalan, F. C.; Okamoto, T.; Kawata, S. *Journal of Raman Spectroscopy* **2012**, *43*, 656–661.

[98] Frontiera, R. R.; Gruenke, N. L.; Van Duyne, R. P. *Nano Letters* **2012**, *12*, 5989–5994.

[99] Buchanan, L. E.; Gruenke, N. L.; McAnally, M. O.; Negru, B.; Mayhew, H. E.; Apkarian, V. A.; Schatz, G. C.; Van Duyne, R. P. *Journal of Physical Chemistry Letters* **2016**, *7*, 4629–4634.

[100] Buchanan, L. E.; McAnally, M. O.; Gruenke, N. L.; Schatz, G. C.; Van Duyne, R. P. *The Journal of Physical Chemistry Letters* **2017**, *8*, 3328–3333.

[101] Crampton, K. T.; Zeytunyan, A.; Fast, A. S.; Ladani, F. T.; Alfonso-Garcia, A.; Banik, M.; Yampolsky, S.; Fishman, D. A.; Potma, E. O.; Apkarian, V. A. *The Journal of Physical Chemistry C* **2016**, *120*, 20943–20953.

[102] Wickramasinghe, H. K.; Chaigneau, M.; Yasukuni, R.; Picardi, G.; Ossikovski, R. *ACS Nano* **2014**, *8*, 3421–3426.

[103] Jahng, J.; Brocious, J.; Fishman, D. A.; Huang, F.; Li, X.; Tamma, V. A.; Wickramasinghe, H. K.; Potma, E. O. *Physical Review B* **2014**, *90*, 155417.

[104] Jahng, J.; Brocious, J.; Fishman, D. A.; Yampolsky, S.; Nowak, D.; Huang, F.; Apkarian, V. A.; Wickramasinghe, H. K.; Potma, E. O. *Applied Physics Letters* **2015**, *106*, 083113.

[105] Jahng, J.; Fishman, D. A.; Park, S.; Nowak, D. B.; Morrison, W. A.; Wickramasinghe, H. K.; Potma, E. O. *Accounts of Chemical Research* **2015**, *48*, 2671–2679.

[106] Tamma, V. A.; Huang, F.; Nowak, D.; Kumar Wickramasinghe, H. *Applied Physics Letters* **2016**, *108*, 233107.

[107] Ladani, F. T.; Potma, E. O. *Physical Review B* **2017**, *95*, 205440.

[108] Rajapaksa, I.; Kumar Wickramasinghe, H. *Applied Physics Letters* **2011**, *99*, 161103.

[109] Nowak, D.; Morrison, W.; Wickramasinghe, H. K.; Jahng, J.; Potma, E.; Wan, L.; Ruiz, R.; Albrecht, T. R.; Schmidt, K.; Frommer, J.; Sanders, D. P.; Park, S. *Science Advances* **2016**, *2*, e1501571.

[110] McAnally, M. O.; McMahon, J. M.; Van Duyne, R. P.; Schatz, G. C. *The Journal of Chemical Physics* **2016**, *145*, 094106.

[111] Mandal, A.; Erramilli, S.; Ziegler, L. *The Journal of Physical Chemistry C* **2016**, *120*, 20998–21006.

[112] Bloembergen, N.; Shen, Y. *Physical Review Letters* **1964**, *12*, 504–507.

[113] Shen, Y.; Bloembergen, N. *Physical Review A* **1965**, *137*, 1787–1805.

[114] Freudiger, C. W.; Min, W.; Saar, B. G.; Lu, S.; Holtom, G. R.; He, C.; Tsai, J. C.; Kang, J. X.; Xie, X. S. *Science* **2008**, *322*, 1857–1861.

[115] Wei, L.; Hu, F.; Shen, Y.; Chen, Z.; Yu, Y.; Lin, C.-C.; Wang, M. C.; Min, W. *Nature Methods* **2014**, *11*, 410–412.

[116] McCamant, D. W.; Kukura, P.; Mathies, R. A. *Journal of Physical Chemistry A* **2003**, *107*, 8208–8214.

[117] McCamant, D. W.; Kukura, P.; Yoon, S.; Mathies, R. A. *Review of Scientific Instruments* **2004**, *75*, 4971–4980.

[118] Fleischmann, M.; Hendra, P. J.; McQuillan, A. J. *Chemical Physics Letters* **1974**, *26*, 163–166.

[119] Albrecht, M. G.; Creighton, J. A. *Journal of the American Chemical Society* **1977**, *99*, 5215–5217.

[120] Fano, U. *Physical Review* **1961**, *124*, 1866–1878.

[121] Miroshnichenko, A. E.; Flach, S.; Kivshar, Y. S. *Reviews of Modern Physics* **2010**, *82*, 2257–2298.

[122] Neubrech, F.; Pucci, A.; Cornelius, T. W.; Karim, S.; García-Etxarri, A.; Aizpurua, J. *Physical Review Letters* **2008**, *101*, 157403.

[123] Chng, B. X. K.; Dijk, T. V.; Bhargava, R.; Carney, P. S. *Physical Chemistry Chemical Physics* **2015**, *17*, 21348–21355.

[124] Roelli, P.; Galland, C.; Piro, N.; Kippenberg, T. J. *Nature Nanotechnology* **2016**, *11*, 164–169.

[125] Schmidt, M. K.; Esteban, R.; González-Tudela, A.; Giedke, G.; Aizpurua, J. *ACS Nano* **2016**, *10*, 6291–6298.

[126] Lee, S.-Y.; Zhang, D.; McCamant, D. W.; Kukura, P.; Mathies, R. A. *Journal of Chemical Physics* **2004**, *121*, 3632.

[127] Sun, Z.; Qiu, X. Q.; Lu, J.; Zhang, D. H.; Lee, S.-Y. *Journal of Raman Spectroscopy* **2008**, *39*, 1568–1577.

[128] Sun, Z.; Lu, J.; Zhang, D. H.; Lee, S.-Y. *Journal of Chemical Physics* **2008**, *128*, 144114.

[129] Zhao, B.; Niu, K.; Li, X.; Lee, S.-Y. *Science China Chemistry* **2011**, *54*, 1989–2008.

[130] Yoon, S.; McCamant, D. W.; Kukura, P.; Mathies, R. A. *Journal of Chemical Physics* **2005**, *122*, 024505.

[131] Placzek, G. In *Handbuch der Radiologie*; Marx, E., Ed.; Academische Verlagsgesellschaft: Leipzig, 1934; pp 205–374.

[132] Mullin, J.; Schatz, G. C. *The Journal of Physical Chemistry A* **2012**, *116*, 1931–1938.

[133] Marinica, D. C.; Kazansky, A. K.; Nordlander, P.; Aizpurua, J.; Borisov, A. G. *Nano Letters* **2012**, *12*, 1333–1339.

[134] Ausman, L. K.; Schatz, G. C. *The Journal of Chemical Physics* **2009**, *131*, 84708.

[135] Baerends, E. et al. ADF2014.

[136] Yang, W.-H.; Schatz, G. C. *The Journal of Chemical Physics* **1992**, *97*, 3831.

[137] Chapman, C. T.; Schatz, G. C. *Unpublished Work* **2017**,

[138] Zrimsek, A. B. Advances in Fundamental Single Molecule Studies with Surface-Enhanced Raman Spectroscopy. Ph.D. thesis, Northwestern University, 2016.

[139] Hamm, P.; Zanni, M. *Concepts and methods of 2D infrared spectroscopy*; Cambridge University Press, 2011.

[140] Brandt, N. C.; Keller, E. L.; Frontiera, R. R. *The Journal of Physical Chemistry Letters* **2016**, *7*, 3179–3185.

[141] Oudar, J.-L.; Smith, R. W.; Shen, Y. R. *Applied Physics Letters* **1979**, *34*, 758.

[142] Toleutaev, B. N.; Tahara, T.; Hamaguchi, H. *Applied Physics B Laser and Optics* **1994**, *59*, 369–375.

[143] Saito, Y.; Ishibashi, T.; Hamaguchi, H. *Journal of Raman Spectroscopy* **2000**, *31*, 725–730.

[144] Frontiera, R. R.; Shim, S.; Mathies, R. A. *The Journal of Chemical Physics* **2008**, *129*, 64507.

[145] Levenson, M. D.; Bloembergen, N. *Physical Review B* **1974**, *10*, 4447–4463.

[146] Levenson, M. D.; Song, J. J. *Journal of the Optical Society of America* **1976**, *66*, 641–643.

[147] Uversky, V. N.; Oldfield, C. J.; Dunker, A. K. *Annual Review of Biophysics* **2008**, *37*, 215–246.

[148] Aida, T.; Meijer, E. W.; Stupp, S. I. *Science* **2012**, *335*, 813–7.

[149] Gruenke, N. L.; McAnally, M. O.; Schatz, G. C.; Van Duyne, R. P. *The Journal of Physical Chemistry C* **2016**, *120*, 29449–29454.

[150] Kauranen, M.; Zayats, A. V. *Nature Photonics* **2012**, *6*, 737–748.

[151] Ferry, V. E.; Smith, J. M.; Alivisatos, A. P. *ACS Photonics* **2014**, *1*, 1189–1196.

[152] Banik, M.; Rodriguez, K.; Hulkko, E.; Apkarian, V. A. *ACS Photonics* **2016**, *3*, 2482–2489.

[153] Schatz, G. C. *Personal Communication*; 2016.

[154] King, R. B. *Annals of the New York Academy of Sciences* **2003**, *988*, 158–170.

[155] McCamant, D. W.; Kukura, P.; Yoon, S.; Mathies, R. A. *Review of Scientific Instruments* **2004**, *75*, 4971–4980.

[156] Zeytunyan, A.; Crampton, K. T.; Zadoyan, R.; Apkarian, V. A. *Optics Express* **2015**, *23*, 24019–24028.

[157] Kochuveedu, S. T.; Jang, Y. H.; Kim, D. H. *Chemical Society Reviews* **2013**, *42*, 8467–8493.

[158] Hou, W.; Cronin, S. B. *Advanced Functional Materials* **2013**, *23*, 1612–1619.

[159] Ueno, K.; Misawa, H. *Journal of Photochemistry and Photobiology C: Photochemistry Reviews* **2013**, *15*, 31–52.

[160] Zhang, Z.; Deckert-Gaudig, T.; Deckert, V. *Analyst* **2015**, *140*, 4325–4335.

[161] Mukherjee, S.; Zhou, L.; Goodman, A. M.; Large, N.; Ayala-Orozco, C.; Zhang, Y.; Nordlander, P.; Halas, N. J. *Journal of the American Chemical Society* **2013**, *136*, 64–67.

[162] Haller, K. L.; Bumm, L. A.; Altkorn, R. I.; Zeman, E. J.; Schatz, G. C.; Van Duyne, R. P. *The Journal of Chemical Physics* **1989**, *90*, 1237–1252.

[163] Fujiwara, H.; Yanagida, S.; Kamat, P. V. *The Journal of Physical Chemistry B* **1999**, *103*, 2589–2591.

[164] Link, S.; Burda, C.; Mohamed, M.; Nikoobakht, B.; El-Sayed, M. A. *The Journal of Physical Chemistry A* **1999**, *103*, 1165–1170.

[165] Eah, S.-K.; Jaeger, H. M.; Scherer, N. F.; Lin, X.-M.; Wiederrecht, G. P. *Chemical Physics Letters* **2004**, *386*, 390–395.

[166] Li, X.; Lee, J.-P.; Blinn, K. S.; Chen, D.; Yoo, S.; Kang, B.; Bottomley, L. A.; El-Sayed, M. A.; Park, S.; Liu, M. *Energy & Environmental Science* **2014**, *7*, 306–310.

[167] Wang, X.-D.; Luo, A.-P.; Liu, H.; Zhao, N.; Liu, M.; Zhu, Y.-F.; Xue, J.-P.; Luo, Z.-C.; Xu, W.-C. *Optics Express* **2015**, *23*, 22602–22610.

[168] Sung, J.; Kosuda, K. M.; Zhao, J.; Elam, J. W.; Spears, K. G.; Van Duyne, R. P. *The Journal of Physical Chemistry C* **2008**, *112*, 5707–5714.

[169] Dobner, S.; Cleff, C.; Fallnich, C.; Groß, P. *The Journal of Chemical Physics* **2012**, *137*, 174201.

[170] Beier, H. T.; Noojin, G. D.; Rockwell, B. A. *Optics Express* **2011**, *19*, 18885–18892.

[171] Tyler, T. P.; Henry, A.-I.; Van Duyne, R. P.; Hersam, M. C. *The Journal of Physical Chemistry Letters* **2011**, *2*, 218–222.

[172] Harbola, U.; Umapathy, S.; Mukamel, S. *Physical Review A* **2013**, *88*, 011801.

[173] McAnally, M. O.; Phelan, B. T.; Young, R. M.; Wasielewski, M. R.; Schatz, G. C.; Van Duyne, R. P. *Analytical Chemistry* **2017**, *89*, 6931–6935.

[174] Kleinman, S. L.; Sharma, B.; Blaber, M. G.; Henry, A.-I.; Valley, N.; Freeman, R. G.; Natan, M. J.; Schatz, G. C.; Van Duyne, R. P. *Journal of the American Chemical Society* **2012**, *135*, 301–308.

[175] Crampton, K. T.; Fast, A.; Potma, E. O.; Apkarian, V. A. *Unpublished Work* **2017**,

[176] Grumstrup, E. M.; Chen, Z.; Vary, R. P.; Moran, A. M.; Schanze, K. S.; Papanikolas, J. M. *The Journal of Physical Chemistry B* **2013**, *117*, 8245–8255.

[177] Chernyak, V. Y.; Saurabh, P.; Mukamel, S. *The Journal of Chemical Physics* **2015**, *143*, 164107.

[178] McCreery, R. L. *Raman spectroscopy for chemical analysis*; John Wiley & Sons, 2000.

[179] Le Ru, E.; Etchegoin, P. G. *Principles of surface-enhanced Raman spectroscopy and related plasmonic effects*; Elsevier: Amsterdam, The Netherlands, 2009.

[180] Lee, J.; Challa, J. R.; McCamant, D. W. *Journal of Raman Spectroscopy* **2013**, *44*, 1263–1272.

[181] Silva, W. R.; Keller, E. L.; Frontiera, R. R. *Analytical Chemistry* **2014**, *86*, 7782–7787.

[182] Umapathy, S.; Lakshmanna, A.; Mallick, B. *Journal of Raman Spectroscopy* **2009**, *40*, 235–237.

[183] Alberts, B.; Bray, D.; Hopkin, K.; Johnson, A.; Lewis, J.; Raff, M.; Roberts, K.; Walter, P. *Essential cell biology*, 4th ed.; Garland Science, 2013.

[184] Shafer-Peltier, K.; Haynes, C. L.; Glucksberg, M.; Van Duyne, R. P. *Journal of the American Chemical Society* **2003**, *125*, 588.

[185] Shah, N. C.; Yuen, J. M.; Lyandres, O.; Glucksberg, M.; Walsh, J. T.; Van Duyne, R. P. In *In Vivo Glucose Sensing*; Cunningham, D. D., Stenken, J. A., Eds.; John Wiley & Sons, 2010; Chapter 15, pp 421–443.

[186] Wang, X.; Zhang, A.; Zhi, M.; Sokolov, A. V.; Welch, G. R. *Physical Review A* **2010**, *81*, 013813.

[187] Hu, F.; Chen, Z.; Zhang, L.; Shen, Y.; Wei, L.; Min, W. *Angewandte Chemie International Edition* **2015**, *127*, 9959–9963.

[188] Vasko, P.; Blackwell, J.; Koenig, J. *Carbohydrate Research* **1972**, *23*, 407–416.

[189] Mathlouthi, M.; Luu, D. *Carbohydrate Research* **1980**, *81*, 203–212.

[190] Ray, K. G. Spatially resolved Raman spectroscopy of carbon electrode materials: A study of surface microstructure and reactivity. Ph.D. thesis, Ohio State University, 1998.

[191] Schrötter, H. W.; Klöckner, H. W. In *Raman Spectroscopy of Gases and Liquids*; Weber, A., Ed.; Springer Berlin Heidelberg: Berlin, Heidelberg, 1979; pp 123–166.

[192] Trulson, M. O.; Mathies, R. A. *The Journal of Chemical Physics* **1986**, *84*, 2068.

[193] Le Ru, E. C.; Blackie, E. J.; Meyer, M.; Etchegoin, P. G. *The Journal of Physical Chemistry C* **2007**, *111*, 13794–13803.

[194] Arboleda, P. H.; Loppnow, G. R. *Analytical Chemistry* **2000**, *72*, 2093–2098.

[195] Molteni, C.; Parrinello, M. *Journal of the American Chemical Society* **1998**, *120*, 2168–2171.

[196] Mathlouthi, M.; Luu, C.; Meffroy-Biget, A. M.; Vinh Luu, D. *Carbohydrate Research* **1980**, *81*, 213–223.

[197] Mallick, B.; Lakhsmanna, A.; Umapathy, S. *Journal of Raman Spectroscopy* **2011**, *42*, 1883–1890.

[198] Kawata, S.; Inouye, Y.; Verma, P. *Nature Photonics* **2009**, *3*, 388–394.

[199] Nordlander, P.; Oubre, C.; Prodan, E.; Li, K.; Stockman, M. I. *Nano Letters* **2004**, *4*, 899–903.

[200] Fontana, J.; Ratna, B. R. *Applied Physics Letters* **2014**, *105*, 011107.

[201] Fontana, J.; Charipar, N.; Flom, S. R.; Naciri, J.; Pique, A.; Ratna, B. R. *ACS Photonics* **2016**, *3*, 904–911.

[202] Thomann, I.; Pinaud, B. A.; Chen, Z.; Clemens, B. M.; Jaramillo, T. F.; Brongersma, M. L. *Nano Letters* **2011**, *11*, 3440–6.

[203] Chen, H. M.; Chen, C. K.; Chen, C.-J.; Cheng, L.-C.; Wu, P. C.; Cheng, B. H.; Ho, Y. Z.; Tseng, M. L.; Hsu, Y.-Y.; Can, T.-S.; Lee, J.-F.; Liu, R.-S.; Tsai, D. P. *ACS Nano* **2012**, *6*, 7362–7372.

[204] Lee, J.; Mubeen, S.; Ji, X.; Stucky, G. D.; Moskovits, M. *Nano Letters* **2012**, *12*, 5014–9.

[205] Link, S.; El-Sayed, M. A. *Journal of Physical Chemistry B* **1999**, *103*, 8410–8426.

[206] Scarabelli, L.; Sánchez-Iglesias, A.; Pérez-Juste, J.; Liz-Marzán, L. M. *The Journal of Physical Chemistry Letters* **2015**, *6*, 4270–4279.

[207] Park, K.; Hsiao, M.-S.; Koerner, H.; Jawaid, A.; Che, J.; Vaia, R. A. *The Journal of Physical Chemistry C* **2016**, *120*, 28235–28245.

[208] Jung, H.; Cha, H.; Lee, D.; Yoon, S. *ACS Nano* **2015**, *9*, 12292–12300.

[209] Keller, E. L.; Frontiera, R. R. *ACS Photonics* **2017**, *4*, 1033–1039.

[210] Masango, S. S.; Hackler, R. A.; Henry, A.-I.; McAnally, M. O.; Schatz, G. C.; Stair, P. C.; Van Duyne, R. P. *The Journal of Physical Chemistry C* **2016**, *120*, 3822–3833.

[211] Masango, S. S.; Hackler, R. A.; Large, N.; Henry, A.-I.; McAnally, M. O.; Schatz, G. C.; Stair, P. C.; Van Duyne, R. P. *Nano Letters* **2016**, *16*, 4251–4259.

[212] Hackler, R. A.; McAnally, M. O.; Schatz, G. C.; Stair, P. C.; Van Duyne, R. P. *Journal of the American Chemical Society* **2017**, *139*, 2456–2463.

[213] Aaltonen, T.; Alén, P.; Ritala, M.; Leskelä, M. *Chemical Vapor Deposition* **2003**, *9*, 45–49.

[214] Leskelä, M.; Ritala, M. *Thin Solid Films* **2002**, *409*, 138–146.

[215] Ferguson, J.; Smith, E.; Weimer, A.; George, S. *Journal of The Electrochemical Society* **2004**, *151*, G528–G535.

[216] Nalwa, H. S. *Handbook of Advanced Electronic and Photonic Materials and Devices: Semiconductors. Vol. 1*; Academic Press, 2001.

[217] Peters, A. W.; Li, Z.; Farha, O. K.; Hupp, J. T. *ACS Nano* **2015**, *9*, 8484–8490.

[218] Negru, B.; Sprague-Klein, E. A.; Madison, L. R.; McAnally, M. O.; Banik, M.; Hulkko, E.; Apkarian, V. A.; Ratner, M. A.; Schatz, G. C.; Seideman, T.; Van Duyne, R. P. *Journal of the American Chemical Society* **2017**, *In preparation.*

[219] Sprague-Klein, E. A.; McAnally, M. O.; Zhdanov, D. V.; Zrimsek, A. B.; Apkarian, V. A.; Schatz, G. C.; Seideman, T.; Van Duyne, R. P. *Journal of the American Chemical Society* **2017**, *In preparation.*

[220] Shao, Y. et al. *Molecular Physics* **2015**, *113*, 184–215.

[221] Benson, E. E.; Kubiak, C. P.; Sathrum, A. J.; Smieja, J. M. *Chemical Society Reviews* **2009**, *38*, 89–99.

[222] Walter, M. G.; Warren, E. L.; McKone, J. R.; Boettcher, S. W.; Mi, Q.; Santori, E. A.; Lewis, N. S. *Chemical Reviews* **2010**, *110*, 6446–6473.

[223] Warren, S. C.; Thimsen, E. *Energy & Environmental Science* **2012**, *5*, 5133–5146.

[224] Hawecker, J.; Lehn, J.-M.; Ziessel, R. *Chemical Communications* **1983**, *9*, 536–538.

[225] Sullivan, B. P.; Bolinger, C. M.; Conrad, D.; Vining, W. J.; Meyer, T. J. *Chemical Communications* **1985**, *20*, 1414–1416.

[226] Worl, L. A.; Duesing, R.; Chen, P.; Della Ciana, L.; Meyer, T. J. *Dalton Transactions* **1991**, *S*, 849–858.

[227] Sampson, M. D.; Froehlich, J. D.; Smieja, J. M.; Benson, E. E.; Sharp, I. D.; Kubiak, C. P. *Energy & Environmental Science* **2013**, *6*, 3748–3755.

[228] Riplinger, C.; Sampson, M. D.; Ritzmann, A. M.; Kubiak, C. P.; Carter, E. A. *Journal of the American Chemical Society* **2014**, *136*, 16285–16298.

[229] Tan, Y.; Ma, L.; Gao, Z.; Chen, M.; Chen, F. *Nano Letters* **2017**, *17*, 2621–2626.

[230] Tian, H.; Chen, H.-Y.; Gao, B.; Yu, S.; Liang, J.; Yang, Y.; Xie, D.; Kang, J.; Ren, T.-L.; Zhang, Y.; Wong, H.-S. *Nano Letters* **2013**, *13*, 651–657.

[231] Ossig, R.; Kolomijeca, A.; Kwon, Y.-H.; Hubenthal, F.; Kronfeldt, H.-D. *Journal of Raman Spectroscopy* **2013**, *44*, 717–722.

[232] Li, C.; Hsieh, J.; Hung, M.-T.; Huang, B. *Thin Solid Films* **2015**, *587*, 75–82.

[233] Greeneltch, N. G.; Blaber, M. G.; Henry, A.-I.; Schatz, G. C.; Van Duyne, R. P. *Analytical Chemistry* **2013**, *85*, 2297–2303.

[234] FDTD Solutions, Lumerical Solutions, Inc. http://www.lumerical.com/tcad-products/fdtd/.

[235] Kurouski, D.; Large, N.; Chiang, N.; Greeneltch, N.; Carron, K. T.; Seideman, T.; Schatz, G. C.; Van Duyne, R. P. *Analyst* **2016**, *141*, 1779–1788.

[236] Skinner, O. S.; McAnally, M. O.; Haverland, N. A.; Van Duyne, R. P.; Schatz, G. C.; Breuker, K.; Compton, P. D.; Kelleher, N. L. *Analytical Chemistry* **2017**, *R1 Submitted*.

[237] Loo, J. A. *Mass Spectrometry Reviews* **1997**, *16*, 1–23.

[238] Heck, A. J.; van den Heuvel, R. H. *Mass Spectrometry Reviews* **2004**, *23*, 368–389.

[239] Schneeberger, E.-M.; Breuker, K. *Angewandte Chemie International Edition* **2017**, *56*, 1254–1258.

[240] Barrera, N. P.; Di Bartolo, N.; Booth, P. J.; Robinson, C. V. *Science* **2008**, *321*, 243–246.

[241] Hopper, J. T.; Yu, Y. T.-C.; Li, D.; Raymond, A.; Bostock, M.; Liko, I.; Mikhailov, V.; Laganowsky, A.; Benesch, J. L.; Caffrey, M.; Nietlispach, D.; Robinson, C. V. *Nature Methods* **2013**, *10*, 1206–1208.

[242] Belov, M. E.; Damoc, E.; Denisov, E.; Compton, P. D.; Horning, S.; Makarov, A. A.; Kelleher, N. L. *Analytical Chemistry* **2013**, *85*, 11163–11173.

[243] Zhang, H.; Cui, W.; Wen, J.; Blankenship, R. E.; Gross, M. L. *Journal of the American Society for Mass Spectrometry* **2010**, *21*, 1966–1968.

[244] Blackwell, A. E.; Dodds, E. D.; Bandarian, V.; Wysocki, V. H. *Analytical Chemistry* **2011**, *83*, 2862–2865.

[245] Song, Y.; Nelp, M. T.; Bandarian, V.; Wysocki, V. H. *ACS Central Science* **2015**, *1*, 477–487.

[246] Li, H.; Wongkongkathep, P.; Van Orden, S. L.; Loo, R. R. O.; Loo, J. A. *Journal of the American Society for Mass Spectrometry* **2014**, *25*, 2060.

[247] Breuker, K.; McLafferty, F. W. *Angewandte Chemie International Edition* **2003**, *42*, 4900–4904.

[248] Breuker, K.; McLafferty, F. W. *Angewandte Chemie International Edition* **2005**, *44*, 4911–4914.

[249] Roepstorff, P.; Fohlman, J. *Biological Mass Spectrometry* **1984**, *11*, 601–601.

[250] Breuker, K. *International Journal of Mass Spectrometry* **2006**, *253*, 249–255.

[251] Mann, S.; Bannister, J. V.; Williams, R. J. *Journal of Molecular Biology* **1986**, *188*, 225–232.

[252] Theil, E. C. *Current Opinion in Chemical Biology* **2011**, *15*, 304–311.

[253] Haldar, S.; Bevers, L. E.; Tosha, T.; Theil, E. C. *Journal of Biological Chemistry* **2011**, *286*, 25620–25627.

[254] Hempstead, P. D.; Hudson, A. J.; Artymiuk, P. J.; Andrews, S. C.; Banfield, M. J.; Guest, J. R.; Harrison, P. M. *FEBS Letters* **1994**, *350*, 258–262.

[255] Theil, E. C.; Tosha, T.; Behera, R. K. *Accounts of Chemical Research* **2016**, *49*, 784–791.

[256] Behera, R. K.; Theil, E. C. *Proceedings of the National Academy of Sciences* **2014**, *111*, 7925–7930.

[257] Bernacchioni, C.; Pozzi, C.; Di Pisa, F.; Mangani, S.; Turano, P. *Chemistry-A European Journal* **2016**, *22*, 16213–16219.

[258] Theil, E. C. *Annual Review of Biochemistry* **1987**, *56*, 289–315.

[259] Chasteen, N. D.; Harrison, P. M. *Journal of Structural Biology* **1999**, *126*, 182–194.

[260] Grace, J. E.; Van Eden, M. E.; Aust, S. D. *Archives of Biochemistry and Biophysics* **2000**, *384*, 116–122.

[261] Levi, S.; Santambrogio, P.; Cozzi, A.; Rovida, E.; Corsi, B.; Tamborini, E.; Spada, S.; Albertini, A.; Arosio, P. *Journal of Molecular Biology* **1994**, *238*, 649–654.

[262] Carmona, F.; Poli, M.; Bertuzzi, M.; Gianoncelli, A.; Gangemi, F.; Arosio, P. *Biochimica et Biophysica Acta* **2017**, *1861*, 522–532.

[263] Wojcik, R.; Dada, O. O.; Sadilek, M.; Dovichi, N. J. *Rapid Communications in Mass Spectrometry* **2010**, *24*, 2554–2560.

[264] Skinner, O. S.; Do Vale, L. H.; Catherman, A. D.; Havugimana, P. C.; Valle de Sousa, M.; Compton, P. D.; Kelleher, N. L. *Analytical Chemistry* **2015**, *87*, 3032–3038.

[265] Strohalm, M.; Kavan, D.; Novak, P.; Volny, M.; Havlicek, V. *Analytical Chemistry* **2010**, *82*, 4648–4651.

[266] Fellers, R. T.; Greer, J. B.; Early, B. P.; Yu, X.; LeDuc, R. D.; Kelleher, N. L.; Thomas, P. M. *Proteomics* **2015**, *15*, 1235–1238.

[267] Skinner, O. S. et al. *Nature Methods* **2016**, *13*, 237–240.

[268] Cassou, C. A.; Williams, E. R. *Analyst* **2014**, *139*, 4810–4819.

[269] Light-Wahl, K. J.; Schwartz, B. L.; Smith, R. D. *Journal of the American Chemical Society* **1994**, *116*, 5271–5278.

[270] Jurchen, J. C.; Williams, E. R. *Journal of the American Chemical Society* **2003**, *125*, 2817–2826.

[271] Haverland, N. A.; Skinner, O. S.; Fellers, R. T.; Tariq, A. A.; Early, B. P.; LeDuc, R. D.; Fornelli, L.; Compton, P. D.; Kelleher, N. L. *Journal of The American Society for Mass Spectrometry* **2017**,

[272] Zubarev, R. A.; Kelleher, N. L.; McLafferty, F. W. *Journal of the American Chemical Society* **1998**, *120*, 3265–3266.

[273] Syka, J. E.; Coon, J. J.; Schroeder, M. J.; Shabanowitz, J.; Hunt, D. F. *Proceedings of the National Academy of Sciences of the United States of America* **2004**, *101*, 9528–9533.

[274] Schennach, M.; Schneeberger, E.-M.; Breuker, K. *Journal of The American Society for Mass Spectrometry* **2016**, *27*, 1079.

[275] Compton, P. D.; Fornelli, L.; Kelleher, N. L.; Skinner, O. S. *International Journal of Mass Spectrometry* **2015**, *390*, 132–136.

[276] Turano, P.; Lalli, D.; Felli, I. C.; Theil, E. C.; Bertini, I. *Proceedings of the National Academy of Sciences* **2010**, *107*, 545–550.

[277] Carmona, U.; Li, L.; Zhang, L.; Knez, M. *Chemical Communications* **2014**, *50*, 15358–15361.

[278] Sciuto, S. V.; Liu, J.; Konermann, L. *Journal of The American Society for Mass Spectrometry* **2011**, *22*, 1679–1689.

[279] Loo, R.; Loo, J. A. *Journal of The American Society for Mass Spectrometry* **2016**, *27*, 975–990.

[280] Cui, W.; Zhang, H.; Blankenship, R. E.; Gross, M. L. *Protein Science* **2015**, *24*, 1325–1332.

Curriculum Vitae

MICHAEL O. MCANALLY

7649 N. Eastlake Ter. Apt. 2A ◇ Chicago, IL, 60626
(224) · 304 · 3404 ◇ mcanally@u.northwestern.edu

EDUCATION

Northwestern University, Evanston, IL *exp. July 2017*
Advisors: Richard P. Van Duyne and George C. Schatz
Ph.D. in Chemistry

University of Wisconsin - Eau Claire, Eau Claire, WI *May 2011*
Advisor: Stephen Drucker
B.S. in Chemistry & Mathematics

Member of American Chemical Society
Member of Phi Lambda Upsilon

AWARDS

National Science Foundation Graduate Research Fellow (2014-2017)

Recipient of National Research Council Fellowship Award (2017, *declined*)

Marie Sklodowska-Curie Actions Seal of Excellence (2017)

Recipient of National Defense Science and Engineering Graduate Fellowship Award (2013, *declined*)

UW-Eau Claire American Institute of Chemists Outstanding Senior Award (2011)

Department of Education Ronald E. McNair Scholar (2009-2011)

American Chemical Society-Student Affiliate Chemistry Freshman Award (2007)

RESEARCH EXPERIENCE

Northwestern University November 2012 - Present
Graduate Research Assistant *Evanston, IL*

- Developed new plasmonically-enhanced coherent Raman scattering experiments and theories for surface-enhanced femtosecond stimulated Raman scattering (SE-FSRS), surface-enhanced coherent anti-Stokes Raman scattering (SE-CARS), and surface-enhanced femtosecond Raman-induced Kerr-effect scattering (SE-FRIKES).
- Built amplified high-repetition rate setup for surface-enhanced coherent Raman scattering microspectroscopy.
- Studied the fundamentals of plasmonic enhancement in coherent Raman scattering processes to develop an analytic theory of SE-FSRS lineshapes.
- Designed an *in-situ* atomic layer deposition (ALD) localized surface plasmon resonance (LSPR) spectrometer for measuring shifts in LSPR as a function of ALD processing.
- Performed electronic structure calculations for collaborative projects in biological SERS sensing, catalytic SERS applications, and plasmon-assisted surface chemistry.
- Collaborated with mass spectrometry colleagues to develop a laser-assisted electospray ionization process in native mass spectrometry.

University of Wisconsin-Eau Claire May 2008 - May 2012
Undergraduate Research Assistant *Eau Claire, WI*

- Calculated $^3(n,\pi^*)$ and $^3(\pi,\pi^*)$ excited states of conjugated enones by TDDFT and EOM-EE-CCSD methods and performed jet-cooled fluorescence spectroscopy in a molecular beam apparatus.
- Researched the stability of molecular and van der Waals complexed O_4 and O_5 using density functional theory and population analysis techniques of Atoms-In-Molecules (AIM) and Natural Bonding Orbitals (NBO).
- Synthesized and characterized a linear MUC-1 peptide structure and conformation using FMOC-peptide synthesis, HPLC, mass spectrometry, and 2D NMR spectroscopy.

Graz Technical University (TU-Graz) June 2010 - August 2010
International Research Experience for Undergraduates *Graz, Austria*

- Studied effects of solvation and relativity in the NMR chemical shifts of plumbylene, stannylene, and other heavy group XIV complexes using density functional theory software in Gaussian09 and Amsterdam Density Functional.

TECHNICAL SKILLS

Experimental	SERS, LSPR, FSRS, SE-FSRS, CARS, SE-CARS, FRIKES, SE-FRIKES, supercontinuum generation, optical parametric amplification, CW lasers, Ti:Sapphire oscillators, Yb:fiber lasers, aluminum machining
Computational	ADF, Q-CHEM, ORCA, Gaussian, IGOR, LaTeX, MSOffice
Administrative	Grant writing, scientific outreach organization

TEACHING EXPERIENCE

University of Illinois-Chicago Fall 2016
Invited Lecturer *Chicago, IL*

- Presented a week of lectures to graduate students in a surface science chemistry course.
- Discussed fundamentals of catalytic chemistry, volcano plots, and applications Sabatier's principle to current catalysis research.

University of Illinois-Chicago Spring 2016
Invited Lecturer *Chicago, IL*

- Presented a week of lectures to graduate students in an advanced analytical chemistry course.
- Covered the expansion of the macroscopic polarization to describe optical processes including absorption, reflection, refraction, Raman scattering, second harmonic generation, sum and difference-frequency generation, Kerr-nonlinearities, stimulated Raman scattering, and coherent anti-Stokes Raman scattering.

Northwestern University Winter 2015
Graduate Teaching Assistant *Evanston, IL*

- Assisted in teaching the graduate course in time-dependent quantum mechanics.
- Gave lecture on basis sets in different electronic structure codes, graded homework sets and exams, assisted students with computational homework assignments.

Northwestern University Fall 2012 - Summer 2013
Teaching Assistant *Evanston, IL*

- Assisted in teaching an interdisciplinary thermodynamics and kinetics course for medical school bound undergraduates by giving review lectures, writing exams, and grading coursework.

- Assisted teaching general chemistry laboratory courses for first year undergraduates.
- Developed a new computational chemistry laboratory experiment that was used in the Northwestern general chemistry laboratory classes for multiple quarters.

PROFESSIONAL AND COMMUNITY DEVELOPMENT

Gordon Research Seminar on Vibrational Spectroscopy July 2018
University of New England *Biddeford, ME*

- Elected as co-chair of the Gordon Research Seminar on Vibrational Spectroscopy. Duties include scheduling speakers for the seminar, working with Gordon Research Conference organizers on the conference following the seminar, and fundraising for both the seminar and conference.

Science in the Classroom September 2013-Current
Hayt Elementary *Chicago, IL*

- Monthly science demonstrations (including explosions) for a classroom of third grade students allowing opportunities to explore and connect with science in a fun way.

All Scout Nano Day March 2013-March 2016
Northwestern University *Evanston, IL*

- Introduced the world of nanotechnology to boy and girl scouts (∼100 scouts/year) from across the Midwest by hands-on experimentation using colloidal nanoparticles, darkfield microscopy, atomic force microscopy, and SERS.

Sports and STEM Day September 2015
Northwestern University *Evanston, IL*

- Collaborative outreach activity with the Northwestern football team where middle school students interact with graduate students through the day, beginning with science demonstrations in the morning then a college football game in the afternoon.

PRESENTATIONS

1. Nanoscale Vibrational Spectroscopy with Ultrahigh Vacuum Tip-Enhanced Raman Spectroscopy, 1st NSC-CaSTL Symposium, University of Jyväskylä, June 2017. *Poster presentation.*
2. Understanding molecule-plasmon coupling in SE-FSRS: Combined experimental-theoretical studies, Naval Research Laboratory, May 2017. *Oral presentation, invited.*
3. Understanding molecule-plasmon coupling in SE-FSRS: Combined experimental-theoretical studies, Lawrence Berkeley National Laboratory, April 2017. *Oral presentation, invited.*
4. Understanding molecule-plasmon coupling in SE-FSRS: Combined experimental-theoretical studies, National Meeting of the American Chemical Society, April 2017. *Oral presentation.*
5. Multiplex determination of the Raman scattering cross-sections of glucose, Sonoma State Chemistry Department Colloquium, January 2017. *Oral presentation, invited.*
6. Spicing up SERS substrates with Ramen Raman Scattering, Richard P. Van Duyne Symposium: To SERS with Love, University of Minnesota, September 2016. *Poster presentation.* **Best poster award**.

7. Coupled-wave theory of surface-enhanced femtosecond stimulated Raman scattering, Gordon Research Conference on Vibrational Spectroscopy, University of New England, July 2016. *Poster presentation.* **Best poster award**.
8. Surface-enhanced femtosecond Raman-induced Kerr effect spectroscopy: Improving the signals of surface-enhanced femtosecond stimulated Raman spectroscopy by polarization sensitive excitation and detection, XVII International Conference on Transient Raman and Vibrational Spectroscopy, University of Wisconsin-Madison, June 2015. *Poster presentation.*
9. Beyond SERS: Chemistry at the Space-Time Limit, UW-Eau Claire Chemistry Department, November 2013. *Oral presentation, invited.*
10. Computational Investigation of the $\mathrm{T}_1(n,\pi^*)$ state in 2-Cyclohexen-1-one, International Symposium on Molecular Spectroscopy, The Ohio State University, June 2013. *Oral presentation.*
11. Computational Approaches to the Determination of the Molecular Geometry of Acrolein in its $\mathrm{T}_1(n,\pi^*)$ state, International Symposium on Molecular Spectroscopy, The Ohio State University, June 2012. *Oral presentation.*
12. Computed low-frequency vibrational modes of 2-cyclohexen-1-one in its $\mathrm{T}_1(n,\pi^*)$ state, Midwest Theoretical Chemistry Conference, University of Wisconsin-Madison, June 2012. *Poster presentation.*
13. Computational studies of chemical bonding in stable O_4, Midwest Theoretical Chemistry Conference, University of Wisconsin-Madison, June 2012. *Poster presentation.*
14. Computational examination of NMR chemical shifts for low-valent Sn and Pb complexes, 13th International Conference on the Coordination and Organometallic Chemistry of Germanium, Tin, and Lead, Graz TU, July 2010. *Poster presentation.* **Best poster award**.
15. Analysis of Structure and Conformation of a Linear MUC-1 peptide, 239th Meeting of the American Chemical Society, San Francisco, March 2010. *Poster presentation.*

PUBLICATIONS

1. Negru, B.; **McAnally, M.O.**; Schatz, G.C.; Van Duyne, R.P., Robust colloidal substrates for surface-enhanced femtosecond stimulated Raman scattering, *J. Phys. Chem. C*, **2017**, *In preparation.*
2. Sprague-Klein, E.A.; **McAnally, M.O.**; Zhdanov, D.V.; Zrimsek, A.B.; Apkarian, V.A.; Schatz, G.C.; Seideman, T.; Van Duyne, R.P., Plasmon-Driven Hot Electron Chemistry in Isotopically Edited 4,4'-Bipyridine Gold Nanoantennas, *J. Am. Chem. Soc.*, **2017**, *In preparation.*
3. Cardinal, M.F.; George, C.; Thornburg, N.E.; **McAnally, M.O.**; Notestein, J.M.; Schatz, G.C.; Stair, P.C.; Van Duyne, R.P., Surface-Enhanced Raman Scattering Detection of Plasmonic Substrate-Supported Peroxide Catalysis, *ACS Catalysis*, **2017**, *In preparation.*
4. Negru, B.; Sprague-Klein, E.A.; Madison, L.R.; **McAnally, M.O.**; Banik, M.; Hulkko, E.; Apkarian, V.A.; Ratner, M.A.; Schatz, G.C.; Seideman, T.; Van Duyne, R.P., Plasmon-Driven Electron Transfer Chemistry in Au Nanodumbells, *J. Am. Chem. Soc.*, **2017**, *In preparation.*
5. Skinner, O.S.*; **McAnally, M.O.***; Van Duyne, R.P.; Schatz, G.C.; Breuker, K.; Compton, P.D.; Kelleher, N.L., Native Electron Capture Dissociation Characterizes Iron-Binding Channels in Horse Spleen Ferritin, *Anal. Chem.*, **2017**, *R1 Submitted.* (**equal contribution*)

6. Chiang, N.; Goubert, G.; Pozzi, E.A.; **McAnally, M.O.**; Chapman, C.T.; Jiang, N.; Schatz, G.C.; Van Duyne, R.P., Ultrahigh Vacuum Tip-Enhanced Raman Spectroscopy, *Recent developments in plasmon supported Raman spectroscopy*, Eds., Katrin Kneipp, Yukihiro Ozaki, and Zhong-Qun Tian, **2017**, *Accepted.*
7. **McAnally, M.O.**; Phelan, B.T.; Young, R.M.; Wasielewski, M.R.; Schatz, G.C.; Van Duyne, R.P., Quantitative Determination of the Differential Raman Scattering Cross-Sections of Glucose by Femtosecond Stimulated Raman Scattering, *Anal. Chem.*, **2017**, *89*, 6931-6935.
8. Buchanan, L.E.; **McAnally, M.O.**; Gruenke, N.L.; Schatz, G.C.; Van Duyne, R.P., Studying Stimulated Raman Activity in Surface-Enhanced Femtosecond Stimulated Raman Spectroscopy by Varying the Excitation Wavelength, *J. Phys. Chem. Lett.*, **2017**, *8*, 3328-3333.
9. Hackler, R.A.; **McAnally, M.O.**; Schatz, G.C.; Stair, P.C.; Van Duyne, R.P., Identification of Dimeric Methylalumina Surface Species during Atomic Layer Deposition via Surface-Enhanced Raman Spectroscopy, *J. Am. Chem. Soc.*, **2017**, *139*, 2456-2463.
10. Cardinal, M.F.; Vander Ende, E.R.; Hackler, R.A.; **McAnally, M.O.**; Stair, P.C.; Schatz, G.C.; Van Duyne, R.P., Expanding SERS Applications Thanks to Versatile Nanomaterials Engineering, *Chem. Soc. Rev.*, **2017**, *46*, 3886-3903.
11. Zrimsek, A.B.; Chiang, N.; Mattei, M.; Zaleski, S.; **McAnally, M.O.**; Chapman, C.T.; Henry, A.-I.; Schatz, G.C.; Van Duyne, R.P., Single-Molecule Chemistry with SERS and TERS, *Chem. Rev.*, **2017**, *117*, 7583-7613.
12. Pozzi, E.A.; Goubert, G.; Chiang, N.; Jiang, N.; Chapman, C.T.; **McAnally, M.O.**; Henry, A.-I.; Seideman, T.; Schatz, G.C.; Hersam, M.C.; Van Duyne, R.P., Ultrahigh Vacuum Tip-Enhanced Raman Spectroscopy, *Chem. Rev.*, **2017**, *117*, 4961-4982.
13. **McAnally, M.O.**; Guo, Y.; Balakrishnan, G.; Schatz, G.C.; Van Duyne, R.P., Understanding the vibrational mode specific polarization effects in femtosecond Raman-induced Kerr-effect spectroscopy, *Opt. Lett.*, **2016**, *41*, 5357-5360.
14. **McAnally, M.O.**; McMahon, J.M.; Van Duyne, R.P.; Schatz, G.C., Coupled-wave theory of surface-enhanced femtosecond stimulated Raman scattering, *J. Chem. Phys.*, **2016**, *145*, 094106.
15. Gruenke, N.L.; **McAnally, M.O.**; Schatz, G.C.; Van Duyne, R.P., Balancing the effects of extinction and enhancement for optimal signal when combining stimulated and surface-enhanced Raman spectroscopies, *J. Phys. Chem. C*, **2016**, *120*, 29449-29454.
16. Buchanan, L.E.; Gruenke, N.L.; **McAnally, M.O.**; Negru, B.; Mayhew, H.E.; Apkarian, V.A.; Schatz, G.C.; Van Duyne, R.P., Surface-Enhanced Femtosecond Stimulated Raman Spectroscopy at High Repetition Rates and Ultralow Raman Pump and Probe Energies, *J. Phys. Chem. Lett.*, **2016**, *7*, 4629-4634.
17. Gruenke, N.L.; Cardinal, M.F.; **McAnally, M.O.**; Frontiera, R.R.; Schatz, G.C.; Van Duyne, R.P., Ultrafast surface enhanced Raman spectroscopy for molecular plasmonics, *Chem. Soc. Rev.*, **2016**, *45*, 2263-2290.
18. Masango, S.S.; Hackler, R.A.; Henry, A.-I.; **McAnally, M.O.**; Schatz, G.C.; Stair, P.C.; Van Duyne, R.P., Probing the Chemistry of Alumina Atomic Layer Deposition Using *Operando* Surface-Enhanced Raman Spectroscopy, *J. Phys. Chem. C*, **2016**, *120*, 3822-3833.
19. Masango, S.S.; Hackler, R.A.; Large, N; Henry, A.-I.; **McAnally, M.O.**; Schatz, G.C.; Stair, P.C.; Van Duyne, R.P., High-Resolution Distance Study of Surface-Enhanced Raman

Scattering Enabled by Atomic Layer Deposition, *Nano Lett.*, **2016**, *16*, 4251-4259.

20. **McAnally, M.O.***; Zabronsky, K.L.*; Stupca, D.J.; Phillipson, K.; Pillsbury, N.R.; Drucker, S., Lowest triplet (n,π*) state of 2-cyclohexen-1-one: Characterization by cavity ringdown spectroscopy and quantum-chemical calculations, *J. Chem. Phys.*, **2013**, *139* (21), 214311. (**equal contribution*)
21. Hlavacek, N.C.; **McAnally, M.O.**; Drucker, S., Lowest triplet (n,π*) electronic state of acrolein: Determination of structural parameters by cavity ringdown spectroscopy and quantum-chemical methods, *J. Chem. Phys.*, **2013**, *138* (6), 64303.